

The Fatigue of Carbon Fibre Composites Containing Interlaminar Inkjet Printed Polymer Droplets

Andrew Lewis Cartledge

A Thesis Presented for the Degree of
Doctor of Philosophy



The
University
Of
Sheffield.

Department of Mechanical Engineering

Faculty of Engineering

The University of Sheffield, UK

September 2017

ABSTRACT

The objective of this research was to investigate a novel method of increasing the interlaminar toughening of prepreg composites to improve their fatigue performance, with particular emphasis on the retardation of delamination.

Thermoplastic polymers droplets were deposited onto a composite prepreg using inkjet printing. Poly(methyl methacrylate) (PMMA) and polyethylene glycol (PEG) were dissolved in suitable solvents, creating polymer solutions that could be deposited onto prepreg substrates with excellent volume and position control. The prepreg laminae were then laid up to create complete laminates which contained the toughening polymers exclusively in their interlaminar regions, therefore leaving the bulk matrix properties unchanged.

Both four point bending and tensile mechanical tests were used to evaluate the performance of printed composites. Results showed that multidirectional laminates printed with a solution of 10% by weight 20,000 molecular weight (M_w) PEG in deionised water exhibited significant retardation of delamination, being shown to reduce the rate of delamination by almost half in comparison to unprinted laminates. These laminates also showed increases of tensile strength and modulus of 4.9% and 12.3% respectively. Whilst laminates printed with PMMA and lower molecular weight PEG solutions were also shown to improve static mechanical properties, they also resulted in greatly increased rates of delamination in cyclic loading.

Scanning electron microscopy was also used to analyse the delaminated surfaces of tensile samples. It was found that PMMA did not affect the bulk matrix properties in the interlaminar region. However, PEG was shown to result in increased matrix toughness and fibre/matrix bonding. PEG 20,000 M_w was shown to exhibit the greatest increase of fibre/matrix bonding, whilst PEG 1,500 M_w was shown to increase the ductility of the interlaminar matrix to an extent which was detrimental to the delamination resistance of laminates.

The work presented in this thesis generated new understanding of the damage mechanisms operating at the interlaminar interface of cyclically loaded inkjet printed composites. It also demonstrated that such printed composites could potentially outperform unprinted laminates.

The Fatigue of Carbon Fibre Composites
Containing Interlaminar Inkjet Printed
Polymer Droplets

Andrew Lewis Cartledge

September 2017

CONTENTS

Chapter 1: Introduction	1
1.1 Motivation.....	1
1.2 Key Objectives.....	2
1.3 Project Novelty	3
1.4 Project Legacy	3
Chapter 2: Literature Review.....	7
2.1 Composite materials.....	7
2.1.1 Fibres.....	7
2.1.2 Matrices.....	12
2.1.3 Manufacturing Methods.....	13
2.2 Inkjet Printing	18
2.3 Fatigue of Composites	21
2.3.1 Damage Mechanisms	23
2.3.2 Free-Edge stresses.....	29
2.3.3 Stacking Sequence	31
2.4 Interlaminar Toughening of Composites	32
2.4.1 Fibrous Interlaminar Reinforcements	33
2.4.2 Interleaving and Additive Toughening	34
2.5 Experimental Fatigue of Composites.....	36
2.6 Damage Analysis Techniques.....	40
2.6.1 Stiffness Degradation.....	40
2.6.2 Sample Replication	41
2.6.3 Scanning Electron Microscopy	43
2.6.4 Fractography	44
2.6.5 X-Ray Computed Tomography.....	51
2.7 Concluding Remarks.....	52
Chapter 3: Material Selection, Manufacture, and Characterisation	55

3.1 Introduction.....	55
3.2 Materials Selection.....	55
3.2.1 Prepreg.....	55
3.2.2 Inks.....	57
3.3 Inkjet Printing	59
3.3.1 Printing Process	61
3.3.2 Printed Pattern.....	64
3.4 Material Coverage, Volume, and Mass.....	66
3.5 Manufacture of Composite Laminates.....	71
3.6 Direct Scanning Calorimetry	74
3.6.1 DSC Procedure.....	75
3.6.2 DSC Results	76
3.7 Dynamic Mechanical Thermal Analysis.....	77
3.7.1 DMTA Procedure.....	78
3.7.2 DMTA Results	79
3.8 Durability of Printed Prepregs	81
3.9 Printed Resin Slides	82
3.9.1 Preparation of Slides	83
3.9.2 Results.....	84
3.9.3 Conclusions.....	95
3.10 Concluding Remarks.....	96
Chapter 4: Mechanical Testing Procedures	99
4.1 Flexural Testing	99
4.1.1 Development of Four Point Bending Jig.....	101
4.1.2 Four Point Bending Jig Dimensions	104
4.1.3 Test Frame Calibration.....	107
4.1.4 Measurement of Midpoint Deflection.....	108
4.1.5 Static Flexural Tests.....	108
4.1.6 Development of LabView Data Acquisition Software	111

4.1.7 Optimisation of Data Acquisition Rate	113
4.1.8 Test control Modes.....	114
4.1.9 Cyclic Flexural Tests	114
4.2 Tensile Testing.....	118
4.2.1 Stacking Sequence of Tensile Specimens	118
4.2.2 Sample Deflection Measurement	119
4.2.3 Cellulose Acetate Replica Method.....	121
4.2.4 Static Tensile Tests	122
4.2.5 Cyclic Tensile Tests	124
4.2.6 Cyclic Tensile Tests at $0.5\sigma_t$	126
Chapter 5: Mechanical Test Results.....	129
5.1 Static Flexural Tests.....	129
5.2 Cyclic Flexural Tests	132
5.2.1 Fatigue Life	132
5.2.2 Stiffness Degradation.....	134
5.2.3 Evaluation of the Test Method.....	142
5.3 Static Tensile Tests	144
5.4 Cyclic Tensile Tests	149
5.4.1 Fatigue Life	149
5.4.2 Stiffness Degradation.....	150
5.5 Discussion	167
5.5.1 Flexural Testing	167
5.5.2 Tensile Testing.....	170
5.6 Conclusions	183
Chapter 6: Fractography and Crack Density Analysis	187
6.1 Introduction to SEM	187
6.2 Experimental Procedures	187
6.2.1 Fractography	188
6.2.2 Crack Densities	191

6.3 Experimental Results	195
6.3.1 Fractography	195
6.3.2 Crack Densities	209
6.4 Discussion	218
6.4.1 Fractography	218
6.4.2 Crack Density Measurements	228
6.5 Conclusions	230
Chapter 7: Conclusions and Further Work	233
7.1 Conclusions	233
7.2 Further Work	237
References	241

LIST OF FIGURES

Figure 1.1: G_{Ic} comparison between virgin and printed composite laminates in double cantilever beam tests conducted by Zhang [12]. Error bars represent standard deviation.	4
Figure 1.2: a) A printed hexagonal pattern on carbon fibre prepreg. b) Illustration of how printed prepreg laminae are laid up to make a laminate containing interlaminar droplets.....	4
Figure 2.1: Exploded view of a laminate construction consisting of unidirectional plies [1]	8
Figure 2.2: a) A representation of a complex 3D interlocking woven fabric composite [14] b) A finite element model of woven composite showing stresses placed on fibre bundles when under tensile loading [15]	8
Figure 2.3: Ashby plot comparing commonly used engineering materials [16]	9
Figure 2.4: Illustration of the structure of carbon fibres in cross-section consisting of folded graphite layers [22].....	11
Figure 2.5: Chemical structure of an epoxide group [27]	12
Figure 2.6: Unit cell dimensions of a collection of close packed, circular cross-section fibres	14
Figure 2.7: Illustration of the spray layup process [31]	15
Figure 2.8: a) Resin transfer moulding b) Vacuum assisted resin transfer moulding [31]	16
Figure 2.9: Illustration of autoclave curing [31]	17
Figure 2.10: Illustration of continuous inkjet printing [41]	20
Figure 2.11: Illustration of droplet on demand printing [41]	20
Figure 2.12: Electrical actuation of a piezo-electric DOD system [42]	21
Figure 2.13: Degradation of composite strength by wear-out until residual strength falls below the peak cyclic stress [4]	22
Figure 2.14: Damage modes during fatigue life [1]	22
Figure 2.15: SEM image of matrix cracking propagating through an off-axis ply, jumping between fibre/matrix interfaces [52]	24
Figure 2.16: Transverse matrix cracking in a cross-ply laminate [53].....	24
Figure 2.17: Path that cracks may take when travelling perpendicular to fibres. a) Crack progressing to adjacent fibres causing b) fibre/matrix interface debonding by blunting crack tip and/or c) fibre-bridged crack growth. d) A fibre break away from the crack tip [56]	25

Figure 2.18: SEM micrograph of carbon fibre laminate showing transverse ply cracking and delaminations extending from where the crack meets the adjacent ply of perpendicular orientation [65]	27
Figure 2.19 Delamination process zones in a) composites with brittle resins, and b) composites with ductile resins [63]	27
Figure 2.20: Free-body diagram for a cross-ply laminate in tension in the x direction [68]	28
Figure 2.21: A four-ply laminate under uniform axial strain. Shows the stresses acting upon a unit cell of a central ply. [68].....	30
Figure 2.22: Stress distribution at the edge interface ranging from the centreline ($y/b=0$) to edge ($y/b=1$) [68].....	31
Figure 2.23: Electro-spun Nylon-6,6 fibre interleaf under mode I loading [85].....	33
Figure 2.24: Illustration of interleaving [11]	34
Figure 2.25: Generalised model of the decrease in stiffness associated with composite fatigue with increasing numbers of cycles. Stage I: Matrix cracking and delamination. Stage II: Crack coupling and interfacial debonding. Stage III: Damage coalescence and fibre breaking. [141].....	41
Figure 2.26: Comparison between a) optical and b) SEM viewing a replica at high magnification, illustrating the difference in depth of field of the two techniques [142]	43
Figure 2.27 Unprinted sample showing fibres and fibre imprints in a) fibre dominated surface, b) matrix dominated surface [5].....	45
Figure 2.28 Mechanism for the formation of cusps due to shear. In this case shear is caused by flexural geometry, but is applicable to any case where a strain difference exists between plies. [5]	46
Figure 2.29 Mechanism for the growth and coalescence of cusps. The shear stress ahead of the crack tip can be resolved to a tensile traction which is inclined at 45° . a) Angled cracks develop in the matrix ahead of the crack tip, usually originating at fibre interfaces. b) Cracks extend under shear stress. c) The presence of fibres at the interlaminar boundary cause the crack tips to rotate. d) Cracks converge to create characteristic ‘S’ shaped cusps. [5].....	46
Figure 2.30 Scallops on the surface of a sample [5]	47
Figure 2.31 Cusps being driven ahead of a crack front. Cusps form on the tensile surface, and negative ‘scallop’ form on the compressive surface. [5].....	47
Figure 2.32 Gouges on the surface of a delaminated ply [5]	48
Figure 2.33 Mechanism for gouge formation at a $0^\circ/90^\circ$ interface. Cracks develop at the fibre boundary in the compressive ply and propagate through the matrix at	

45° due to the same resolved tensile stresses caused by mixed mode loading which cause cusp formation [5].....	48
Figure 2.34 Debris on a delaminated surface [5]	49
Figure 2.35 Matrix rollers on a mode II fatigue fracture surface. a) Untoughened matrix. b) Toughened matrix [5].....	50
Figure 2.36 Representative cusps in a) a brittle matrix, and b) a relatively ductile matrix [5]	51
Figure 2.37 Fibrillation in a highly ductile matrix [5]	51
Figure 2.38 X-ray CT and ultrasound C-Scans obtained by Tsao and Hocheng [170] showing the extent of delamination in composite laminates featuring holes drilled by various methods	52
Figure 3.1: Jetlab 4 droplet on demand printer manufactured by Microfab Inc.	59
Figure 3.2: CT-PT4 pneumatics controller [181].....	60
Figure 3.3: MJ series droplet on demand piezoelectric printhead with glass capillary nozzle [182].....	60
Figure 3.4: Cabinet interior of Jetlab 4 inkjet printer a) printing stage b) printhead c) ink reservoir d) droplet jet camera.....	61
Figure 3.5: Electrically heated reservoir jacket used to increase the solubility of PMMA in DMF at low room temperatures	61
Figure 3.6: Jetlab control software graphical user interface	62
Figure 3.7: Clean ejection of a droplet.....	63
Figure 3.8: Main droplet ejected with a satellite droplet. Scale minor divisions 0.1mm. [11]	63
Figure 3.9: Images presented by Zhang showing PMMA droplets in a hexagonal pattern a) before, and b) after heating. During heating, the surface tension of the melted PMMA pulled the droplets into a small area in the centre [11].....	65
Figure 3.10: Images presented by Zhang showing a printed PMMA film a) before heating, and b) after heating. During heating, surface tension between the droplets was uneven and caused them to break up into unevenly dispersed droplets of varying sizes [11]	65
Figure 3.11: Examples of a) square arrays and b) hexagonal arrays. c) Illustration of how a hexagonal array is made off three identical rectangular arrays offset from each other. The different colours represent different printing passes.....	66
Figure 3.12: Illustrations of a unit cell of a rectangular array. a) Representative unit cell. b) Repeating unit cell transposed onto an optical microscope image of a hexagonal printed array of droplets.....	67

Figure 3.13: a) Vacuum bagged prepreg laminate and b) Cross-section of a typical vacuum bag [186].....	71
Figure 3.14: Cure cycle for 977-2 prepreg.....	72
Figure 3.15: Interpretation of how different composite plate manufacturing methods may affect panel shape. Gaps between steel plates create a vacuum gap which extrudes to composite panel.	73
Figure 3.16: DSC may be used to measure the degree of cure by direct comparison of exothermic troughs. The area of exothermic troughs caused by resin curing may be compared to the area of smaller post-cure troughs to directly quantify the level of cure. [188].....	75
Figure 3.17: PerkinElmer DSC 8000 Double-Furnace testing machine	76
Figure 3.18: DSC heating cycle for tests used to evaluate degree of cure.....	76
Figure 3.19: Result of a DSC test conducted on cured 977-2 composite. Different colours represent the separate heating cycles that the sample was subjected to. Both cycles begin at 20°C and 0mW heat flow and continue in a clockwise direction as indicated by the arrows. The second heating cycle was conducted immediately once the first cycle returned to 20°C.....	77
Figure 3.20: PerkinElmer DMA 8000.....	78
Figure 3.21: A sample mounted in the three point bend test configuration. The mechanical actuator is attached to the central loading point.	79
Figure 3.22: Example graph of 977-2 CFRP (sample 6) tested in three point bending DMA at 1Hz. Red lines represent the intersecting gradients of the separate linear portions of the curves. The dashed line represents their intersection point along the temperature axis.....	80
Figure 3.23: Example of smeared PMMA droplets on uncured 977-2 prepreg.....	82
Figure 3.24: Comparison of PMMA droplets printed onto a) uncured 977-2 prepreg b) glass microscope slide	85
Figure 3.25: Microscope images of PMMA droplets printed onto a part-cured resin film. The resin was partially cured at 180°C for a) 5 minutes b) 10 minutes c) 20 minutes. The contrast of images a and b were digitally enhanced.	86
Figure 3.26: Post-curing microscope images of PMMA droplets printed onto a part-cured resin film. The resin was partially cured at 180°C for a) 5 minutes b) 10 minutes c) 20 minutes. d) Enlarged view of PMMA droplets in resin partially cured for 20 minutes. The contrast of all images were digitally enhanced.	88
Figure 3.27: Comparison of PEG 1,500M _w droplets printed onto a) uncured 977-2 prepreg b) glass microscope slide.....	89

Figure 3.28: Microscope images of PEG 1,500M _w droplets printed onto a part-cured resin film. The resin was partially cured at 180°C for a) 5 minutes b) 10 minutes c) 20 minutes	91
Figure 3.29: Cavitation forming behind a sphere dropped into water and the air bubble which is formed by the water closing around the cavity [202].....	91
Figure 3.30: Comparison of PEG 20,000M _w droplets printed onto a) uncured 977-2 prepreg b) glass microscope slide.....	92
Figure 3.31: Microscope images of PEG 20,000M _w droplets printed onto a part-cured resin film. The resin was partially cured at 180°C for a) 5 minutes b) 10 minutes c) 20 minutes. The contrast of images <i>a</i> and <i>b</i> were digitally enhanced.....	93
Figure 3.32: Microscope images of PEG 20,000M _w droplets printed onto a part-cured resin film. The resin was partially cured at 180°C 20 minutes. PEG droplets on the glass slide only are broken up, whereas droplets on the resin spread. The contrast of the image was digitally enhanced.....	94
Figure 3.33: DMF printed in hexagonal pattern onto resin partially cured at 180°C for 10 minutes. The contrast of both images were digitally enhanced.....	95
Figure 4.1: Illustration of a laminate under flexural loading. Flexural samples experience varying degrees of strain throughout their thickness. [203]	100
Figure 4.2: Comparisons of transverse loads and bending moments in three and four point loading scenarios [204].....	101
Figure 4.3: Initial four point bend jig design	102
Figure 4.4: Four point bend jig with leg attachments	102
Figure 4.5: Anti sample rotation jaws attached to the supporting roller blocks.....	103
Figure 4.6: Roller bearing mounts and increased diameter rollers	104
Figure 4.7 Technical drawing of main four point bend jig blocks. Two of these are used in the jig, and are the main body. They have slots cut in them to allow adjustment of the roller blocks so that the jig can accommodate samples of varying dimensions. Drawing not to scale.	105
Figure 4.8 Technical drawing of a roller block. These blocks hold the rollers in place. They are attached to the main blocks by a single M10 cap screw bolt. Two M6 threaded holes were added in later revisions in order to allow the fitment of roller bearings. Drawing not to scale.	105
Figure 4.9 Technical drawing of anti-rotation arms. These were attached to the upper main block and kept the two halves of the jig aligned with each other. Drawing not to scale.....	106

Figure 4.10 Technical drawing of a bearing block. These were added to the loading roller blocks in later revisions to hold 19x10x5mm spherical roller bearings. The bearings were held captive by bearing retaining compound. Drawing not to scale.....	106
Figure 4.11 Assembly drawing of the components in the intended configuration. Also features M16 treaded bars which allow the jig to be mounted in the testing machine. Lock nuts were used on the threaded bar in order to prevent jig rotation. M6 cap bolts were used for the fixture of all other components. Drawing not to scale.....	107
Figure 4.12: Lever arm arrangement to capture sample midpoint deflection	108
Figure 4.13: Schematic of four point bend test dimensions.....	110
Figure 4.14: A composite sample under compression in four point bending	110
Figure 4.15: Nene 12.5kN servo-hydraulic test machine, and MOOG SmarTEST ONE controller	110
Figure 4.16: LabView DAQ: a) User interface, b) Visual program design	112
Figure 4.17: Example waveforms captured by LabView DAQ.....	112
Figure 4.18: Maximum error at numbers of data points from 1 to 100.....	113
Figure 4.19: Illustration of load parameters used in cyclic tests.....	117
Figure 4.20: Stacking sequence used in tensile tests. Ply orientations are relative to the direction of loading.	119
Figure 4.21: LVDT setup used to measure grip separation in tensile tests.....	120
Figure 4.22: Image of DAQ measurements of cyclic data. Data captured by the external LVDT (green) shows considerably more accuracy than the internal machine LVDT (red).....	121
Figure 4.23: An acetate replica mounted on a glass microscope slide prepared for SEM observation	122
Figure 4.24: Tensile specimen geometry	123
Figure 4.25: Tensile sample in situ in the Mayes 100kN servo-hydraulic test frame.....	124
Figure 5.1: Averaged load-displacement curves for static flexural tests of unprinted and PMMA printed laminates. The points at which the gradient was calculated are marked on the plot. The location of these points varied slightly depending upon the strain at which the individual samples fractured. The limited range of these points stems from a misunderstanding in the requirements of the test standard.	130
Figure 5.2: Fatigue life diagram of 977-2 laminates under cyclic flexural loading before the introduction of four point bending jig modifications: R=0.1, f=5Hz. ■→	

indicates overlap of printed and unprinted sample types which did not fracture at 1×10^6 cycles.	133
Figure 5.3: Fatigue life diagram of 977-2 laminates under cyclic flexural loading after the introduction of four point bending jig modifications: $R=0.1$, $f=5\text{Hz}$. ■→ indicates overlap of printed and unprinted sample types which did not fracture at 1×10^6 cycles.	134
Figure 5.4: a) Flexural modulus of samples in cyclic flexural loading at a stress factor of 0.85. b) Normalised Flexural modulus of samples in cyclic flexural loading at a stress factor of 0.85.....	137
Figure 5.5: a) Flexural modulus of samples in cyclic flexural loading at a stress factor of 0.8. b) Normalised Flexural modulus of samples in cyclic flexural loading at a stress factor of 0.8.....	138
Figure 5.6: a) Flexural modulus of samples in cyclic flexural loading at a stress factor of 0.7. b) Normalised Flexural modulus of samples in cyclic flexural loading at a stress factor of 0.7.....	139
Figure 5.7: a) Flexural modulus of samples in cyclic flexural loading at a stress factor of 0.65. b) Normalised Flexural modulus of samples in cyclic flexural loading at a stress factor of 0.65.....	140
Figure 5.8: a) Flexural modulus of samples in cyclic flexural loading at a stress factor of 0.6. b) Normalised Flexural modulus of samples in cyclic flexural loading at a stress factor of 0.6.....	141
Figure 5.9: Delamination observed in an unprinted flexural sample under cyclic loading at a stress factor of 0.7.....	142
Figure 5.10: Randomly selected samples of ranging stress factors that failed in cyclic loading. In all cases, fracture occurred at the loading points.....	143
Figure 5.11: SEM micrograph of an incomplete fatigue crack extending through the thickness of a flexural sample. The crack originated on the left of the image, propagating inwards to the right of the image.....	143
Figure 5.12: SEM micrograph of the fracture surface of a flexural sample. Fracture was through the thickness of the sample, and showed two distinct regions. On the left, tensile fracture. And on the right, a fatigue crack surface.....	144
Figure 5.13: Typical stress/strain curves for multidirectional 977-2 tensile test specimens. The points at which the gradient was calculated are marked on the plot. The location of these points varied slightly depending upon the strain at which the individual samples fractured. The limited range of these points stems from a misunderstanding in the requirements of the test standard.	146

Figure 5.14: Tensile strengths of multidirectional 977-2 laminates. Error bars indicate standard deviation.....	148
Figure 5.15: Tensile moduli of multidirectional 977-2 laminates. Error bars indicate standard deviation.....	148
Figure 5.16: Fatigue life diagram of 977-2 laminates under cyclic tensile loading: R=0.1, f=5Hz. ■→ indicates overlap of printed and unprinted sample types which did not fracture at 1×10^6 cycles.	150
Figure 5.17: a) Tensile modulus of samples in cyclic tensile loading at a stress factor of 0.8. b) Normalised tensile modulus of samples in cyclic tensile loading at a stress factor of 0.8.	152
Figure 5.18: a) Tensile modulus of samples in cyclic tensile loading at a stress factor of 0.7. b) Normalised tensile modulus of samples in cyclic tensile loading at a stress factor of 0.7.	154
Figure 5.19: a) Tensile modulus of samples in cyclic tensile loading at a stress factor of 0.7. The x axis is scaled to view the initial stiffness degradation of samples. b) Normalised tensile modulus of samples in cyclic tensile loading at a stress factor of 0.7 with scaled x axis.....	155
Figure 5.20: a) Tensile modulus of samples in cyclic tensile loading at a stress factor of 0.6. b) Normalised tensile modulus of samples in cyclic tensile loading at a stress factor of 0.6.	156
Figure 5.21: a) Tensile modulus of samples in cyclic tensile loading at a stress factor of 0.6. The x axis is scaled to view the initial stiffness degradation of samples. b) Normalised tensile modulus of samples in cyclic tensile loading at a stress factor of 0.6 with scaled x axis.....	157
Figure 5.22: a) Tensile modulus of samples in cyclic tensile loading at a stress factor of 0.5. b) Normalised tensile modulus of samples in cyclic tensile loading at a stress factor of 0.5.	159
Figure 5.23: a) Tensile modulus of samples in cyclic tensile loading at a stress factor of 0.5. The x axis is scaled to view the initial stiffness degradation of samples. b) Normalised tensile modulus of samples in cyclic tensile loading at a stress factor of 0.5 with scaled x axis.....	160
Figure 5.24: a) Tensile modulus of PEG printed samples in cyclic tensile loading at a stress factor of 0.5. b) Normalised tensile modulus of PEG printed samples in cyclic tensile loading at a stress factor of 0.5.....	162
Figure 5.25: a) Tensile modulus of PEG printed samples in cyclic tensile loading at a stress factor of 0.5. The x axis is scaled to view the initial stiffness	

degradation of samples. b) Normalised tensile modulus of PEG printed samples in cyclic tensile loading at a stress factor of 0.5 with scaled x axis...	163
Figure 5.26: a) Average curves of all sample types in cyclic tensile loading at a stress factor of 0.5. b) Normalised average curves of all sample types in cyclic tensile loading at a stress factor of 0.5.	165
Figure 5.27: a) Average curves of all sample types in cyclic tensile loading at a stress factor of 0.5. The x axis is scaled to view the initial stiffness degradation of samples. a) Normalised average curves of all sample types in cyclic tensile loading at a stress factor of 0.5 with scaled x axis.	166
Figure 5.28: Fatigue life diagram published by Jones et al. showing the fatigue lives of $\pm 45^\circ$ tensile laminates consisting of carbon, glass, and Kevlar reinforced epoxy matrix laminates: $R=0.1$, constant load rate of 100kNs^{-1} [220].....	168
Figure 5.29: Possible crack mechanisms in PMMA printed laminates, where cracks are represented by dashed lines. a) A crack circumventing a droplet by travelling around its boundary, b) A crack propagating through a droplet, c) A crack meeting the separated interface of a droplet, halted by crack tip blunting.	173
Figure 5.30 Example of a fatigued tensile specimen cycled to 1×10^6 cycles. Compressive force was applied to the ends of the specimen by hand in order to open and emphasis the delamination.	175
Figure 5.31 Stiffness degradation curves obtained by Poursartip et al. for $[45/90/-45/0]_s$ laminates at a stress factor of 0.56. These curves show excellent resemblance to the stiffness degradation curves obtained in these tests.	176
Figure 5.32: Experimental stiffness degradation data obtained by Paepegem and Degrieck [131]. Taken from fully reversed flexural fatigue tests on unidirectional samples.	177
Figure 5.33: Typical stiffness degradation curve for a wide range of fibre-reinforced composite materials. Based on work by Nijssen [141]. This curve is considered to have three phases (I, II, and III) which are not mutually exclusive. The damage mechanisms operating in these phases are: I) Matrix cracking and delamination in off axis plies, II) Delamination growth and interfacial debonding, III) Fibre fracture and crack coupling resulting in ultimate failure. These mechanisms are also shown in the figure, where red lines indicate cracks and delaminations.	178
Figure 5.34: Newly proposed model of stiffness degradation in composites. This curve recognises the same phases as the above figure, but further divides phase I into two (Ia and Ib) in which matrix cracking and delamination are sequential. The damage mechanisms operating in these phases are: Ia)	

Matrix cracking, Ib) Delamination at off-axis ply boundaries, II) Continued delamination growth and interfacial debonding, III) Fibre fracture and crack coupling resulting in ultimate failure. These mechanisms are also shown in the figure, where red lines indicate cracks and delaminations.	179
Figure 6.1: Emscope SC 500 gold vapour deposition machine	189
Figure 6.2: Examples of carbon fibre composite samples mounted on brass SEM specimen stubs a) before gold coating, and b) after gold coating. These samples were used for the observation of cracks propagating through the width of specimens.	190
Figure 6.3: Electron microscope used for microscopic analysis. Hitachi TM3030Plus tabletop microscope.....	191
Figure 6.4 Example SEM micrograph of an edge replica. a) Unmodified image, and b) the same image with the individual plies labelled.	193
Figure 6.5 a) A typical replica micrograph displaying both transverse cracks and delaminations. b) The same image overlaid with lines indicating the locations of cracks and delaminations.....	195
Figure 6.6 Unprinted sample a) 0° delamination surface, b) 90° delamination surface	196
Figure 6.7 Cusps on the 0° surface of an unprinted specimen	196
Figure 6.8 Rollers on the 90° surface of an unprinted specimen	197
Figure 6.9 PMMA printed sample a) 0° delamination surface, b) 90° delamination surface.	197
Figure 6.10 Cusps on the 0° surface of a PMMA printed specimen.....	198
Figure 6.11 Rollers on the 0° surface of a PMMA printed specimen	198
Figure 6.12 a) A group of hemispherical voids of varying diameters within the surface resin of a delaminated specimen. b) & c) Magnified views of individual voids.	199
Figure 6.13 Spherical particles contained within voids in the matrix of PMMA printed samples	200
Figure 6.14 PEG 1,500M _w printed sample a) 0° delamination surface, b) 90° delamination surface	200
Figure 6.15 0° delamination surface with matrix showing a significant degree of plasticity. Cusps are flat and possibly smeared. Also note that there is no significant step change between fibre and matrix dominated regions, indicating that the resin-rich region was very thin in these samples.	201
Figure 6.16 Unprinted 90° delaminated surface showing significant ridges where the surface transitions from matrix dominated to fibre dominated	202

Figure 6.17 Optical micrographs showing the resin-rich regions (lighter shade) of a) unprinted, b) PMMA, c) PEG 1,500M _w , and d) PEG 20,000M _w samples. All micrographs were taken at the same magnification, and hence are the same scale.	202
Figure 6.18 PEG 20,000M _w printed sample a) 0° delamination surface, b) 90° delamination surface.....	203
Figure 6.19 Transition between matrix and fibre dominated surfaces on a 0° ply	203
Figure 6.20 Cusps on a 0° PEG 20,000M _w delaminated surface	204
Figure 6.21 Rudimentary rollers on a 0° PEG 20,000M _w delaminated surface. In most cases rollers never separated from the surrounding matrix.	205
Figure 6.22 a) Cusps leaning towards the origin of a delamination in a fibre dominated ply. b) Cusps leaning away from the origin of a delamination in a matrix dominated ply. The delaminations were seeded by transverse cracks in 90° plies.	206
Figure 6.23 Delaminated face of a 90° ply close to both a free edge and a transverse crack. The approximate orientation and lean of the cusps indicate that the delamination front took a path as indicated by lines and arrows. The dashed areas denoted <i>a</i> and <i>b</i> are shown in the figure below.	207
Figure 6.24 Magnified views of regions <i>a</i> and <i>b</i> from the previous figure. Lines indicate the approximate orientation of cusps in those areas.	207
Figure 6.25 Images of incomplete delaminations between 0°/90° interfaces in a sample halted before the test was complete. Images are of the same delaminations taken at a) termination, and b) origin. Loading axis of the specimen is towards the reader.	208
Figure 6.26 A transverse crack in a 90° ply terminating somewhere in the centre of the ply.....	209
Figure 6.27 Photograph of a (gold coated) delamination surface (0° horizontal fibre orientation). Transverse crack lines are clearly visible. Delamination fronts propagated outwards from these cracks, driven forward by free edge stresses.	209
Figure 6.28 SEM micrographs of cracked sample edges and their acetate replicas. a) Full view of a sample edge showing extensive cracking. b) Acetate replica of <i>a</i> . Showing highly accurate replication of cracks. c) Higher magnification micrograph of a transverse crack. d) Replica of <i>c</i> . e) Micrograph of crack with a delamination stemming from it. The delamination terminates to the right of the image. f) Replica of <i>e</i> . Delamination terminates at a point just slightly short of the original.	211

Figure 6.29 Total length of 90° transverse cracks per mm² occurring in samples testing in tensile fatigue with increasing numbers of loading cycles. Also shows the averaged normalised curves of all sample types in cyclic tensile loading at a stress factor of 0.5. The region where stiffness degradation was found to transition from Phase Ia to Ib is marked in the hashed area. 213

Figure 6.30 Total length of 45° transverse cracks per mm² occurring in samples tested in tensile fatigue with increasing numbers of loading cycles. Also shows the averaged normalised curves of all sample types in cyclic tensile loading at a stress factor of 0.5. The region where stiffness degradation was found to transition from Phase Ia to Ib is marked in the hashed area. 214

Figure 6.31 Total length of all transverse cracks per mm² occurring in samples tested in tensile fatigue with increasing numbers of loading cycles. Also shows the averaged normalised curves of all sample types in cyclic tensile loading at a stress factor of 0.5. The region where stiffness degradation was found to transition from Phase Ia to Ib is marked in the hashed area. 215

Figure 6.32 Total length of 0°/90° interface delaminations per mm² occurring in samples tested in tensile fatigue with increasing numbers of loading cycles. Also shows the averaged normalised curves of all sample types in cyclic tensile loading at a stress factor of 0.5. The region where stiffness degradation was found to transition from Phase Ia to Ib is marked in the hashed area. 216

Figure 6.33 Total length of 90°/45° interface delaminations per mm² occurring in samples tested in tensile fatigue with increasing numbers of loading cycles. Also shows the averaged normalised curves of all sample types in cyclic tensile loading at a stress factor of 0.5. The region where stiffness degradation was found to transition from Phase Ia to Ib is marked in the hashed area. 217

Figure 6.34 Total length of interface delaminations per mm² occurring in samples tested in tensile fatigue with increasing numbers of loading cycles. Also shows the averaged normalised curves of all sample types in cyclic tensile loading at a stress factor of 0.5. The region where stiffness degradation was found to transition from Phase Ia to Ib is marked in the hashed area. 218

Figure 6.35 Image taken from Zhao et al. [242] showing an epoxy matrix fracturing along the plane of added microcapsule spheres. In some cases the microcapsules remained within the voids they caused, and in others they were absent. 221

Figure 6.36 An illustration of the theorised way in which delamination propagated through samples. Delamination fronts are driven both forwards and outwards as transverse cracks lengthen, meeting in the centre. a) Transverse cracks and delaminations form at the free edges, seeded by free edge stresses. b)

Transverse cracks extend inwards, forcing delaminations inwards with them.

c) Transverse cracks and delaminations meet in the centre. The remaining non delaminated area extends inwards due to free edge stresses. 227

LIST OF TABLES

Table 2.1: Typical properties of unidirectional composites with varying fibre reinforcements, Barbero [19].....	11
Table 3.1: Typical properties of CYCOM® 977-2 composite laminates at room temperature (21°C) compared to other aerospace materials [173-176].....	56
Table 3.2: Properties of 977-2 epoxy resin system at room temperature (21°C) [174]	57
Table 3.3: Mechanical Properties of PMMA [177]	58
Table 3.4: Mechanical properties of PEG 20,000M _w [180]. Properties are heavily dependent on temperature.....	58
Table 3.5: Percentage coverage of various inks used using Equation 3.1	68
Table 3.6: Densities of polymers and solvents used in inks [178, 183-185].....	70
Table 3.7: Volume and mass fractions for inks	70
Table 3.8: Cure cycle for 977-2 prepreg	71
Table 3.9: Results of DMA testing	80
Table 3.10: List of printed resins used.....	84
Table 5.1: Effect of experimental procedure changes upon the static flexural strength of unprinted 977-2 unidirectional laminates in static four point bending.....	129
Table 5.2: Results of static flexural testing on unidirectional 977-2 laminates	132
Table 5.3: Results of static tensile testing on multidirectional 977-2 laminates.....	147

NOMENCLATURE

A	Area/Cross-sectional area	m^2
	Objective aperture	m
A_0	Total interfacial area	m^2
b	Width	m
C	Constant	-
D	Current level of damage in the composite	-
	Diameter	m
d	Density	kgm^{-3}
d_c	Crack density	mm^{-1}
d_d	Delamination density	mm^{-1}
E	Elastic modulus	Pa
E'	Storage modulus	Pa
E''	Loss modulus	Pa
E^*	Elastic modulus of delaminated composite	Pa
E_0	Initial elastic modulus	Pa
E_f	Flexural modulus of elasticity	Pa
E_{norm}	Normalised elastic modulus	Pa
E_t	Tensile modulus of elasticity	Pa
F	Force/Load	N
F_{amp}	Load amplitude	N
F_{max}	Maximum cyclic load	N
F_{min}	Minimum cyclic load	N
ΔF	Maximum force in the observed loading cycle	N
f	Frequency	Hz
G	Shear modulus	Pa
G_{IC}	Interlaminar fracture toughness (mode I)	Jm^{-2}
G_{IIC}	Interlaminar fracture toughness (mode II)	Jm^{-2}
H	Depth of field	m
h	Thickness	m
L	Span of bending samples	m
	Length	m
M	Magnification	-
	Bending moment	Nm

M_w	Molecular weight	-
m	Mass	kg
mf	Mass fraction	-
N	Number of cycles	-
n	Number of droplets in a unit cell	-
	Refractive index	-
	Number of data points	-
Oh	Ohnesorge number	-
R	Stress Ratio	-
S	Permissible defocus	m
SP	Load setpoint	N
T	Temperature	°C
T_g	Glass transition temperature	°C
t	Thickness	m
V	Volume	m^3
	Transverse load	N
Vf	Volume fraction	-
W	Working distance	m
x	Gauge length	m
Δx	Change in gauge length	m
δx	Horizontal distance between droplet centres	m
δy	Vertical distance between droplet centres	m
β	Percentage of area covered	%
θ	Angle of fibres	°
δ	Percentage error	-
$\Delta\sigma$	Cyclic stress amplitude	-
σ	Stress	Pa
	Surface tension	Nm^{-1}
σ_{max}	Peak cyclic stress	Pa
σ_f	Flexural strength	Pa
σ_t	Tensile strength	Pa
σ_{xy}	Interlaminar shear stress	Pa
σ_z	Interlaminar normal stress	Pa
Δs	Midpoint deflection corresponding to ΔF_{max}	m
ε	Strain	-

ε_f	Flexural strain	-
ε_t	Tensile strain	-
ρ	Density	kgm^{-3}
η	Viscosity	Pas
\varnothing	Diameter	m

ACRONYMS

CIP	Continuous inkjet printing
CFRP	Carbon fibre reinforced polymer
CSA	Cross-sectional area
CT	Computed tomography
CTBN	Carboxyl-terminated butadiene-acrylonitrile
DA	Diels-Alder
DAQ	Data acquisition
DCB	Double cantilever beam
DMTA	Dynamic mechanical thermal analysis
DMF	Dimethylformamide
DOD	Droplet on demand
DSC	Differential scanning calorimetry
FEA	Finite element analysis
FEM	Finite element model/modelling
GFRP	Glass fibre reinforced polymer
GUI	Graphical user interface
LVDT	Linearly variable differential transformer
NI	National instruments
PAN	Polyacrylonitrile
PE	Polyethylene
PEAA	Poly(ethylene-co-acrylic acid)
PEG	Poly(ethylene glycol)
PMMA	Poly(methyl methacrylate)
PP	Polypropylene
PTFE	Polytetrafluoroethylene
PVC	Polyvinyl Chloride
RSA	Random sequential adsorption algorithm
RTM	Resin transfer moulding
RVE	Representative volume elements
SEM	Scanning electron microscope/microscopy
UFS	Ultimate flexural strength
UTS	Ultimate tensile strength
VARTM	Vacuum-assisted resin transfer moulding

CHAPTER 1: INTRODUCTION

1.1 MOTIVATION

The use and popularity of fibre reinforced polymer (FRP) composites has increased in recent decades. This is owing to their excellent tensile strength and stiffness [1, 2]. Of these materials, carbon fibre reinforced composites offer the highest specific stiffness and strength. Industries such as aerospace, which demand extreme weight savings without compromising performance, have long been a major driving force behind composites research. Both Airbus and Boeing now manufacture civil aircraft that have fuselages comprising over 50% composite materials: the A350 XWB and 787 Dreamliner respectively [3].

Fatigue may be defined as the decrease of a material's load-bearing capacity under cyclic loading, resulting in failure at stress levels below its normal engineering strength. It was common at one time for designers of composite structures to consider composites, (specifically carbon fibre reinforced polymer (CFRP) composites), as immune to fatigue, especially since well-designed structures tend not to develop fatigue damage below about 60% of static failure stress [4, 5]. However, it is now firmly established that composite materials, like metals, suffer from degradation of material properties under cyclic loading which may be described as fatigue. In safety critical industries such as aerospace it is gravely important to understand how fatigue damage develops in in-service components so that timely repairs and replacements can be made before catastrophic failure occurs.

Fatigue in metals is a well-established area of research, and has been studied for more than a century. Fatigue in metals often progresses by the initiation of a single crack, which then extends through the component until failure occurs. The bulk material away from the crack is generally unchanged throughout the process, although the material may harden somewhat. The mechanisms of composite fatigue however, are vastly different to those in metals. Composites accumulate damage in a general rather than a localized fashion, and failure does not always occur by the propagation of a single macroscopic crack. The micro-structural mechanisms of damage accumulation, including fibre fracture, matrix cracking, fibre/matrix debonding, transverse-ply cracking, and delamination occur sometimes independently and sometimes interactively, and the predominance of one or the other may be strongly affected by both material variables and testing conditions [4].

Delamination growing under fatigue is potentially the more critical mode of damage. Although it may not cause total failure of the load bearing capabilities of the composite, it is usually a precursor to it, severely impairing mechanical performance [6, 7]. Therefore, if

delaminations (or the mechanisms which cause delaminations) can be slowed or arrested then the structure may maintain some integrity, and the working life of the component will be extended.

Numerous investigations have been carried out which investigate interlaminar toughened composites as a potential method of preventing or retarding delamination progression in composites. However, these methods typically utilise additives which must be added to the resin system at the manufacturing stage. Or alternatively, polymer interleaving methods which can create unevenly distributed amounts of toughening polymer within laminates.

In the work presented in the following chapters, a solution containing a thermoplastic polymer is deposited in a regular array of droplets by inkjet printing onto the surface of a unidirectional carbon fibre prepreg. A series of these prepreg layers are then laid up into a composite panel, and are cured in an autoclave. It is hypothesised that these droplets may inhibit fatigue crack and/or delamination growth in a similar way to existing toughening methods, but whilst allowing excellent control over the placement and volumes of polymers added.

Inkjet printing is a non-contact, highly scalable technique, which can be used to deposit nanolitre volume droplets onto the surface of a substrate in a precise manner [8]. This capability means that droplets may be deposited exclusively where they might be required, greatly reducing the weight of polymer that must be added to gain the benefits of doing so.

1.2 KEY OBJECTIVES

This project investigates how inkjet printed polymers may be used to toughen fibre-reinforced polymer composites, and how this toughening may be developed further to influence their fatigue performance. This will be investigated through a range of static and cyclic tests. The results from these tests will then be analysed to determine what effect, if any, printing may have upon fatigue properties. Therefore, the key objectives of this research are:

1. To review existing techniques which use interlaminar toughening. Particularly those which focus on fatigue properties.
2. To investigate the behaviour of polymer inks when printed onto a composite prepreg substrate.
3. To investigate a range of polymer inks, and how their properties affect the performance of printed composites, with particular emphasis on fatigue.
4. To understand the underlying micro and macro-mechanical mechanisms of fatigue which differentiate printed composites from unprinted composites.

1.3 PROJECT NOVELTY

It is anticipated that the work presented in this thesis will contribute to the understanding of inkjet printed thermoplastic polymers as a toughening mechanism for composite laminates in fatigue. These include poly(methyl methacrylate) and varying molecular weights of poly(ethylene glycol), which have been studied by others as a toughening agents in composites, but their effects upon fatigue performance have never before been investigated.

Previous attempts to understand fatigue in toughened composites have almost exclusively focussed on toughening techniques which use randomly dispersed particulates or fluids that must be diffused into the liquid resin at the manufacturing stage. Interleaving techniques have also been investigated. However, matrix toughening is usually restricted to low cross-linking density resin systems, and interleaving struggles to create an evenly distributed and constant morphology of toughening materials within laminates. Also, the mechanical benefits are usually accompanied by other compromises, such as reductions in interlaminar shear strength. This work differs greatly in that inkjet printing offers the ability to very accurately control the dispersion and concentration of the toughening material, allowing fine adjustment of the composite toughening. It also means that any standard prepreg material may be used; a highly desirable option for industries where good control of the layup process is vital. This level of control of a toughening additive is unexplored, and so it provides extensive opportunities for process developments.

1.4 PROJECT LEGACY

The work done in this project was built upon initial research conducted by Zhang [9-11]. In this work she investigated several different polymer and solvent combinations, with poly(ethylene glycol) (PEG) in deionised water, and poly(methyl methacrylate) (PMMA) in dimethylformamide (DMF) producing the most favourable results, as shown in Figure 1.1. Zhang's work focussed on identifying polymers which could improve the interlaminar fracture toughness (G_{Ic}) of carbon fibre prepreg composites, but did not build on those findings to investigate printed composites in realistic testing scenarios.

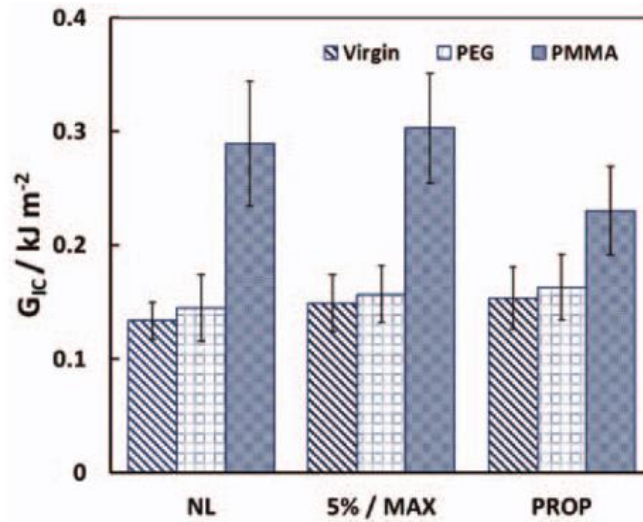


Figure 1.1: G_{IC} comparison between virgin and printed composite laminates in double cantilever beam tests conducted by Zhang [12]. Error bars represent standard deviation.

The polymer solution (or ‘inks’) were printed onto a carbon fibre prepreg substrate in a regular hexagonal array, which was then laid up in the usual manner to form a composite laminate that contained polymer droplets in its interlaminar region, as shown in Figure 1.2. However, Zhang’s work was unable to determine with certainty how printed polymers behaved once printed onto prepreg substrates. Particularly, whether they dissolved into the surrounding matrix, or if they remained as discrete droplets.

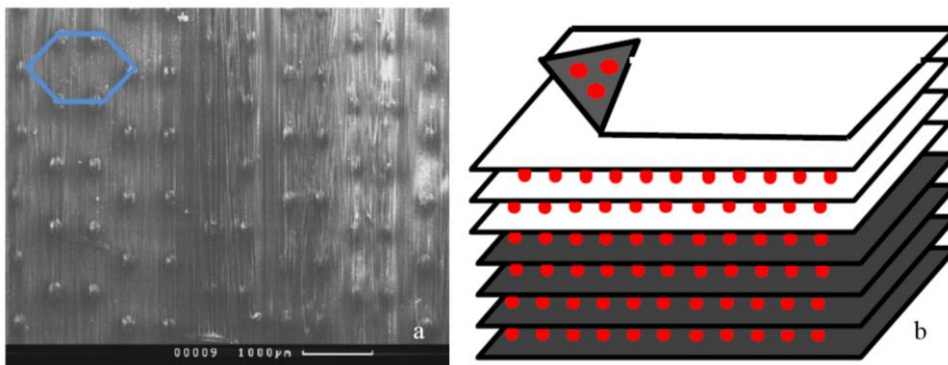


Figure 1.2: a) A printed hexagonal pattern on carbon fibre prepreg. b) Illustration of how printed prepreg laminae are laid up to make a laminate containing interlaminar droplets

Zhang conducted double cantilever beam (DCB) tests in order to establish the interlaminar mode I fracture toughness (G_{IC}) of printed composites. It was found that the interlaminar

fracture toughness of the printed laminates were increased by up to 40%. The increase was of a similar magnitude to that observed in previous work by Yasaei et al. in which thermoplastic toughening materials were applied [13]. The most significant increase in G_{IC} was found using a 10% PMMA in DMF ink printed onto CYCOM® 977-2-35-12KHTS-268-300 prepreg. However, although mode I fracture provides a very simple and reliable method of testing interlaminar fracture toughness, most real-world failures do not occur in mode I loading. Typically, mode II is the dominant loading method. In mode I, laminates tend to fracture within the bulk matrix in the interlaminar region. But in mode II, failure tends to occur at the fibre/matrix interface in the interlaminar region. And therefore DCB tests tend to test the best case scenario for interlaminar toughened laminates.

The work presented in this thesis expands on this new method, moving focus from simplistic interlaminar fracture tests to cyclic testing regimes which are more representative of real-world structures. It is anticipated that this work will lead to new understanding of the performance of inkjet printed composites, with particular emphasis on the characterisation of performance in fatigue.

CHAPTER 2: LITERATURE REVIEW

This chapter discusses the fundamental principles necessary to understand the work presented in following chapters. It also presents relevant experimental data from other authors, and discussed gaps in the literature.

2.1 COMPOSITE MATERIALS

Composite materials are defined as two or more materials that are combined in order to create a material that has optimised properties by the interaction of its constituent components. For example, in steel reinforced concrete, steel rods are used to improve neat concrete's inherently low tensile strength and ductility. Polymer composites work in much the same way, with various types of short or long fibres or particles embedded in a polymer matrix [1]. The fibres are usually made from a material with a high stiffness and/or tensile strength. The role of the polymer matrix is to give the fibres rigidity, keeping them aligned in the direction of loading, and also to distribute loads evenly between fibres.

2.1.1 *Fibres*

Polymer composites are often used because of their high specific stiffness and strength. Those containing continuous fibres tend to have the highest of these properties, so these are generally the most frequently used in high performance applications such as aircraft and automobiles.

Continuous fibres may then also be split into unidirectional and woven categories. In unidirectional composites, all fibres run parallel to one another. This maximises load carrying capabilities and stiffness in the fibre direction, but limits the perpendicular strength almost to that of the matrix material. In structures where loading is multidirectional, it is necessary to laminate multiple layers as shown in Figure 2.1, so that fibres can be oriented in the directions of multiple loads. Laminates must be designed carefully though, as the differing Poisson's ratios or adjacent laminae (or 'plies') may encourage delaminations to develop. This will be explained further in Section 2.3.1.3.

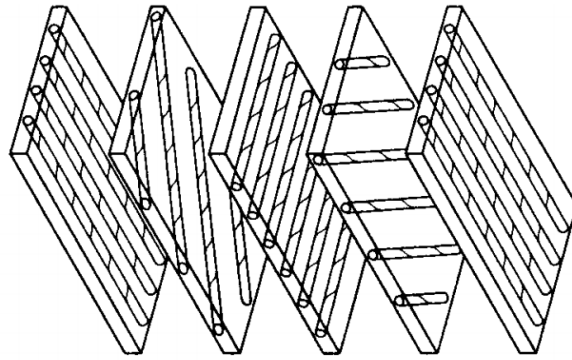


Figure 2.1: Exploded view of a laminate construction consisting of unidirectional plies [1]

Fibres may also be woven to create fabrics. The advantage of this method of manufacture is that the resulting fabric has good strength in both directions in which the fibres are running. They are also more flexible than unidirectional fibre bundles, so they can be moulded much more easily into complex shapes. This flexibility comes from the way in which the fibres curve around each other to create the weave. This is illustrated in Figure 2.2a, which shows a model of a weave, constructed from fibre bundles. When tension is placed upon the fabric, the fibre bundles will straighten slightly. Because of this, woven fabrics do not have the same level of stiffness as unidirectional ones. This straightening also places stresses on the fibres where they bridge perpendicular ones. A finite element model representation of this is shown in Figure 2.2b.

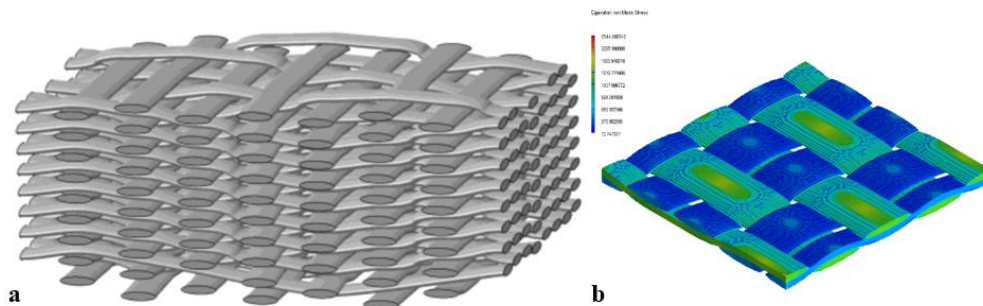


Figure 2.2: a) A representation of a complex 3D interlocking woven fabric composite [14] b) A finite element model of woven composite showing stresses placed on fibre bundles when under tensile loading [15]

Various materials are used in composite materials, including: metals, natural fibres, polymers, glass, carbon etc. Each material has its own inherent advantages. But strength, stiffness, weight, and cost are often the main factors considered when choosing which material to use.

The Ashby plot shown in Figure 2.3 is an important reference when designing structures. It shows where engineering composites lie with respect to more traditional materials. It can be seen here, that they possess very high specific strength (and stiffness). Wood may also be considered fibre composite materials, and are also shown here to have very good strength to weight properties.

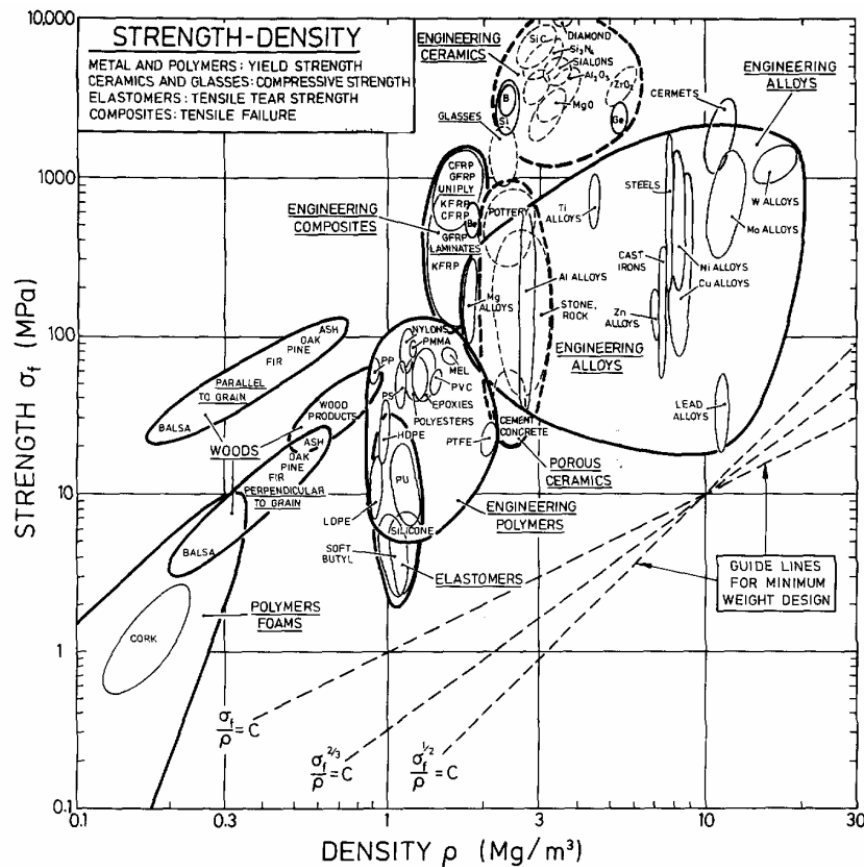


Figure 2.3: Ashby plot comparing commonly used engineering materials [16]

The most commonly used fibre types are glass, aramid, and carbon. Glass is by far the most prolific of these. Glass fibres come in several varieties, but the most common are E-glass and S-glass. E-glass, which is alumina-borosilicate glass, makes up most of the glass fibres produced globally. This is because it has good strength, stiffness, chemical resistance, and is relatively cheap. It is however, susceptible to chloride ion attack, and so is a poor choice for marine applications [17]. S-glass (S standing for strength) is usually made from magnesium aluminosilicate glass [18]. It is used in applications where chemical resistance and electrical insulation are needed, and also where higher strength and stiffness than E-glass are required. S-glass has around 10-30% higher strength and stiffness than E-glass [18]. However, it is

generally much more expensive than E-glass due to factors such as the cost of materials, processes, and production quantities. Typical glass reinforced polymer composite properties are shown in Table 2.1.

Aramid fibres (often colloquially known by their DuPont brand name, Kevlar®), are a range of organic polymer fibres processed from polyamide [19]. They have a higher strength and stiffness than glass fibres, and like glass, have good chemical resistance and electrical insulation. They are also very resistant to abrasion and have good vibration damping characteristics [20]. It also has the aesthetic advantage that being an organic polymer, they are easy to colour, and so are often used where designers wish to add visual flair. The cost of aramid fibres is higher than glass though. Additionally, their mechanical properties are also compromised by UV light and heat, losing 75-80% of their tensile strength at 177°C [21]. Typical aramid fibre reinforced polymer composite properties are also shown in Table 2.1.

Carbon fibres are made from carbon in its graphitic allotrope. The process for making carbon fibres is part chemical and part mechanical. A precursor, usually polyacrylonitrile (PAN) or 'pitch', is drawn out into long strands and then heated anaerobically. This heating expels most of the non-carbon atoms, leaving tightly packed graphite layers as shown in Figure 2.4. They dominate the aerospace market, having excellent strength and stiffness; exceeding that of both glass and aramids. The cost of carbon fibres though, is much higher than either glass or aramid. Unlike glass fibres, carbon fibres have a broad range of stiffness values, which is highly dictated by their precursor and thermal treatment. Three different types of carbon fibre composites are shown in Table 2.1, showing some of the range which their properties may span. Some of the limitations of carbon fibres are their low impact resistance and susceptibility to chemical attack in the presence of oxygen [19]. The major limiting factor for carbon fibres being implemented in everyday design is their cost. Glass is a much cheaper alternative, so the cost of making structures bulkier is still less than using more expensive carbon fibres. Carbon would be used in cases where weight is critical, such as in aerospace, where fuel costs and environmental obligations are increasingly forcing manufacturers to become more efficient. Carbon fibre's extremely high strength/stiffness to weight ratio means that manufacturers are willing to pay a higher initial expense to reduce fuel usage.

Table 2.1: Typical properties of unidirectional composites with varying fibre reinforcements, Barbero [19]

		E-Glass -Epoxy	S-Glass -Epoxy	Kevlar 49™ -Epoxy	Carbon T300 -914-C	Carbon T800 -3900-2	Carbon IM7 -8552
Density (g/cc)	ρ	2.076	1.993	1.380	-	-	1.55
Modulus Longitudinal (GPa)	E_1	45	55	75.8	138	155.8	171.4
Ultimate Tensile Strength Longitudinal (MPa)	F_1	1020	1620	1380	1500	2698	2326.2
Ultimate Tensile Strain Longitudinal (%)	ϵ_1	1.29	1.68	1.45	1.087	1.68	1.62
In-plane Shear Modulus (GPa)	G_{12}	5.5	7.6	2.07	5.5	5.14	5.29

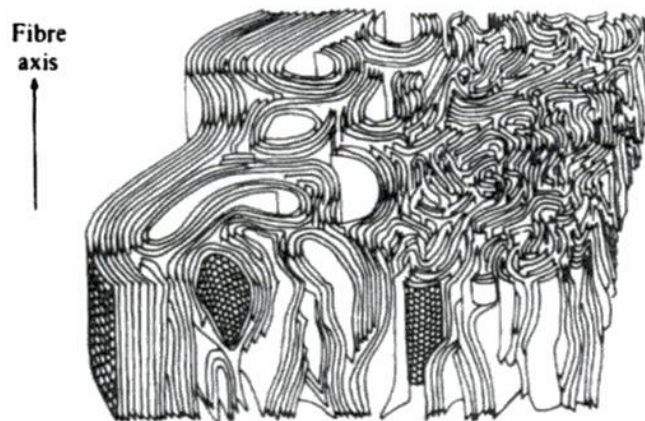


Figure 2.4: Illustration of the structure of carbon fibres in cross-section consisting of folded graphite layers [22]

2.1.2 Matrices

The matrix is the element of a composite which bonds the load carrying elements. It transfers loads between fibres, and protects them from abrasion and environmental damage. It also plays an important role in determining the mechanical performance of the composite, including carrying much of the intralaminar and transverse loading [23]. It also has a large effect upon interlaminar and shear behaviour, which in turn can affect delamination initiation when subject to static or cyclic loading. It is therefore a primary concern that the matrix should have good strength and stiffness, but should also have a high level of toughness and resistance to delamination. It is however, difficult to achieve all of this, as these properties are usually mutually exclusive. This is a problem which the work described in the following chapters investigates; introducing softer, tougher material where crack initiation was more likely to occur, and leaving the bulk, stronger and more brittle matrix to provide stiffness and load transfer.

Matrix materials are as varied as fibres. In general, any material that can be infused into the fibres, and that can transfer loads between them is a viable matrix material. These include polymers, metals and ceramics. By far the most common of these are polymer matrices. Because the matrix needs to be a solid, liquid resins which can be subjected to a thermal curing cycle are the preferred materials, as melted thermoplastics are difficult to process.

Resin is a generic term used to describe a polymer and/or reactive additive or catalyst. Epoxy resins are the most commonly used of these. They generally consist of a polymer containing epoxide groups (one oxygen atom and two carbon atoms, as shown in Figure 2.5), and a curing agent [24, 25]. Epoxy chemistry is a broad subject, and beyond this limited section to explain fully. But in principle, any molecule containing a reactive hydrogen may react with the epoxide groups of the epoxy resin. Common classes of hardeners for epoxy resins include amines, acids, acid anhydrides, phenols, alcohols and thiols [26].

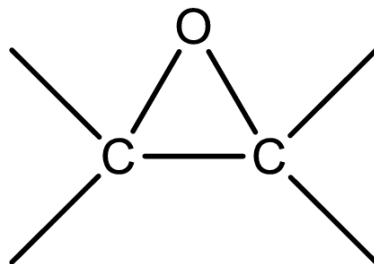


Figure 2.5: Chemical structure of an epoxide group [27]

When cured, epoxy resins form thermoset polymers where the polymer chains are crosslinked and locked in place [25]. Crosslinking is the coupling of one polymer chain to another into three-dimensional networks. In thermoplastics, the polymer chains are independent of each other, and can move as such, resulting in reduced stiffness and strength. In thermosets, there is an electrophilic attack on the oxygen atom in the epoxide group, breaking one of its C-O bonds, and allowing it to join with other epoxide groups [28]. The formation of polymer chains is not limited to linear molecules, and so can branch and interact with other chains, eventually forming a rigidly linked polymer structure.

2.1.3 *Manufacturing Methods*

There are numerous way of manufacturing composite materials. Each one has advantages and disadvantages. It has previously been mentioned that the key competing factors are cost and performance. Manufacturing methods are no exception to this.

2.1.3.1 *Fibre Volume Fraction*

Fibre volume fraction is a very important factor in deciding an appropriate manufacturing method because the fibres are the major load bearing component, and therefore a higher fibre volume fraction will result in a higher specific strength. In the case of the 977-2 resin system used in the work presented in later chapters, the tensile strength is just 2.5% of that of the completed composite. Therefore, excess resin is highly detrimental where high strength to weight ratio is required.

The volume (V) of a composite element can be described as;

$$V = V_f + V_m + V_v \quad 2.1$$

where the subscripts f , m , and v refer to fibres, matrix, and voids. This is often simplified to;

$$V = V_f + V_m \quad 2.2$$

as void contents are often negligible.

Because volume may be described as;

$$V = \frac{m}{\rho} \quad 2.3$$

where m is mass, and ρ is density. It may be concluded that;

$$m_{comp} = V_f \rho_f + V_m \rho_m \quad 2.4$$

The fibre volume fraction can never be 100% as fibres tend to have a near circular cross-section. Figure 2.6 shows a representative diagram of fibres with a circular cross-section packed as tightly as theoretically possible.

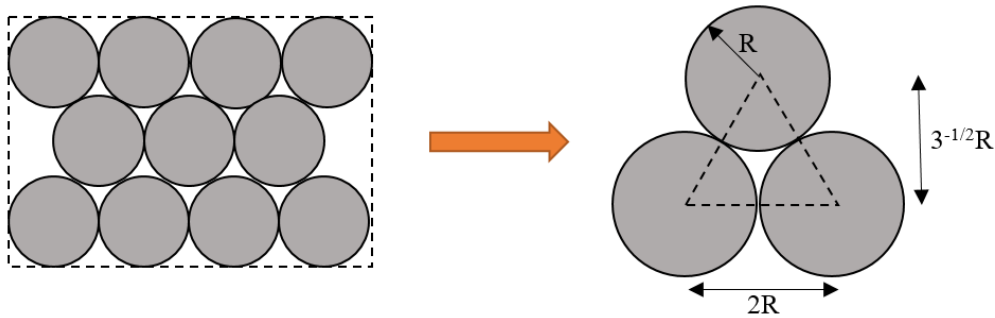


Figure 2.6: Unit cell dimensions of a collection of close packed, circular cross-section fibres

Where R is radius. In this case;

$$V_{f_{max}} = \frac{\pi R^2}{2\sqrt{3}R^2} = \frac{\pi}{2\sqrt{3}} = 0.907 \approx 91\% \quad 2.5$$

Of course this is only applicable for perfectly cylindrical fibres in a unidirectional composite. This is simply never true. Hence, fibre volume fractions over 70% or so are very difficult to achieve [29].

2.1.3.2 *Wet Layup*

Perhaps the most basic method of composite manufacture is wet layup. In this method, fibres or woven fabrics are combined with a pre-mixed resin. Broadly, this may be divided into two types, spray layup and wet hand layup.

In spray layups, fibres and resin are mixed by a spray gun and sprayed at the layup surface. Industrially, continuous fibre reels are fed into the gun, which chops them into short lengths. Resin is fed from a reservoir, and mixed with a curing catalyst as it is ejected. This prevents cured resin blocking and destroying the spray gun. This is illustrated in Figure 2.7. This is usually the most common method for making such products as bathtubs and light marine craft hulls. This method produces a composite with randomly orientated fibres, resulting in a relatively weak structure. Composites manufactured in this way also have very low fibre volume fractions; typically in the range of 25-40% [30].

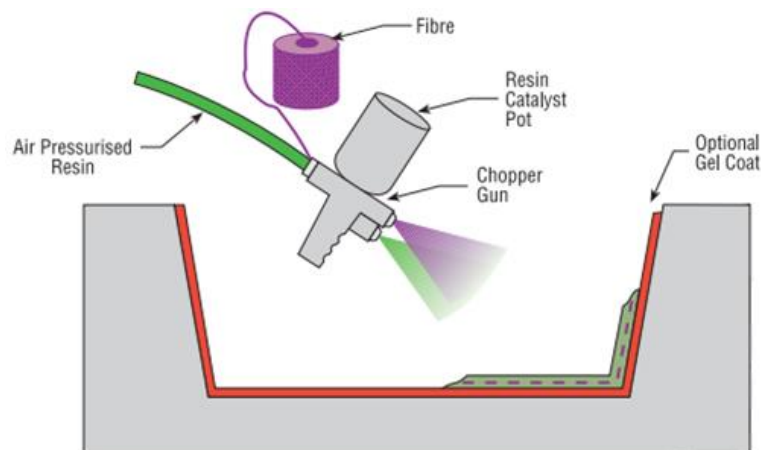


Figure 2.7: Illustration of the spray layup process [31]

In wet hand layup, the dry material is usually applied to the layup surface and then wet with resin in situ. The resin helps to stick the fibres in place. The advantage of this over spray layup is that it is possible to orient the fibres as desired, aligning them with the designed loading path, creating a stronger composite than spraying allows. However, this method is much more labour intensive than spraying. This method usually results in a low fibre volume fraction, ranging from 25-40% [30]. Additionally, once infused with resin, the part may be placed under vacuum to draw out excess resin, increasing the fibre volume fraction further.

2.1.3.3 Resin Infusion

Resin infusion may be divided into two types: resin transfer moulding (RTM), and vacuum assisted resin transfer moulding (VARTM). These are illustrated in Figure 2.8. Both methods work on the same principle. Dry fibres are laid into the desired position. The part is then placed in a vacuum bag or preform mould, and resin is infused into the fibres. In RTM, the resin is pushed from the inlet port by compressed air to an outlet port. The fibres are held in place by the solid preform. In VARTM, the resin is pulled from the inlet to the outlet by a vacuum. In both cases, the fibres are compressed, so it is possible to infuse the fibres with a minimal amount of excess resin. Both methods are very similar in principle. They differ in that RTM uses a more expensive mould consisting of two halves. These halves must also be heavier than in RTM since they must be able to withstand large positive pressures. This does however produce a part that has two moulded surfaces, whereas VARTM only produces one smooth moulded surface [32]. Both methods result in fibre volume fractions of up to 65% [25].

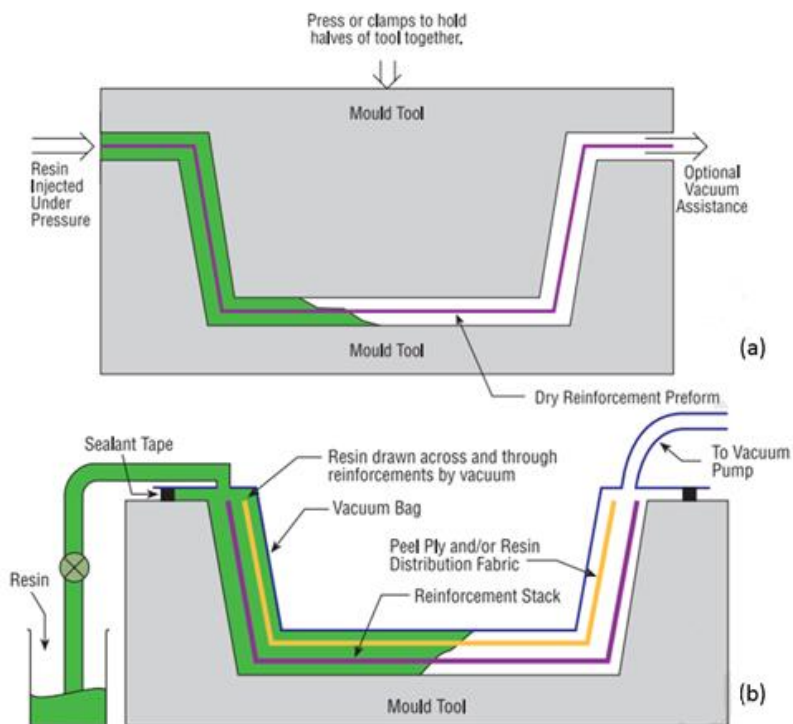


Figure 2.8: a) Resin transfer moulding b) Vacuum assisted resin transfer moulding [31]

2.1.3.4 Prepregs - Autoclave

Pre-impregnated or ‘prepreg’ composites consist of fabrics or fibres impregnated with resin, usually in a partially cured state with a moderately self-adhesive ‘tack’, which helps it to adhere to the mould surface and to other laminae [25]. It is produced in continuous flat sheets of set thickness, and wound onto rolls for compact shipping, protected by a non-stick sheet on either surface. In most prepreg systems there is more than the desired amount of resin. Removal of the excess under vacuum aids in the removal of air bubbles and volatiles, which may otherwise cause voids [19]. For each 1% of void content there is around 7% reduction in interlaminar shear strength and significant reductions in compressive strength over 2% voids [33, 34].

The method of creating prepreg laminates is relatively simple. And is, simply put, a case of applying the material in layers with the fibres running in the desired orientations until the desired thickness is achieved. Once laminated, prepreg materials are usually vacuum bagged and either oven or autoclave cured. This is illustrated in Figure 2.9. An autoclave is a temperature regulated pressure vessel which applies additional pressure to the laminated part, further reducing voids and removing excess resin. Although autoclaved composites are labour and energy intensive, they are used with high performance in mind. To many, the large cost of autoclave curing is therefore worth the relatively small improvement of an already optimised product.

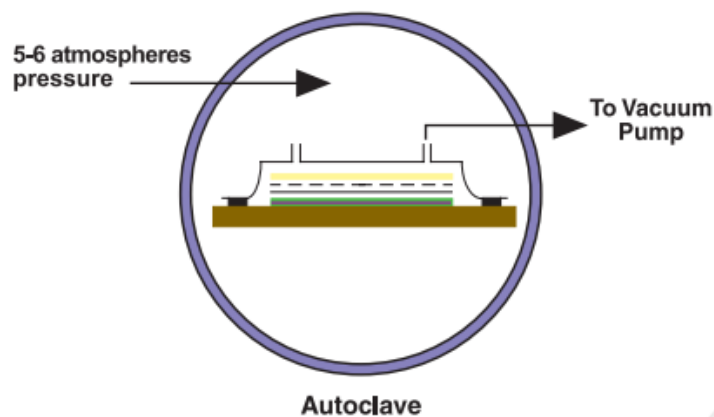


Figure 2.9: Illustration of autoclave curing [31]

Prepregs are usually used because they produce much stronger and stiffer laminates than wet layup processes. Because the resin is carefully pre-mixed at the factory under carefully controlled conditions, it is possible to get an optimal level of strength and cure. The fibre

volume fraction can also be controlled very accurately, with most prepregs having a fibre volume fraction somewhere in the range of 50-70% [25, 30]. Of course, the obvious disadvantage is cost, which limits their use greatly to most users. It also doesn't have the physical flexibility of wet layup composites when laying them up. Because the resin is partially cured, fibres are not so free to move, reducing the degree to which they can be shaped and bent into corners. Although, complex geometries are still easily achievable by building the desired shape from cut prepreg pieces. Another disadvantage of prepregs is that although they are highly optimised, they are sensitive to delaminations since the interlaminar region is susceptible to voids, contamination, and debris infiltration before the laminae or laid up. The interlaminar region is also more resin-rich than the intralaminar regions. This region is not very thick, and this results in a large change in Poisson's ratio within a very small distance, creating strain differences, and hence stress under loading. Therefore, delamination reduction of prepregs is a very important consideration, and the work presented in this thesis is built around this.

2.2 INKJET PRINTING

Inkjet printing is a computer-aided additive technology which is now regarded as a domestic technology, with many homes having their own inkjet printer for the purpose of printing documents. These printers are specialised for printing specific ink formulations, but inkjet printing may be applied to practically any liquid. Raleigh first conceived of the fundamentals behind inkjet technology in 1878 [35], observing how a jet was broken up into droplets as it passed through a narrow orifice under pressure.

Inkjet printing is a very versatile method. It is a relatively inexpensive, highly precise, and highly scalable technique which produces very little waste [36]. It is already used in specialised industrial areas such as electronics and tissue engineering because of its ability to quickly deposit minute quantities of materials onto various substrates [8]. The 'inks' used vary extensively. Many materials are soluble in the appropriate solvent. This enables manufacturers to print an incredibly wide range of materials, including long chain polymers.

Printability depends highly upon viscosity and surface tension. A high viscosity ink will absorb too much of the energy from the pressure wave used to eject it from the nozzle. Although conversely, a low viscosity ink will be easy to eject, but its droplets will be less stable and break up easier. A high surface tension will have the effect of requiring a higher energy to eject it from the nozzle, and may not be printable at all. De Gans et al. demonstrated that the surface tension of inks which ranges from 28 mNm⁻¹ to 350 mNm⁻¹ can be printed [8].

In practice then, the properties of the ink should lie in a specific range in order to be printable. These values can be manipulated though by changing the dilution of the ink or by temperature changes.

The Ohnesorge number (Oh) may be used as an indication of the printability of inks. It is a ratio of the viscous and inertial resistances to spreading.

$$Oh = \frac{\eta}{\sqrt{\rho d \sigma}} \quad 2.6$$

Where η is the viscosity, ρ is the density, σ is the surface tension of the ink, and d is the diameter of the orifice [11]. Some researchers have suggested that $0.1 < Oh < 1$ inks are generally printable [37, 38]. Although these numbers are a guide, and the properties of individual inks will affect printability. The Ohnesorge number is based on Newtonian fluid mechanics, but polymer solutions may also be non-Newtonian. Non-Newtonian fluids comprise of polymer chains or particles which interact with each other, increasing viscosity under shear. When under pressure and forced the narrow orifice of the nozzle, the shear force on the fluid may align the chains in the direction of shear. This means that the viscosity and hence Ohnesorge number of some inks during jetting may be different from their static value [11, 39].

There are two main methods of inkjet printing, continuous inkjet printing (CIP), and droplet on demand (DOD) printing. This work deals exclusively with DOD printing. CIP (Figure 2.10) utilises a continuous stream of electrically charged liquid. The Rayleigh instability is induced in the stream, breaking it up into individual uniform droplets [37]. These droplets remain charged, and may be manipulated by an electrostatic or magnetic field to form the desired pattern. Unwanted droplets are directed into a catchment gutter and disposed of or recycled [40].

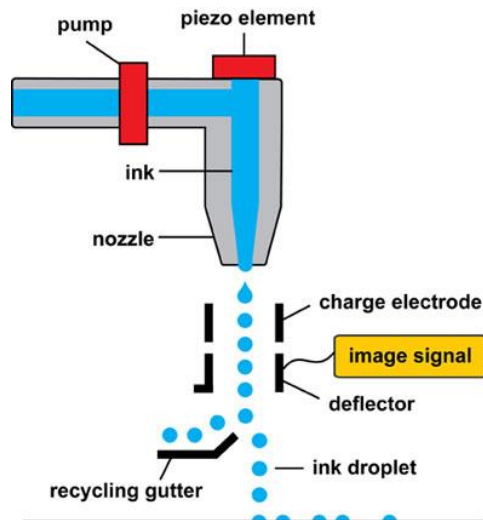


Figure 2.10: Illustration of continuous inkjet printing [41]

Unlike CIP, DOD printing (Figure 2.11) does not use a continuous jet. Instead, each droplet is ejected as required by the perturbation of the ink inside the nozzle. This perturbation comes from either a piezo-electric crystal, or from a heating element. A heating element immediately vaporises the liquid contacting it, creating a bubble, and hence a positive pressure in the volume. This pressure travels as a wave through the liquid, pushing it out of the nozzle. By controlling the rate and level of heating, the pressure wave, and hence the droplet, can be influenced. In piezo-electric nozzles a voltage is applied to the crystal causing it to pulse, again creating a pressure wave. An illustration of the action of this electric signal is shown in Figure 2.12. The advantage of DOD over CIP is that there is less waste, since the ink is ejected only when needed. Although CIP often recycles the undeposited ink, this is often a cause of ink contamination.

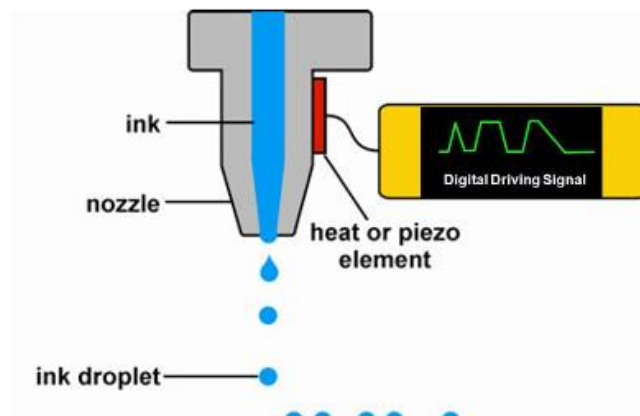


Figure 2.11: Illustration of droplet on demand printing [41]

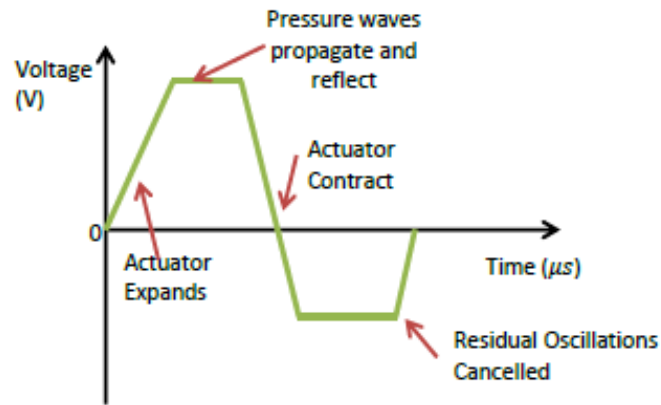


Figure 2.12: Electrical actuation of a piezo-electric DOD system [42]

2.3 FATIGUE OF COMPOSITES

Fatigue may be defined as the decrease of the material's load-bearing capacity under cyclic loading, resulting in failure at stress levels below its normal engineering strength. This is illustrated in Figure 2.13

The mechanisms by which composite materials deteriorate are very different to those experienced by metals. They are also much more complex. Unlike metals, composite materials are inhomogeneous (on a global scale) and anisotropic. They accumulate damage in a general rather than a localised fashion, and failure does not always occur by the propagation of a single macroscopic crack. For polymer matrix composites, fatigue failure is primarily a matrix-dominated event. Fatigue damage begins with microcrack accumulation in the polymer. These microcracks accumulate rapidly in the early stages of fatigue life, with the accumulation rate slowing with increasing number of cycles. Ultimately, the microcracks coalesce to form macroscopic damage that quickly propagates (see Figure 2.14) [43]. Eventually the accumulated damage will reduce the residual strength of the composite to a level lower than the peak cyclic stress put upon it, resulting in failure, as shown in Figure 2.13. Composites have several damage accumulation mechanisms: fibre/matrix debonding, matrix cracking, delamination, and fibre fracture. These damage mechanisms can occur independently or interactively depending on material properties and loading conditions [44].

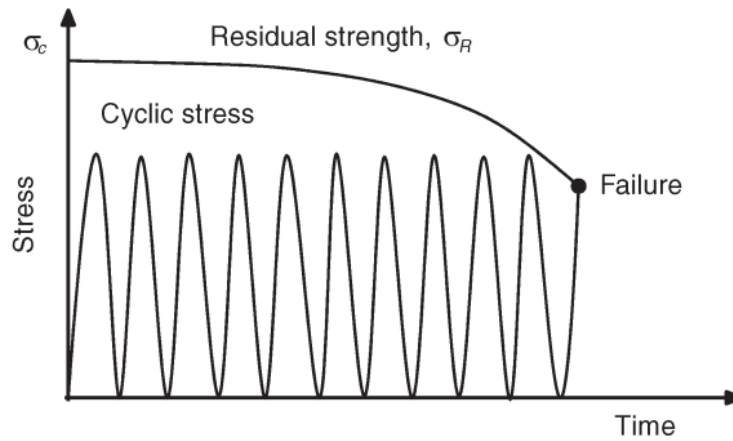


Figure 2.13: Degradation of composite strength by wear-out until residual strength falls below the peak cyclic stress [4]

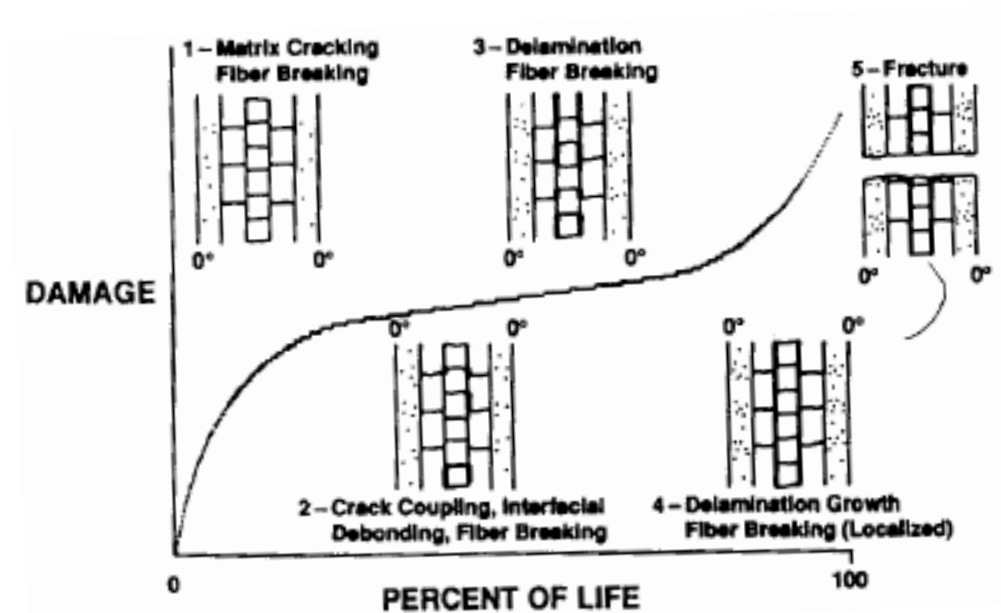


Figure 2.14: Damage modes during fatigue life [1]

Since about the 1960s, the fracture and fatigue behaviour of composite materials based on reinforcing polymers with long strong fibres has been the subject of extensive experimentation and analytical investigation. Yet despite this acquisition of vast collections of mechanical property data, our ability to predict the structural integrity of a damaged composite subjected to mechanical and thermal stresses and hostile environments remains restricted. This is because our understanding of composite failure is based almost entirely on this store of information being empirical in nature with limited knowledge of the structural changes taking place in the material over time [45].

Some of the earliest work published in the area of composite fatigue of fibre-reinforced composites were by Pagano and Pipes [46] in the 1970s, followed by Foye and Baker [47]. At this time, Whitney and Browning [48] also began work on characterising fatigue in metal matrix composites. Researchers such as Reifsnider [49] and Talreja [50] have also been prolific in the advancement of the understanding of fatigue in composite materials.

2.3.1 *Damage Mechanisms*

As mentioned in Section 2.3, composite fatigue is complex, and works through the interaction of several different damage mechanisms which are themselves heavily influenced by such factors as material properties, layup orientation, loading scenarios etc. The following sections describe what these mechanisms are, and how they influence the performance of composites.

2.3.1.1 *Matrix and Transverse Ply Cracking*

Due to the large difference in stiffness between the fibres and matrix, substantial strain magnification occurs in the matrix when a ply is loaded in the transverse direction. The strain at which failure occurs in off-axis plies is lower than in those aligned in the direction of loading [51]. Once matrix cracks are initiated they propagate perpendicular to the loading direction, often jumping between individual fibres (Figure 2.15), initiating fibre pull-out (Section 2.3.1.2 below). Matrix cracking can occur in longitudinal plies, but is much more prolific in off-axis plies. Transverse ply cracks are often followed by delamination of ply interfaces with large differences in orientation. These delaminations begin at the top of the transverse crack at the interface between them, and from there can quickly propagate throughout the rest of the interface. This damage progression is illustrated in Figure 2.16.

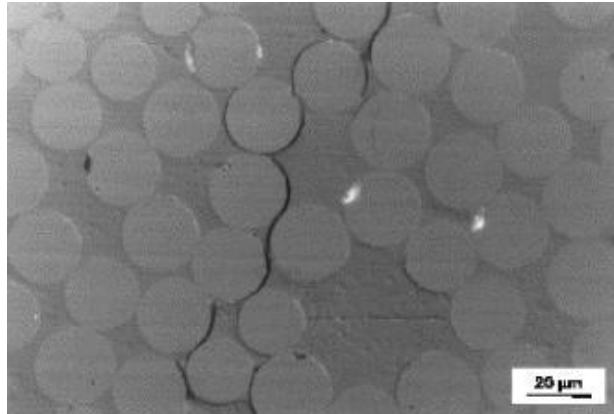


Figure 2.15: SEM image of matrix cracking propagating through an off-axis ply, jumping between fibre/matrix interfaces [52]

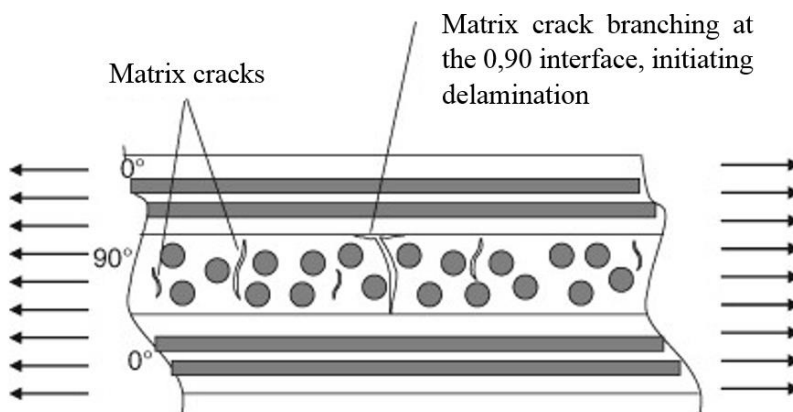


Figure 2.16: Transverse matrix cracking in a cross-ply laminate [53]

Matrix cracks are often the first stage of composite damage in fatigue, yet they greatly affect the performance of the composite. The crack density (total length of matrix cracks per unit area) was found by Ogin et al. [54] to be directly proportional to the reduction in stiffness of the composite. They found that matrix cracking produced a 17% stiffness reduction in a 0°/90° GFRP laminate which was cyclically loaded.

2.3.1.2 Fibre/matrix Debonding

Fibre/matrix debonding and ‘pull-out’ is the fracture of the bond between fibre and matrix. Without this bond in place, the fibre’s load bearing capacity is severely affected since it can only carry loads in bonded regions, or where friction allows some load transference. This in turn places increased loads on the remaining fibres, reducing the stiffness of the composite.

Fibre/matrix debonding often occurs as a consequence of matrix cracking. As shown in Figure 2.15, matrix cracks often encounter fibres, favouring cracking along the stressed region at the interface. Figure 2.17 illustrates the path that matrix cracks may take when encountering fibres. In this case a crack is progressing through a ply. Upon reaching the fibre/matrix interface, debonding will probably occur. From here the crack tip may be blunted, arresting the crack (Figure 2.17b); although repeated loading cycles may progress the crack further. The matrix crack may also create a stress concentration where the crack tip intersects the fibre, breaking the fibre at that point (Figure 2.17c). Finally, the crack may pass around the fibre without breaking it directly. However, it is likely that the tensile load of the opening crack will break the fibre at some point along the debonded length (Figure 2.17d) [55]. Although fibre/matrix debonding is often caused by matrix cracking, it is by no means the only cause. Fracture may occur at the fibre/matrix interface directly since it is also a stressed region.

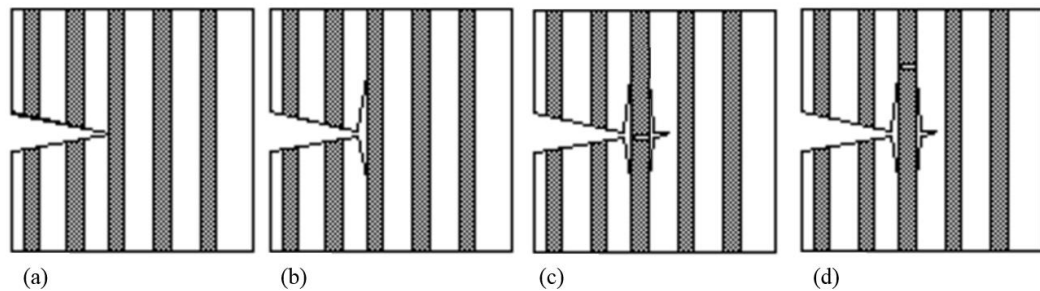


Figure 2.17: Path that cracks may take when travelling perpendicular to fibres. a) Crack progressing to adjacent fibres causing b) fibre/matrix interface debonding by blunting crack tip and/or c) fibre-bridged crack growth. d) A fibre break away from the crack tip [56]

Once debonding and fibre fracture have occurred, fibre pull-out may occur. Pull-out refers to the movement of fractured fibres from their matrix sockets once debonding has taken place. Although pull-out is not beneficial to the composite structure, it may slow further damage. Although debonded, the fibres will usually be held in place by friction. Therefore, in order to move the fibre, energy must be spent. This absorbs energy that would otherwise create or propagate damage elsewhere in the composite. This mechanism is one of the main factors in energy absorption in impact of composite structures [57]. The energy absorbed in composites is dependent on the length of the debonding pull-out.

2.3.1.3 Delamination

Delamination is the separation of adjacent layers. Delaminations reduce stiffness significantly. They also reduce the strength of the laminate by removing the load sharing capabilities

between plies. Significantly, under repeated loading cycles, delaminations may grow to a critical point, leading to failure of the structure [58]. Although, there is evidence that under tension dominated cyclic loading, if delamination develops, it can prolong fatigue life by isolating the failure of the individual lamina from others [59-61]. Delaminations tend to develop between plies due to differences in moduli and Poisson's ratios between plies of differing orientations creating stresses at their interface [1]. Transverse cracks in off-axis plies also heavily influence the formation of delaminations, as shown by Figure 2.18, which shows delaminations originating from the tips of transverse ply cracks. Ply interfaces are also susceptible to contamination and debris, particularly in prepreg laminates where the part-cured resin retains particulates that come into contact with it. Additionally, the interlaminar region is usually resin-rich, meaning that the matrix in this region has little or no fibrous reinforcement. This region is often very thin in comparison to the overall laminate thickness. Nonetheless, it does contribute to delamination propagation. The thickness of the resin-rich region can greatly affect laminate fracture toughness.

The interlaminar fracture toughness of a composite is a result of complex interactions between two important properties, namely the matrix ductility and the fibre/matrix interface bond strength [62]. Both properties are beneficial to fracture toughness, yet both must be optimised for complementary interaction with one another. If increased ductility results in decreased fibre/matrix bonding then a decrease in interlaminar fracture toughness may result. The thickness of the resin-rich region also plays an important role. Figure 2.19 shows how the crack process zone (a region of increased stress in which material separation takes place) is affected by the ductility of the matrix. In brittle matrices, the process zone is small, and it is extended greatly in ductile matrices [63]. An increase in the process zone translates to a greater dissipation of fracture energy. But if the resin-rich region is thinner than the thickness of the process zone then it is constrained. The additional constraint imposed by the neighbouring fibres then induces a higher maximum principle stress component around the crack tip, producing a longer process zone which advances delamination more rapidly [64]. Therefore, in order to be beneficial, the thickness of the resin-rich region should be carefully controlled in order to optimise the toughening effect gained by increased matrix ductility.

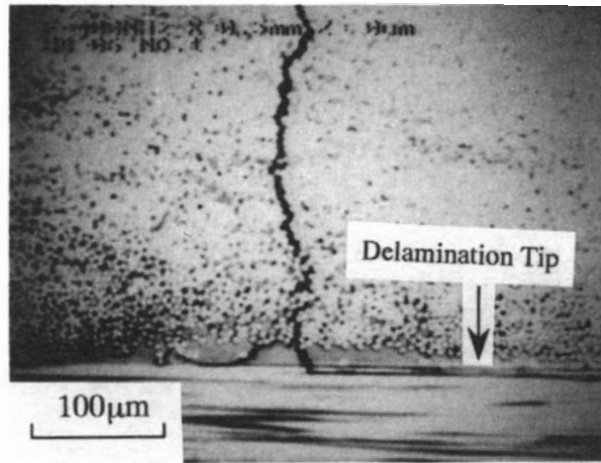


Figure 2.18: SEM micrograph of carbon fibre laminate showing transverse ply cracking and delaminations extending from where the crack meets the adjacent ply of perpendicular orientation [65]

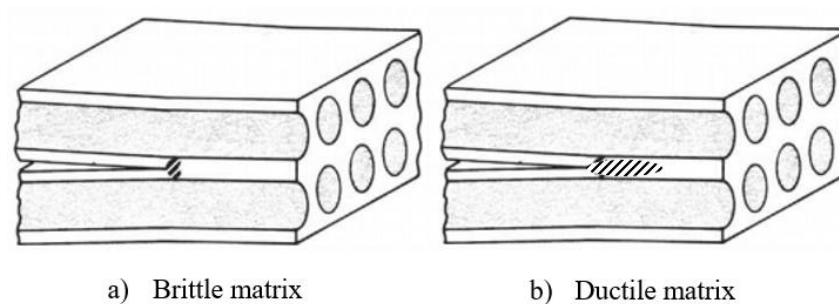


Figure 2.19 Delamination process zones in a) composites with brittle resins, and b) composites with ductile resins [63]

Since the methods developed in this work deal primarily with interlaminar toughening, it is reasonable to assume that any effects would be observed in damage events occurring in the interlaminar region; namely delamination. Therefore it is important to understand how delaminations affect the performance of composite materials, and also how they may be purposely induced so that they may be observed as the dominant damage mechanism.

Delaminations may be caused by either the extension of matrix cracks (Section 2.3.1.1), or by shear stresses caused by strain differences between plies. The former may come as a result of fatigue testing, but does not guarantee that delaminations will occur. That is dependent on the materials, geometry, test parameters etc. The latter may be induced by either flexural testing, in which the strain levels vary throughout the thickness of the material, or by using multidirectional laminates. Multidirectional laminates are those which use many plies varying in orientation to give the effective properties required for the application. Since composites

have different properties (including Poisson's ratios) in different principle directions, they exhibit differing levels of strain under loading, causing interlaminar shear stresses. Most composite structures are multidirectional, and as a result, research has been carried out to characterise delaminations caused by multidirectional layups.

Pagano and Pipes [66] investigated the influence of stacking sequence on the strength of laminates. Their work was aimed at reducing the risk of delaminations. They cited work by Foye and Baker [67]. Both groups investigated layups consisting of $[\pm 15^\circ, \pm 45^\circ]_s$ (symmetric) laminates. Foye and Baker investigated these laminates in fatigue, testing laminates of $[15^\circ/-15^\circ/45^\circ/-45^\circ]_s$ and $[15^\circ/45^\circ/-45^\circ/-15^\circ]_s$. They noted that although in classical laminate theory stacking sequence has no effect upon tensile stiffness or strength, they observed differences in fatigue strengths of about 173MPa between the laminates, and cited progressive delamination as the failure mode. Pagano and Pipes suggested that the interlaminar normal stress, σ_z , is responsible for delamination. Considering the free body diagram in Figure 2.20 it can be seen that the 90° ply shown will experience tension at its interface, which may lead to delamination. This is because its modulus is highest in its fibre direction. It will therefore resist the tendency of the adjacent 0° ply to compress (in the y direction due to tension in the x direction) by imposing an opposite (tensile) force on the compressive force to balance it. In summary, laminates with large differences in fibre orientation between plies are more likely to delaminate than those with small differences. In later sections this will be discussed further, and this theory put to practical use in order to encourage delaminations.

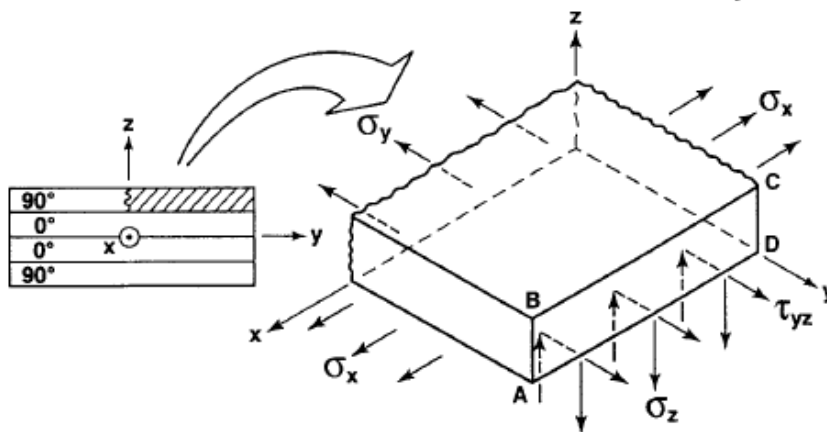


Figure 2.20: Free-body diagram for a cross-ply laminate in tension in the x direction [68]

2.3.1.4 *Fibre Fracture*

Fibre fractures are of course the most critical damage mechanism since the fibres are the main load bearing component of the composite. In general, excessive fibre failure results in catastrophic failure of the composite structure. In aerospace applications, fibre failure is usually in the compressive mode, since aerospace structures are usually designed to withstand flexural loads [69]. However, in many other applications, tension dominates fibre failure. Failure of the composite may occur in two ways. Firstly, the fibre/matrix interfacial bond may be broken by shear stresses within the composite, leading to reduced load transfer between fibres, and hence leading to the failure of the structure. Or secondly, fibre fractures can propagate through the matrix, as shown in Figure 2.17a, eventually resulting in the fracture of the structure [1]. If the integrity of the fibre/matrix interfacial bond remains, then fibre strength may be described by a statistical distribution. The Weibull distribution [70] is typically used to describe the variation of fibre strengths in a composite, and characterises the distribution fairly well.

2.3.2 *Free-Edge stresses*

Classical laminate theory holds extremely well for composites, but applies to infinitely wide laminates. That is, composite structures with no free edges. At and near the free edges (extending inwards a distance approximately equal to the laminate thickness [25]) there is a state of three-dimensional stress which exists. In certain circumstances, this can create rather large interlaminar stresses, which can lead to delaminations and matrix cracking, and hence premature laminate failure.

The out-of-plane normal and shear stresses which exist near laminate free edges are known to influence the initiation and growth of delaminations. For this reason many studies have been conducted in recent years to determine the gradient of the free edge stresses due to mechanical, thermal, and hygroscopic loading [71-75].

Pagano and Pipes [68] investigated this effect by considering a laminate of four plies under uniform axial strain as shown in Figure 2.21. Classical laminate theory states that each ply is in a state of plane stress. The stress varies between the differently orientated plies, but is constant within the plies. This is fine for laminates of infinite width, but since there is no material at the edge to keep it constrained, the shear stress at the edge is not opposed.

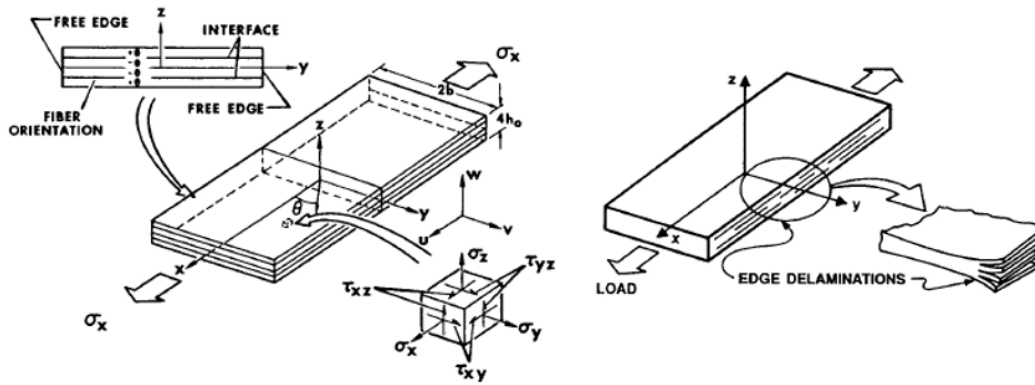


Figure 2.21: A four-ply laminate under uniform axial strain. Shows the stresses acting upon a unit cell of a central ply. [68]

Also from Pagano and Pipes, Figure 2.22 shows that the in plane shear stress (σ_{xy}) is in accordance with classical laminate theory, and the axial stress (σ_x) also follows for $y/b < 0.5$. σ_y , σ_z , and σ_{yz} increase slightly close to the edge, but are small. However, σ_{xy} increases dramatically at the free edge, and falls to approximately zero at $y/b=0.5$, or approximately equal to the total laminate thickness. These results were later confirmed by Pipes and Daniel [76] using the Moiré technique to observe micro surface displacements of laminates in axial tension.

Rybicki et al. [77] also investigated the free-edge delamination mode of failure in a $(\pm 30/\pm 30/90/90)_s$ boron/epoxy laminates. They evaluated the initiation and growth of delaminations using ultrasonic techniques. They then used basic finite element techniques to model the delamination behaviour using an energy release rate technique. This work was a precursor to many others who investigated crack growth as a function of energy release rate, such as O'Brien [78].

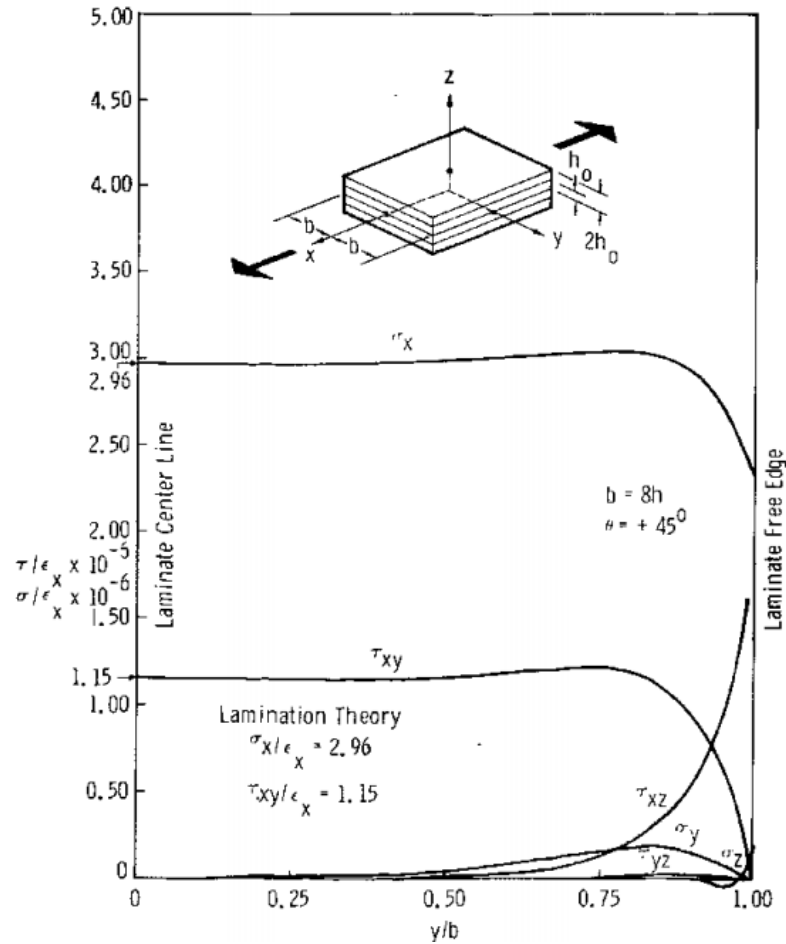


Figure 2.22: Stress distribution at the edge interface ranging from the centreline ($y/b=0$) to edge ($y/b=1$) [68]

2.3.3 Stacking Sequence

An important result of the previous section is that free edge stresses are influenced by stacking sequence [73, 76]. That is the order in which the plies are laminated, and hence which plies contact each other.

Pagano and Pipes investigated angle-ply laminates of $[\pm 15/\pm 45]_s$ and $[\pm 45/\pm 15]_s$ and showed that the interlaminar normal stress (σ_z) switched from tension to compression as the stacking sequence was switched. This resulted in the $[\pm 15/\pm 45]_s$ having poorer mechanical properties because delamination was initiated more easily in tension than in compression at the free edge.

Whitney [79] noted the same effects in carbon/epoxy laminates in fatigue loading. He observed that a laminate with a stacking sequence causing tensile interlaminar stress would

cause delaminations to occur long before ultimate failure. Whereas when the stacking sequence was changed to create compressive stresses, few delaminations were observed.

It was also discussed by Gamstedt and Anderson [80] that if the off-axis plies contribute to a substantial part of the laminate, the damage that develops in those plies will affect the damage evolution in the longitudinal plies. This means that a large number of off-axis plies will invariably lead to the evolution of additional damage in the main load bearing plies. This is a principle that will later be utilised to encourage interlaminar damage in samples.

Another effect which stacking sequence may have is upon the interlaminar region. Where two plies of the same orientation are stacked adjacent, nesting of the fibres can occur. This is where the fibres of adjacent plies intermingle with each other, allowing the plies to come closer to each other, and reducing the resin-rich region greatly. If these plies delaminate then the delamination propagates through fibre bridging, resulting in a rough surface with fibre imprints. Naturally, the opposite is true for adjacent plies of differing orientations. In this case they would have thicker interlaminar regions and any delaminations would mostly propagate along the tensile ply/resin-rich region interface, and would generally result in a smoother surface. [5]

2.4 INTERLAMINAR TOUGHENING OF COMPOSITES

Since delamination is a significant factor in composite failure, the toughness and resistance to crack propagation of the interlaminar region is of particular importance. Thermoset matrix polymers have good mechanical strength and chemical resistance, but due to crosslinking they can be brittle. This often results in microcracking, which may then lead to further damage. Thermoplastics have good resistance to impacts and resist crack propagation, but result in decreased stiffness, particularly in bending. In applications such as aircraft wings, this is simply unacceptable since stiffness is one of the key reasons why composites are used in the first place. The ideal scenario would be one in which the mechanical properties of a thermoset matrix are preserved, but the toughening effects of thermoplastics are utilised. This is obviously an unrealistic goal. However, it is possible to tailor the material properties in regions where damage is most likely to occur. Since delamination is often a critical damage mechanism, and the interlaminar region is easily accessible during manufacture, interlaminar toughening is the focus of wide research.

2.4.1 Fibrous Interlaminar Reinforcements

Numerous types of laminated CFRPs with different interlaminar toughening mechanisms have been reported to date. Carbon nanotube deposition is one such method that has received a lot of attention. In this method, carbon nanotubes are deposited on the surface of the carbon fibre weave so that they are orientated in the through thickness direction.

Veedu et al. [81] used chemical vapour deposition to grow multiwalled carbon nanotubes on the surface of carbon fibre woven fabrics. In this way they were able to gain a 348% increase in interlaminar fracture toughness (G_{IC}), while the interlaminar shear sliding fracture toughness G_{IIC} was improved by 54% compared to the base material. Arai et al. [82] also obtained very similar results. Similarly, Lee et al. [83] coated non-woven carbon tissue with nanotubes. They reported a 353% increase in G_{IC} and a 246% increase in G_{IIC} . White and Sue [84] took this method further, and used a carbon nanotube and polyamide-12 epoxy thin film as a toughening layer. The increase in G_{IIC} values was nearly 250% higher compared to the reported untreated CFRP values.

Although carbon nanotubes are currently a popular method of fibrous interlaminar reinforcement, other authors have also investigated other fibrous materials to a lesser degree. Hamer et al. [85] demonstrated approximately 300% improvement in G_{Ic} values compared to the untreated laminates using an electro-spun Nylon-6,6 nanofibrous mat as the interlaminar toughener (Figure 2.23).



Figure 2.23: Electro-spun Nylon-6,6 fibre interleaf under mode I loading [85]

2.4.2 Interleaving and Additive Toughening

One of the most common methods for improving the interlaminar fracture toughness is interleaving, in which a distinct interlayer (thermoset or thermoplastic) is added between the laminate plies. This is illustrated in Figure 2.24. This introduces a tough region which absorbs energy and inhibits cracks which may otherwise propagate between plies. Additive toughening is similar to interleaving in that a foreign element is introduced into the interlaminar region in order to change the material properties specifically in that area.

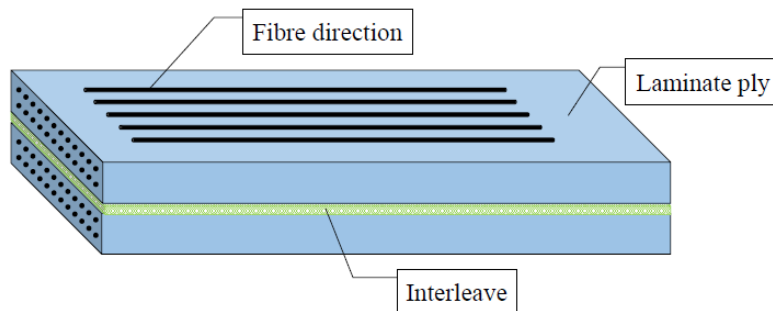


Figure 2.24: Illustration of interleaving [11]

Askoy and Carlsson [86] experimented with both thermoset and thermoplastic interleaves to determine what effect the thickness of the interleaf had on the mechanical properties. They found that thicker interleaves increased fracture toughness and shear yielding of the material around the crack tip up to a point at which the effects levelled off. This is in line with what was discussed in Section 2.3.1.3, which described how increasing the ductility of the matrix increases the size of the crack process zone. Predictably, they found that thermoset interleaves proved less effective than thermoplastic ones. Thermoplastics allow much greater plastic deformation with less microcracking and therefore crack tip shielding. However, they did not comment on what effects this had on other mechanical properties.

Lu et al. [87] inserted thin (~0.1mm) sheets of poly(ethylene-co-acrylic acid) (PEAA) between plies of carbon fibre prepreg. Interestingly, they noted a significant change in the failure mechanism of the composite in both impact and static bending. The presence of the interleaved layer provided a barrier to prevent compressive cracks from propagating into the tensile plies of the samples. This also had the effect of slightly decreasing the flexural modulus of the composite, which they attributed to the interleaved layer allowing the adjacent plies to move past each other more easily.

Hojo et al. [88] used the epoxy matrix as the interleaf material by sequentially laying up half-cured epoxy films and prepregs. It was reported that the G_{Ic} values of the laminates with the self-same epoxy interleaves were almost identical to those of the base laminates. However, the values of G_{Ic} in the laminates with interleaves were up to 340% higher than those of the untreated laminates.

Takeda et al. [89, 90] used fine, randomly dispersed polyamide particles to create a toughened interlaminar layer between prepreg plies. The particles were scattered by hand, so placement was highly uneven. They found that delamination onset and growth in fatigue loading were suppressed by the toughened interlaminar layers, although they don't directly quantify this improvement. Using a modified Paris' Law they characterised the transverse crack multiplication and delamination growth. The premise of this work most closely resembles that presented in this thesis. Unfortunately, Takeda's work is vague and lacking experimental data in places, and it is likely that the investigation was brief and not followed up.

PEG printed laminates are investigated in this thesis. Some studies investigated PEG as a plasticiser for other polymer blends [91-96], but few others report using it as a composite toughening agent, and none were found that investigated its toughening properties in fatigue loading

Zavareh and Samandari [97] found that by adding up to 10% low (600) molecular weight (M_w) PEG to the bulk matrix, they could achieve an impact toughness increase of up to 570% compared to that of neat epoxy with only minimal detriment to tensile strength and modulus. Morphological properties of this epoxy/PEG hybrid were obtained through SEM studies and a two-phase morphology was revealed in which nano-sized PEG domains were uniformly distributed in the epoxy matrix. They concluded that increases in impact toughness could be attributed to strong interactions between PEG and epoxy in the interfacial region, but did not elaborate on these claims.

Sala [98] conducted impact tests upon glass fibre reinforced isocyanate-epoxy composites toughened using 15% PEG by volume. They did not state the molecular weight of PEG used. They found that the tensile strength, tensile modulus, compressive strength, compressive modulus, shear modulus, and strain to failure of toughened composites were all higher than base values by around 10% in all cases. They also found that the impact strength of composites were increased by as much as 49% by the addition of PEG. However, they did not attempt to evaluate the mechanisms of damage other than generally attributing behaviour to 'toughening effects'.

PMMA printed laminates were also investigated in this thesis as a potential toughening agent. Similarly to PEG, little literature could be found on the toughening effects of PMMA, and none was found on its use as a toughening agent in fatigue.

Garoushi et al. [99] conducted compressive fatigue tests upon epoxy matrix based samples containing PMMA impregnated E-glass fibres. They investigated the effects of fibre orientation upon the properties of composites, but did not quantify how the PMMA filler affected this behaviour.

Söderholm [100] investigated the relationship between compressive yield strength and filler fractions of PMMA matrix composites reinforced with soda lime glass beads. They found that increased bead volume fractions increased compressive strength, but did not comment on the nature of the PMMA matrix or its behaviour under loading.

Gilbert et al. [101] investigated the properties of high ductility PMMA fibres in a PMMA self-same matrix in three point flexural fatigue. They found that these composites exhibited far greater fatigue energy dissipation and creep fatigue displacement than pure PMMA samples. In this study they did not mention the molecular weight of PMMA that was used, so it is difficult to assess the toughening capabilities they obtained in relation to the polymers used in this thesis.

In this section it was discussed that there are multiple studies which have investigated the interlaminar toughening of composites. Many of these use interleaves, fibrous elements such as carbon nanotubes, or nanoparticles. However, very few investigate the addition of polymer particles. Of those that did, most investigated their addition into the bulk matrix rather than solely the interlaminar region. Additionally, papers which look at interlaminar toughening almost exclusively investigate interlaminar fracture toughness (G_{IC}), with occasional focus on impact damage [82, 84, 85, 102-107]. This was also true of PEG and PMMA toughened composites, where no literature was found on their effect upon the fatigue performance of laminates. With delamination being a key factor, fatigue damage is an obvious research area for toughened composites.

2.5 EXPERIMENTAL FATIGUE OF COMPOSITES

Due to the complex nature of composite fatigue, and its far-reaching research areas, the catalogue of published experimental data is consequently vast. The methods of composite fatigue have previously been covered in Section 2.3, so this section attempts to highlight some of the published work that is most applicable to this thesis.

Flexural fatigue tests are often ignored in favour of tension/tension or tension/compression fatigue tests. However, they have advantages such as better representation of in-service loads, greatly reduced risk of buckling, and greatly reduced testing forces. They are also often accompanied by stiffness degradation analysis since flexural tests inherently produce large specimen deflections, and so don't require accurate or complex instrumentation to measure it. But these advantages are sometimes disregarded in favour of the less complex and more easily modelled tensile tests. As a result, applicable literature which utilises flexural fatigue does exist [108-119], but is somewhat uncommon. The most applicable method of flexural testing is also disputed, with some authors favouring cantilever based tests, and some favouring loading roller based tests. This disparity only adds further ambiguity to the results obtained by various research groups.

Agarwal and Joneja [111] determined that variations in the flexural fatigue strengths with fibre orientation at different cyclic lives were similar to the variations in static strength. Weber and Schwartz [113] monitored the behaviour of unidirectional carbon fibre epoxy strands by both their changes in resistivity and bending modulus. Similarly, Couillard and Schwartz [114] reported on a study on carbon-fibre/epoxy strands subjected to repeated, fully reversed cycles of pure bending. Using the change in bending moment as an indicator of accumulated damage, they noted an exponential decay on the bending modulus as a function of the number of cycles. They determined that, at the decay rate observed, the bending modulus would reach zero after 7.6×10^{18} cycles.

Caprino and D'Amore [115] conducted four point bending fatigue tests on a random continuous fibre reinforced polypropylene composite. Comparing the experimental results with similar data available in the literature for thermoset-based composites, it was shown that the presence of an inherently ductile thermoplastic matrix does not sensibly affect the fatigue sensitivity of the material, probably because of the constraint action of the reinforcement. From their fatigue model, a statistical model was developed, assuming a distribution of the static fibre strength according to a two-parameter Weibull distribution [70]. The data was in excellent agreement with theoretical predictions, indicating that a fatigue characterisation for probabilistic design can be achieved by a minimum of experimental tests.

Cox et al. [112] performed flexural fatigue experiments on a glass/carbon hybrid composite with an unbalanced layup. Cantilever bending fatigue was performed to a maximum of 1×10^6 cycles at varying load amplitudes. The flexural loads led to stiffness reductions from matrix cracking and small delamination regions, and ultimate failure was due to delaminations between the glass/carbon interfaces on the tensile side.

Belingardi et al. [116] investigated the flexural fatigue of hybrid glass-carbon epoxy composites. Using an R ratio of 0.1, and load amplitudes of up to 85%, they observed early damage after just a few hundred cycles. They observed the stiffness reduction of the composite, and noted that it was a function of the applied fatigue amplitude. They also performed post-fatigue static tests, but discovered that the residual strength of the composite wasn't necessarily linked to the reduction in stiffness.

The experimental setup is extremely important in flexural testing, and care should be taken to optimise the procedures and geometries in order to reduce roller contact stresses. Cui and Wisnom [120] carried out detailed stress analysis of both three and four point bending unidirectional glass fibre specimens using ABAQUS. They found that the specimens were very sensitive to the length of the contact surface and the distribution of contact stresses. They also showed that the stresses at the loading points were higher than was indicated by classical beam theory. Their results indicated that larger rollers resulted in greatly reduced contact stresses. It was also demonstrated that the use of four point bending reduced contact stresses by 20% over three point bending.

As well as flexural fatigue experiments, tensile fatigue experiments were carried out as part of the work presented in this theses. These tests adhered to international standards.

Jamison et al. [121] conducted investigations into the damage mechanisms in tension-tension fatigue of graphite/epoxy laminates. They looked closely at the global change in stiffness of the material under increasing fatigue cycles, and in doing so were able to obtain reproducible characteristic correlation with the percentage of life that had been expended. Although, they found that this correlation differed significantly between different layup geometries. They also observed several new damage mechanisms related to differing layup geometries, such as the production of interior delaminations at the 0/90-deg interfaces of $[0,90_2]_s$ laminates by the gradual growth of longitudinal cracks in the 0° plies.

Zhang et al. [122] investigated the effects of nano-silica and CTBN (carboxyl terminated butadiene acrylonitrile) rubber reinforced matrices upon both the interlaminar fracture toughness and fatigue delamination growth behaviour of CFRP composites in tensile fatigue. They noted improved delamination growth resistance in both 10%/wt nano-silica and 10%/wt CTBN rubber reinforced composites, which they attributed to the synergistic contribution of toughening mechanisms induced by the particles.

Manjunatha et al. [123] also investigated the fatigue life of GFRP composites blended with a CTBN rubber microparticles and silica nanoparticles. They found that the cyclic fatigue life of a composite containing 10%/wt of both particles was up to ten times higher than that of a

neat resin composite. This was attributed to suppressed matrix cracking and reduced crack growth rate.

Hojo et al. conducted fatigue tests using two types of interleaves [124]. One, a heterogeneous layer with fine polyamide particles, and the other with an interleaf of a thermoplastic resin UT500/111/ionomer. These tests, like many others focusing on interlaminar toughening, utilised the double cantilever beam test as a fatigue testing method. The double cantilever beam test is purely a mode I (tension) test, and incorporates very little mode II (shear). However, using this method, they found that the delamination resistance of T800H/3900-2 composites was about three times higher than the control value in the initial stages of stiffness degradation. Although this ratio decreased to 1.5 later on where delamination was the dominant damage mechanism.

Likewise, Chan et al. [125, 126] investigated the delamination arresting capability of adhesive strips under both static and fatigue loading using the edge delamination test. Strips were placed on the free edge delamination region or slightly away from the free edges. Static tests showed that delamination was arrested at the boundary of the adhesive strips until further loading drove the delamination through the adhesive zone. In samples with the strip along the free edges, delamination was effectively prevented until final failure. Although this study focussed mainly on static loading, they also conducted these tests in cyclic loading, and found that delamination growth rate was reduced due to the interleaves [127]. They found that although initial fatigue was not arrested to any significant degree, delamination growth rate was reduced with increasing numbers of cycles. They stated however, that delamination was not arrested, simply slowed.

The texts cited in this section cover a broad area of composite fatigue using both flexural and tensile fatigue. Elements of these investigations were incorporated into the work presented in this thesis. And references will be made back to them at various points. It should be noted that of the many papers that were read prior to these investigations, very few incorporated interlaminar toughening. And those that did focussed on rubber particles or interleaves. Both of these methods require the addition of significant amounts of material, increasing mass. Also, whilst interleaves may be applied selectively to desired areas where certain damage mechanisms may be most prevalent, their composition is difficult to tailor. The novelty of this work then, lies in the selective addition of polymer reinforcements that can be suited (perhaps by region or gradual transition from one reinforcement material to another) to the load case in any given area of a structure.

2.6 DAMAGE ANALYSIS TECHNIQUES

Numerous techniques have been developed for the detection and analysis of damage in composites. Techniques may be divided into active and passive techniques, and further divided into destructive and non-destructive. Each have their own benefits and disadvantages. Destructive techniques such as residual strength analysis are incredibly useful, but require large numbers of tests to be conducted, and only offer predictive or post-mortem techniques for the properties of in-service components [128-130]. Non-destructive techniques may be applied to in-service components, but require instrumentation to detect physical material changes.

The best analysis techniques then are dependent upon the individual requirements of the prescribed test regime. The following sections outline the fundamentals of the damage analysis techniques used in subsequent chapters, as well as other relevant methods.

2.6.1 *Stiffness Degradation*

Stiffness degradation is the gradual reduction of the elastic modulus of a material as it is cyclically loaded. Tracking this change can give insight into what damage has accumulated in the material up to that point.

Naturally, the stiffness degradation of a given laminate will be highly dependent upon the matrix, reinforcement, stacking sequence etc. But the sequence may be generalised as described by Van Paepegem and Degrieck [131]. Generally, stiffness degradation may be divided into three sections (I, II, and III) as shown in Figure 2.25. In stage I a rapid reduction in stiffness may be observed. The development of transverse matrix cracks dominates the stiffness reduction in this stage. A stiffness reduction of 2-5% is typical. In the second stage an additional 1-5% stiffness reduction may occur in a roughly linear way. Predominant damage mechanisms in this region are the development of edge delaminations and additional longitudinal cracks along the 0° fibres. In the final region, localised damage events accumulate quickly as load distribution between fibres is affected to a level which allows weak fibres to fracture. This damage grows exponentially as fibres continue to break, eventually leading to the ultimate failure of the laminate. [131]

Stiffness change is a precise, easily measured, and easily interpreted indicator of damage. It is also attractive because it is a non-destructive test method. Typically, fatigue damage accumulates within the material in a general manner. With this, the stiffness of the material is reduced. However, the change is not necessarily constant, as damage features such as

macroscopic cracks and delaminations may develop and/or be arrested, and in this manner alter the rate of stiffness degradation accordingly. Several authors have published work outlining how the reduction in stiffness may be used to model the fatigue life of the composite [132-140]. However, all of these focus on the prediction of fatigue strength and life. Where they do discuss the damage mechanisms which lead to stiffness degradation, they describe them very generally, and do not use stiffness degradation as a method to infer specific damage events. Many authors refer to the generalised model referred to above in Figure 2.25, which further leads to the inaccurate generalisation of stiffness degradation, and ignores the specific intricacies of each individual test.

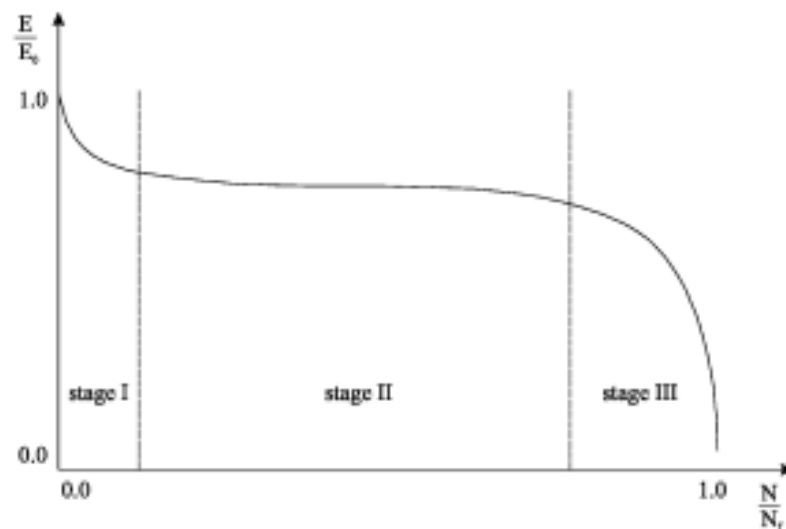


Figure 2.25: Generalised model of the decrease in stiffness associated with composite fatigue with increasing numbers of cycles. Stage I: Matrix cracking and delamination. Stage II: Crack coupling and interfacial debonding. Stage III: Damage coalescence and fibre breaking. [141]

2.6.2 Sample Replication

Because of the progressive and destructive nature of mechanical testing, it is highly advantageous to be able to record physical damage for later analysis and reference. The most popular method of doing this is the cellulose acetate replica technique. Dental media is also often used for replication where the cellulose acetate method may not be applicable, but acetate provides better resolution at higher magnifications [142]. Cellulose acetate has many advantages: it is simple to apply, reproducible, has low distortion and volume changes, and is resistant to harsh environmental conditions. This technique is highly advantageous where

removing samples from a test may affect the results, or where the samples are physically too big (eg. to fit in an SEM chamber) for analysis.

Cellulose acetate is readily available as sheets from numerous microscopy equipment retailers, and is available in varying thicknesses from 10 μ m upwards. The thickness of the sheet affects the resolution that can be expected. Thicknesses around 35 μ m have been found to give excellent results [142]. However, thin acetate sheets may prove problematic, as they may tear easily, and may distort around particularly large artefacts. The thickness also determines the amount of workable time the operator has to apply the sheet. Cellulose acetate is softened with acetone in order to take replicas. Therefore, if the softened sheet is not supported quickly by application to the sample surface then it will disintegrate rapidly. Thicker sheets allow greater working time, but as previously mentioned, this comes at the cost of reduced resolution. Once obtained, replicas may be stored indefinitely if stored correctly.

The microscopic observation of replicas is straightforward. The replica is laid flat on a glass microscope slide and fixed down in position using something such as sticky tape. Replicas may be observed optically by either transmitted or incident light. Although transmission microscopy may be affected by contamination between the glass slide and the replica, or by impressions on the reverse side of the replica caused by poor application. Optical observation may also suffer because of the difficulty of applying the replica perfectly flat against the glass slide. If it is not flat then focussing may be difficult because the depth of field of optical microscopes is poor, particularly at high magnifications.

The replica technique is also compatible with scanning electron microscopy (SEM) [142, 143] and is used regularly in various research fields [144-150]. Although they must be made conductive by a method such as vapour deposition in order to maximise the resolution of the micrographs (described further in Section 6.2.1.1). SEM observations of progressive damage is of course possible, but requires the dismantling of the specimen at various points, and also requires the total dedication of the SEM during the test. The advantage of SEM over optical microscopy is that the depth of field is much greater, so the difficulty of applying the replica flat to the glass slide is less troublesome. The problem caused by uneven specimens under optical microscopy compared to SEM is illustrated in Figure 2.26, where it can be seen that in the optical image, all but a narrow region surrounding the crack is out of focus.

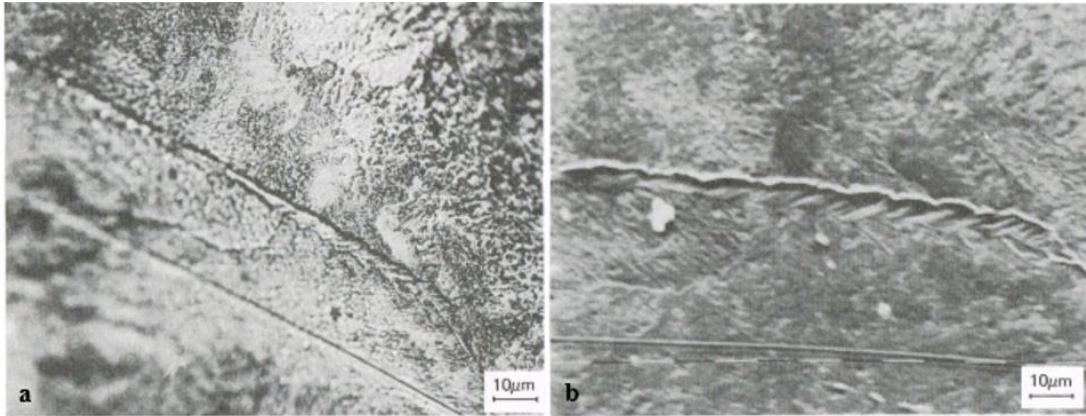


Figure 2.26: Comparison between a) optical and b) SEM viewing a replica at high magnification, illustrating the difference in depth of field of the two techniques [142]

2.6.3 Scanning Electron Microscopy

Scanning electron microscopy (SEM) is the most widely used method for studying fracture surfaces. The high resolution and good depth of field of the images it produces make it highly suitable for examining polymer composite surfaces. Also, due to the way SEM works, the images it produces are similar in appearance to optical images, making them more intuitive to interpret [5]. Microscopic methods not only provide a quantitative measure of such things as crack length, no matter how small the crack may be, but they can also identify the path that cracks take and their relationship to microstructural parameters [142].

Broadly, SEM works by firing a beam of electrons onto the sample. The beam is generated by a filament (typically made of tungsten) which is heated to a very high temperature. This high temperature provides enough energy for electrons to escape the filament. The beam is passed through an anode with an aperture to form the beam. Magnetic lenses then focus and direct the beam across the sample surface. The electron beam scans the surface in lines, much like a cathode ray television. When the electron beam hits the sample surface, different types of secondary radiation may be produced. Backscattered electrons and x rays can be used for elemental analysis. Although CFRP comprises of different components, they are primarily organic, and hence carbon containing, and therefore elemental analysis is of little use. Secondary electrons may also be produced. These are generated as ionisation products, and are primarily ejected from the surface atoms. These can be used to analyse the topography of the sample, and so are very useful for fractography [151].

The depth of field of SEM (H) is an important factor in SEM and is calculated by:

$$H = \frac{2SW}{AM} \quad 2.7$$

Where S is the permissible defocus, W is the working distance (distance between the objective and the specimen), A is the objective aperture, and M is the magnification [142, 152].

2.6.4 *Fractography*

One of the main uses of SEM in the context of mechanical testing is in fractography; which is the study of fracture surfaces. Fractography can provide important clues about the cause of failure in a component, the location of the source of failure, and the consequent sequence of events that then resulted.

Numerous visual artefacts may be created when composites fracture, which together may be used to infer the properties and fracture mechanisms of composite materials. The following sections introduce many of the artefacts and observations that were common to samples in tests in the following chapters, and that will be used later in this thesis to analyse fracture surfaces.

2.6.4.1 *Fibre dominated and Matrix Dominated Surfaces*

The fracture surfaces of adjacent plies are easily mistaken for one another because when plies delaminate, the resin-rich region (a thin layer between plies containing few or no fibres) tends to fracture at the interface between itself and the fibre boundary of either ply. At this interface, fibres leave negative imprints in the resin. An example of this is shown in Figure 2.27. It is most common for the resin-rich region to delaminate at the ply in tension, and therefore remain adhered to the ply in compression [5, 153-155]. These are referred to as the fibre dominated and matrix dominated surfaces. However, which ply interface it delaminates from may be changed according to local variables such as interface strength and toughness. The resin-rich region may also fracture through its middle where both interfacial strength and matrix ductility are both suitably high [5].

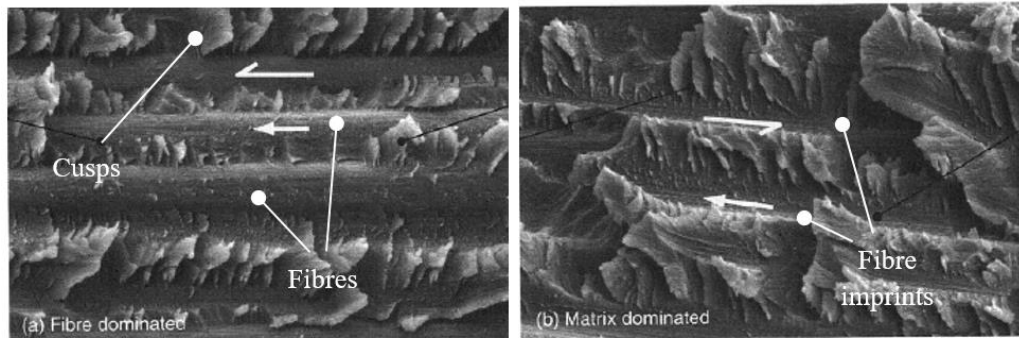


Figure 2.27 Unprinted sample showing fibres and fibre imprints in a) fibre dominated surface, b) matrix dominated surface [5]

2.6.4.2 *Cusps*

Another notable artefact is ‘cusps’ (or ‘hackles’ in the USA). These are visible in Figure 2.27. These features appear as inclined scales or platelets within the resin regions of fractured surfaces. They are formed as a result of mode II loading. Their tilt directions oppose each other on opposing faces, giving an indication of the relative directions of shear of both surfaces [5, 156, 157]. The process of cusp development is illustrated in Figure 2.28 and Figure 2.29. The crack front of a delamination creates a process zone ahead of it. The process zone is a region of increased stress in which material separation takes place. The shear stress in the process zone may be resolved into a principle stress at 45° to the laminate plane. This causes angled fractures to develop, which extend through the resin-rich region until they are rotated due to the presence of fibres above or below them. This gives cusps a characteristic ‘S’ shape. Once the surfaces detach, one surface typically retains the cusps, whilst the other displays smaller cusps or ‘scallops’ (negative impressions where cusps detached from the opposite surface) (Figure 2.30).

It can be seen in Figure 2.27a that the size of cusps differs greatly throughout the image. The size and distribution of cusps is affected by a number of factors. The intermatrix spacing between surface fibres is a predominant factor, but factors such as moisture content, temperature, matrix chemistry, and processing conditions can all influence the formation of cusps [5, 157-159]. Importantly, matrix toughness may also play a significant role in their formation too. With increased plasticity, cusp thickness increases due to less microcracks forming in the matrix [5, 160]. This may be a useful comparative tool later on to compare printed and unprinted fracture surfaces. Although, due to the wide range of factors which affect cusp thickness, it is not necessarily an indicator of matrix toughness by itself.

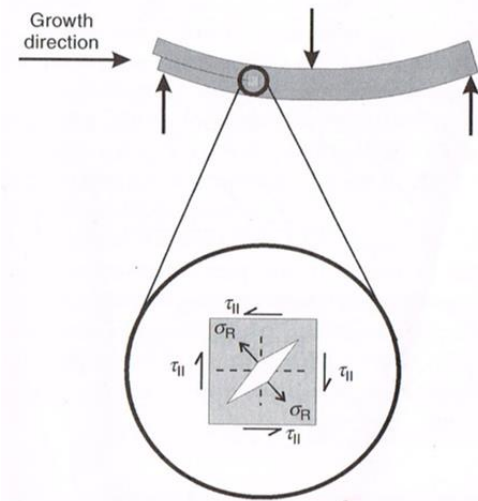


Figure 2.28 Mechanism for the formation of cusps due to shear. In this case shear is caused by flexural geometry, but is applicable to any case where a strain difference exists between plies. [5]

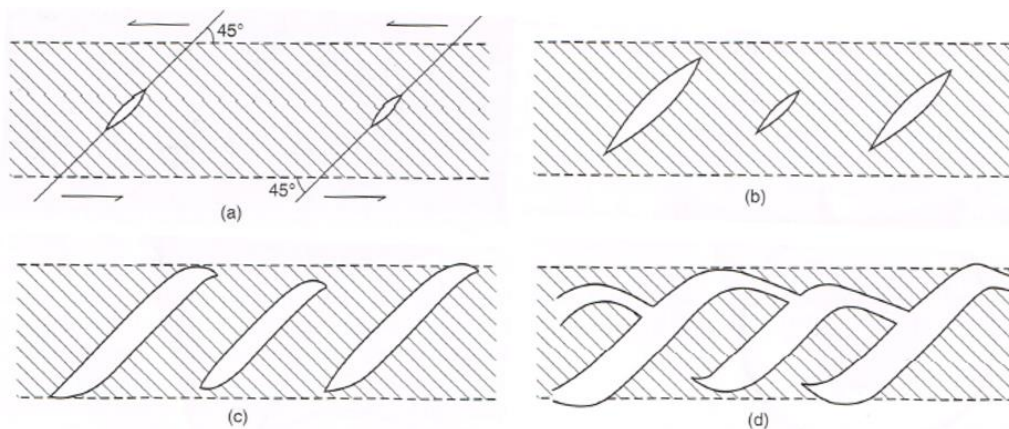


Figure 2.29 Mechanism for the growth and coalescence of cusps. The shear stress ahead of the crack tip can be resolved to a tensile traction which is inclined at 45°. a) Angled cracks develop in the matrix ahead of the crack tip, usually originating at fibre interfaces. b) Cracks extend under shear stress. c) The presence of fibres at the interlaminar boundary cause the crack tips to rotate. d) Cracks converge to create characteristic 'S' shaped cusps. [5]

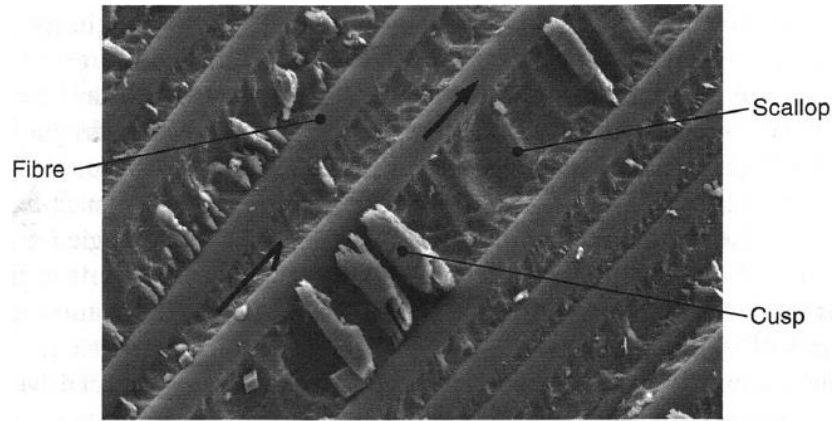


Figure 2.30 Scallops on the surface of a sample [5]

A useful property of cusps is that they may be used to deduce the direction of delamination growth. As discussed above, cusps form when the damage state ahead of the delamination front is such that cracks form at 45° to the laminate plane. As a consequence of this, these cracks are driven forwards, ahead of the delamination front, rather than towards it [5]. This mechanism is illustrated in Figure 2.31. An important consequence of the information in this figure is that cusps on the matrix dominated ply inherently lean away from the direction in which the crack front travels, and will lean towards it on the fibre dominated surface. Therefore, by identifying which surface (fibre dominated or matrix dominated) is being observed, the direction of travel may be inferred [5]. Whether the surface/region is fibre or matrix dominated is easily identified by locating either fibres or fibre imprints on the surface.

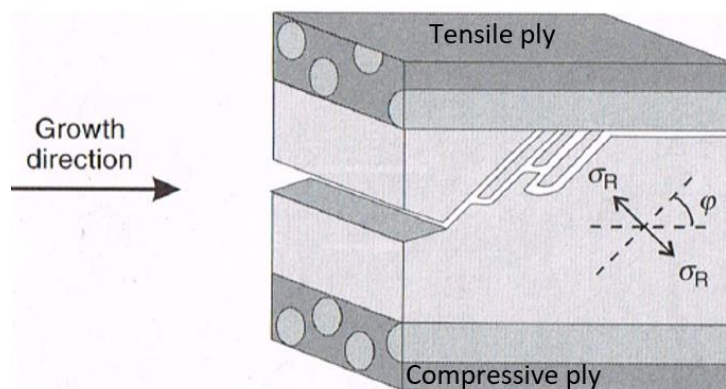


Figure 2.31 Cusps being driven ahead of a crack front. Cusps form on the tensile surface, and negative ‘scallops’ form on the compressive surface. [5]

2.6.4.3 Gouges

Gouges (Figure 2.32) are grid-like features which only appear at non-zero interfaces [5, 155, 161, 162]. They look much like cracks, but they are not. They are instead associated with cusp formation, such that adjacent cusps are aligned. The mechanism which is presumed to cause gouges is shown in Figure 2.33. In this mechanism cracks develop at the fibre boundary in the compressive ply and propagate through the matrix at 45° due to the same resolved tensile stresses caused by mixed mode loading which cause cusp formation. Because of this, gouges are very common where cusps are formed. Because of this mechanism, gouges are typically formed at the matrix dominated surface. Unfortunately, gouges do not give much information about the fracture surface. Although, the depth of gouges has been shown to change with the mixity of loading modes [153], increasing in depth as mode II dominates over mode I.

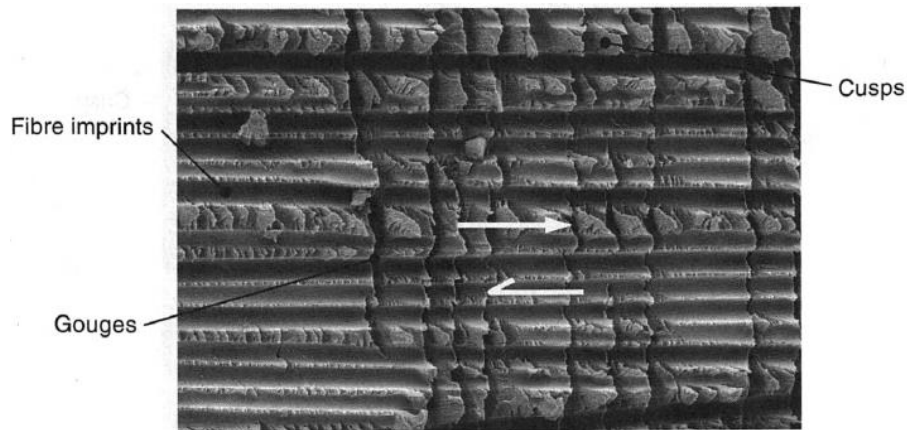


Figure 2.32 Gouges on the surface of a delaminated ply [5]

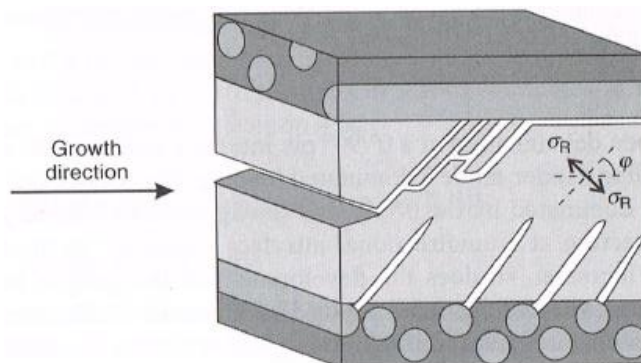


Figure 2.33 Mechanism for gouge formation at a $0^\circ/90^\circ$ interface. Cracks develop at the fibre boundary in the compressive ply and propagate through the matrix at 45° due to the same resolved tensile stresses caused by mixed mode loading which cause cusp formation [5]

2.6.4.4 *Rollers and Debris*

Another artefact prevalent in fatigued samples are ‘rollers’ and debris. Examples of debris are shown in Figure 2.34, and rollers in Figure 2.35. Rollers are rounded shafts of resin, orientated approximately perpendicularly to the fibre direction [5, 156, 157]. The mechanism which creates rollers is not fully understood. They were thought by some to be caused by ‘fretting’ actions between adjacent plies [157], but this theory does not appear to hold true in all cases. Others have attributed them to increased plasticity of the matrix under hysteresis [88, 156, 157, 163, 164], but again, this has not been proven. The morphology of rollers has been shown to be strongly dependent upon matrix toughness and fibre/matrix interface strength, becoming more elongated as toughness increases. This is illustrated in Figure 2.35. In highly toughened composites, smearing of rollers may also occur [5, 88, 165, 166], and in some highly toughened systems, few or no rollers form [157, 167].

Debris may develop due to the deterioration of cusps and other matrix elements from fracture surfaces through fretting. Debris may sometimes be used as an indication of the sequence of delamination. Generally, the longer a fracture surface has been in existence, the more debris will be present [5, 153, 167]. Although this is generally only used as an indicator, and is not typically quantifiable. Debris may also be produced in higher quantities where the mode mixity is dominated by mode II loading.

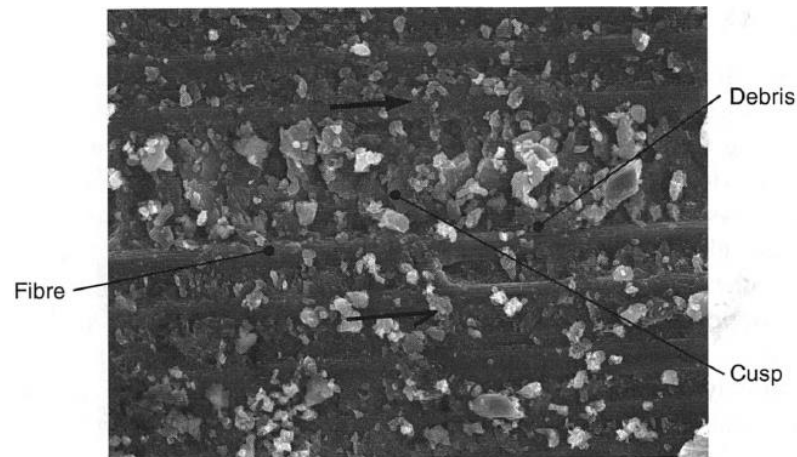


Figure 2.34 Debris on a delaminated surface [5]

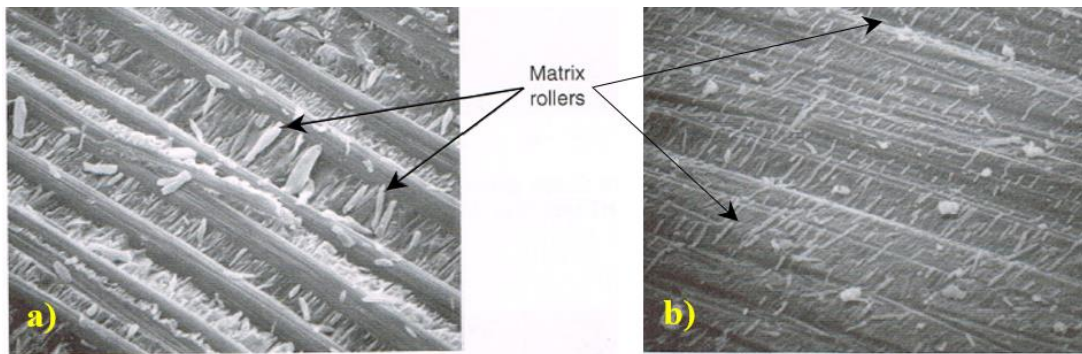


Figure 2.35 Matrix rollers on a mode II fatigue fracture surface. a) Untoughened matrix. b) Toughened matrix [5]

2.6.4.5 Influence of Matrix Toughness

Matrix toughening can affect the appearance of fracture surfaces. In general, tougher matrices result in rougher fracture surfaces [168], and surfaces may be dimpled or granular in appearance. It was also previously mentioned in Section 2.6.4.1 that matrix toughness may affect how the resin-rich region separates at the fibre boundaries either side of it, decreasing its tendency to separate preferentially at the tensile surface.

Tougher materials exhibit considerable plastic deformation. As a result, artefacts such as cusps are often less well defined in tougher materials. Examples of this are shown in Figure 2.36. It can clearly be seen in Figure 2.36a that the more brittle material resulted in cusps with much more clearly defined edges, whereas cusps in the toughened matrix system shown in Figure 2.36b are uneven and irregular due to plastic deformation. Some toughened and thermoplastic matrices also exhibit ‘fibrillation’, in which the matrix material is drawn out into peaks as it deforms and fractures [5]. Although these features only tend to appear in very ductile materials. An example of this is shown in Figure 2.37. In very tough matrix systems, cusp formation may be no longer possible, and fracture occurs due to mechanisms such as plastic deformation and void coalescence.

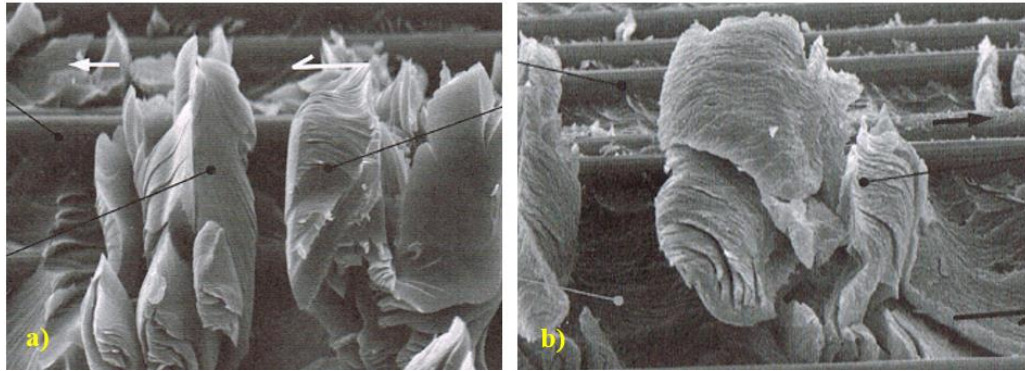


Figure 2.36 Representative cusps in a) a brittle matrix, and b) a relatively ductile matrix [5]

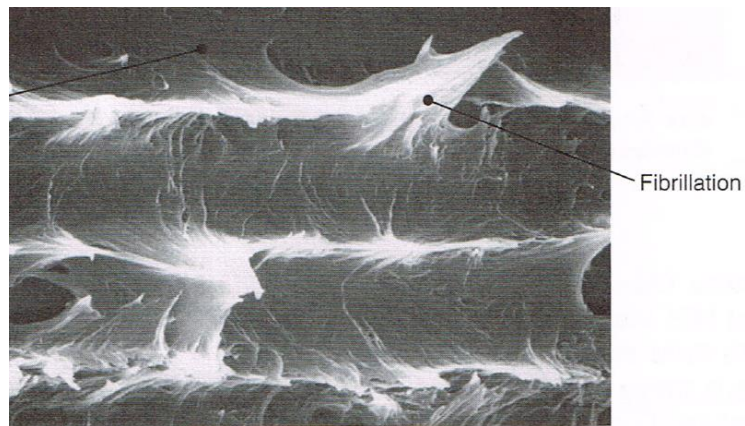


Figure 2.37 Fibrillation in a highly ductile matrix [5]

2.6.5 X-Ray Computed Tomography

X-ray computed tomography (CT) is based on similar technology to that used in the medical field to examine the internals of patients. In medicine, single images are taken to create two dimensional radiographs. However, in materials science, x-ray CT takes multiple two dimensional images as the object being examined is rotated. The series of two dimensional radiographs can then be mathematically reconstructed into a three dimensional image [169].

The main advantage of x-ray CT is that it is non-destructive. X-rays also have the ability to penetrate materials that other electromagnetic waves such as light cannot. The short wavelength of x-rays also gives the technique excellent resolution. However, the availability of x-ray CT facilities is a limiting factor. But where utilised, it is an invaluable tool, for example in the non-destructive observation of delaminations, such as those shown in Figure 2.38.

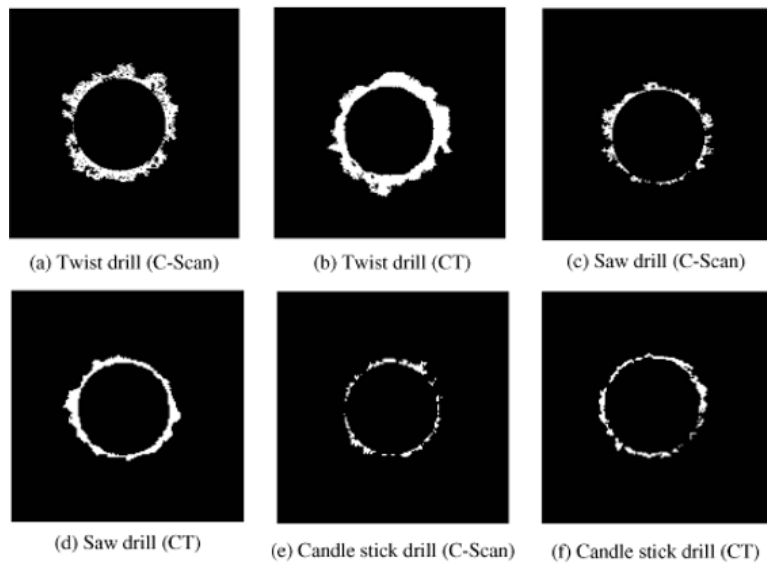


Figure 2.38 X-ray CT and ultrasound C-Scans obtained by Tsao and Hocheng [170] showing the extent of delamination in composite laminates featuring holes drilled by various methods

2.7 CONCLUDING REMARKS

Due to the growing interest of fibre composite materials in high performance areas such as aerospace, where the high specific stiffness and strength of composites is being utilised to decrease weight in order reduce fuel consumption, new research aimed at understanding the complex damage mechanisms operating in composite laminates is necessary. In this chapter the fundamental characteristics of composite materials were introduced. An overview of fibres, matrices, and manufacturing methods were also discussed.

The major obstacle of applying these materials is the nature of the complex damage mechanisms with accumulate within them. The cost of composite parts is comparatively high against traditional materials, but this is accepted due to the weight saving brought by their high specific stiffness and strength. However, damage is shown to accumulate in composites with repeated loading cycles which reduces their stiffness and strength, ultimately offsetting the benefit of using them. This is usually managed by creating structures with generous safety factors in order to keep them out of the range of their fatigue limit; which again offsets much of the benefit of using them. One of the key factors affecting stiffness is delamination of adjacent plies. Therefore, retarding and/or preventing delamination, particularly under cyclic loading, is a key goal in fully utilising the properties of composite materials.

Since delamination occurs in the interlaminar region, this should be the focus of toughening research. Many groups focus on the toughening of the bulk matrix as a whole. This is not

intrinsically bad, but many toughening methods often come at the detriment of other mechanical properties, so localising the toughening method purely to where it is required benefits the structure as a whole. Toughening the matrix as a whole also adds cost to the material since in high performance methods such as prepreg layup it must be done at the manufacturing stage and not by the end user. Interleaving has been explored by many as a way of achieving this, with many reporting promising results. However, the matrix toughening is usually restricted to low cross-linking density resin systems, and interleaving struggles to create an evenly distributed and constant morphology of the toughening materials. Also, the mechanical benefits are usually accompanied by other compromises, such as reductions in interlaminar shear strength [11].

If interlaminar toughening could be done by the end user then it would enable them to use it selectively. Inkjet printing then is an ideal method for toughening material deposition since it is highly scalable to the users' requirements, and allows them to tailor the formulation as needed. It also deposits minute amounts, ultimately adding negligible weight to the structure.

The following chapters concentrate on the promising results Zhang [9, 11, 12] conducted on inkjet deposition of polymers for interlaminar toughening. Zhang showed that the interlaminar fracture toughness (G_{IC}) of carbon fibre laminates may be improved by up to 33% by the addition of certain polymer inks, including PMMA and PEG. However, her work concentrated on the identification of promising polymers and the refining of the printing process. No work was done to extend the technology into working laminates.

The work in this thesis extends this technique and explores its ability to potentially retard delaminations caused by cyclic loading. It is anticipated that this work will lead to new understanding of the performance of inkjet printed composites, with particular emphasis on the characterisation of performance in fatigue. It will also introduce understanding of poly(methyl methacrylate) and poly(ethylene glycol) as toughening agents in fatigue for the retardation of damage. Topics which have not been investigated at this point.

CHAPTER 3: MATERIAL SELECTION, MANUFACTURE, AND CHARACTERISATION

3.1 INTRODUCTION

This chapter outlines the materials, equipment, and processes involved in the preparation of test specimens. Details such as printing parameters and patterns are given, as well as any technical information related to the manufacture of the inkjet printed laminates. Studies relating to the behaviour of printed polymers and solvents during the curing process are also presented.

3.2 MATERIALS SELECTION

As previously mentioned, the method of inkjet deposition of polymers used here is based upon the work carried out by Zhang [11]. Therefore, the materials used, at least initially, were the same as those used by Zhang. Nevertheless, the selection process and justification of these materials is outlined below, as well as any deviations from her specifications.

3.2.1 *Prepreg*

A prepreg system was chosen for a number of reasons. Firstly, prepreg composites are the most widely used method of composite manufacture in high performance applications such as aerospace. And it is in industries such as these, where weight saving is essential, that this technology would be most appropriate. Secondly, using other manufacturing methods such as wet layup or resin infusion, would introduce significant challenges associated with applying the printing process. The wet resin would flow and disrupt the printed pattern, and the use of vacuum would be impossible as it would distort the pattern or remove it completely as excess resin is removed. Prepreg materials then are the ideal choice since they use a part-cured resin system which makes the material durable, easy to handle, and a good substrate to print upon. Also, since there is very little excess resin impregnated, there is less chance that the printed pattern would be removed when under vacuum and autoclave pressure during the curing process.

The chosen prepreg used in all tests was CYCOM® 977-2-35-12KHTS-268-300 (hereafter referred to as 977-2) unidirectional prepreg manufactured by Cytec. This carbon/epoxy prepreg tape is 0.25-0.27mm thick and distributed in continuous rolls of 300mm wide. It

contains continuous carbon fibres, which provide greater strength and stiffness over discontinuous fibres. This prepreg is widely used in civil and military aerospace applications. For example, it is used in the manufacture of wing spars for the Airbus A400M military transport aircraft [171]. It is a toughened resin system. Critically however, unlike other prepregs used in the aerospace industry such as Hexcel M21, it is not already toughened in the interlaminar region [172]. The mechanical properties of 977-2 laminates compared to other typical aerospace materials can be found in Table 3.1. It can be seen that the specific modulus and strength of 977-2 is extremely good. Compared to that of aluminium, which accounts for the bulk of the fuselages of most civil aircraft at this point, its advantages are significant.

Table 3.1: Typical properties of CYCOM® 977-2 composite laminates at room temperature (21°C) compared to other aerospace materials [173-176]

Mechanical Property	CYCOM® 977-2 (0°)	Aluminium 6061-T6	Stainless steel AISI 302
Tensile strength (MPa)	2690	310	585
Specific strength (kPam ³ kg ⁻¹)	1681	115	74
Tensile modulus (GPa)	165	69	193
Specific modulus (MNmkg ⁻¹)	103	25	25
Density (kg/m ⁻³)	1600	2700	7860

The properties of the 977-2 resin system can be found in Table 3.2. The function of the resin cannot be overstated. It is integral in maintaining the rigidity of the composite, and therefore keeping the fibres aligned in the loading direction. It also transfers loads between the fibres. The 977-2 resin system is a thermoplastic toughened epoxy which is highly desirable in aerospace structures where impacts from ‘bird-strike’ can cause enormous amounts of damage. Critically though, as mentioned above, it is manufactured without any interlaminar toughening mechanisms.

Table 3.2: Properties of 977-2 epoxy resin system at room temperature (21°C) [174]

Property	Value
Tensile strength (MPa)	81.4±11
Tensile modulus (GPa)	3.52±0.14
Flexural strength (MPa)	197±7
Flexural modulus (GPa)	3.45±0.07
Glass transition temperature, T_g (°C)	212
Density (kgM ⁻³)	1310

3.2.2 Inks

In the context of this thesis, an ink is defined as a chemical solution which may be printed by inkjet deposition.

3.2.2.1 *Poly(methyl methacrylate) Ink*

Zhang [11] showed that a 10% by weight (/wt) solution of PMMA in dimethylformamide (DMF) increased the interlaminar fracture toughness of 977-2 laminates by up to 40% in double cantilever beam (DCB) tests. Therefore, this was determined to be the most likely ink to affect delamination development in cyclic loading tests.

The mechanical properties of PMMA can be found in Table 3.3. Its properties are slightly lower than those of 977-2 resin (Table 3.2), making it ideal for toughening, whilst retaining overall mechanical strength. It is also a thermoplastic, so the relatively free movement of polymer chains makes it ductile. PMMA of 15,000 molecular weight (M_w) (Sigma Aldrich) was dissolved in DMF to create a 10%/wt solution. In order to increase the solubility of the solution, the solvent was heated to around 40°C before adding the PMMA powder. The dissolution of PMMA in DMF quickly turns the PMMA into a gel, sticking the particles together, greatly reducing their surface area, and resulting in slower dissolution. Mechanical stirring was required until the PMMA was completely dissolved so that the particles did not clump. An ultrasonic bath was also used to aid the dissolution. The resulting ink is a clear, slightly viscous liquid. Care was taken to keep the solution anhydrous, as PMMA is not soluble in water, and precipitates out of solution when small amounts of water are present. Temperature also affects the solubility of solutions, and even at room temperature, if left to settle, crystals in a 10%/wt solution PMMA can sometimes precipitate out of saturated solutions. This can cause problems during the printing process which will be described in later

sections. Crystal formation may be minimised by reducing dust contamination, which reduces the number of nucleation sites for crystals to form.

Table 3.3: Mechanical Properties of PMMA [177]

Property	Value
Tensile Strength (MPa)	72.4
Tensile Modulus (GPa)	3
Impact Strength (J/m)	21
Density (kgm^{-3})	1200

3.2.2.2 Polyethylene Glycol Inks

Polyethylene glycol (PEG) inks were also investigated because of their strong interaction with epoxy resins as described by Zavareh et al. [97] (Section 2.4.2). Solutions of 10%/wt in deionised water were made using both 1,500M_w and 20,000M_w PEG (Sigma Aldrich). PEG is a thermoplastic which is highly soluble in water, with 20,000M_w having a solubility of approximately 500g/l [178]. Mechanical stirring was again used, but elevated temperatures and ultrasonic bathing were not necessary. The resulting solutions were clear, slightly viscous liquids, with 1,500M_w being noticeably less viscous. Two different molecular weights of PEG were used because, as will be described in later sections in this chapter, the solubility of PEG in 977-2 resin varies greatly with molecular weight, so different toughening mechanisms became achievable.

The mechanical properties of PEG 20,000M_w are given in Table 3.4. No reference could be found for mechanical properties of PEG 1,500M_w, perhaps because they are highly temperature dependent [179]. But it is reasonable to assume that they would be lower than those of PEG 20,000M_w.

Table 3.4: Mechanical properties of PEG 20,000M_w [180]. Properties are heavily dependent on temperature.

Property	PEG 20,000M _w
Tensile Strength (MPa)	1.5±0.04
Tensile Modulus (GPa)	1.33±0.1
Density (kgm^{-3})	1200

3.3 INKJET PRINTING

The printer used for the manufacture of all printed specimens was a Jetlab 4 DOD printer manufactured by Microfab Inc. (Plano, Texas, USA) shown in Figure 3.1. It has a printable area of approximately 130x250mm. The printing stage is located in an enclosed cabinet to minimise the effects of draughts, temperature fluctuations, and contamination. The printing stage is controlled by stepper motors driving leadscrews in the x and y directions. The z axis is static in the x and y directions to increase printing accuracy. Inks were pressure fed from a reservoir into the printhead by a pneumatics controller shown in Figure 3.2 (also Microfab Inc.). The controller can also apply negative pressure in order to suck ink out of the printhead, which aided in cleaning and removing blockages. Negative pressures were also necessary during printing. A small negative pressure of around 10mbar was applied to the reservoir to negate the effects of the pressure head created by the column of ink in the printhead, preventing ink from being ejected from the nozzle due to gravity.

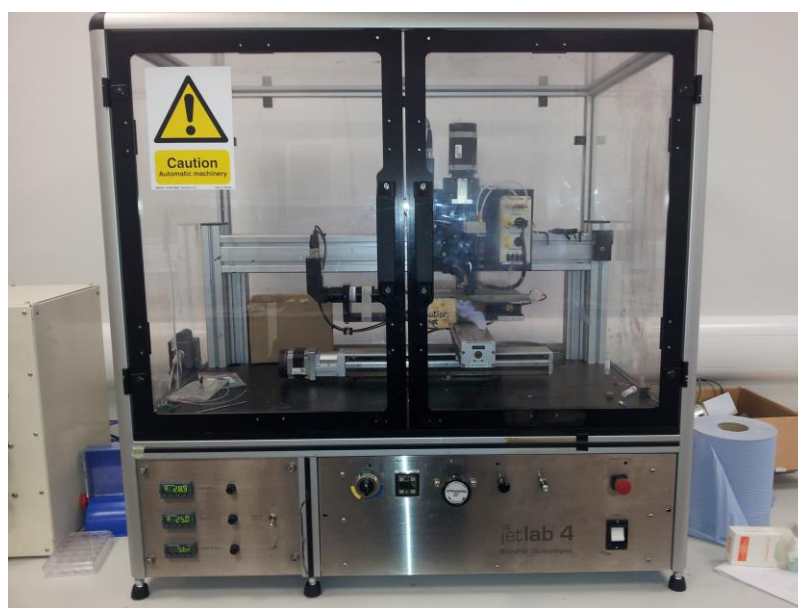


Figure 3.1: Jetlab 4 droplet on demand printer manufactured by Microfab Inc.

All inkjet printing of preregs was performed using an MJ-AT-01 piezoelectric printhead with a nozzle diameter of 60 μ m (Figure 3.3). The nozzle of the printhead is a glass capillary, so care was taken when printing that it was not chipped or broken. Figure 3.4 shows the interior view of the printer. The ink reservoir is located on the z axis along with the printhead holder, and the two are connected via pneumatic tubing. The reservoir is also connected to the pneumatic controller in a similar way. As mentioned in Section 3.2.2.1, 10%/wt solutions of

PMMA can prove problematic because PMMA crystals began to precipitate out of solution at temperatures below approximately 25°C. To mitigate this issue, a heated jacket (Figure 3.5) was sometimes used to heat the ink in the reservoir if room temperatures were low enough to cause problems with printing PMMA. The jacket was typically set to 30°C, as this produced the most consistent printing. The room temperature was also monitored to ensure that a stable temperature above 20°C was maintained. Below 20°C, there was a risk that certain inks may crystallise within the nozzle, potentially causing blockages.



Figure 3.2: CT-PT4 pneumatics controller [181]

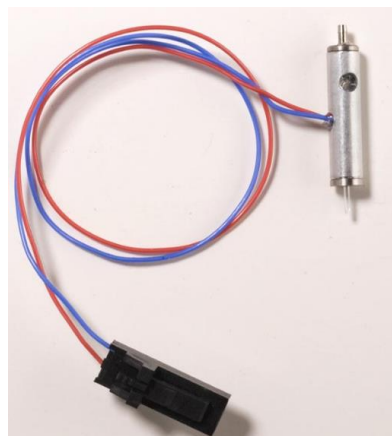


Figure 3.3: MJ series droplet on demand piezoelectric printhead with glass capillary nozzle [182]

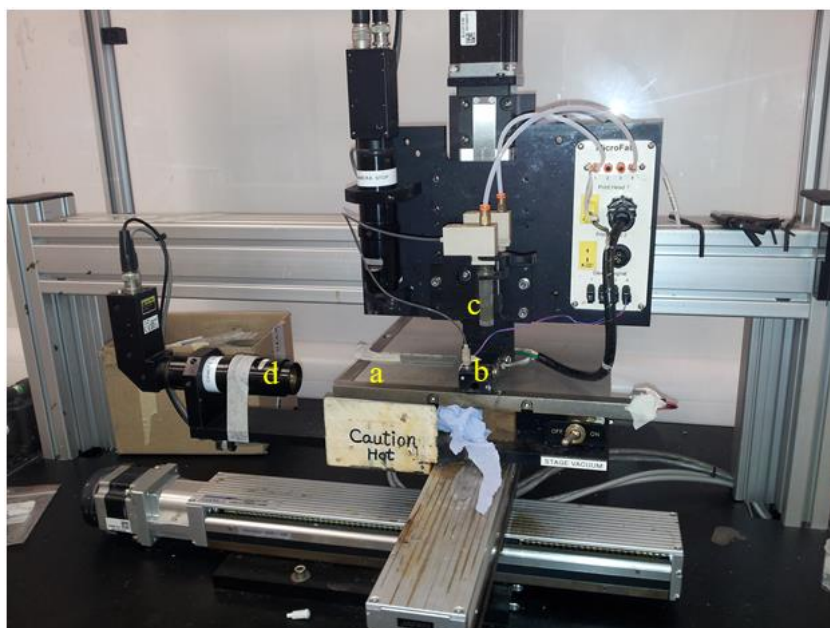


Figure 3.4: Cabinet interior of Jetlab 4 inkjet printer a) printing stage b) printhead c) ink reservoir d) droplet jet camera

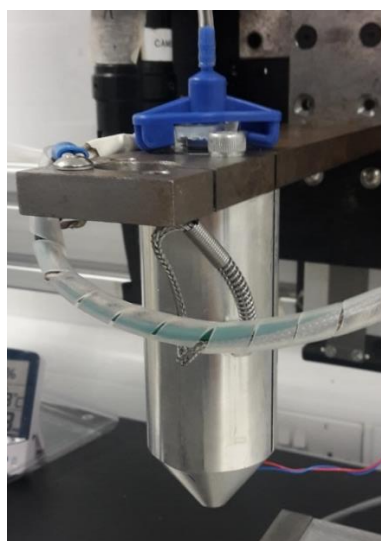


Figure 3.5: Electrically heated reservoir jacket used to increase the solubility of PMMA in DMF at low room temperatures

3.3.1 *Printing Process*

A single printhead was used to print all specimens, although the Jetlab 4 has the ability to print using four printheads at a time. Obviously this would decrease printing time by a factor of 4, but this was avoided as the chance of one nozzle becoming blocked was considered too high.

If a nozzle became blocked there was no way of telling at which point it did so. Because uniform and complete prints were necessary for the specimens to be valid, any prints where the printhead became blocked were discarded. The Jetlab 4 has a maximum linear printing velocity of 50mms^{-1} . However, slower printing velocities increase accuracy, so a velocity of 30mms^{-1} was chosen for all prints.

A graphical user interface (GUI) was used to control the printer. Figure 3.6 shows the GUI as well as the initial settings that were used in the printing process. This was used to set the printing parameters to obtain a continuous jet of stable droplets before printing onto a substrate. A stable droplet is one which ejects cleanly from the nozzle and does not have ‘satellite droplets’. A clean droplet ejection can be seen in Figure 3.7. As well as information on the waveform used to eject the nozzle, the GUI had a feed from a camera aimed at the nozzle (Figure 3.4d). This was a stroboscopic camera illuminated by infrared light. By strobing the infrared light source in time with droplet ejection the ejected droplets could be viewed as static, greatly aiding setup.

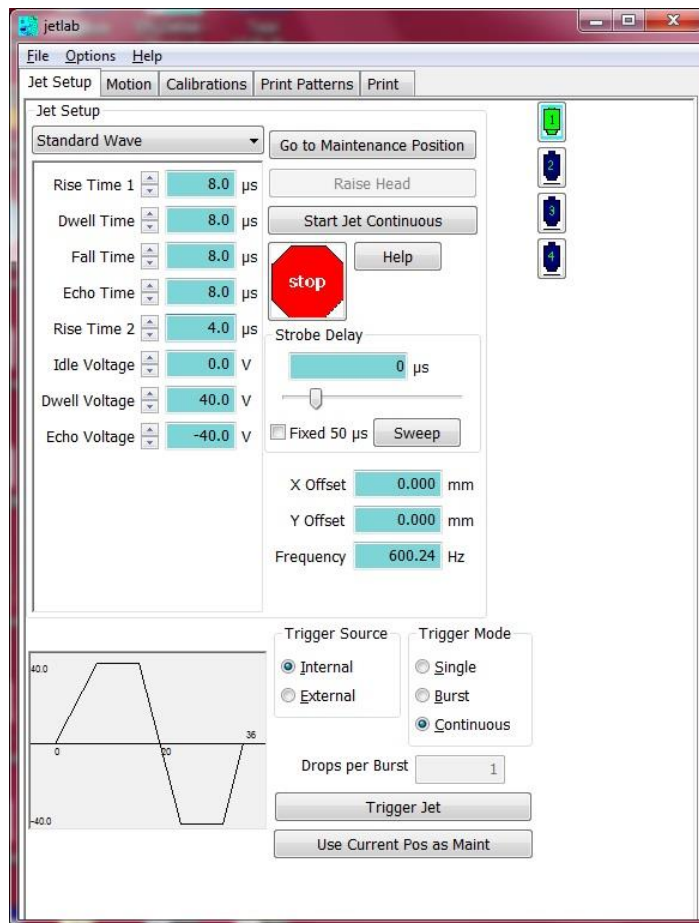


Figure 3.6: Jetlab control software graphical user interface

Satellite droplets are smaller droplets which are ejected as well as the main one. They are usually formed when the velocity of the ejected main droplet is too high. When ejected, droplets develop a tail which connects it to the liquid in the nozzle. This tail breaks as the droplet continues away. But if the velocity is high then the momentum of the tail breaks it up as surface tension pulls it back towards the nozzle, causing a second, smaller droplet to also be ejected along with the main droplet. This is shown in Figure 3.8.

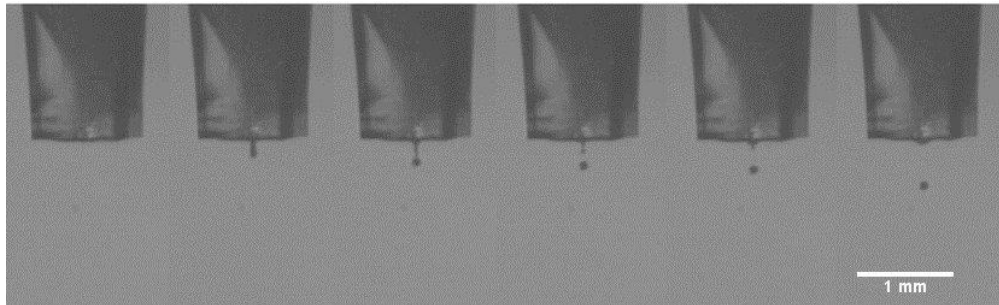


Figure 3.7: Clean ejection of a droplet

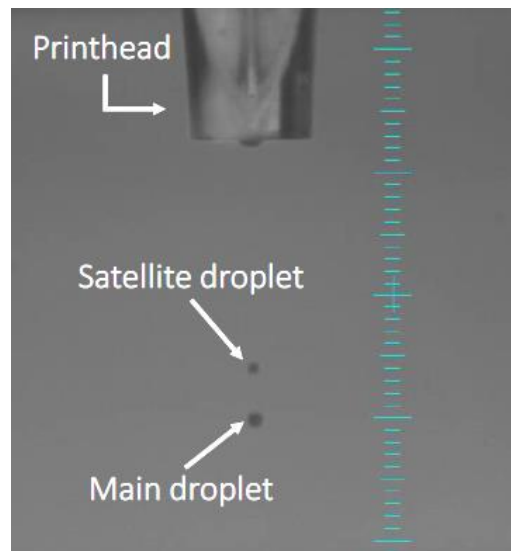


Figure 3.8: Main droplet ejected with a satellite droplet. Scale minor divisions 0.1mm. [11]

Once a stable droplet was obtained, the printing process was started. The vertical height of the nozzle tip to the top surface of the substrate was set to around 1-3mm. This height was maintained throughout the entire printing process. A low vertical gap reduces the tendency of the jet to be blown off course by convection currents caused by heat changes within the cabinet. However, there is a risk that loose fibres on the prepreg substrate may brush the

nozzle, affecting droplet formation. There is also a risk that the edges of the prepreg may lift slightly during printing. If the nozzle strikes an edge during its horizontal movement then it will almost certainly fracture the delicate glass capillary. Because of this, vertical heights below 1mm were avoided. The prepreg substrate was fixed to the printing platform using double sided sticky tape. This is a simple method which kept the prepreg laid flat.

Once deposited, the solvent quickly evaporates from the ink leaving behind a dome-shaped deposit of the polymer, an example of which can be seen in Figure 3.9. The diameter of these domes is influenced by the surface tension of the ink and also by the surface texture of the substrate. In the case of the 977-2 prepreg, capillary action between fibres on the surface also caused a very slight increase in droplet spreading.

After printing, sheets were stored in individual press-seal bags. The printed surface was covered with polytetrafluoroethylene (PTFE) non-stick sheet to prevent the prepreg from sticking to the bag, minimising disruption of the printed pattern. Bags were stored in a freezer at -18°C until needed.

Prepreg sheets of 130x250mm were used in printing except where particularly small samples were required. When cured, laminates had a tapered edge due to the fact that they were cured under pressure. Therefore, around 20mm was trimmed from each edge to make them uniform thickness. Printing large sheets and cutting multiple samples from them greatly reduced wasted material and time in comparison to printing individual samples. 130x250mm was found to be the maximum printable area of the Jetlab printer, so this is the sheet size that was used. Prepreg was cut to the same dimensions at different orientations from the prepreg tape roll to get laminae of different fibre orientations.

3.3.2 *Printed Pattern*

Because of the versatility of inkjet printing, and its ability to print almost any pattern, there were multiple possibilities for printing patterns. Zhang investigated patterns including films, lines, square arrays, and hexagonal arrays [11]; in the end finding that the highest interlaminar fracture toughness values were achieved using a hexagonal array. It is for that reason and others that a hexagonal pattern that was adopted for all inkjet printing work presented in this thesis.

Firstly, films and lines were excluded from consideration. These are created when the printed distance between two droplets is less than the diameter of a single droplet, making them overlap. Doing this for a single printed row creates a continuous line. And repeating for multiple rows, also with distance between rows of less than the diameter of a droplet, creates

a continuous film. Although this may seem a good method since the potential benefit of the polymer addition is widespread; in reality it creates uneven distribution of droplets, particularly when using PMMA inks. Zhang showed that when heated, the wide diameter of singular PMMA droplets was pulled into a small area in the centre of the droplet by surface tension. This can be seen in Figure 3.9. But when droplets were overlapped, surface tension was uneven, and the droplets broke up into smaller droplets that were unevenly dispersed. This can be seen in Figure 3.10.

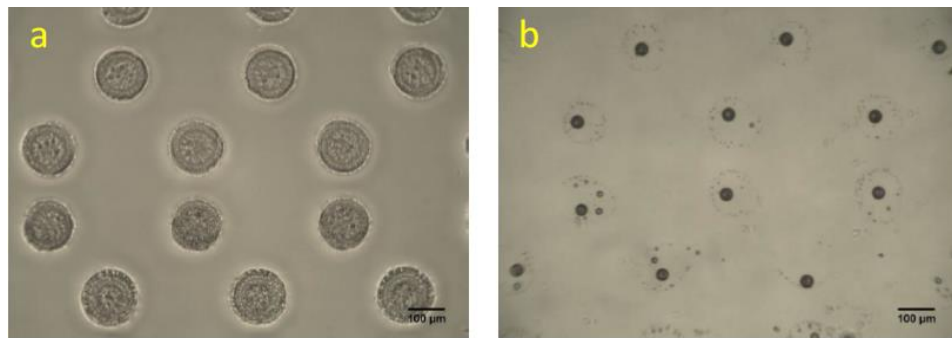


Figure 3.9: Images presented by Zhang showing PMMA droplets in a hexagonal pattern a) before, and b) after heating. During heating, the surface tension of the melted PMMA pulled the droplets into a small area in the centre [11]

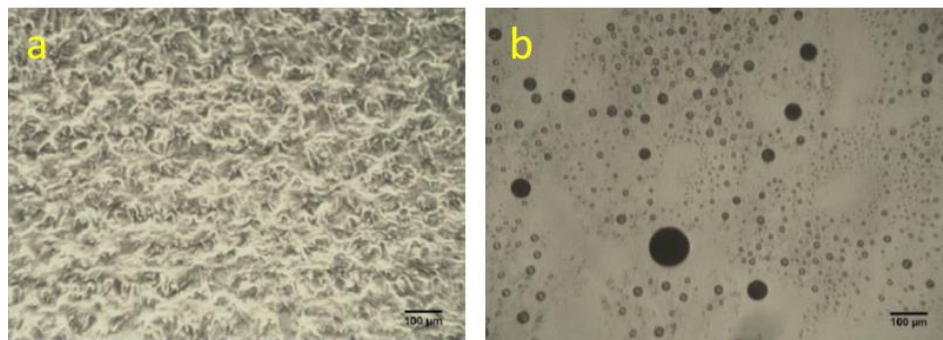


Figure 3.10: Images presented by Zhang showing a printed PMMA film a) before heating, and b) after heating. During heating, surface tension between the droplets was uneven and caused them to break up into unevenly dispersed droplets of varying sizes [11]

The two other patterns that were considered were square and hexagonal arrays. Square arrays as shown in Figure 3.11 are simply evenly spaced linear rows of droplets. They allow for even and tight packing of the pattern as desired. Hexagonal patterns are more complex, and are created by printing three identical rectangular arrays offset from each other. This is illustrated in Figure 3.11c. Different colours are used in this figure to represent the different printing

passes. From a micromechanics viewpoint, the advantage of hexagonal arrays is that a delamination front traveling across the pattern would be more likely to be interacting with a droplet at any given time since its shape is less regular than a square array. But most importantly, Zhang [11] investigated different printed patterns, and found that hexagonal arrays produced higher interlaminar fracture values than square arrays. For these reasons, a hexagonal array was adopted for all inkjet printing in this thesis.

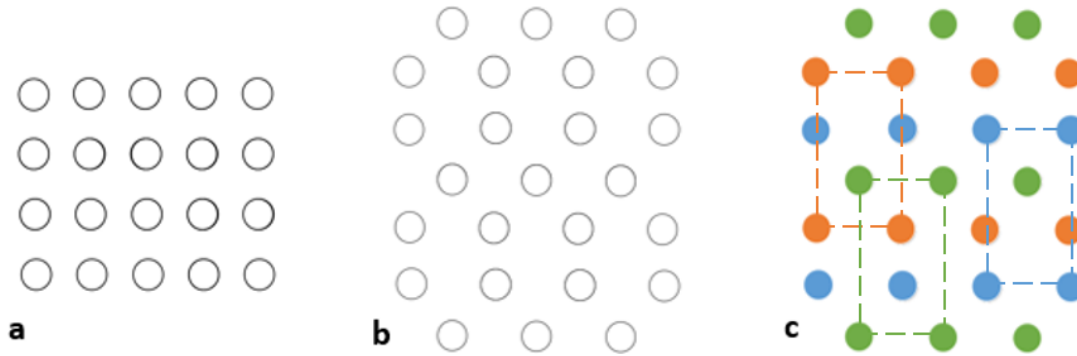


Figure 3.11: Examples of a) square arrays and b) hexagonal arrays. c) Illustration of how a hexagonal array is made off three identical rectangular arrays offset from each other. The different colours represent different printing passes.

3.4 MATERIAL COVERAGE, VOLUME, AND MASS

The dimensions used for the hexagonal array affect surface area coverage, as well as the volume and mass of polymer added to the composite. The percentage of coverage may be calculated knowing the spacing and the diameter of the deposited droplets, although the exact coverage after curing was difficult to determine since, as will be discussed later, both PMMA and PEG behave differently when heated to autoclave temperatures. Despite this, it was helpful to calculate the percentage of coverage since it helped to quantify different droplet spacings.

As previously mentioned, the hexagonal array can be considered as three rectangular arrays. Because of this, the method of calculating the coverage of hexagonal arrays is the same as for square arrays. Considering a unit cell as shown in Figure 3.12a, which represents the repeating unit from a hexagonal array which is also shown Figure 3.12b, then the coverage (β) as a percentage of the total area is;

$$\beta = \frac{A_{droplet}}{A} \cdot 100 = \frac{\pi D^2}{4\delta x\delta y} \cdot 100 \quad 3.1$$

where $A_{droplet}$ is the area covered by the deposited droplets when viewed from above, A is the total area of the unit cell, δx is the horizontal distance between the centres of droplets in the same row, δy is the vertical distance between the centres of droplets in the same column, and D is the diameter of the deposited droplet when viewed from above.

$A_{droplet}$ is simply the area of a circle, and is calculated by;

$$A_{droplet} = \pi r^2 = \frac{\pi D^2}{4} \quad 3.2$$

where r is the radius of the droplet. In these calculations droplet measurements are referred to in terms of D rather than r , as droplets are typically measured in terms of their diameter.

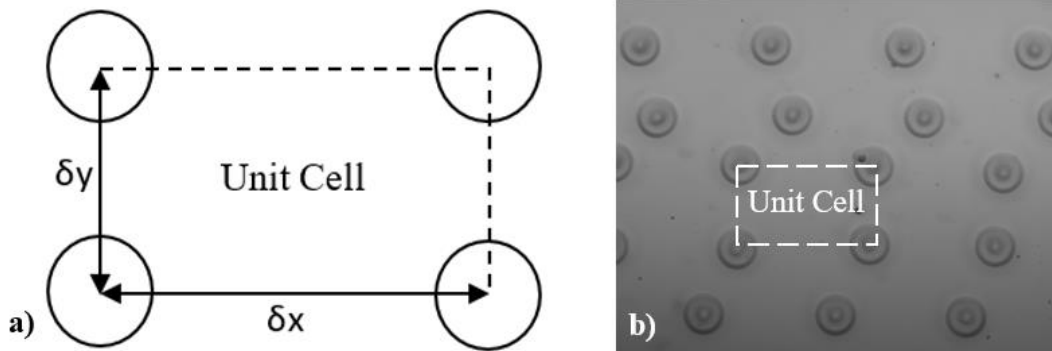


Figure 3.12: Illustrations of a unit cell of a rectangular array. a) Representative unit cell. b) Repeating unit cell transposed onto an optical microscope image of a hexagonal printed array of droplets.

β was found for all three inks discussed in Section 3.2.2 by taking an average of the diameters of at least five deposited droplets that were printed onto 977-2 prepreg. The calculated average values may be seen in Table 3.5. These measurements were taken from the droplet images

presented later in Section 3.9. In all specimens manufactured in this work, the printing dimensions used unit cell dimensions of $\delta x=0.4\text{mm}$ and $\delta y=0.2\text{mm}$.

Table 3.5: Percentage coverage of various inks used using Equation 3.1

Ink	Average droplet diameter (μm)	Coverage, β (%)
10%/wt PMMA (15,000M _w) in DMF	132	17.1
10%/wt PEG (1,500M _w) in water	137	18.4
10%/wt PEG (20,000M _w) in water	143	20.1

The volume and therefore the mass of the toughening polymer added to the composite may also be calculated by the measurement of the droplets as they were jetted. Presuming that the droplets ejected from the nozzle were perfectly spherical then the volume fraction of polymer in the laminate is;

$$Vf = \frac{V_{polymer}}{V_{laminate}} \quad 3.3$$

where V is volume.

$V_{laminate}$ is straightforward since the thickness of 977-2 prepreg is 0.25mm. However, to calculate the volume of polymer in a droplet, we must consider the density of both the polymer and solvent because the ink formulations were calculated by weight (mass) rather than by volume. The densities of the polymers and solvents used can be found in Table 3.6. Using these values, the percentage volume taken up by the polymer may be calculated by;

$$Vf_{droplet} = \frac{P}{d_{polymer}} \cdot \frac{d_{solvent}}{(1 - P)} \quad 3.4$$

where P is the fraction ($0 < P < 1$) of polymer by weight in the ink (0.1 in all inks), and d is the density of the material. Inserting the values from Table 3.6 into Equation 3.4, gives values that are shown in Table 3.7.

From these values it is simple to calculate V_f of the polymer in the laminate since the volume of a sphere is;

$$V = \frac{4\pi r^3}{3} = \frac{\pi D^3}{6} \quad 3.5$$

Putting this information into Equation 3.3, gives;

$$V_f = \frac{V_{polymer}}{V_{laminate}} = \frac{(n-1)\pi D^3 V_{droplet}}{6\delta x \delta y \cdot nt} \quad 3.6$$

where t is the thickness of a single ply of the laminate (0.25mm), and n is the number of plies in the laminate. $n-1$ represents the number of ply interfaces, since in any multiply laminate there is always one less interface than there are plies. Eight plies were used in all laminates tested in this thesis. In these calculations, the droplet diameter is considered to be that of the nozzle orifice (60 μ m), and the calculation considers a unit cell volume of a rectangular array.

The total additional volume added as a percentage may also be calculated;

$$\%V = 1 - \frac{V_{laminate} + V_{polymer}}{V_{laminate}} \quad 3.7$$

However, for very low values of $V_{polymer}$, as is the case here, $\%V \approx V_f$. And the same is true when calculating the percentage of mass added.

Finally, and perhaps most critically, we may calculate the mass fraction (m_f) of polymer in the laminate. Since mass is calculated by;

$$m = dV \quad 3.8$$

where m is mass and d is density. Therefore we may rearrange Equation 3.6 to get;

$$m_f = \frac{m_{polymer}}{m_{Laminate}} = \frac{V_{droplet} d_{polymer}}{V_{laminate} d_{laminate}} = \frac{(n-1)\pi D^3 V_f d_{polymer}}{6\delta x \delta y n d_{laminate}} \quad 3.9$$

The density of 977-2 prepreg is 1600kgm⁻³ as stated in Section 3.2.1. All of the values calculated using these formulae are presented in Table 3.7.

Table 3.6: Densities of polymers and solvents used in inks [178, 183-185]

Material	Density (kgm ⁻³)
PMMA (15,000M _w)	1200
PEG (1,500M _w)	1200
PEG (20,000M _w)	1200
DMF	897
Deionised water	1000

Table 3.7: Volume and mass fractions for inks

Ink	Volume fraction of polymer in ink	Volume fraction of polymer in laminates	Percentage volume added to laminate (%)	Mass fraction of polymer in laminates	Percentage mass added to laminate (%)
10%/wt PMMA (15,000M _w) in DMF	0.083	0.41x10 ⁻³	0.041	307x10 ⁻⁶	0.031
10%/wt PEG (1,500M _w) in water	0.093	0.46x10 ⁻³	0.046	345x10 ⁻⁶	0.035
10%/wt PEG (20,000M _w) in water	0.093	0.46x10 ⁻³	0.046	345x10 ⁻⁶	0.035

It can be seen from the values given in Table 3.7 that both the volume and mass added to the printed laminates was effectively negligible for the printing dimensions that were used. As previously mentioned, this is an enormous advantage over other toughening methods where the toughening material adds significant volume and mass, reducing the specific properties of the composite. This effectively means that any benefits caused by the addition of inkjet printed polymers essentially come at negligible cost to specific properties.

3.5 MANUFACTURE OF COMPOSITE LAMINATES

Laminates were constructed of multiple plies of 977-2 prepreg, which were ‘laid up’ prior to autoclave curing. Manual lamination is a common and well known technique, so it will not be covered in this section.

Laminates were cured inside a vacuum bag (Figure 3.13), which applied uniform atmospheric pressure without exposing laminates to air which may react with the resin during curing. 977-2 prepreg is specifically designed to be cured in an autoclave, so this was done using the manufacturer’s recommended cure cycle shown in Table 3.8 and illustrated in Figure 3.14.

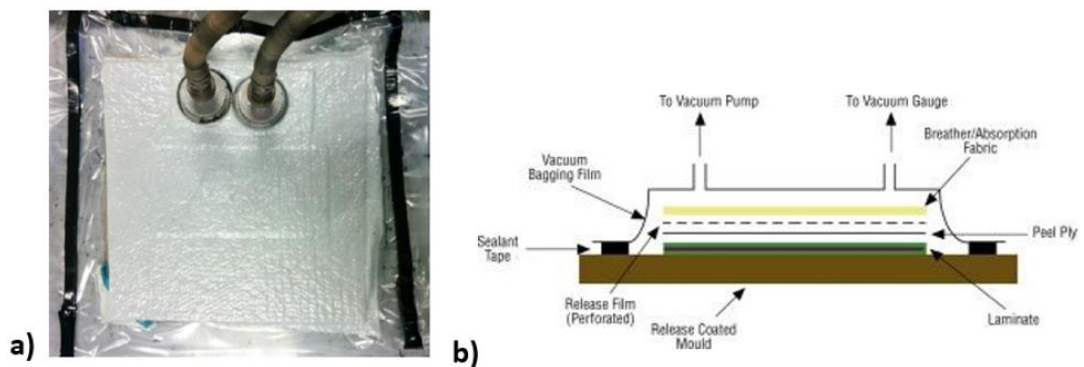


Figure 3.13: a) Vacuum bagged prepreg laminate and b) Cross-section of a typical vacuum bag [186]

Table 3.8: Cure cycle for 977-2 prepreg

	Stage 1: Ramp	Stage 2: Dwell	Stage 3: Ramp
Temperature	20°C → 180°C (2°C/min)	180 min	180°C → 20°C (2°C/min)
Pressure	0 → 90psi (5psi/min)	300 min	90 → 0psi (5psi/min)

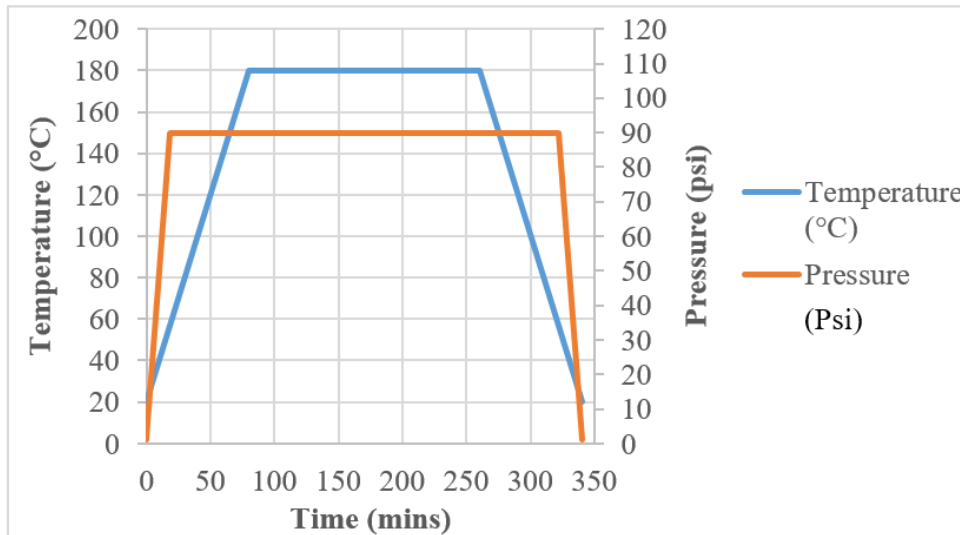


Figure 3.14: Cure cycle for 977-2 prepreg

As previously mentioned, polymers were printed in the interlaminar region. Therefore, the lamination process and stacking sequence had to be considered when the prepreg was printed upon. In most cases a laminate thickness of 2mm (8 plies) was used. Therefore only seven plies were printed since in all cases there was one less interface than there were plies. The lamination process is inherently harsh since manual force is applied to remove as much of the air as possible from between the plies. If the printed pattern were on top of the ply being laminated then the delicate pattern could be manipulated, spread, or even removed in places. It was important then that the pattern was located on the bottom of the ply being laminated. And in the case of multi-directional laminates, this had to be considered at the printing stage since printing on the wrong surface of a $0^\circ < \theta < 90^\circ$ ply, where θ is the angle direction of the fibres with respect to the 0° direction, would result in a printed ply of equal but opposite orientation to that desired.

There are multiple ways in which flat composite plates can be manufactured. Several possibilities were explored. However, many of them proved to be impractical.

Several methods of layup were trialled. It was suspected that a smoother sample surface finish would yield better fatigue results due to there being fewer stress concentrations on the sample surface. To achieve this, panels were cured sandwiched between two mirror-finish steel plates coated with a polymer release agent (Loctite 44-NC). This had the added benefit that heat would be transferred to the panel more evenly than in the normal vacuum bag method, in which one side is exposed to heated air, and the other to a steel plate. However, this method of cure resulted in significant levels of panel spreading. This was due to the vacuum gap between the plates at the edge of the panel drawing the resin outwards as shown in Figure

3.15. It would be possible to create a mould to contain the panels, but this would prevent pressure from being applied; and a more elaborate mould would be too complex, costly, and would not truly represent industrial manufacturing methods.

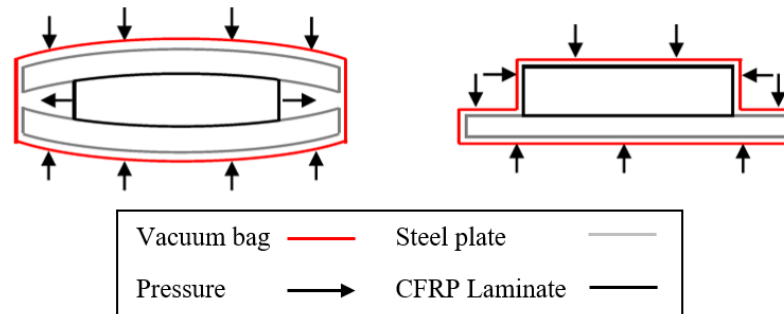


Figure 3.15: Interpretation of how different composite plate manufacturing methods may affect panel shape. Gaps between steel plates create a vacuum gap which extrudes to composite panel.

In the end, the most feasible solution was found to be to use a single steel plate covered in polytetrafluorethylene (PTFE) coated glass fibre sheet, with a PTFE top cover to ensure a consistent surface finish. This was not as desirable as a smooth finish, and heat transfer was not as even, but it was the most practical and representative of industrial methods.

After curing, the panels were removed from the vacuum bag and trimmed to the relevant size using a water-fed diamond cutting saw. The samples were deliberately cut oversized by around 1-5% so that a secondary sanding stage could be performed using a flat sanding wheel. This sanding stage provided greater control of the dimensions, and also created a smoother edge than sawing alone. Sanding wheels of 600 grit or finer were used on all samples. After cutting, samples were hand dried and placed in an oven at 50°C until dry to reduce the effects of water infiltration.

Where tensile samples were produced, it was necessary to attach glass fibre end tabs to aid sample gripping. These were created in accordance with BS EN ISO 527-4:1997 [187], which dictated the sample dimensions used in tensile tests. The CFRP panels were lightly abraded with 120 grit sanding paper where the end tabs were to be attached. The end tabs were created using a wet layup method (described in Section 2.1.3.2) on a PTFE coated steel plate. A dry glass fibre fabric of $\pm 45^\circ$ unidirectional stitched fibres (0.5mm ply thickness) was used along with a matrix of EasyComposites EL2 two-part laminating resin (room temperature cure). A panel thickness of 2mm (4 plies) was created and subsequently placed in a vacuum bag with a perforated peel ply to remove excess resin. It was then left for 24 hours to cure at room

temperature. After curing it was then placed in an oven at 50°C for around 2 hours to ensure full curing. $\pm 45^\circ$ wet layup laminates were used for the end tabs because they have a relatively soft surface to allow steel machine grips to bed into them. Their slight compliance under strain also reduces the chance that they will separate from the CFRP sample under loading. End tabs were bonded to the CFRP samples using Araldite® Standard two-part epoxy resin. A thin layer was applied to both the end tabs and CFRP sample, and the two were clamped together using spring clamps until fully cured.

3.6 DIRECT SCANNING CALORIMETRY

A method that was used in this project to quantify the quality of curing was differential scanning calorimetry (DSC). An inconsistent degree of cure between samples may affect material toughness, strength and stiffness, and would make differentiating between changes in material characteristics problematic.

In DSC, a sample sealed in an aluminium pan and a control sample (empty aluminium pan) are heated very precisely at the same rate but in separate chambers. The machine measures the heat flow required to heat the specimen compared to the control. The underlying principle is that when the specimen undergoes a chemical change or phase transition, more or less heat energy must flow to the sample to heat it to the required temperature.

DSC is commonly used to measure glass transition temperature (T_g), but may also be used to calculate the degree of cure of epoxy-based composite materials [188]. This is done by comparing the exothermic troughs that curing produces (illustrated by Figure 3.16). By direct comparison of troughs between cured and uncured prepregs, the degree of cure can be obtained.

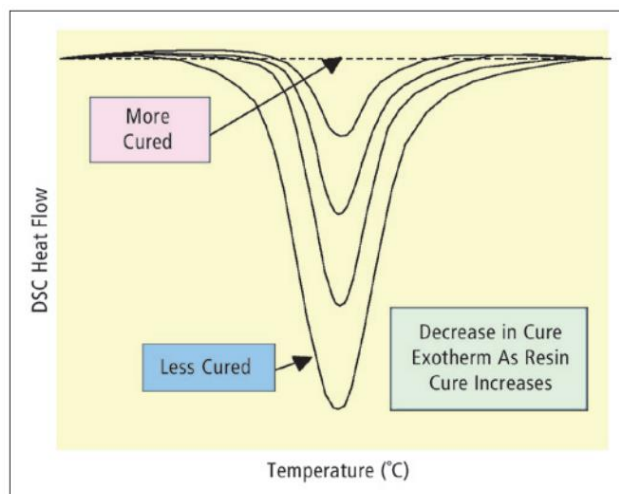


Figure 3.16: DSC may be used to measure the degree of cure by direct comparison of exothermic troughs. The area of exothermic troughs caused by resin curing may be compared to the area of smaller post-cure troughs to directly quantify the level of cure. [188]

3.6.1 DSC Procedure

Samples of composites cured using the manufacturer’s recommended cure cycle were tested using a PerkinElmer DSC 8000 Double-Furnace testing machine (Figure 3.17). The samples were accurately weighed prior to loading, and then placed in metal pans which were then sealed. All samples tested were from separate batches, with unprinted and printed samples taken from each. That is samples that were manufactured from the same 977-2 prepreg and using the same curing cycles, but at different times.

Samples were exposed to a heating cycle as in Figure 3.18. From the recorded data, it was possible to determine the level of cure, as well as any significant events which occurred in the heating cycle. The data sample rate was 1 sample/sec.

Prior to using this thermal cycle, several tests were conducted using different cycles. These tests helped to determine the best cycle to use. Any temperature change in the cycle had to be done at less than 20°C/min in order to give the uncured resin reasonable time to liquefy and react. Taking it to 300°C ensured that the sample had enough time to do this completely.

The sample was heated and cooled twice in order to determine changes that occurred due to heating. In the first cycle, any uncured resin fully cured due to the elevated temperature. Since curing is an exothermic reaction, less heat energy will be required to be put into the sample pan by the machine. It will therefore register this reaction as a trough. In the second cycle there should be no further curing and the trough will not be present. By calculating the area of

the trough and comparing it to the second heating cycle, it should be possible to determine the level of cure of the sample before the test.



Figure 3.17: PerkinElmer DSC 8000 Double-Furnace testing machine

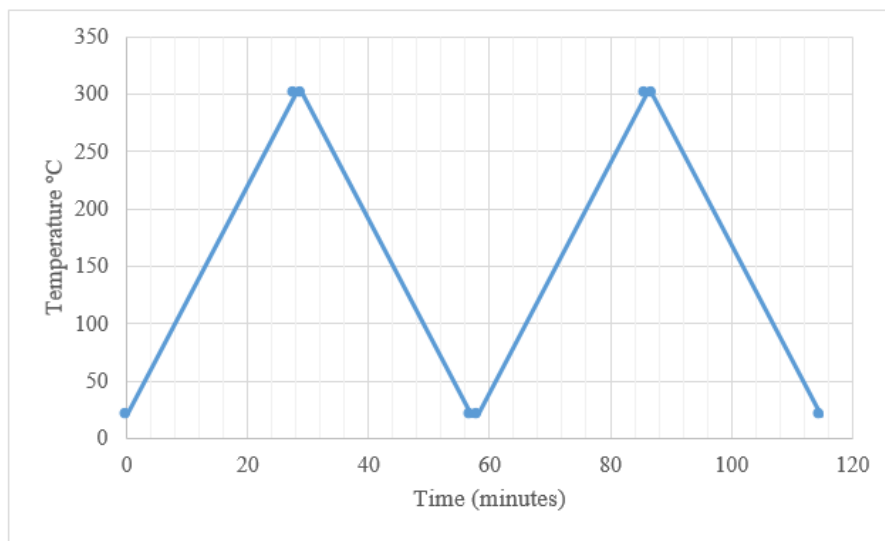


Figure 3.18: DSC heating cycle for tests used to evaluate degree of cure

3.6.2 DSC Results

Figure 3.19 shows a plot of heat flow against time for one of the tests conducted on cured unprinted 977-2 composite. A trough was observed on the initial thermal cycle between 200°C and 300°C, indicating further resin cure. This trough was not present in the second thermal cycle. When the data was evaluated, the average cure of the cured 977-2 composites was found

to be 98.2%, which was in line with or better than typical values [189-191]. There was no difference found between printed and unprinted composites. This gave confidence to the validity and consistency of mechanical testing of composites cured in this way since all samples should have the same degree of cure. An inconsistent degree of cure between samples may affect material toughness, strength and stiffness, and would make differentiating between changes in material characteristics problematic.

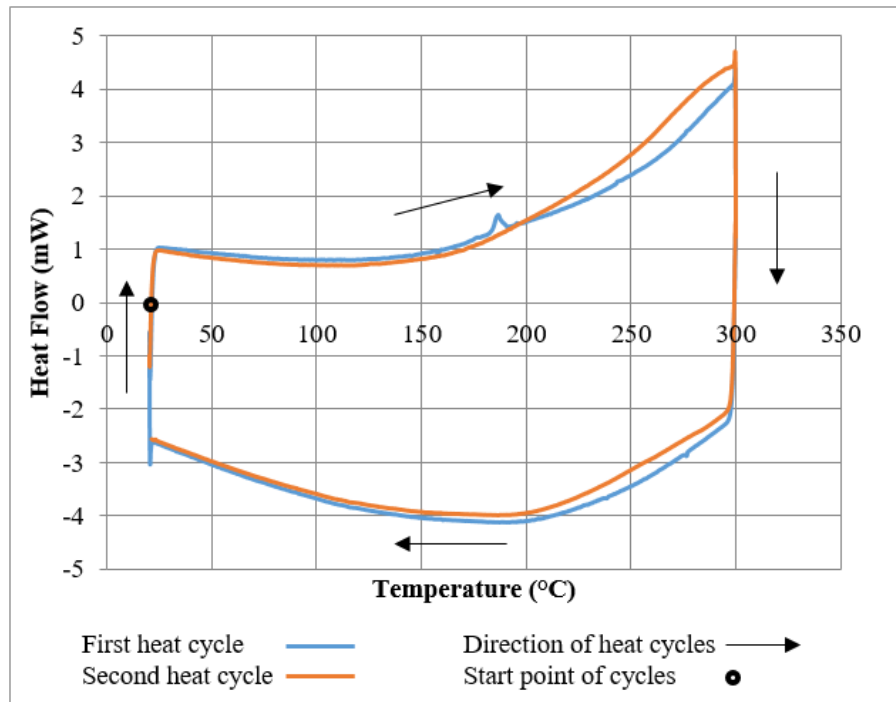


Figure 3.19: Result of a DSC test conducted on cured 977-2 composite. Different colours represent the separate heating cycles that the sample was subjected to. Both cycles begin at 20°C and 0mW heat flow and continue in a clockwise direction as indicated by the arrows. The second heating cycle was conducted immediately once the first cycle returned to 20°C.

3.7 DYNAMIC MECHANICAL THERMAL ANALYSIS

Dynamic mechanical thermal analysis (DMTA) may be simply described as applying an oscillating load or displacement to a sample and analysing the material's response [192]. A range of test geometries may be used with DMTA. The one chosen for these tests was a miniaturised three point bend test which was run over a wide range of temperatures. In these tests the primary information obtained was the glass transition temperature (T_g). The measured value of T_g was later used to validate cyclic tests, ensuring that temperature rises due to

internal viscous heating were not so great as to affect the mechanical properties of the materials during tests.

3.7.1 DMTA Procedure

In these tests, unprinted unidirectional samples of 1-2mm square cross-section, and approximately 40mm in length were placed in three point bending in a PerkinElmer DMA 8000. The span of the three point setup was 30mm, with a knife edge loading beam at the centre point, and knife edge supports at each end. Samples were measured using digital Vernier callipers with a manufacturer's quoted accuracy of 0.01mm. Measurements of width and thickness were taken at three points evenly spaced along the length of the samples and then averaged. Test samples were cut using a circular diamond cutting saw, and subsequently sanded to the correct measurements using sanding paper of 600 grit. Five unprinted samples were tested to evaluate the T_g of 977-2 composites. All samples tested were from separate batches. That is samples that were manufactured from the same 977-2 prepreg and using the same curing cycles, but at different times.

Tests were run from room temperature up to 250°C at a rate of 2°C/min. The test frequency was fixed at 1Hz, and 0.5mm displacement. A single thermal cycle was run on each specimen.



Figure 3.20: PerkinElmer DMA 8000



Figure 3.21: A sample mounted in the three point bend test configuration. The mechanical actuator is attached to the central loading point.

3.7.2 DMTA Results

Glass transition temperature (T_g) is often quoted wrongly as being a single precise temperature at which the material becomes pliant. However, this is not true. And in reality, T_g is a region [192]. However, the simplicity of describing it as a point rather than a region means that it is generally accepted this way. The precise T_g as a point may be taken in one of two ways. It may be taken as the point at which the linear portions of the storage modulus (E') slopes intersect (illustrated as a red dashed line in Figure 3.22), or as the peak of the tan delta curve [193]; tan delta being the ratio of the loss modulus (E'') to the storage modulus, and representing the point at which complete breakdown of the elastic properties occurs. Either method is generally acceptable. The tan delta peak method is favoured for its ease of interpretation. The intersecting lines method is more conservative however, and is therefore used more in structural applications where safety is a concern. For these tests, T_g was measured using the intersecting lines method. This was easily done by taking points before and after the T_g , giving two lines which could then be used to calculate the intercept point along the temperature axis as illustrated in Figure 3.22.

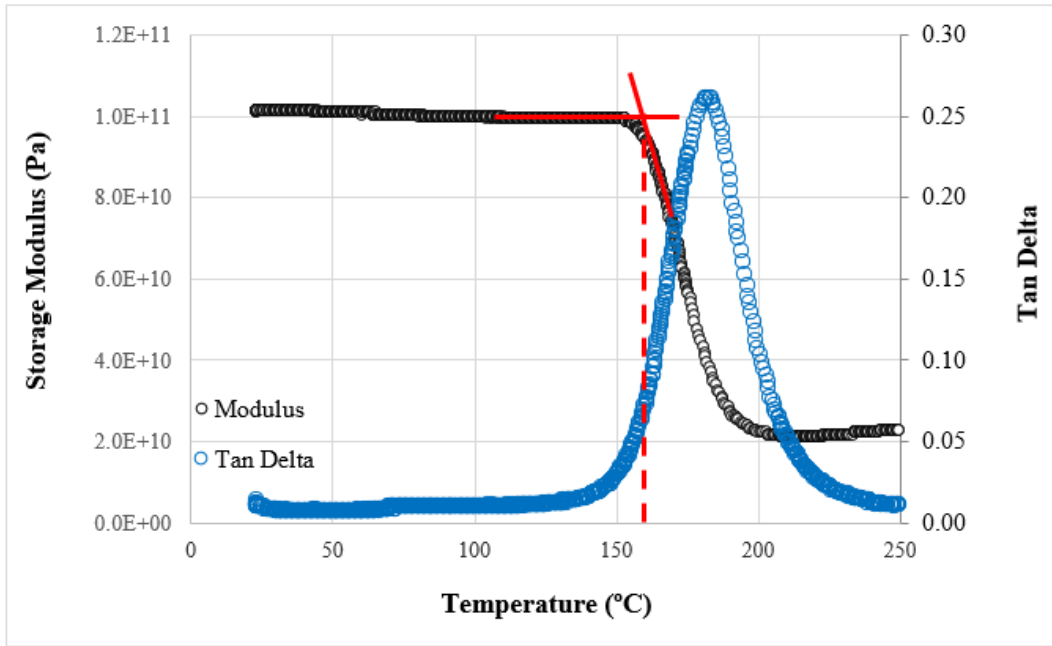


Figure 3.22: Example graph of 977-2 CFRP (sample 6) tested in three point bending DMA at 1Hz. Red lines represent the intersecting gradients of the separate linear portions of the curves. The dashed line represents their intersection point along the temperature axis.

The results of these tests are shown in Table 3.9. Using the storage modulus intersection results it was calculated that the average value of T_g was 167°C, having a calculated standard deviation of 6.6°C.

Table 3.9: Results of DMA testing

Sample Number	Sample Width (mm)	Sample Thickness (mm)	T_g Intersection (°C)
1	2.09	1.69	169
2	1.45	1.61	158
3	2.13	1.54	161
4	1.47	2.20	172
5	2.27	1.62	167
6	1.60	1.27	172

DMTA is a well-established technique for determining the T_g of materials. The results obtained from these tests showed that cured 977-2 composites had a T_g of 167°C. Cytec quote

the T_g of cured 977-2 to be 212°C. However, Sabzevari et al. found that following Cytec's cure schedule, a T_g of just 177°C was achieved. They also found that curing the prepreg at a temperature of 200°C (20°C over the recommended temperature) resulted in a maximum T_g of 195°C [194]. No other literature could be found which listed experimental values of the T_g of 977-2 composites. Because of the similar results obtained by Sabzevari et al. it therefore seems likely that the results obtained here were correct for the specific manufacturing processes, age of prepreg etc. used.

3.8 DURABILITY OF PRINTED PREPREGS

It was initially unclear if the act of placing something on top of the printed substrate would interfere with the droplets or pattern. One of the key concerns was storage of the printed prepreg. Being unable to place any sort of cover over the material would prevent the sealing of the material during freezing. This would allow water to condense on the prepreg during thawing, potentially affecting its properties. Another concern was in manufacture. The prepreg must be handled in order to prepare it for layup. This involves tools and gloved hands touching the prepreg.

These concerns seem trivial, but a prepreg that cannot tolerate any one of the above activities has very limited practical applications. A simple set of tests were therefore devised to investigate this. The materials used in these tests were printed (hexagonal array 10%/wt PMMA in DMF) Cytec 977-2 resin system unidirectional prepreg.

In order to test the printed prepreg's capability to withstand being stacked in piles, several different covering materials that are typically used were laid down on top of uncured samples. A flat, heavy object applying a pressure of approximately 300Pa was then placed on top of the sample, ensuring that it made full and even contact with the surface. This represents a pressure greater than any that it would typically encounter under normal static stacking conditions. The pressure was left on for 1 minute. This procedure was carried out with PTFE coated glass fibre fabric, non-stick prepreg backing paper, and polyethylene (PE) film. When observed under a microscope, it was found that there was no noticeable disruption to the pattern or the droplets, indicating that any of these materials would be suitable as materials with which to cover the printed surface.

A continuation of this test, aimed at determining the durability of the printed prepreg during preparation for layup was then carried out. The covering materials with mass on top were dragged across the printed surface for a distance of around 50mm. The samples were then observed under an optical incident microscope, and investigated in several areas. The images

showed slight shifts in the pattern in some places, indicating that the resin had flowed slightly along with the droplets. In others, the droplets were smeared slightly, as in Figure 3.23, with the possibility that some may have been transferred to the covering material. No areas were observed where the droplets were removed completely. All covering materials showed approximately the same outcome.

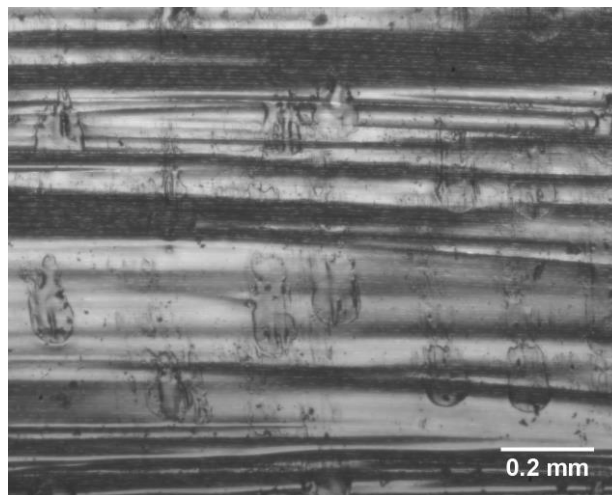


Figure 3.23: Example of smeared PMMA droplets on uncured 977-2 prepreg

This test was designed to investigate how the pattern may be disrupted in a controlled manner more extreme than it would encounter under normal manufacturing conditions. Although the results are favourable, it would still be advisable that extra care be taken when handling printed composites in order to maintain the integrity of the pattern as much as possible.

3.9 PRINTED RESIN SLIDES

It is vital to understand how droplets are deposited onto resin substrates, and hence how they are likely to behave when printed onto prepreg in manufactured composite panels. In this section, 76mmx26mm glass microscope slides were prepared by coating them with CYCOM® 977-20 liquid RTM resin part-cured to a range of levels, and printed with either PMMA or PEG based inks. The slides were then observed under an optical transmission microscope to understand how the different inks and their solvents interact with the resin.

Particularly, attention was directed to understanding what droplets do when they are cured and sealed within the resin. This was key to understanding the mechanisms by which printed

composites differ from non-printed composites. This was not possible with prepreg samples because the carbon they contain is opaque to most practical forms of observation.

3.9.1 *Preparation of Slides*

CYCOM® 977-20 RTM resin (the liquid form of the part-cured resin used in 977-2 prepreg) was spread on glass microscope slides using a wooden tongue depressor in a layer approximately 0.5mm thick. These slides were then placed in an oven at 180°C (peak curing temperature of 977-2) for 5, 10, or 20 minutes in order to partially cure them since the resin that prepregs contain is normally partially cured. The partial curing is known as B-staging [195]. The resin is thickened by both cross linking and the evaporation of volatile solvents. This was done in hopes of replicating the partial curing of the resin in 977-2 prepreg, and thus replicating how the inks interact with the prepreg without being limited by the minimal amount of surface resin on the prepreg or by the sub-surface opacity of laminates. A number of samples were prepared as detailed in Table 3.10. Three of each sample were produced. After printing onto the partially-cured resin, another partially-cured resin slide was placed over the top of the printed surface. This ‘sandwich’ was then fully cured according to the normal curing schedule for the resin (described in Section 3.5). The samples were observed under an optical transmission microscope both before and after curing.

The purpose of observing the uncured samples was to determine what the solvents, polymers, and inks did upon contact with the resin substrate. The purpose of observing the cured samples was to determine what the solvents, polymers, and inks did when fully encased in resin and exposed to resin curing temperatures.

Table 3.10: List of printed resins used

Resin Cure Time (minutes)	Ink
Prepreg	10% PMMA 15,000M _w in DMF
Prepreg	10% PEG 1,500M _w in Water
Prepreg	10% PEG 20,000M _w in Water
0	10% PMMA 15,000M _w in DMF
0	10% PEG 1,500M _w in Water
0	10% PEG 20,000M _w in Water
5	10% PMMA 15,000M _w in DMF
5	10% PEG 1,500M _w in Water
5	10% PEG 20,000M _w in Water
5	Water
5	DMF
10	10% PMMA 15,000M _w in DMF
10	10% PEG 1,500M _w in Water
10	10% PEG 20,000M _w in Water
10	Water
10	DMF
20	10% PMMA 15,000M _w in DMF
20	10% PEG 1,500M _w in Water
20	10% PEG 20,000M _w in Water
20	Water
20	DMF

3.9.2 Results

Optical microscopy is a very versatile method for assessment of visual artefacts. It is both quick and easy in its methods, and the equipment is widely available at relatively low cost. Many images were captured as part of the analysis of these samples. A representative collection of images are presented here which show how the various inks behaved once printed onto the various substrates.

3.9.2.1 *PMMA 15,000M_w in DMF Ink*

Figure 3.24 shows PMMA droplets printed onto a prepreg substrate and a glass substrate. These were used as control images. Because the glass was smooth and inert, droplet interaction with it should have been minimal. The prepreg substrate showed how the ink interacted when printed upon real prepreg. The droplets printed on prepreg showed a degree of what appeared to be dissolution into the resin, but remained mostly intact. The diameter of the droplets remained unchanged however, so they were not dissolving into the matrix around the outer diameter greatly. The edge of the droplets was also clearly defined. From the results of printing pure solvents presented later in Section 3.9.2.4, the most likely explanation for the low definition of the droplets compared to the glass control is that the DMF solvent dissolved the resin slightly before evaporation, allowing a small amount of droplet flow.

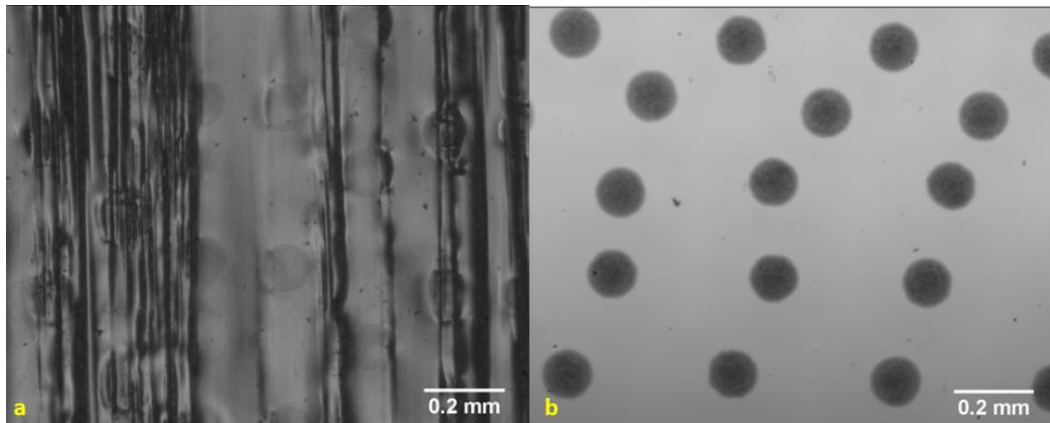


Figure 3.24: Comparison of PMMA droplets printed onto a) uncured 977-2 prepreg b) glass microscope slide

Figure 3.25 shows droplets printed onto resin films of different degrees of cure. This was done in order to match the ideal resin cure time to the prepreg control image. In the case of resins cured for 5 and 10 minutes, the contrast of the image was digitally enhanced because the droplets appeared faint against the resin background. This may have been caused by dissolution, or a comparatively thicker resin film allowing less light to pass through. PMMA is clear, and its refractive index ($n=1.49$) [196] is very similar to that of standard epoxy resins ($n\approx 1.5$) [197]. This added to the difficulty of optically viewing PMMA droplets.

It was observed that the shape of the droplets across all cure times was approximately the same. With all exhibiting a dimple in their centre to some degree. The diameter of the droplets also remained more or less constant, being on average $118\mu\text{m}$, $114\mu\text{m}$, and $115\mu\text{m}$ on resin

partially cured for 5, 10, and 20 minutes respectively. The diameter of the droplets on prepreg was measured to be $113\mu\text{m}$. This may indicate that PMMA has very low solubility in 977-2 resin. In cured samples it may therefore be expected that droplets remain discrete from the resin phase, and that the degree of cure should not affect how droplets behave. Although elevated temperatures may influence solubility.

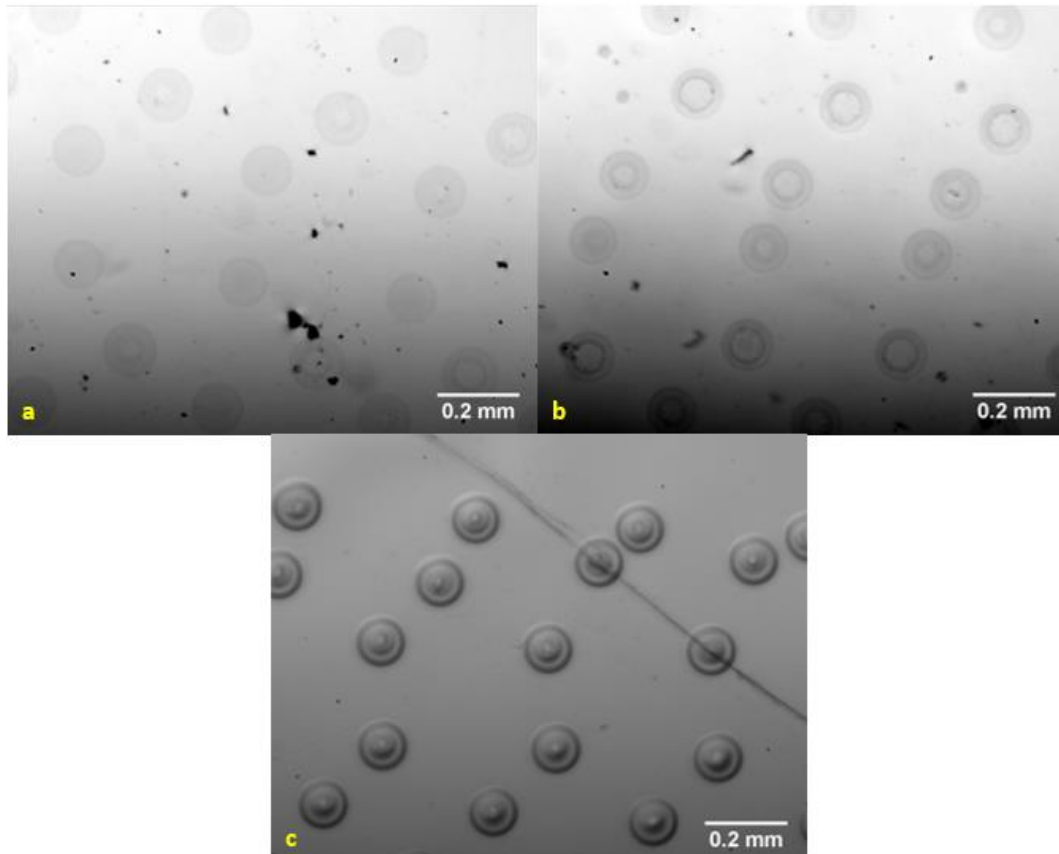


Figure 3.25: Microscope images of PMMA droplets printed onto a part-cured resin film. The resin was partially cured at 180°C for a) 5 minutes b) 10 minutes c) 20 minutes. The contrast of images a and b were digitally enhanced.

Figure 3.26 shows post-cure images of PMMA printed slides. It is clear from these that the resin cure time had a significant effect upon the behaviour of the droplets during curing.

During curing the droplets broke up into smaller droplets of varying diameters resembling images obtained by Zhang [11] (Figure 3.10) of printed PMMA films. The largest of these droplets located in the centre were around $5\text{-}10\mu\text{m}$. The droplets were broken up when the PMMA melted in a process called dewetting. Wetting is only possible when the surface energy of the substrate is higher than the surface energy of the fluid on it [198]. Therefore raising the surface energy of either the substrate or the fluid on it will negatively affect wetting. In the

case of epoxy resin, once crosslinking occurs, the surface energy of the substrate is raised significantly, reducing its ability to be wet. Once this occurs, the droplets will break up as follows. Firstly, holes form in the surface of the fluid film due to perturbations in the fluid film. Secondly, holes coalesce, breaking up the surface. Finally, individual droplets are formed as holes cause the film to separate and surface tension pulls the remaining droplets together [199]. In these droplets the wide area of the spread droplet may be considered a thin liquid film which covers a limited area. It is in fluid films that dewetting causes breakup [200]. It is thought that the thin film nature of the deposited droplets adequately explains why droplets are able to display this dewetting behaviour.

This evidence of droplets breaking up into smaller ones contradicts what Zhang found in similar tests. She found that droplets formed single smaller droplets (Figure 3.9). However, evidence will later be shown in Section 6.3.1.2 of this thesis that supports the observations here. Zhang's observations may have been caused by using aged prepreg. The partial curing, and hence low wetting ability of the aged prepreg would cause the droplets to be initially deposited with smaller diameters. The smaller diameter droplets would no longer be analogous to a thin film, and dewetting behaviour would cause them to form single compact droplets rather than being broken up into smaller ones.

It was also seen that fewer and smaller droplets formed in resins with a lower degree of cure, with the larger central droplets not present in Figure 3.26a. The presence of fewer droplets may be explained by the presence of volatile solvents. These would be present in larger amounts where the resin was cured for less time, resulting in wider dispersal of the PMMA. However, the reason why the outer droplets were not dissolved when the larger, inner droplets were is as yet unexplained.

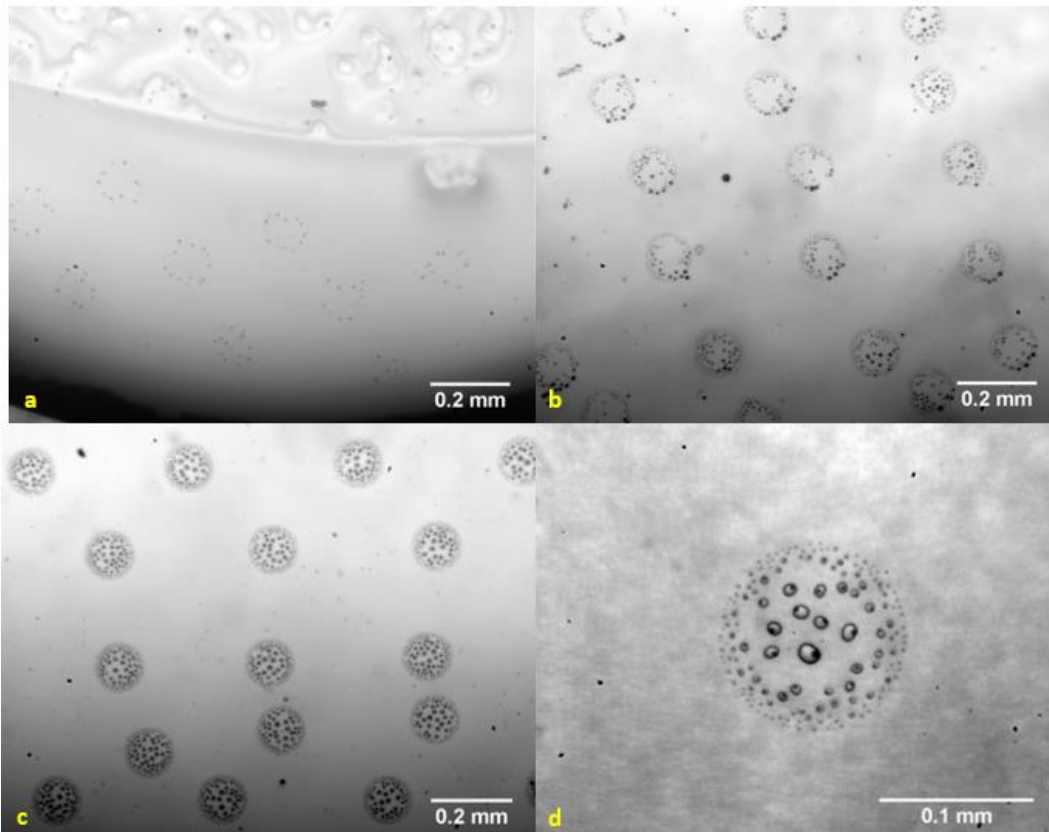


Figure 3.26: Post-curing microscope images of PMMA droplets printed onto a part-cured resin film. The resin was partially cured at 180°C for a) 5 minutes b) 10 minutes c) 20 minutes. d) Enlarged view of PMMA droplets in resin partially cured for 20 minutes. The contrast of all images were digitally enhanced.

3.9.2.2 PEG 1,500M_w in Deionised Water Ink

Figure 3.27 shows PEG 1,500M_w droplets printed onto a prepreg substrate and a glass substrate. The droplets appeared as very smooth domes which are highly contrasted at their edges, indicating a high contact angle, and therefore low wetting.

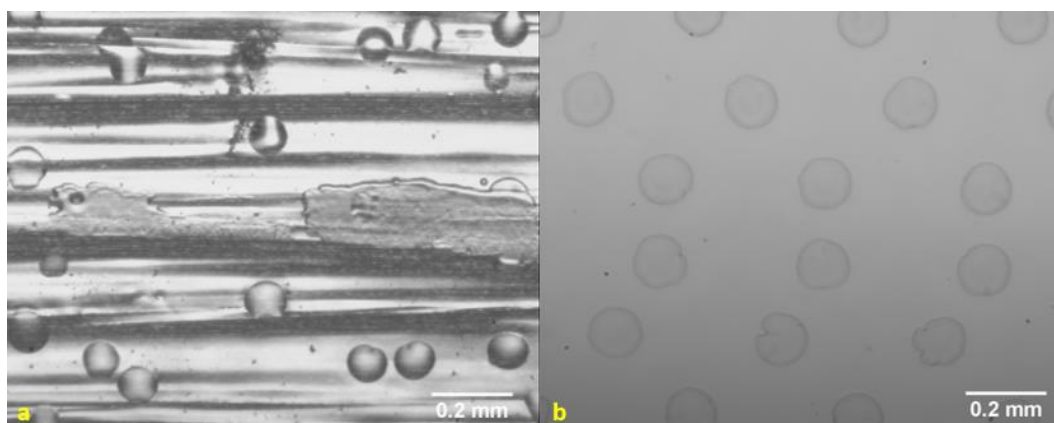


Figure 3.27: Comparison of PEG 1,500M_w droplets printed onto a) uncured 977-2 prepreg b) glass microscope slide

Figure 3.28 shows droplets printed onto resin films of different degrees of cure. All three images show starkly different results. Figure 3.28a shows the edge of the resin film. On most samples the glass slides were not covered completely with resin. They were however, printed completely. No droplets were observed in the main body of resin. Looking at the edge of the film it became apparent why. The droplets dissolved into the resin wherever contact was made. It was seen within the resin that the boundaries between dissolved droplets were straight, which reduced the surface energy of the boundary. On the right side of the image, two droplets are visible which were only partially contacting the resin. In these cases the contacting side dissolved, increasing the surface tension of the resin, which can be seen from the way in which it has pulled away from the droplet before it fully dissolved. The dissolution of the droplet was either (as it was with PMMA) due to the presence of quantities of volatile solvents or due to the miscibility of PEG in the resin at the lower partial cure. However, without knowing the exact formulation of the resin, it is difficult to assess which theory is correct. The low molecular weight of the PEG also made it disperse more easily due to its higher configurational entropy.

Figure 3.28b shows a hexagonal pattern of bubbles rather than droplets. No evidence of PEG was visible anywhere within the resin. Two hypotheses are presented which may explain this phenomenon. Firstly, to some degree the droplet may impact the resin, penetrating it before dissolving, and leaving behind it a cavity which the surrounding resin then fills. An illustration of this is Figure 3.29 in which a ball is dropped into water. In this case the air bubble created by the cavity would rise to the surface. However, if the liquid is suitably viscous, as was the case with the partially cured resin, then the bubble would become trapped and unable to rise. This hypothesis explains why the less viscous resin in Figure 3.28a did not feature these bubbles. The local viscosity of the resin would be low enough that the bubbles could rise to

the surface of the resin. And in the high viscosity resin, the droplets would be unable to penetrate the surface, so that they could only form droplets which sit on the surface. Secondly, it is possible that the hexagonal edges formed by the areas of resin of differing surface tensions collapsed into the centre as the PEG dissolved from the surface into the bulk resin (therefore changing its viscosity and surface tension), trapping air within. In this case, the degree of partial cure of the resin would affect both the rate of dissolution and the properties of the PEG/resin mixture. In resin of lower partial cure, the PEG may dissolve too rapidly to develop the exact conditions in which bubbles form. And evidently at higher partial cures the PEG did not dissolve at all, preventing the mechanism from occurring. Unfortunately, no further evidence was collected which substantiated either of these hypotheses.

Droplets are clearly visible in Figure 3.28c. This image closely matches what was observed in the uncured prepreg. All of the images in Figure 3.28 (particularly Figure 3.28a and Figure 3.28c) show a progressive decrease in the miscibility of PEG in the resin at higher partial cures. This was almost certainly due to the decrease in configurational entropy of the resin as crosslinking increased. This decrease is caused by the reduced mobility of polymer chains as they become crosslinked [201]. Hence at higher partial cure, phase separation of the droplets on the resin surface occurs more easily. This difference in phase separation at different partial cures is something that was observed in all resin slide tests to some degree. Ultimately, the key principle of these tests was attempting to achieve a similar phase separation to that observed in printed prepreg samples as this was a key indicator of a good match between the partial cure of the resin on the slides and in the prepreg.

The resin slides were observed after curing, as in Section 3.9.2.1. However, no evidence at all of droplets was seen. It is likely, considering their tendency to dissolve at room temperature, that the PEG completely dissolved into the resin at elevated temperatures. In laminates this would result in a homogeneous dispersal of PEG in the resin rich region rather than a pattern of discreet droplets. The application of inkjet printing is still justified though as means of very evenly distributing PEG in amounts that interleaving and manual ink application would be unable to achieve.

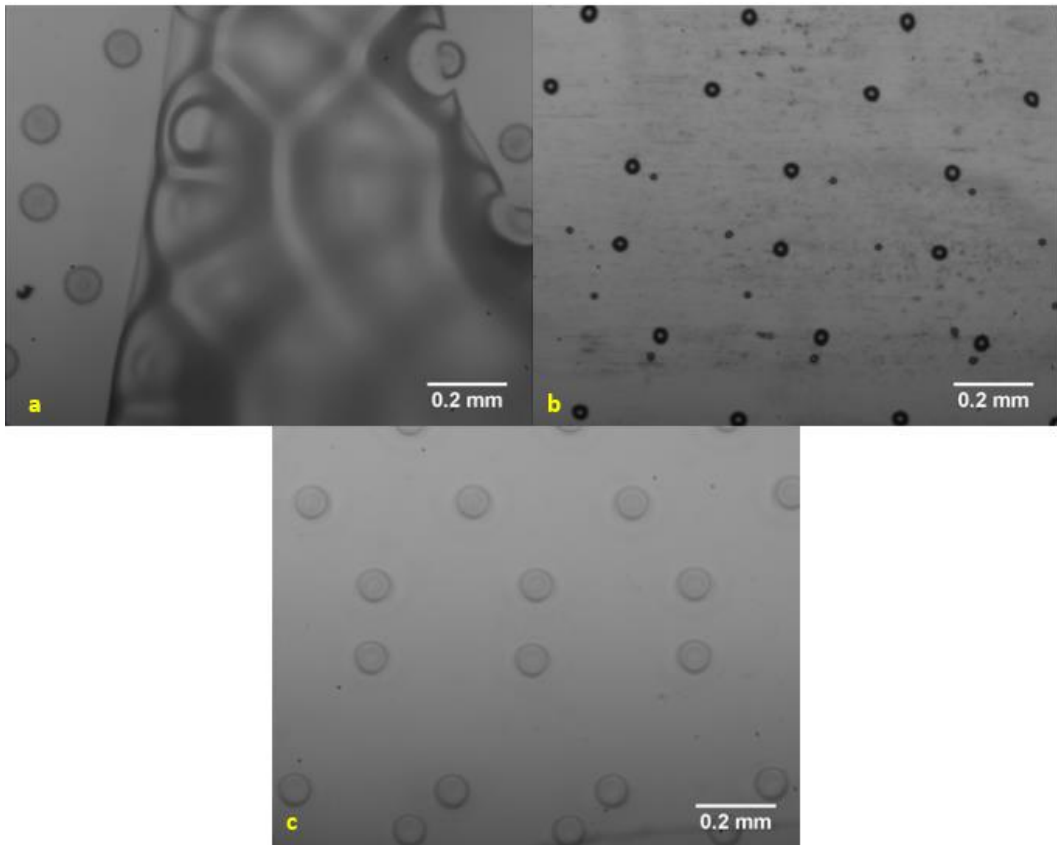


Figure 3.28: Microscope images of PEG 1,500M_w droplets printed onto a part-cured resin film. The resin was partially cured at 180°C for a) 5 minutes b) 10 minutes c) 20 minutes

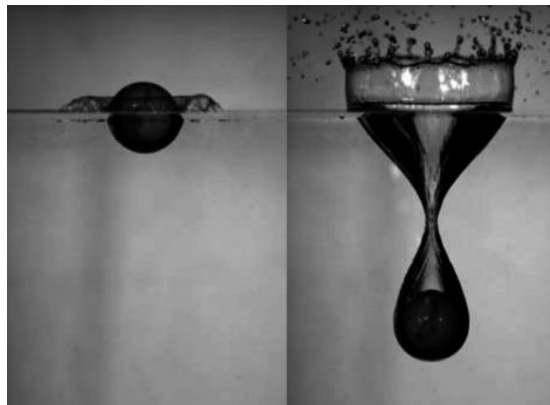


Figure 3.29: Cavitation forming behind a sphere dropped into water and the air bubble which is formed by the water closing around the cavity [202]

3.9.2.3 PEG 20,000M_w in Deionised Water Ink

Figure 3.30 shows PEG 20,000M_w droplets printed onto a prepreg substrate and a glass substrate. The appearance of the droplets on the uncured prepreg substrate was indistinguishable from that of PEG 1,500M_w in Figure 3.27a. However, those printed on glass, although similar in diameter, were markedly different. They featured long cracks across their surface. It is likely that this was due to the shrinkage of the droplet as the solvent evaporated. This was not evident in PEG 1,500M_w because it is more ductile due to its shorter polymer chains. These cracks were not visible when printed onto uncured prepreg perhaps because the slight solvent content of the prepreg reduced the rate at which the droplets crystallised, allowing them more time to deform.

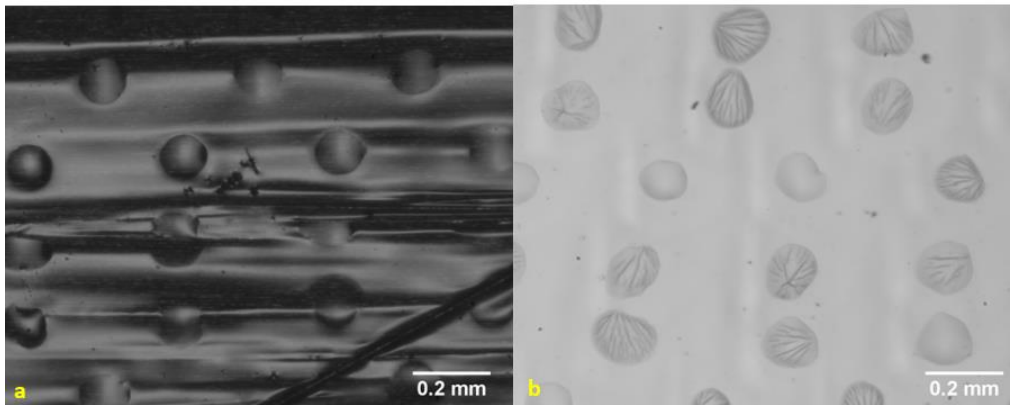


Figure 3.30: Comparison of PEG 20,000M_w droplets printed onto a) uncured 977-2 prepreg
b) glass microscope slide

Figure 3.31 shows droplets printed onto resin films of different degrees of cure. Droplets were visible in all cases, but their diameter varied with the degree of cure, having smallest diameter when printed on 20 minute part-cured resin due to lower resin solvent content. Once again, image *c* best matched the droplets printed onto uncured prepreg.

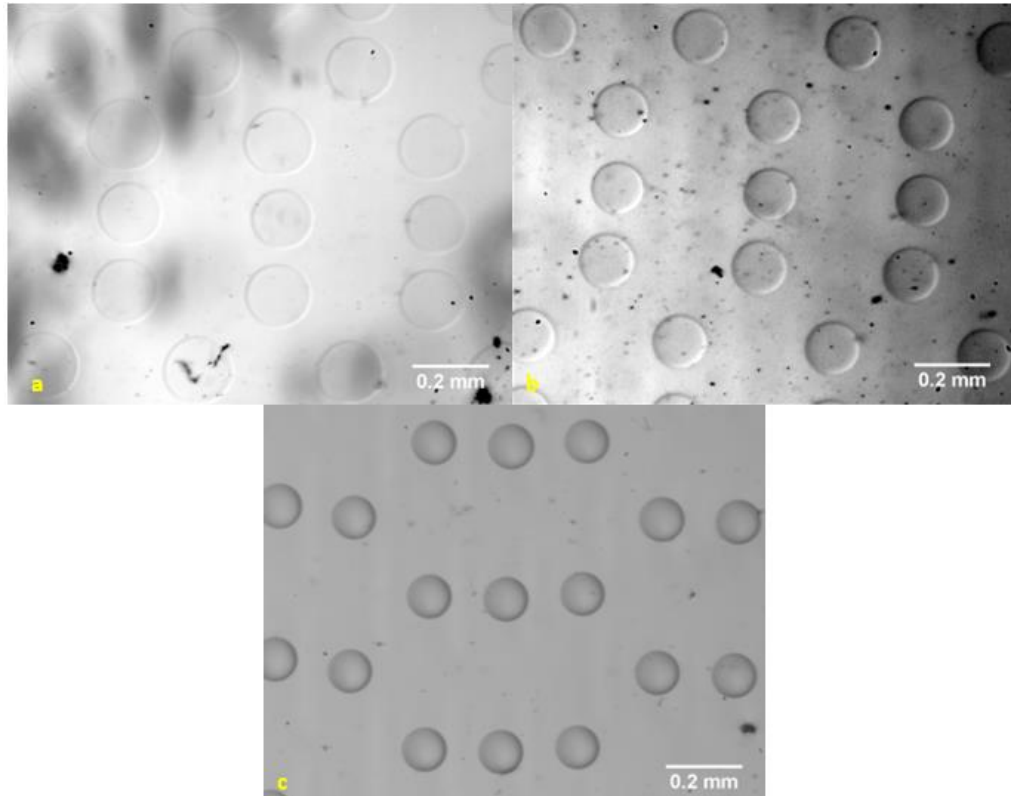


Figure 3.31: Microscope images of PEG 20,000M_w droplets printed onto a part-cured resin film. The resin was partially cured at 180°C for a) 5 minutes b) 10 minutes c) 20 minutes. The contrast of images *a* and *b* were digitally enhanced.

Once cured, no evidence at all of PEG was observed in resins partially cured for 5 or 10 minutes. Nor was it found in the bulk of the resin partially cured for 20 minutes. However, Figure 3.32 clearly shows evidence of PEG droplets on the edge of the resin (20 minute pre-cure) where it was not covered by a second layer of resin. Droplets were visible on the glass away from the resin, and spread droplets were visible on the resin itself. It is therefore likely that droplets within the bulk resin also remained discreet to a degree, but blended gradually into the matrix around them, rendering them indiscernible from the resin surrounding them. The almost identical refractive indices of PEG and epoxy resin (1.467 and 1.5 respectively [178, 197]) would also make such dispersed droplets impossible to view using optical microscopy.

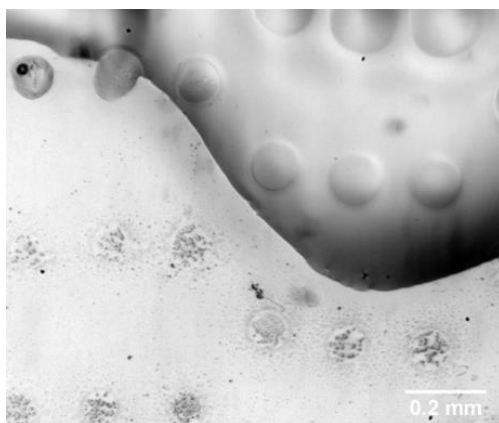


Figure 3.32: Microscope images of PEG 20,000M_w droplets printed onto a part-cured resin film. The resin was partially cured at 180°C 20 minutes. PEG droplets on the glass slide only are broken up, whereas droplets on the resin spread. The contrast of the image was digitally enhanced.

3.9.2.4 Solvents

Further investigation was also conducted into the effects of the solvents used. The reason for this was twofold. Firstly, to investigate any negative interactions that the solvents may have with the resin. And secondly, to confirm that the droplets observed in the previous sections were in fact droplets and not artefacts of the solvent deposition.

Printing pure DMF produced results in all uncured samples as shown in Figure 3.33. A hexagonal pattern is clearly visible, consisting of smooth resin discs. It is thought that these were caused by the DMF dissolving the top surface of the resin before evaporating, allowing it to flow and become smooth. No evidence of DMF was identified after the samples were cured, indicating that there was little or no lasting effect of DMF.

Pure deionised water was also printed onto partially cured resin. No artefacts were seen on any of the resin films, nor in any of the cured samples. It may be concluded then that there was little or no effect of using water as a solvent.

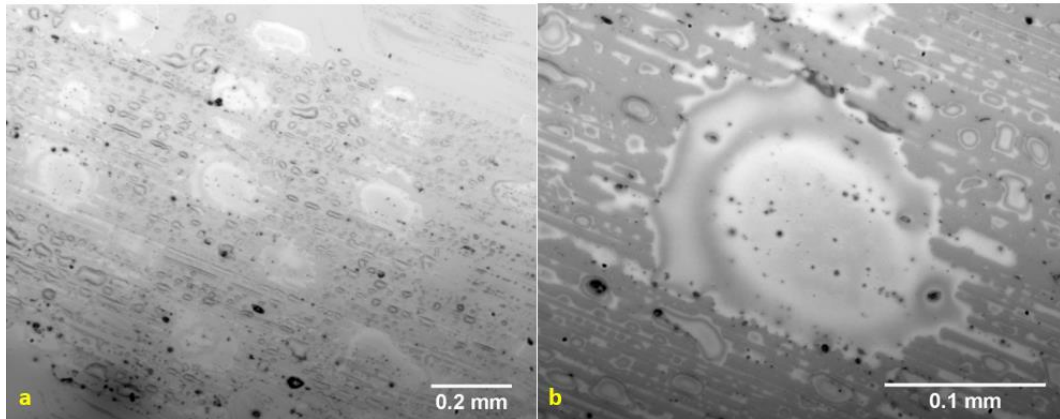


Figure 3.33: DMF printed in hexagonal pattern onto resin partially cured at 180°C for 10 minutes. The contrast of both images were digitally enhanced.

3.9.3 Conclusions

Evidence has been presented in the above sections showing that all three of the inks used in this work produce different results when cured in 977-2 resin.

PMMA ink produced groups of small spheroidal droplets that remained as a discrete phase from the resin. These groups retained their printed pattern. Because the mechanical properties of these droplets are less than those of cured 977-2 resin, it was hypothesised that a toughening effect should be observed.

PEG inks were shown to behave differently dependent upon their molecular weight. It was concluded that PEG 1,500M_w completely dissolved into the surrounding resin. In composite laminates this would create a homogeneous toughened layer between plies. It is unlikely that the PEG would be able to diffuse far beyond the interlaminar region as it would be blocked by the tightly packed carbon fibres of the adjacent plies. Although the printed pattern was not retained, inkjet printing is still an appropriate method of deposition as it allows very accurate control of the quantities of polymer added, which manual techniques cannot provide.

It was found that PEG 20,000M_w dissolved within the resin at lower partial cures. However, at a partial resin cure time of 20 minutes, discrete droplets were observed at the edges of the resin regions. These droplets appeared to blend into the resin around them to some degree. No droplets were observed in the bulk resin, but this was most likely due to the very similar refractive indices of the PEG and resin.

The effect of DMF and deionised water solvents on printed laminates was also investigated. In both cases little or no effect was observed in cured resins. This suggested that any physical

effects caused by printed inks in mechanical tests were likely to be purely due to the addition of polymer, and not due to the solvent.

In all cases, resin that was partially cured for 20 minutes produced results which most closely resembled those seen in printed uncured prepreg, suggesting that the result of those tests was most likely a valid model of polymer/resin interaction during curing.

3.10 CONCLUDING REMARKS

This chapter described the materials used to manufacture test specimens for mechanical tests. CYCOM® 977-2 unidirectional prepreg was selected due to its applicability to such industries as aerospace. It is a thermoplastic-toughened prepreg material that critically does not already contain any method of interlaminar toughening.

PMMA and PEG inks were selected for their varying mechanical properties, giving a range of toughening capabilities. Investigations by Zhang [11] also showed that these polymers increased interlaminar fracture toughness by up to 40%, and exhibited good printability and resin interaction.

Manufacturing methods were also described. The printing process and apparatus was detailed for the inks used. It was demonstrated how the shape and spacing of the printed pattern influences surface coverage and the volumes and masses of polymers added to the completed laminates. In all cases it was calculated that no more than 0.046% additional volume, and 0.035% additional mass was added to laminates. Compared to other methods of global toughening and interlaminar toughening, which add significant mass to laminates, inkjet printing may provide significant increases in mechanical performance at negligible costs to specific mechanical properties.

The durability of the printed pattern was investigated. If the printed polymer is disturbed or removed too easily then the applicability of this technology as an industrial method is compromised. Tests were performed which tested the integrity of the printed pattern in a controlled manner to a degree greater than it would experience in normal manufacturing methods. Using optical microscopy it was found that no significant movement of the droplets occurred. Although in some areas smeared droplets were observed. It was concluded that despite minimal risk to the integrity of the droplets, care should still be taken during the manufacturing process.

DSC was used to confirm the curing schedule of 977-2 according to the manufacturer's specification. Attention was paid to the degree of cure achievable by this schedule, confirming

that material properties were consistent between cures. Variations in the degree of cure may affect tensile modulus and matrix toughness. However, the samples tested were found to be very consistent, exhibiting an average degree of cure of 98.2%.

Finally, partially cured resin slides were prepared in order to determine the behaviour of printed polymers when cured within laminates. Greatly different behaviours were identified between the different polymer inks. PMMA droplets remained as a discrete phase within the cured resin, whereas PEG polymers were found to dissolve into the resin to different degrees dependent on their molecular weight. These differences provide a range of mechanisms by which the polymers may interact with the surrounding material, allowing a range of effects to be investigated in mechanical tests.

The following chapters continue on from the work presented in this chapter, extending it to cyclic mechanical testing in order to determine if differences in polymers or the morphology of droplets affects the formation of fatigue damage within composite laminates.

CHAPTER 4: MECHANICAL TESTING PROCEDURES

This chapter discusses the experimental procedures used to evaluate the mechanical performance of inkjet printed composites under cyclic loading. The procedures of tests that were necessary for the calculation of experimental parameters and baseline values relating to these tests are also presented. Aspects relating to experimental measurement and data capture are also covered.

4.1 FLEXURAL TESTING

This section outlines the procedures of both static and cyclic four point bending tests as well as the development of the necessary testing jigs, measurement techniques, and data acquisition techniques.

Flexural loading was selected as a method of testing interlaminar fatigue damage. Many structures such as aircraft wing sections are often subjected to high cyclic flexural loads, so flexural tests were considered a good representation of in-service components. Flexural loading also creates a strain gradient within the laminate which encourages delamination development. This also allows the use of unidirectional laminates because strain differences are created between plies without the need for plies with differing Poisson's ratios. Ultimately this makes results easier to interpret because any potentially unusual effects of off-axis plies do not have to be considered.

Because toughening polymers were introduced exclusively into the interlaminar region, any effects would present themselves where interlaminar damage is prevalent. Flexural tests were determined to be an appropriate method of introducing interlaminar stresses because of the strain gradient that naturally occurs through them which can cause delaminations, as illustrated in Figure 4.1. It can be seen that the top face experiences compression, and the bottom face experiences tension. The central dashed line represents the neutral axis, about which these loading modes switch. As previously mentioned in Section 2.3.1.3 strain differences between plies are one of the major factors which cause delamination growth, and are the main reason that multidirectional laminates must be carefully designed to avoid sudden orientation changes between plies.

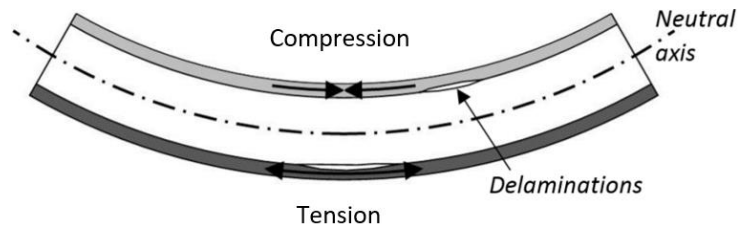


Figure 4.1: Illustration of a laminate under flexural loading. Flexural samples experience varying degrees of strain throughout their thickness. [203]

Flexural fatigue tests are often ignored in favour of tension/tension or tension/compression fatigue tests. However, they have advantages such as better representation of in-service loads, greatly reduced risk of buckling, and greatly reduced testing forces. They are also often accompanied by stiffness degradation analysis, since flexural tests inherently produce large specimen deflections, and so don't require accurate instrumentation to measure deflection. But these advantages are sometimes disregarded in favour of the less complex and more easily modelled tensile tests.

Where flexural tests are used, the favoured method is three point bending. This is because of its simplicity and ease of setup. However, three point bending tests inherently create a high level of shear loading at the central roller. This can cause premature fracture at the roller contact point. Four point bending tests also create shear loads at the roller contact points, but these loads are spread between the rollers, so premature failure is less likely. Four point bending tests were used in this work for this reason, and because of the uniform bending moment between the loading rollers. This is illustrated in Figure 4.2, which compares transverse loading (V) and bending moment (M).

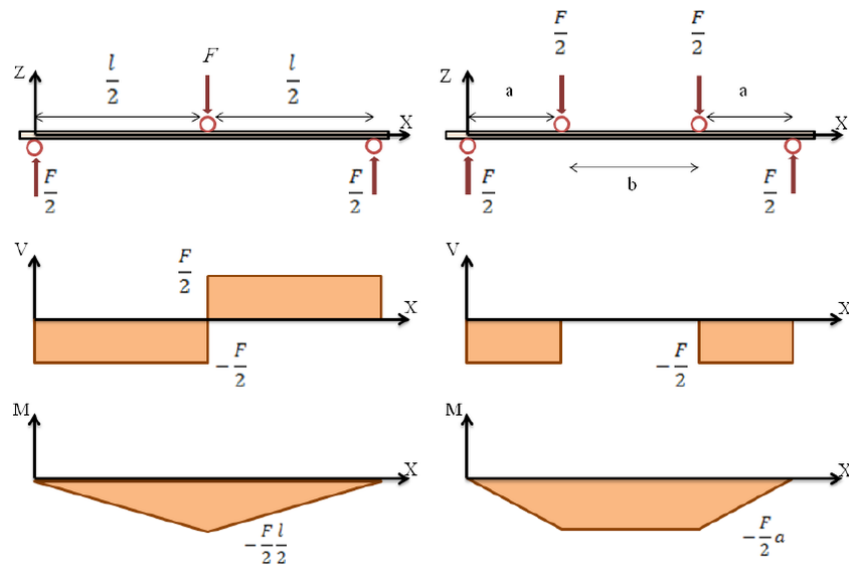


Figure 4.2: Comparisons of transverse loads and bending moments in three and four point loading scenarios [204]

4.1.1 Development of Four Point Bending Jig

Before these tests could be conducted reliably, the test procedure went through a stage of iterative development. All four point bending tests were conducted in accordance with ISO 14125 (1998+A1:2011) [205]. In order to meet the requirements of this standard, a new test jig was designed. Initially, this jig was designed to simply fulfil the basic requirements of the standard, but it became apparent that more functionality was required. It was gradually developed to counteract issues as they arose so that it provided good, reliable test data. This section outlines the development process step by step, along with the justification for each modification.

Figure 4.3 shows the initial design of the four point bend jig. It consists of two steel blocks, which may be attached to the test machine by threaded bars, and locked in place with nuts. Two roller mounting blocks, which support the 5mm diameter rollers in machined channels, were then attached to each block. The position of these blocks was fully adjustable in order to allow specimens of varying dimensions to be accommodated if necessary. This design allowed initial flexural tests to be conducted. However, upon the commencement of fatigue testing using this setup, it became apparent that modifications would have to be made to the jig in order to improve experimental accuracy.

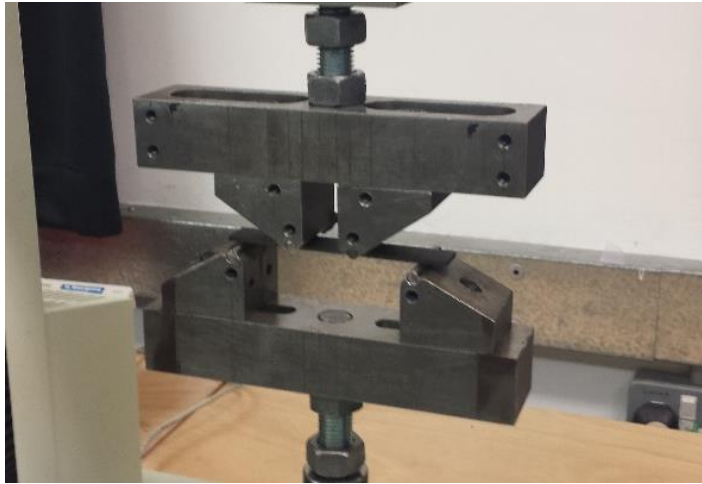


Figure 4.3: Initial four point bend jig design

Due to the cyclic nature of these tests, many inherent problems surfaced which were not encountered in static testing. Fatigue testing was conducted on a Nene 12.5kN servo-hydraulic testing machine. This machine had a ‘floating’ actuator, which allowed rotation of the bottom half of the jig relative to the top half. This was resolved by attaching legs to the fixed half of the jig as shown in Figure 4.4, completely preventing rotation, and ensuring alignment of both halves of the jig at all times.

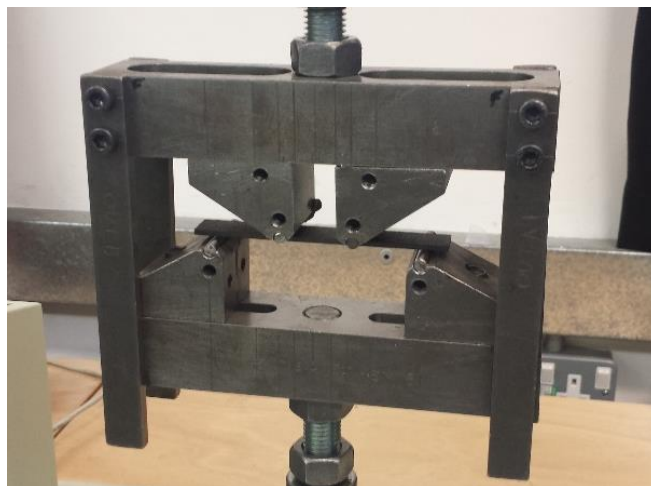


Figure 4.4: Four point bend jig with leg attachments

The second issue observed was that of sample rotation (about the vertical axis) under cyclic loading. This was corrected by the addition of jaws on the supporting roller blocks as shown

in Figure 4.5. These jaws kept the sample captive, but allowed free longitudinal movement as the sample rolled and deformed.

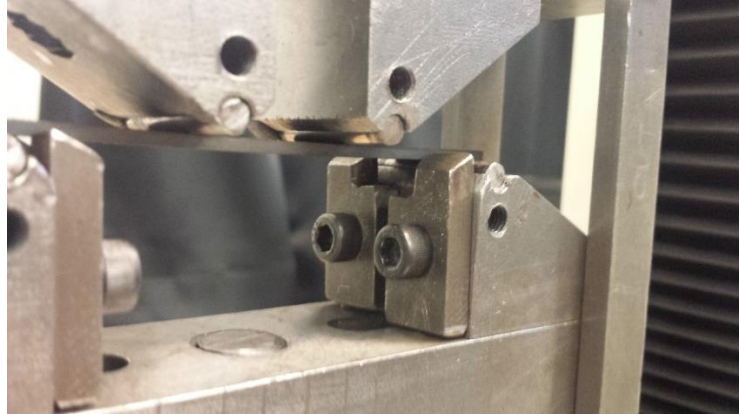


Figure 4.5: Anti sample rotation jaws attached to the supporting roller blocks

Finally, and perhaps most critically, the issue of experimental data scatter was addressed. It will later be shown in Section 5.2.1, that the measured fatigue lives of the samples, particularly at lower load levels, were found to vary by as much as three orders of magnitude. It was determined that uneven loading and stress concentrations at the loading rollers were the cause of these issues. This caused localised damage at the rollers which developed at a faster rate than global fatigue damage, causing premature failure in samples. The design of the load application rollers was therefore changed to that shown in Figure 4.6. No indication of ideal roller diameter was otherwise given in BS EN ISO 14125 (1998+A1 2011).

Spherical roller bearings were added in order to allow roller rotation, preventing unnecessary tensile/compressive stresses from occurring at the sample surface. Larger (10mm) diameter steel rollers were also added in order to reduce the stress concentrations at these points. This design allowed the height of the rollers to be adjusted at both ends of the roller. This allowed the rollers to be aligned perpendicular to the surface of the sample, giving much better load distribution along the length of the rollers.

Following this modification an increase in apparent ultimate flexural strength (UFS) was observed in static tests. The accuracy of cyclic tests was also increased dramatically, with scatter of S-N reduced from three orders of magnitude to less than one.

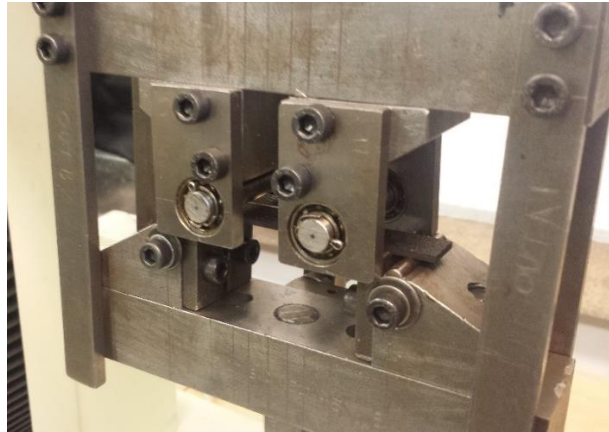


Figure 4.6: Roller bearing mounts and increased diameter rollers

4.1.2 *Four Point Bending Jig Dimensions*

Drawings relating to the dimensions of the four point bend jig at its final revision are presented in this section. The jig consisted of two main steel blocks (Figure 4.7) machined with slots in them that allowed the attached roller blocks (Figure 4.8) to be movable so as to allow different testing geometries. Although only a single sample geometry was used, this design redundancy was seen as advantageous at the design stage. M10 cap bolts were used to fix the roller blocks to the main blocks. A scale was scribed onto the side of the main blocks to allow easy repositioning of the roller blocks. Anti-rotation arms (Figure 4.9) were attached to the upper main block using M6 cap bolts to keep the top and bottom halves of the jig aligned with each other. In later revisions, bearing blocks (Figure 4.10) were attached to the loading roller blocks to allow the use of larger ($\phi 10\text{mm}$) diameter rollers. 19x10x5mm spherical roller bearings were used and held captive by bearing retaining compound. The blocks were attached to the roller blocks by M6 cap bolts. In the supporting roller blocks, smaller 5mm hardened steel rollers were used. These were placed in the machined channels. Because stress concentrations were much higher at the loading rollers, it was not necessary to increase the diameter or rolling resistance of these rollers. Their limited rotational capability was advantageous as it kept the samples from gradually sliding out of the jig. Finally, Figure 4.11 shows an assembly drawing of how the listed components fit together. M16 threaded bar was used to attach the jig halves to the testing machine, and locking nuts were used to prevent rotation of the jig in the machine.

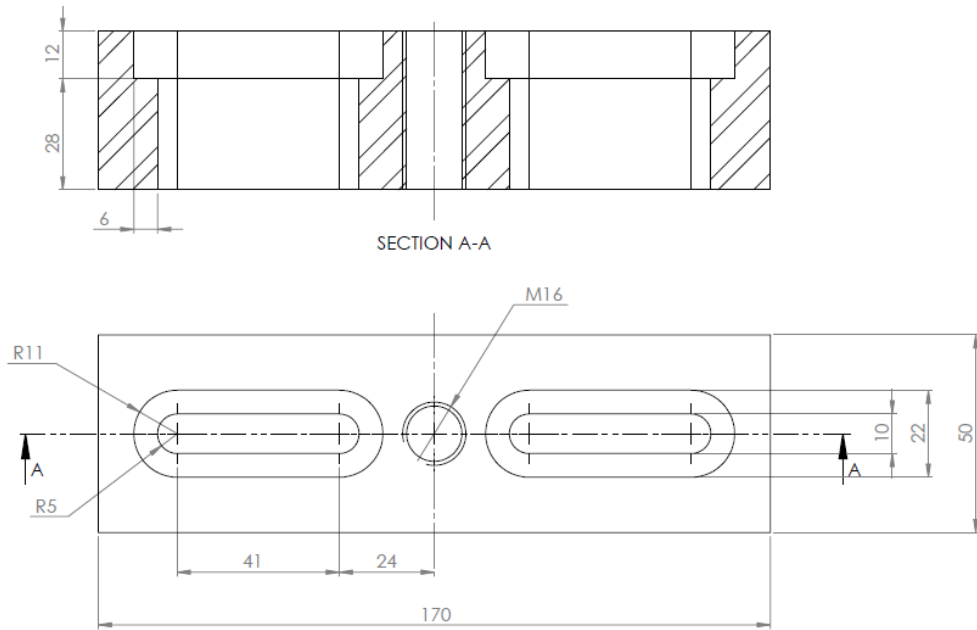


Figure 4.7 Technical drawing of main four point bend jig blocks. Two of these are used in the jig, and are the main body. They have slots cut in them to allow adjustment of the roller blocks so that the jig can accommodate samples of varying dimensions. Drawing not to scale.

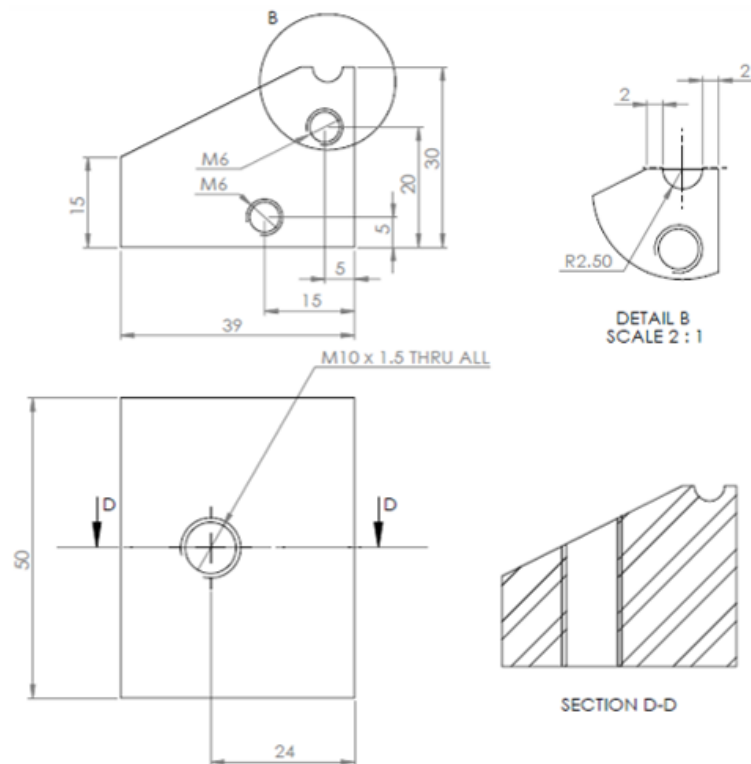


Figure 4.8 Technical drawing of a roller block. These blocks hold the rollers in place. They are attached to the main blocks by a single M10 cap screw bolt. Two M6 threaded holes were added in later revisions in order to allow the fitment of roller bearings. Drawing not to scale.

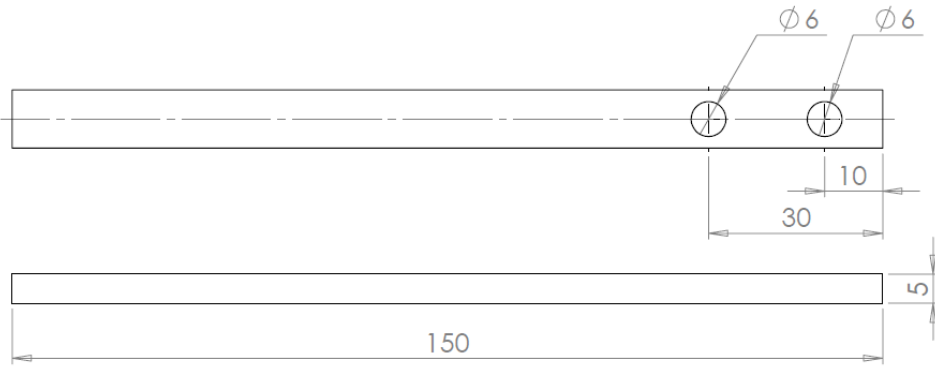


Figure 4.9 Technical drawing of anti-rotation arms. These were attached to the upper main block and kept the two halves of the jig aligned with each other. Drawing not to scale.

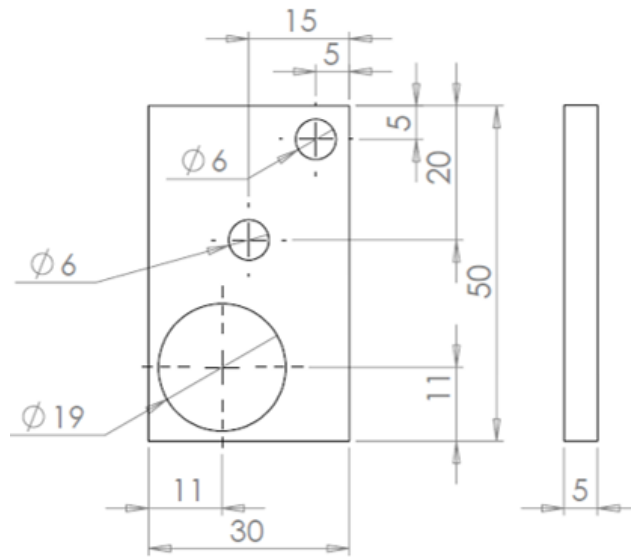


Figure 4.10 Technical drawing of a bearing block. These were added to the loading roller blocks in later revisions to hold 19x10x5mm spherical roller bearings. The bearings were held captive by bearing retaining compound. Drawing not to scale.

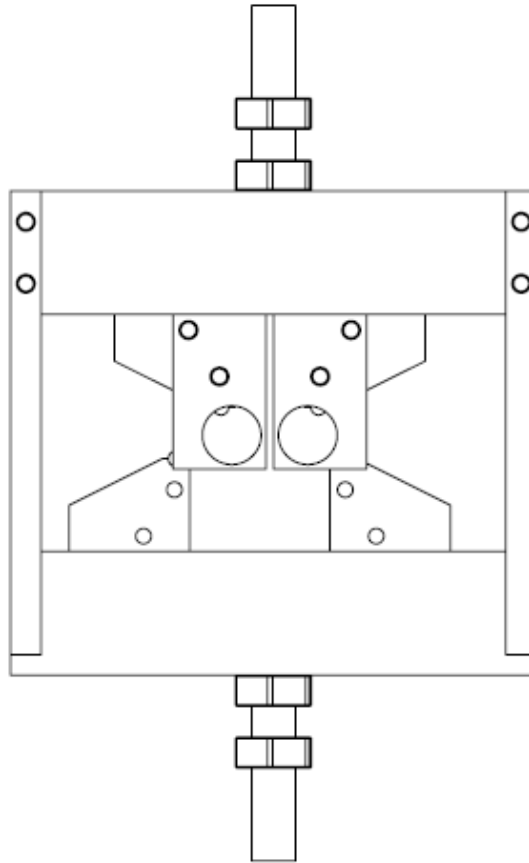


Figure 4.11 Assembly drawing of the components in the intended configuration. Also features M16 threaded bars which allow the jig to be mounted in the testing machine. Lock nuts were used on the threaded bar in order to prevent jig rotation. M6 cap bolts were used for the fixture of all other components. Drawing not to scale.

4.1.3 Test Frame Calibration

Before conducting tests, calibration of the load frame was conducted to ensure accuracy of the experimental results. The testing machine used was a Nene servo-hydraulic test frame (Figure 4.15) equipped with an Interface 1020 12.5kN load cell, which had a static error rating of $\pm 0.05\%$. A rigid shear pinned connection was set up between the actuator and load cell in series with a 10kN calibration load cell. Comparisons were made between the load cells at varying deflections to obtain a calibration curve. The static error of the load cell prior to calibration was found to be $>10\%$. This method of calibration was repeated until an accuracy of $\geq 99\%$ was achieved.

The displacement calibration of the test frame was also checked. This was found to be correct within 1%.

4.1.4 Measurement of Midpoint Deflection

In order to calculate the flexural modulus of samples during tests in accordance with the test standard, a way of measuring the midpoint deflection of the samples was necessary. An attachment was designed and manufactured which allowed this measurement to be taken. The attachment consisted of a supporting structure which held a lever arm (of leverage ratio 1:1) in place as shown in Figure 4.12. This lever rested on the underside of the sample, and was moved when the sample deflected. This then pushed on a linear variable differential transformer (LVDT) position sensor. The spring return action of the LVDT kept the lever arm in contact with the sample at all times as it flexed. This design was chosen to avoid placing a sensor directly underneath the sample, which would have required a complex jig design. The LVDT used was an RDP D5/300AG.

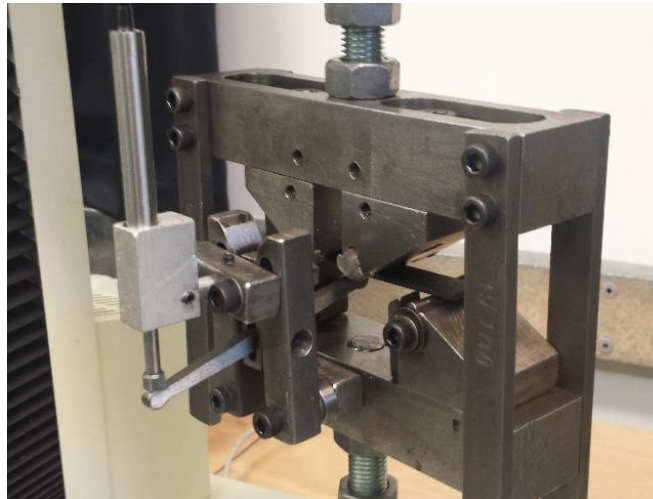


Figure 4.12: Lever arm arrangement to capture sample midpoint deflection

4.1.5 Static Flexural Tests

Static four point bend tests were used to provide the baseline values for fatigue tests of the same material, as well as to investigate the static flexural properties of inkjet printed composites. Flexural tests in this section were conducted according to BS EN ISO 14125 (1998+A1 2011) [205]. It should be noted that samples in these tests were not necessarily manufactured in the same batch. Generally, samples were manufactured in bulk over several batches cured at separate times and subsequently mixed, so variations between batches are statistically accounted for in the results. 2x15x100mm rectangular 0° unidirectional

specimens were manufactured from 977-2 unidirectional prepreg using the methods outlined in Section 3.5. All samples were cut from 130x250mm panels using a diamond cutting saw. They were then ground to within 2% of the specified dimensions using a 600 grit sanding wheel or finer. Samples were measured using digital Vernier callipers with a manufacturer's quoted accuracy of 0.01mm. Measurements of width and thickness were taken at three points evenly spaced along the length of the specimen and then averaged.

Samples were placed in four point flexural loading using the four point bend jig described in Section 4.1.1 in accordance with BS EN ISO 14125 (1998+A1 2011). The jig was arranged so that a support span of 81mm and a top roller separation of 27mm was used, leaving an overhang of 9.5mm past the support rollers. A schematic of the test dimensions is shown in Figure 4.13, and an image of a sample placed in the jig is shown in Figure 4.14. The rollers were levelled so that they contacted the face of the sample along their full length. This was achieved by the use of a 0.05mm steel feeler gauge. The machine crosshead was raised until equal resistance was felt upon the feeler gauge at both edges of the rollers. The mechanical lever arm described in Section 4.1.4 was then set against the bottom face of the sample, and the LVDT set, placing spring compression on the opposite side of the arm. The LVDT reading was then set to zero position.

Five specimens of each sample type were placed under compressive force at a rate of 2mm/min until ultimate failure using a Nene 12.5kN servo-hydraulic testing machine controlled by a MOOG SmarTEST ONE test controller (Figure 4.15). Load, crosshead displacement, and midpoint deflection were recorded in all tests. The data from these tests was then analysed in order to calculate the UFS and flexural modulus of each sample.

It is stated in ISO 14125 (1998+A1:2011) that 'a 0.2mm thick shim of polypropylene (PP) has been found to be successful in reducing failures of the compressive face associated with the loading member'. Instead of PP, it was decided that polyvinyl chloride (PVC) electrical insulation tape would be a suitable alternative since it has similar mechanical properties [206], has the advantage of being adhesive, and it is generally around 0.1mm in thickness. Therefore, two layers of PVC electrical tape were applied to roller contact points in all static and cyclic tests. When insulation tape was used, a 37% increase in UFS was observed compared to tests conducted with no tape in otherwise identical setups. Following these results, insulation tape was used in all future static and fatigue four point bend tests.

In these tests, only two types of laminate were used: unprinted, and 10%/wt PMMA in DMF printed. Flexural tests were initially used to establish the properties of printed composites. But a change was made later to a tensile testing regime. During the time that flexural testing was

used, only unprinted and PMMA printed composites were tested. A hexagonal printing pattern of $\delta x, \delta y = 0.4\text{mm}, 0.6\text{mm}$ was used for all printed samples (Section 3.3.2).

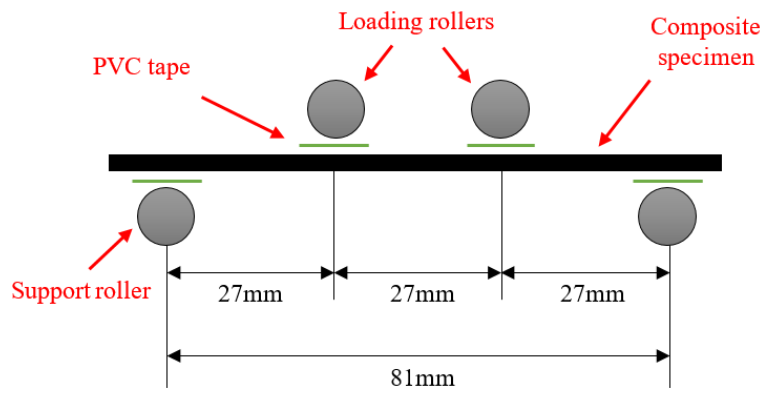


Figure 4.13: Schematic of four point bend test dimensions

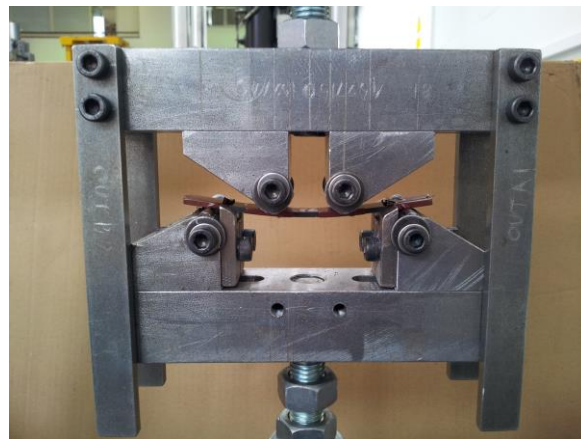


Figure 4.14: A composite sample under compression in four point bending



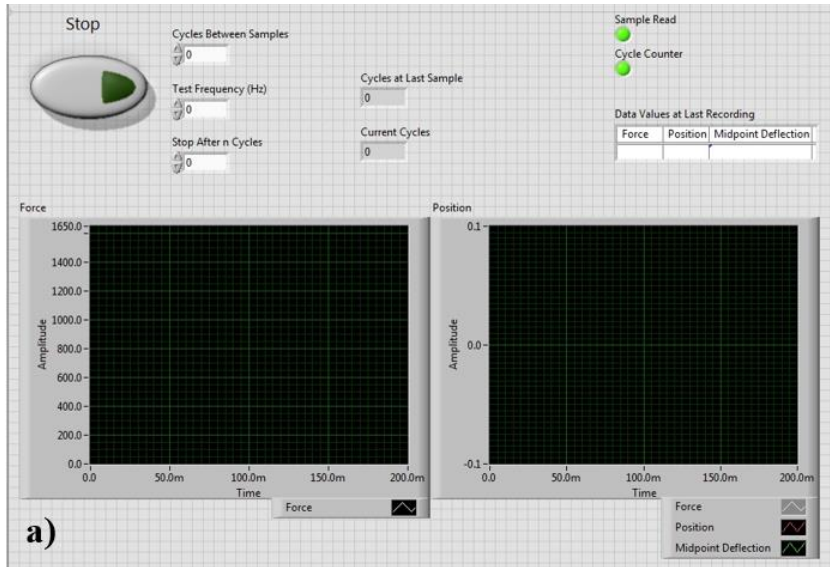
Figure 4.15: Nene 12.5kN servo-hydraulic test machine, and MOOG SmarTEST ONE controller

4.1.6 *Development of LabView Data Acquisition Software*

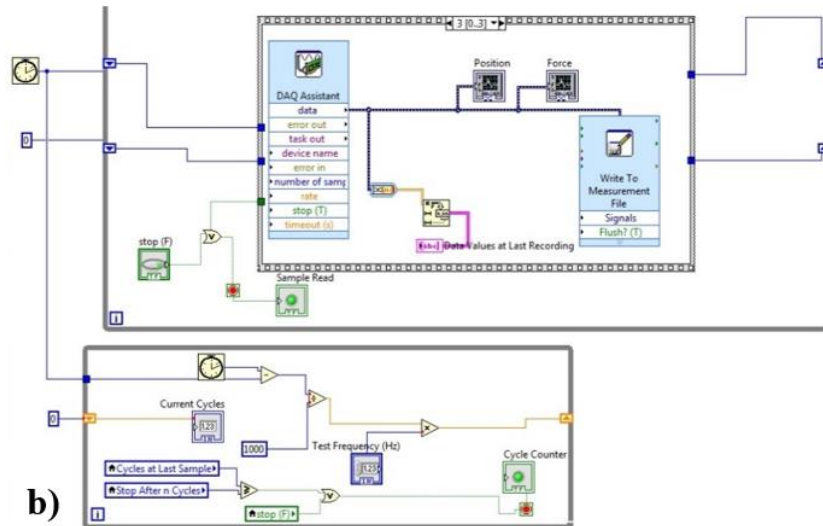
Before any cyclic testing could be conducted, a method of data acquisition had to be developed. The MOOG SmarTEST ONE test controller had built in data capture software, but was incapable of periodic sampling. Since fatigue experiments may continue for days, it was decided that periodic sampling of the data would reduce the size of the output files to manageable sizes. However, the clock speeds of the MOOG test controller and any external data capture system would differ slightly, and would become desynchronised over the long time periods associated with fatigue tests. It was therefore not possible to simply capture singular data points at the peaks of each measured loading cycle. Instead, what was required was a system that could periodically capture data over an entire individual cycle of the tests. This would produce a waveform of the experiment, which could then be analysed to give peak load and displacement readings at the time of measurement. The peak readings could then be used to calculate the mechanical properties of samples at that measurement point.

The chosen solution was to design a custom data acquisition (DAQ) macro in National Instruments (NI) LabView. Force, position, and midpoint deflection data could be read from the MOOG SmarTEST ONE controller using a National Instruments USB-6008 analogue DAQ module. Following manual calibration, this data could then be recorded using the LabView DAQ shown in Figure 4.16. Using this simple user interface, the user could input the desired cycles between samples, the test frequency, and the point at which to stop recording. The sample period was decided by the user based upon previous test results. If no previous data was known about a particular stress level then a suitable sample period was conservatively guessed, and then adjusted in subsequent tests. All fatigue tests were run at 5Hz, so the DAQ was set to sample 50 data points at a frequency of 250Hz, which captured one complete 360° waveform. The choice of this sample frequency is described further in Section 4.1.7. The user interface also incorporated visual data outputs in the form of time plots, which plotted the data on screen for the user as it was recorded. An example of a typical waveform sample is shown in Figure 4.17.

An added benefit of this method of data capture was that of remote access. Because the software was PC based rather than test controller based, an internet or intranet connection could be used to monitor the test progress, and even alter DAQ settings, greatly reducing the need for regular manual inspection.



a)



b)

Figure 4.16: LabView DAQ: a) User interface, b) Visual program design

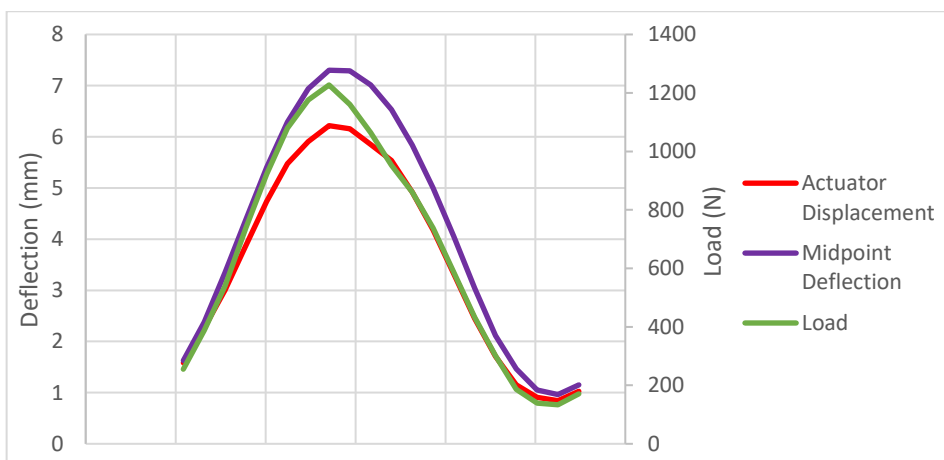


Figure 4.17: Example waveforms captured by LabView DAQ

4.1.7 Optimisation of Data Acquisition Rate

Because the DAQ system captured a number of data points in order to ensure the capture of waveform peaks, the number of data points captured per cycle was important. Too many would have created large data files, whilst too few would have resulted in a factor of error. Consider a single data point in the captured waveform. Because it is not possible to know if the data capture and waveform are in phase, it is possible for that point to be out of phase from the peak by up to 180° , creating an error of 200% about the midplane of the waveform. This potential error is reduced exponentially with an increasing number of data points.

The maximum percentage error (δ) about the midplane of the waveform may be calculated by;

$$\delta = 100 \sin \left(\frac{\left(90 - \left(\frac{360}{n} \right) \right) \cdot \pi}{180} \right) \quad 4.1$$

where n is the number of data points.

By inserting $1 < n < 100$ into Equation 4.1, the resulting maximum error may be calculated as shown in Figure 4.18.

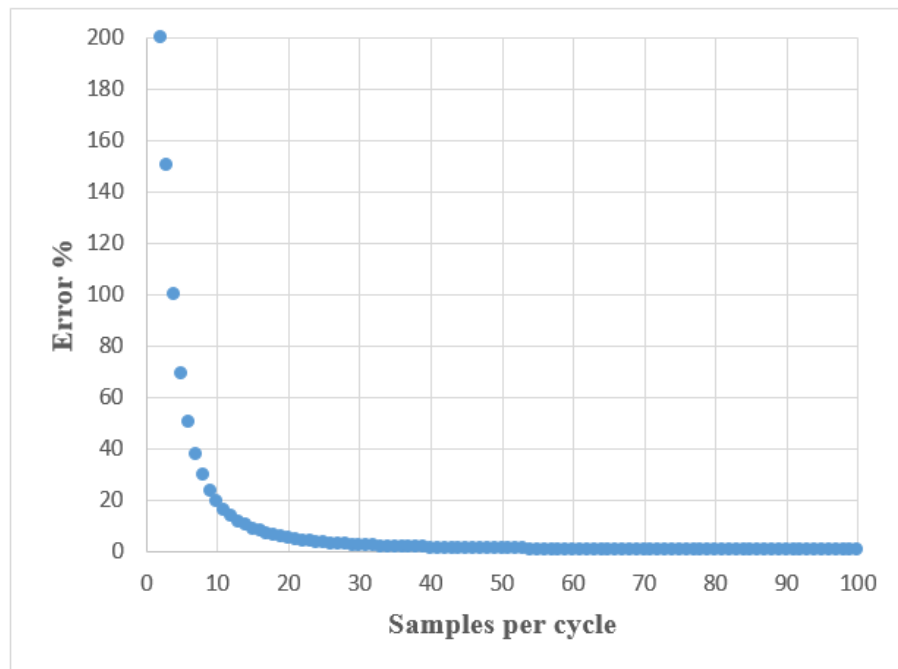


Figure 4.18: Maximum error at numbers of data points from 1 to 100

By using this information, it was calculated that the ideal number of data points per cycle was 50. This was found to be the lowest number of points (rounded up to the nearest ten) that produced a maximum error of less than 1%. The maximum calculated error at a sample rate of 50 samples per second was 0.79%.

4.1.8 *Test control Modes*

There are two main methods of loading fatigue samples. These are displacement control and load control. In displacement control tests, the sample is deflected to a consistent strain level in every cycle. This is a good method of controlling fibre composite fatigue tests because the failure strains of fibres of the same material are more or less consistent, but the strength of individual fibres may vary. However, strain controlled tests are not representative of in-service components, which are almost always subject to loading cycles rather than strain cycles. Therefore load control was chosen as the method of controlling cyclic tests in this thesis.

4.1.9 *Cyclic Flexural Tests*

The procedure for cyclic tests was similar to that of static tests (Section 4.1.5). The fatigue tests described in this section were conducted according to BS EN ISO 13003:2003, and with specimen dimensions dictated in BS EN ISO 14125 (1998+A1:2011). As in static tests, it should be noted that samples in these tests were not necessarily manufactured in the same batch. Generally, samples were manufactured in bulk over several batches cured at separate times and subsequently mixed, so variations between batches are statistically accounted for in the results. 2x15x100mm 0° unidirectional samples were mounted in the four point bending jig in the same manner as in static tests, ensuring as before that the loading rollers contacted the top face of the specimen evenly. PVC insulation tape was also used in cyclic tests to reduce stress concentrations at the loading rollers. Samples were measured using digital Vernier callipers with a manufacturer's quoted accuracy of 0.01mm. Measurements of width and thickness were taken at three points evenly spaced along the length of the specimen and then averaged.

Strict procedures were followed when operating servo-hydraulic equipment in order to ensure operator safety. Failure to adhere to this procedure may have resulted in injury. The MOOG SmarTEST ONE test controller was set to position control mode in order to load the samples. If set to load control, the controller changes the position of the hydraulic actuator to maintain constant load. If there was no sample in the jig to apply an opposing force then the actuator would continue to move at increasing velocity until it made contact with something, or until

it reached its maximum possible position. This presented a significant hazard for the operator, as their hands may be easily crushed.

To avoid damage to the samples or the testing jig, position and load safety limits were set. These limits were set just outside of the extreme limits of the maximum calculated sample load and deflection. If these limits were exceeded then the hydraulic pressure feed to the machine would instantaneously be shut off.

Once in place, a preload of around 10N was placed on the sample to ensure secure contact with the rollers. The mechanical lever arm described in Section 4.1.4 was then set against the bottom face of the sample, and the LVDT set in position, placing spring compression on the opposite side of the arm. The LVDT reading was then set to zero position. The LVDT was held in position by a lightly tightened grub screw which provided enough friction to keep the LVDT in place under normal loading, but allowed it to slip out of position in the event that excessive force was placed on it e.g. when the sample fractured. Finally, the test controller was set to load control mode, and the loading parameters were entered.

The control parameters needed to control cyclic tests in load control were frequency (f), stress ratio (R), and maximum cyclic load (F_{max}).

The ideal test frequency was determined to be 5Hz. This was determined from literature concerning fatigue of composites e.g. [4, 207-211]. 5Hz is commonly used in composite fatigue tests as it is low enough to avoid significant viscous heating of the matrix which may cause a decrease in material stiffness.

The stress ratio is defined as;

$$R = \frac{F_{min}}{F_{max}} \quad 4.2$$

The stress ratio was set at 0.1. Again, this was determined from literature to be the ideal value, and most compressive (as opposed to fully reversed) cyclic tests use this value e.g. [210-213].

F_{max} (otherwise defined in terms of stress as σ_{max}) is the peak cyclic load, and is defined as the calculated breaking force of the specimen multiplied by a factor (referred to in this work as the load or stress factor) between 0 and 1. In these tests, the stress factor was initially set at 0.8 and lowered in subsequent tests until the fatigue limit of the material was reached. The fatigue limit (or endurance limit) is defined as the maximum cyclic load at which the material can be considered to have infinite life (described further in Section 2.3).

F_{max} may be calculated by;

$$F_{max} = \frac{\sigma_f b h^2}{l} \quad 4.3$$

where σ_f is the ultimate flexural strength of the material (determined by static testing), b is the sample width, h is the sample thickness, and l is the span of the sample between the support rollers (81mm).

Loading parameters were set by defining the load amplitude either side of the load setpoint (SP). SP may be defined as;

$$SP = \frac{(F_{max} + F_{min})}{2} \quad 4.4$$

where F_{min} is the minimum cyclic load and is calculated by;

$$F_{min} = R F_{max} \quad 4.5$$

The load amplitude (F_{amp}) may then be defined as;

$$F_{amp} = F_{max} - SP \quad 4.6$$

An illustration of these parameters is shown in Figure 4.19.

Once the load parameters were set, the test was started. Data acquisition was started simultaneously. Load, displacement, and midpoint deflection were recorded. The sample period (described in Section 4.1.6) was different for each stress factor, and was chosen arbitrarily for the first test of each set. The sample period was adjusted accordingly in subsequent tests. This was done because the expected number of cycles to failure was initially unknown. The ideal sample period was determined to be the maximum period which produced 100-2,000 data points by the conclusion of the test. This range was chosen in order to give sufficient data points for analysis whilst avoiding large data files. The number of data samples per recorded cycle was set to 50, as previously reasoned in Section 4.1.6.

Sample temperature was also monitored periodically using an infrared handheld thermometer. BS EN ISO 14125 (1998+A1:2011) dictated that ‘the test frequency shall be chosen to avoid an excessive rise in the specimen temperature through autogenous (self-generated) heating’, but was not specific about what constitutes excessive heating, as this is dependent upon the

specific material being tested. However, dynamic mechanical thermal analysis (DMTA) results presented in Section 3.7.2 showed that the glass transition temperature (T_g) of 977-2 composites was 167°C. A value of 74°C was therefore chosen (mid-way between 20°C and T_g) as the upper limit that any sample should safely reach without detriment to mechanical properties, and therefore compromising the tests.

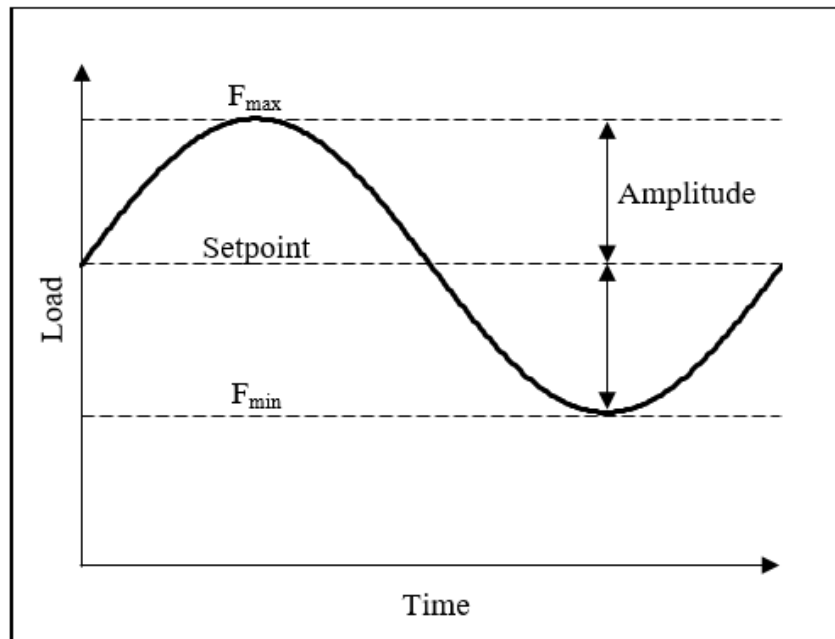


Figure 4.19: Illustration of load parameters used in cyclic tests

The range of stress factors used was defined by a starting value of $0.8\sigma_f$. This was lowered by $0.1\sigma_f$ at a time until the fatigue limit of the samples was reached. A minimum of three samples were tested at each stress factor.

Tests were run until failure or until 1×10^6 cycles, whichever came first. Past 1×10^6 cycles the sample was deemed to have infinite life. Failure was defined as the complete fracture of the sample. The number of cycles to failure and fracture location was noted in cases where samples failed.

In these tests, only two 977-2 composite laminate sample types were tested. These were: unprinted, and printed 10%/wt PMMA in DMF. This was because of the lengthy time investment associated with fatigue tests. Simultaneously performing all tests on all specimen types would have required extensive testing. Initially testing only unprinted and PMMA printed samples enabled the identification of significant material changes with only minimal

time expense. A hexagonal printing pattern of $\delta x, \delta y = 0.4\text{mm}, 0.6\text{mm}$ was used for all printed samples.

4.2 TENSILE TESTING

Following flexural tests, tensile testing (more specifically tension-tension testing) was introduced. Flexural testing was initially chosen because of the strain gradient which is created throughout the sample thickness and which may cause delaminations. Figure 4.1 previously illustrated this. Tensile testing however, does not produce significant strain differences between plies in unidirectional samples. Strain differences must therefore be produced by changes in ply orientation relative to one another. As discussed in Section 2.3.1.3, ply orientation coupled with edge stresses can create conditions in which delaminations may initiate and propagate.

Tensile tests are simple in their setup, requiring only simple sample grips. Sample preparation is also simple since basic tensile tests only require rectangular specimens which may be cut from flat composite panels. They do however, require much greater testing loads than flexural tests due to the high tensile strength of fibre composites. The deflections produced by testing are also smaller, requiring more sensitive measurement and control.

4.2.1 *Stacking Sequence of Tensile Specimens*

The stacking sequence of composites plays a major role in the properties of finished laminates. Because of the anisotropic nature of composite materials, their Poisson's ratio is different in different directions, being highest in the 0° direction (conventionally defined along the fibre axis). This results in interlaminar shear stresses at interfaces between plies of differing orientations. These shear stresses may be reduced by either optimising stacking sequence, reducing Poisson's ratio differences between plies, or by introducing interlaminar layers with lower shear moduli [24]. In these tests, the stacking sequence was designed so that the Poisson's ratio differences between plies were accentuated, promoting delamination so that interlaminar toughening could be investigated.

A stacking sequence was chosen which introduced interlaminar stresses to varying degrees. This was limited by the test standard (BS EN ISO 527-4:1997). This standard limited tensile specimens to 2mm in thickness. For 977-2 prepreg this restricted the number of plies in the laminate samples to eight. To avoid complex laminate stresses, the stacking sequence was

designed to be symmetric about its midplane, as is the case in the vast majority of in-service laminates. The chosen stacking sequence of $[45/0/90/-45]_s$ is illustrated in Figure 4.20.

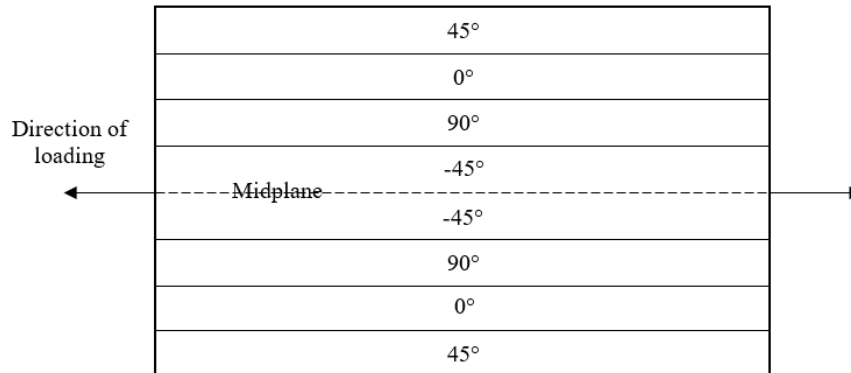


Figure 4.20: Stacking sequence used in tensile tests. Ply orientations are relative to the direction of loading.

A laminate consisting of alternating $0^\circ/90^\circ$ plies (i.e. $[0/90,\dots]_s$) would have resulted in maximum interlaminar stresses, and hence delaminations. However, a laminate was chosen which incorporated varying orientations so that assessment may be made of interlaminar toughening between various contacting orientations. 0° , 45° , and 90° ply orientations were chosen. In the chosen stacking sequence, each of the three ply orientations were adjacent to the other two. i.e. a 90° ply was adjacent to both a 0° and 45° ply etc. An additional benefit of this stacking sequence was that it used only two 0° plies. Composites are strongest when loaded in the direction of their fibres. From the quoted tensile strength of 977-2 laminates [174] it was calculated that the load required to fracture a $[45/0/90/-45]_s$ laminate was approximately 70% lower than a $[0/90/0/90]_s$ laminate of otherwise identical dimensions. Therefore, using this stacking sequence enabled increased flexibility with regards to testing machines.

4.2.2 Sample Deflection Measurement

Because of the high stiffness and therefore low strain to failure of carbon fibre composites, accurate measurement of sample deflections was necessary. In these tests an LVDT was mounted against the bottom machine grip (shown in Figure 4.25) in order to accurately measure grip separation, and hence sample deflection. The LVDT was held in position by a magnetic clamp stand which was attached to the top grip. By measuring between clamping

ends of the machine grips, test frame deflection was effectively eliminated from the measurements.

The machine crosshead displacement was measured internally by an RDP MD5/3000HK LVDT. This LVDT had a 75mm measurement range. The accuracy of LVDTs is generally dependent upon their measurement range. In the case of the machine LVDT, the linearity error was stated by the manufacturer as 0.5%. The external LVDT used to measure sample deflection was an RDP D6/5000A. This also had a quoted linearity error of 0.5%. However, due to its short 5mm measurement range, the resultant measurement error was much lower than that measured by the testing machine's internal LVDT. The internal LVDT was also situated near the bottom of the hydraulic actuator column. It therefore included the deflection of the actuator and test frame. The difference in measurement accuracy is illustrated in Figure 4.22. The external LVDT deflection measurement was therefore used instead of that measured by the internal LVDT in all material property calculations.



Figure 4.21: LVDT setup used to measure grip separation in tensile tests

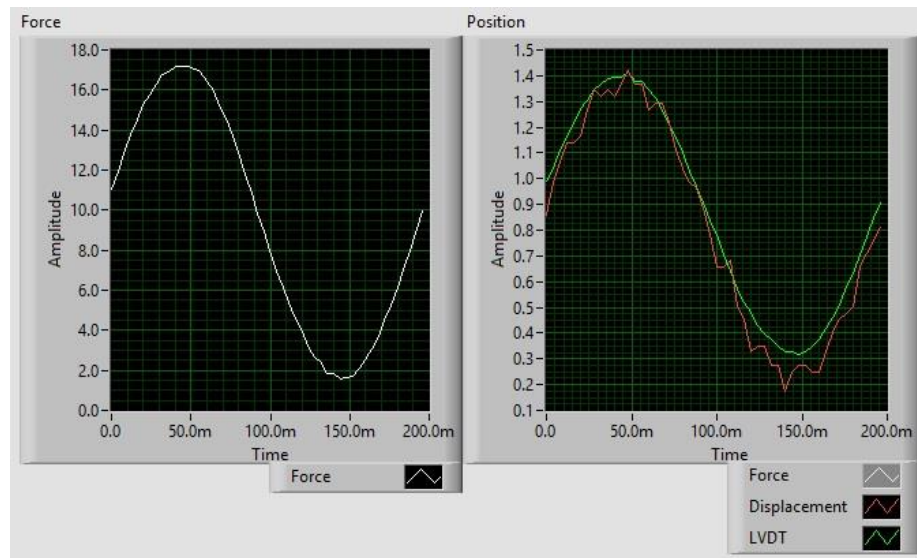


Figure 4.22: Image of DAQ measurements of cyclic data. Data captured by the external LVDT (green) shows considerably more accuracy than the internal machine LVDT (red).

4.2.3 Cellulose Acetate Replica Method

The cellulose acetate replica method described in Section 2.6.2 was used to analyse transverse cracks and delaminations on the outer edges of some tensile fatigue specimens. In the acetate replica technique, a sheet of cellulose acetate is wet with acetone on the surface which will contact the sample. The acetone softens the acetate and also pulls the acetate to the sample surface by surface tension.

Where this method was used, the test was temporarily stopped, and samples were loaded to their peak cyclic load. This allowed cracks to be opened for maximum visibility on the replica. One side of the acetate sheet was wet with several drops of acetone and quickly applied to the sample edge. Very light pressure was applied after application to further force the softened acetate into recesses in the surface. Acetone is highly volatile, and completely evaporated after a few minutes, leaving the acetate dry. It was then carefully peeled off the surface, leaving a negative impression on the acetate. These replicas were then stored in a library system for future reference. This technique was highly advantageous because removing samples from a test may have affected the results. It was also advantageous since the tensile sample dimensions dictated by the testing standard made them physically too big to fit in an SEM chamber for microscopic analysis, whereas replicas could be cut to size as necessary.

As discussed in Section 2.6.2, cellulose acetate is readily available as sheets from numerous microscopy equipment retailers, and is available in varying thicknesses from 10 μ m upwards.

The thickness of the sheet affects the resolution that can be expected. Thinner sheets result in higher resolutions, but provide significantly less workable time compared to thicker sheets because they quickly dissolve. A sheet thickness of 50 μ m was used in all tests where replicas were taken.



Figure 4.23: An acetate replica mounted on a glass microscope slide prepared for SEM observation

4.2.4 Static Tensile Tests

Static tensile tests were used to provide the baseline values for cyclic tests of the same material, as well as to investigate the tensile properties of printed laminates. Tensile tests in this section were conducted according to BS EN ISO 527-4:1997 [187]. 2x25x250mm multidirectional specimens were manufactured from 977-2 unidirectional prepreg using the methods outlined in Section 3.5 and using the stacking sequence detailed in Section 4.2.1. It should be noted that samples in these tests were not necessarily manufactured in the same batch. Generally, samples were manufactured in bulk over several batches cured at separate times and subsequently mixed, so variations between batches are statistically accounted for in the results. The specimen geometry is illustrated in Figure 4.24. All samples were cut from 130x250mm panels using a diamond cutting saw. They were then ground to within 2% of the specified dimensions using a 600 grit sanding wheel or finer. As described in Section 3.5, 50mm glass fibre end tabs were bonded to the samples to aid sample gripping as dictated by BS EN ISO 527-4:1997. Samples were measured using digital Vernier callipers with a manufacturer's quoted accuracy of 0.01mm. Measurements of width and thickness were taken at three points evenly spaced along the length of the samples and then averaged. Gauge length was also measured by taking the average distance between end tabs on both sides of the samples.

Samples were gripped by hydraulic grips as shown in Figure 4.25 to minimise sample slipping. The entire end tab region was gripped, ensuring perpendicularity to the grips. This was achieved by using an engineer’s square set against the grip face and the side of the sample.

Once both ends of the sample were gripped firmly, the LVDT (described in Section 4.2.2) was mounted against the bottom grip (shown in Figure 4.25) in order to accurately measure grip separation, and hence sample deflection. The LVDT was held in position by a magnetic clamp stand which was attached to the top grip.

Five specimens of each sample type were placed under tensile load at a rate of 2mm/min until ultimate failure using a Mayes 100kN servo-hydraulic testing machine controlled by a MOOG modular PC-based test controller. Load, crosshead displacement, and grip separation were recorded in all tests. Samples which fractured within the end tab region were disregarded. The data from these tests was then analysed in order to calculate the ultimate tensile strength (UTS) and tensile modulus of each sample.

In these tests, four 977-2 composite laminate sample types were tested. These were: unprinted, printed 10%/wt PMMA in DMF, printed 10%/wt PEG 1,500M_w in deionised water, and printed 10%/wt PEG 20,000M_w in deionised water. A hexagonal printing pattern of $\delta x, \delta y = 0.4\text{mm}, 0.6\text{mm}$ was used for all printed samples.

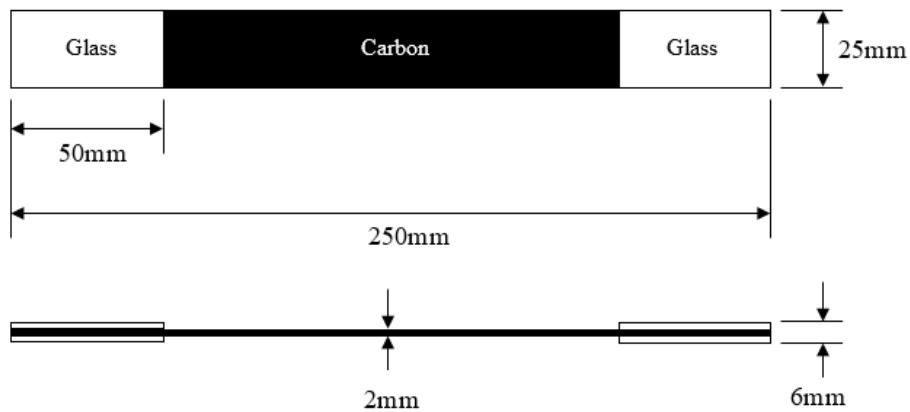


Figure 4.24: Tensile specimen geometry



Figure 4.25: Tensile sample in situ in the Mayes 100kN servo-hydraulic test frame

4.2.5 Cyclic Tensile Tests

The procedure for cyclic tests was similar to that of static tests (Section 4.2.4). The fatigue tests described in this section were conducted according to BS EN ISO 13003:2003, and with specimen dimensions dictated by BS EN ISO 527-4:1997. As in static tests, it should be noted that samples in these tests were not necessarily manufactured in the same batch. Generally, samples were manufactured in bulk over several batches cured at separate times and subsequently mixed, so variations between batches are statistically accounted for in the results. 2x15x250mm multidirectional samples were mounted in the same manner as in static tests, ensuring as before that samples were mounted perpendicular to the grip face. Samples were measured using digital Vernier callipers with a manufacturer's quoted accuracy of 0.01mm. Measurements of width and thickness were taken at three points evenly spaced along the length of the samples and then averaged. Gauge length was also measured by taking the average distance between end tabs on both sides of the samples.

As was the case for flexural fatigue tests (Section 4.1.9), strict procedures were followed when operating servo-hydraulic equipment to ensure operator safety. Failure to adhere to this procedure may have resulted in injury. All operations that did not require hydraulic pressure

were conducted whilst the test machine was inactive. The MOOG test controller was set to position control mode in order to load the samples.

To avoid damage to the samples or the testing jig, position and load safety limits were set. These limits were set just outside of the extreme limits of the maximum calculated sample load and deflection. If these limits were exceeded then the hydraulic pressure feed to the machine would instantaneously be shut off.

A T-type thermocouple was attached to the surface of each sample using high-temperature polyester tape (manufactured by 3M) in order to actively monitor specimen temperature. A twin thermocouple was also attached to a 977-2 multidirectional laminate specimen that was not under load. This specimen was attached to the side of the hydraulic grips so as to be suitably close to the test specimen and therefore provide an accurate reading of atmospheric temperature. This was decided to be a more thorough method of temperature measurement than that used for the previous flexural fatigue tests. Temperature measurements were taken simultaneously with each recorded fatigue cycle. This provided insight into viscous heating within the samples during testing, and helped ensure that excessive temperatures that may have affected material properties were avoided. BS EN ISO 14125 (1998+A1:2011) dictated that ‘the test frequency shall be chosen to avoid an excessive rise in the specimen temperature through autogenous (self-generated) heating’, but was not specific about what constitutes excessive heating, as this is dependent upon the specific material being tested. However, dynamic mechanical thermal analysis (DMTA) results presented in Section 3.7.2 showed that the glass transition temperature (T_g) of 977-2 composites was 167°C. A value of 74°C was therefore chosen (mid-way between 20°C and T_g) as the upper limit that any sample should safely reach without detriment to mechanical properties and therefore compromising the tests.

Once in place, the load upon the sample was set to zero. The LVDT was then set in position contacting the bottom grip as in Section 4.2.4. Finally, the test controller was set to load control mode, and the loading parameters were entered. A cyclic frequency of 5Hz and stress ratio of 0.1 was used in all tests. The justification for these values was previously discussed in Section 4.1.9.

Once the load parameters were set, the test was started. Data acquisition was started simultaneously. Load, displacement, grip separation, sample temperature, and atmospheric temperature were recorded. The sample period (described in Section 4.1.6) was different for each stress factor, and was chosen arbitrarily for the first test of each set. The sample period was then adjusted accordingly in subsequent tests. This was done because the expected number of cycles to failure was initially unknown. The ideal sample period was determined to be the maximum period which produced 100-2,000 data points by the conclusion of the test.

This range was chosen in order to give sufficient data points for analysis whilst avoiding large data files. The number of data samples per recorded cycle was set to 50 as previously reasoned in Section 4.1.6.

The range of stress factors used was defined by a starting value of $0.9\sigma_f$. This was lowered by $0.1\sigma_f$ at a time until the fatigue limit of the samples was reached. A minimum of three samples were tested at each stress factor.

Tests were run until failure or until 1×10^6 cycles, whichever came first. Past 1×10^6 cycles the sample was deemed to have infinite life. Failure was defined as the complete fracture of the sample. The number of cycles to failure was noted in cases where samples failed.

In initial tensile fatigue tests, only two 977-2 composite laminate sample types were tested. These were: unprinted, and printed 10%/wt PMMA in DMF. A hexagonal printing pattern of $\delta x, \delta y = 0.4\text{mm}, 0.6\text{mm}$ was used for all printed samples. Only two laminate types were initially used because of the lengthy time investment associated with fatigue tests. Simultaneously performing all tests on all specimen types would have required extensive testing. Initially testing only unprinted and PMMA printed samples enabled the identification of significant material changes with only minimal time expense. Once significant mechanical changes were identified, PEG polymers were introduced to focus specifically on those areas.

4.2.6 Cyclic Tensile Tests at $0.5\sigma_t$

Following initial tensile fatigue tests, areas were identified which warranted further investigation. Specifically, it was shown that differently printed composites exhibited different stiffness degradations in the initial 100k-200k cycles of $0.5\sigma_t$ tests. The cyclic tensile tests introduced in Section 4.2.5 were therefore extended to focus on these areas.

The experimental setup was identical to that described in Section 4.2.5. These tests differed in that samples were exclusively run at a stress factor of 0.5. The laminate types tested were: unprinted, printed 10%/wt PMMA in DMF, printed 10%/wt PEG 1,500 M_w in deionised water, printed 10%/wt PEG 20,000 M_w in deionised water. A hexagonal printing pattern of $\delta x, \delta y = 0.4\text{mm}, 0.6\text{mm}$ was used for all printed samples.

Samples were cycled for at least 100k cycles, although testing was not necessarily stopped at this value. Tests were only stopped when it was necessary to begin testing the next sample.

In these tests the acetate replica method outlined in Section 4.2.3 was utilised. These replicas were used to provide insight into transverse cracking and delamination growth in these tests. Replicas were taken at 0, 5k, 10k, 20k, 40k, 60k, 80k, and 100k cycles on both free edges of

the samples. Records were kept of which edge the replicas were taken from, the number of cycles, and the specimen number.

CHAPTER 5: MECHANICAL TEST RESULTS

This chapter outlines the experimental results that were produced as a result of both static and cyclic tests upon inkjet printed composites. The results of tests are presented in their relevant sections, and are then discussed in detail at the end of this chapter.

5.1 STATIC FLEXURAL TESTS

Static four point bend tests were conducted on unidirectional 977-2 CFRP laminates in order to establish the flexural strength and modulus of the material in both unprinted and printed (10%/wt PMMA in DMF) varieties. These values were used to provide the basis for future fatigue testing of the material. Tests were conducted as described in Section 4.1.5.

It was previously discussed in Sections 4.1.1 and 4.1.5 that modifications were made to the four point bending jig used to conduct the tests in this section, and also to the testing procedure itself by the addition of electrical insulation tape at sample support points. These changes were implemented iteratively due to the poor initial flexural fatigue results presented later in Section 5.2. It can be seen from Table 5.1 that the final changes made to the experimental setup increased the measured flexural strength of laminates by a total of 57%. It will also be demonstrated later in Section 5.2.1 that experimental data scatter was greatly reduced as a result, giving greater confidence in the results obtained from flexural tests.

Table 5.1: Effect of experimental procedure changes upon the static flexural strength of unprinted 977-2 unidirectional laminates in static four point bending

Test Parameter Change	Average Flexural Strength, σ_f (MPa)	Cumulative Increase
None	1420	-
Electrical insulation tape at support points	1950	37%
Modified jig design	2226	57%

After the test procedure and setup was finalised, it appeared that reliable static flexural data was obtained. Figure 5.1 shows the average of the stress-strain curves obtained for static tests conducted with all procedure changes in place. As is typical of flexural tests, the curves were

initially linear, but the gradient decreased as load was increased. The jagged shape of the curves before failure was indicative of weak fibres fracturing.

Flexural strain, ϵ_f was calculated by;

$$\epsilon_f = \frac{4.7sh}{L^2} \quad 5.1$$

where s is the midpoint deflection of the sample, h is the sample thickness, L is the support span of the sample (81mm).

Flexural strength, σ_f , of the samples was calculated by;

$$\sigma_f = \frac{FL}{bh^2} \quad 5.2$$

where F is the maximum load, L is the support span of the sample (81mm), b is the sample width, and h is sample thickness.

It may also be noted that the gradient, and hence flexural modulus, of both sample types was identical for the majority of the tests, deviating only in the final portion of the tests as critical damage began to develop.

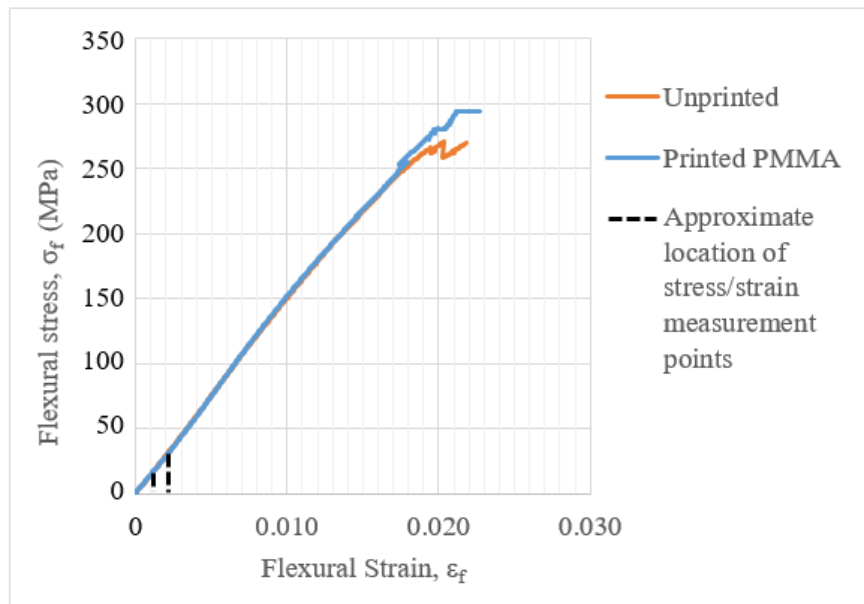


Figure 5.1: Averaged load-displacement curves for static flexural tests of unprinted and PMMA printed laminates. The points at which the gradient was calculated are marked on the plot. The location of these points varied slightly depending upon the strain at which the individual samples fractured. The limited range of these points stems from a misunderstanding in the requirements of the test standard.

Table 5.2 shows the numerical values of flexural modulus (E_f) and ultimate flexural strength (σ_f) obtained in the tests.

The flexural modulus of samples was calculated by;

$$E_f = \frac{0.21L^3}{bh^3} \left(\frac{\Delta F}{\Delta s} \right) \quad 5.3$$

where ΔF is the difference in load between values of $\varepsilon_f'=0.5\%$ and $\varepsilon_f''=2.5\%$ (where ε_f is flexural strain), and Δs is the difference in midpoint deflection between values of $\varepsilon_f'=0.5\%$ and $\varepsilon_f''=2.5\%$. These values were dictated by the test standard. The test standard intends for the modulus to be calculated between 0.5-2.5% strain units. However, the meaning of the test standard was misinterpreted. It was thought that the modulus was to be calculated between values measured at 0.5% and 2.5% of the strain at fracture of the specimen. This was deemed to be very low, so ΔF and Δs were instead measured between values taken at 5% and 10% of the strain at fracture. These points are marked in Figure 5.1 for visual representation. This range was significantly lower than that which was intended by the test standard. However, this mistake was only realised late into the work. Therefore the flexural modulus values carried forward were calculated using this incorrect method. However, the values were recalculated using the dictated method and were found to be in very good agreement with those calculated using the incorrect method. Therefore no further action was taken to correct this mistake.

E_f was very similar for both laminate types, with printed laminates showing a decrease of 0.5% over unprinted laminates, and being well within one standard deviation of one another. This would be expected, as flexural modulus is heavily dictated by fibre and fibre/matrix interface properties, which are unchanged by the printing process.

The ultimate flexural strength of both laminate types differed somewhat, with PMMA printed laminates being on average 2.9% higher than unprinted laminates. It is unclear though if this was a result of the printing process, as σ_f of the PMMA printed laminates lay just within one standard deviation of σ_f of unprinted laminates.

Table 5.2: Results of static flexural testing on unidirectional 977-2 laminates

	Unprinted		PMMA Printed	
	Flexural Modulus (GPa)	Flexural Strength (MPa)	Flexural Modulus (GPa)	Flexural Strength (MPa)
Values	104.8	2163.4	98.3	2186.5
	105.5	2223.8	102.2	2272.2
	105.2	2223.8	112.7	2479.0
	111.1	2262.7	104.9	2278.8
	105.0	2259.8	103.5	2239.2
Average	106.3	2226.7	105.8	2291.2
Standard Deviation	2.4	35.8	4.7	99.5

5.2 CYCLIC FLEXURAL TESTS

Cyclic flexural tests were carried out as described in Section 4.1.9. These tests aimed to assess how the fatigue life of 977-2 laminates were affected by the presence of interlaminar inkjet printed polymer droplets.

5.2.1 Fatigue Life

Cyclic tests were firstly conducted using the initial four point bend jig design outlined in Section 4.1.1, i.e. the unmodified jig, which did not facilitate even load distribution at the loading rollers. The fatigue lives of unprinted and PMMA printed samples at stress factors from 0.8-0.6 (terms explained in Section 4.1.9) are shown in Figure 5.2. The results are given in the form of a fatigue life (or S-N or Wöhler) diagram. In this diagram, ●→ or □→ indicate a sample which did not break after 1×10^6 cycles. ■→ indicates overlap of the sample types. The x axis is a logarithmic scale of the number of fatigue cycles (N).

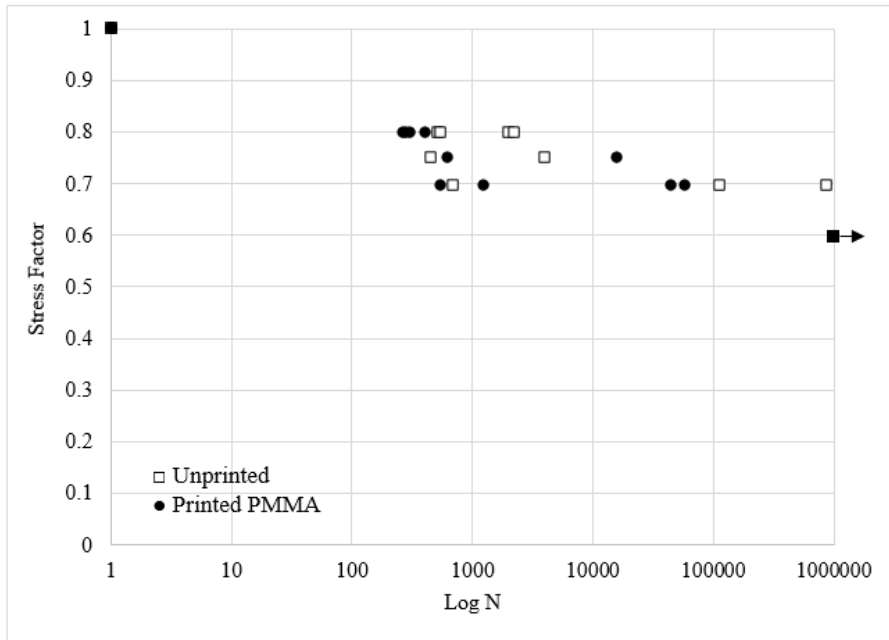


Figure 5.2: Fatigue life diagram of 977-2 laminates under cyclic flexural loading before the introduction of four point bending jig modifications: $R=0.1$, $f=5\text{Hz}$. $\blacksquare \rightarrow$ indicates overlap of printed and unprinted sample types which did not fracture at 1×10^6 cycles.

It was seen that the data points for both sample types became increasingly scattered as the stress factor was lowered. This scatter of unprinted samples was observed at a stress factor of 0.7 to range from 864 cycles to 864633 cycles; a factor of almost exactly one thousand times. Similarly, the range of printed samples at this level was 548 cycles to 43552 cycles; a factor of nearly one hundred times. The cause of this scatter was deemed to be uneven load distribution at the loading rollers. It is widely accepted that fatigue tests may produce results that span orders of magnitude [214], but the results of these tests were considered unacceptable due to the obvious relationship between data scatter and stress factor. Therefore, the jig modifications outlined in Section 4.1.1 were implemented, and tests were repeated.

Due to the scatter of these results, there was little that could reliably be interpreted from them, except that there appeared to be little difference between the fatigue lives of the virgin and printed composites at this point.

Figure 5.3 shows the fatigue life diagram of unprinted and PMMA printed flexural samples after the introduction of the jig modifications. The procedure for these tests remained the same as in the previous tests. By comparison between these results and those shown in Figure 5.2, it was observed that the scatter of the latter data was greatly reduced, ranging over a single order of magnitude rather than three.

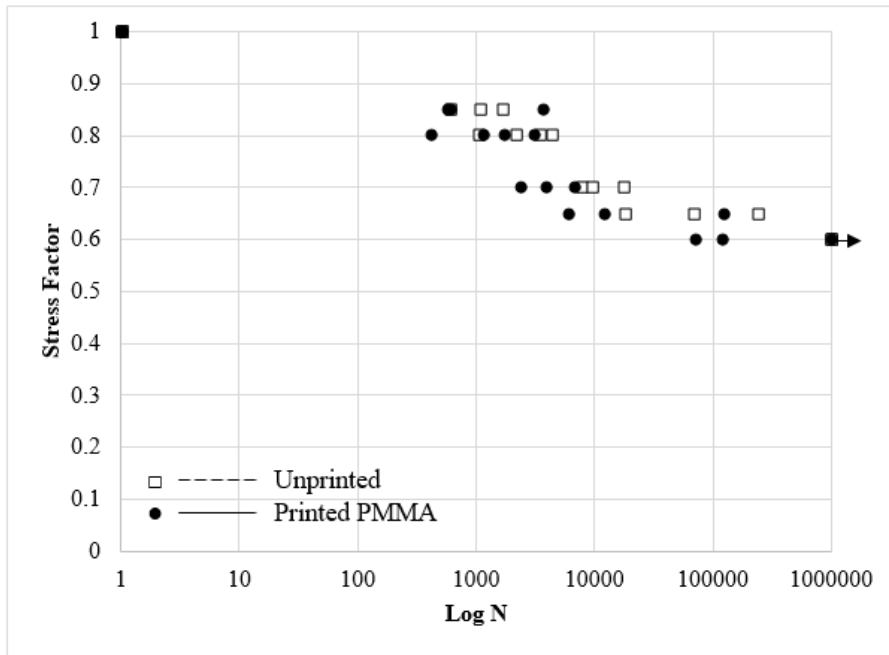


Figure 5.3: Fatigue life diagram of 977-2 laminates under cyclic flexural loading after the introduction of four point bending jig modifications: R=0.1, f=5Hz. ■→ indicates overlap of printed and unprinted sample types which did not fracture at 1×10^6 cycles.

The fatigue life diagram shown in Figure 5.3 shows the fatigue lives of unprinted and PMMA printed samples at varying stress factors. It was seen that the fatigue lives of unprinted composites were generally greater than those of PMMA printed composites. Additionally, unprinted composites reached their fatigue limit at a stress factor of 0.6 (term explained in Section 4.1.9). At this level, printed samples (on average) did not, with only one printed sample reaching 1×10^6 cycles.

5.2.2 Stiffness Degradation

As part of the fatigue tests conducted in this project, the flexural modulus (referred to as stiffness) of the materials were recorded over the course of the tests. This was achieved by the periodic sampling of cyclic data as described in Section 4.1.6. The stiffness data was then analysed in order to observe trends that may give insight into the dominant damage mechanisms at various points during the tests. The flexural modulus of the samples in four point bending was calculated from;

$$E_f = \frac{0.21L^3}{bh^3} \left(\frac{\Delta F}{\Delta S} \right) \quad 5.4$$

where E_f is the flexural modulus of elasticity, L is the support span of the specimen, b is the specimen width, h is the specimen thickness, ΔF is the maximum force (F_{\max}) of the observed loading cycle, and Δs is the midpoint deflection corresponding to F_{\max} . It should be noted that the modulus recorded is the dynamic flexural modulus, since it was recorded under dynamic conditions.

It is typical when analysing stiffness degradation to convert the obtained modulus to a normalised modulus (E_{norm}) by;

$$E_{norm} = \frac{E}{E_0} \quad 5.5$$

where E is the measured modulus, and E_0 is the initial modulus. This allows the direct comparison of results. Because the initial moduli of samples in static tests differed, it was deemed appropriate to keep the data in its measured format to indicate the varied initial moduli. All plots are also accompanied by normalised plots of the same data, in keeping with standard practices.

Figure 5.4 to Figure 5.8 are plots of the change of flexural modulus (stiffness) with respect to the number of fatigue cycles at different stress factors. It is important to note that all figures showing stiffness degradation in this section were manipulated by the use of a moving average function to halve the number of data points shown for each curve. The accuracy of the data remains, but fewer data points are shown. This was done to increase the visibility of each data set for the reader.

Firstly, it may be noted that the recorded values of flexural modulus were significantly higher than those recorded during static tests. In static testing the moduli of unprinted and PMMA printed samples were 106.3MPa and 105.8MPa respectively. In cyclic tests, values were typically around 120MPa to 140MPa. This disparity is typical between static and dynamic structures though [215, 216].

Observation of Figure 5.4, Figure 5.5, and Figure 5.6 revealed that little or no stiffness reduction was recorded in in most cases. Although at high stress factors, low stiffness degradation may be expected since fibre fractures may be considered to be the dominant damage mechanism. Samples with a stress factor of 0.85 (Figure 5.4) exhibited slight stiffness increases over their courses, which may be attributed to the initial alignment of fibres under loading. However, such stiffness increases were not observed in samples tested at a stress factor of 0.8 (Figure 5.5), with stiffness remaining approximately constant until final failure. At a stress factor of 0.7 (Figure 5.6), this trend of decreasing gradient was further observed, with samples exhibiting slight negative gradients until failure. These trends were indicative of

increasing levels of damage mechanisms which lower stiffness, such as delaminations or matrix cracks. Sudden fibre failures would result in much greater stiffness degradation over a shorter period. It was also at this stress factor that delaminations were first observed in samples (see Figure 5.9).

Because of the observed trend of gradient decreases with lowered stress factor, it would be presumed that this would continue further as stress factor was decreased yet further. However, at stress factors of 0.65 and 0.6 (Figure 5.7 and Figure 5.8), trends became more difficult to assess. At a stress factor of 0.65 (Figure 5.7), samples Unprinted 3 and PMMA 2 exhibited this expected gradient decrease. But this was not observed in any other samples in that data set. In these samples, large stiffness reductions were observed immediately prior to sample failure. It is likely that such stiffness reductions were present in higher stress factor tests, but they occurred much more rapidly, and data acquisition periods were simply too low to observe them.

At a stress factor of 0.6 (Figure 5.8), interpretation became problematic. Samples PMMA 1 and PMMA 2 produced similar traces to those discussed above, but others appeared vastly different, exhibiting constant gradients in some cases, and periodic step changes in others.

At this point the applicability of this method of analysis was questioned. It is at low stress factors that delaminations may be expected to be a dominant damage mechanism due to the progressive accumulation of cracks and delaminations. The inability of this test method to achieve reliable and repeatable stiffness measurements at low stress factors was a key factor in the choice to explore tensile tests as an alternative method of testing.

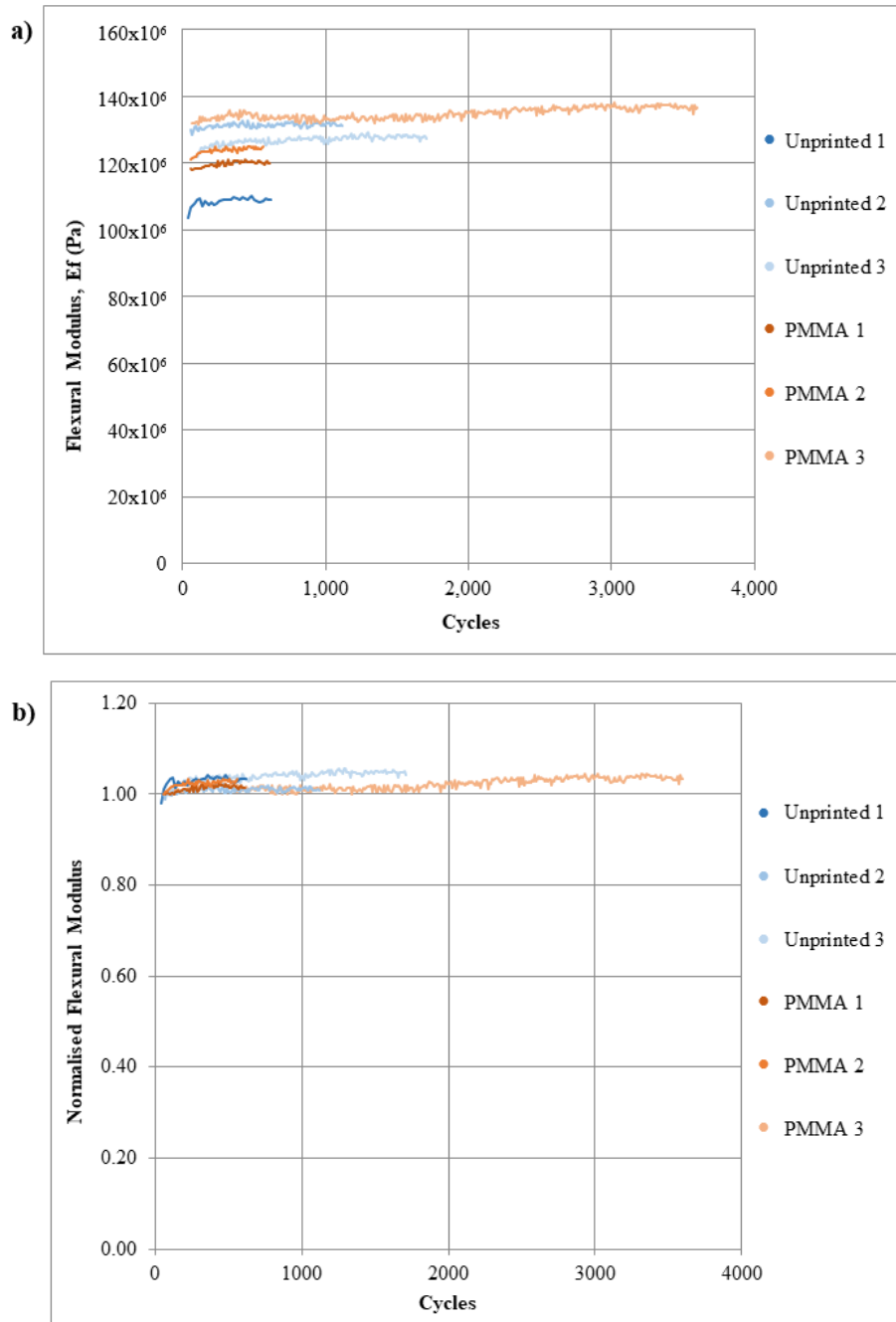


Figure 5.4: a) Flexural modulus of samples in cyclic flexural loading at a stress factor of 0.85. b) Normalised flexural modulus of samples in cyclic flexural loading at a stress factor of 0.85.

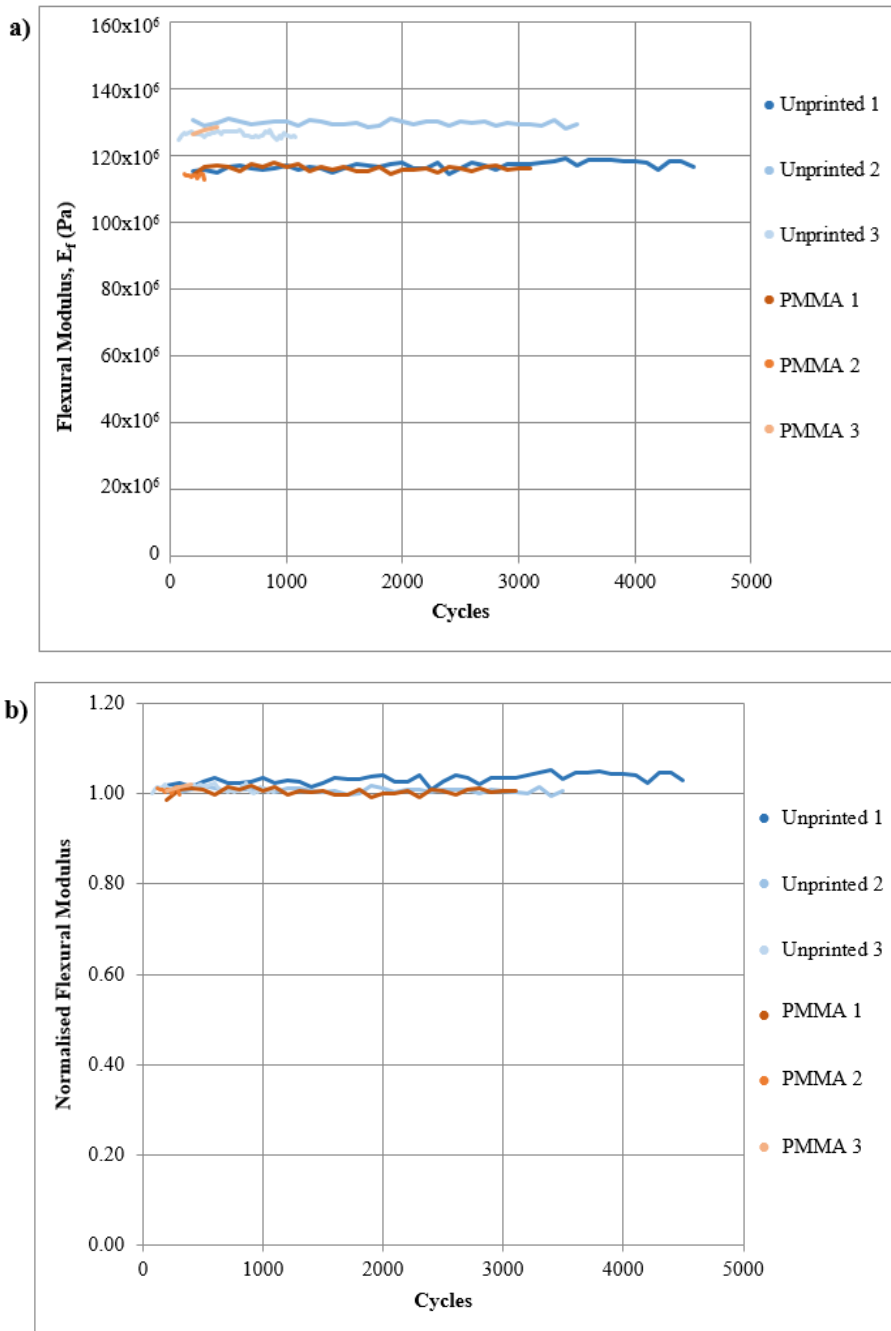


Figure 5.5: a) Flexural modulus of samples in cyclic flexural loading at a stress factor of 0.8. b) Normalised flexural modulus of samples in cyclic flexural loading at a stress factor of 0.8.

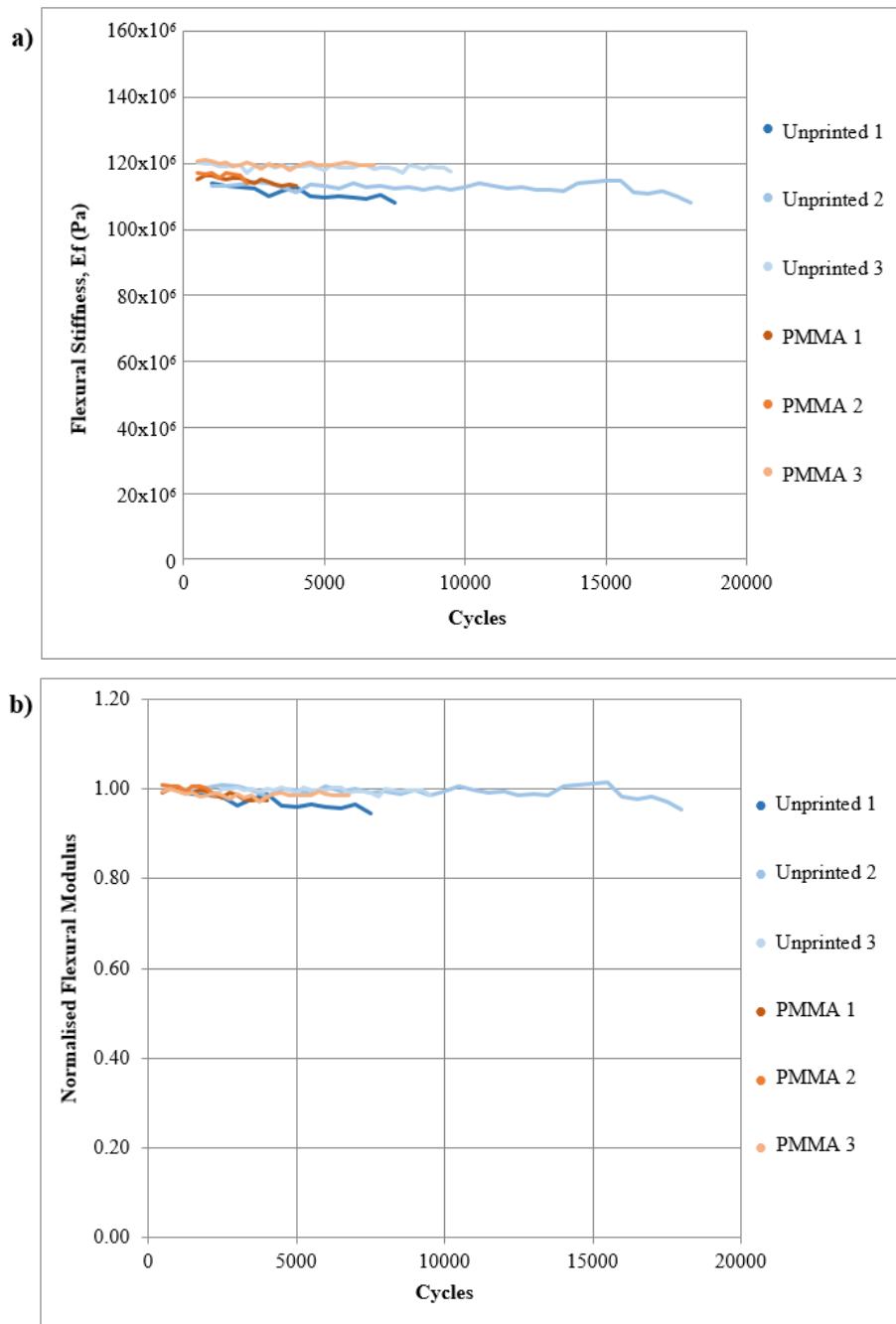


Figure 5.6: a) Flexural modulus of samples in cyclic flexural loading at a stress factor of 0.7. b) Normalised flexural modulus of samples in cyclic flexural loading at a stress factor of 0.7.

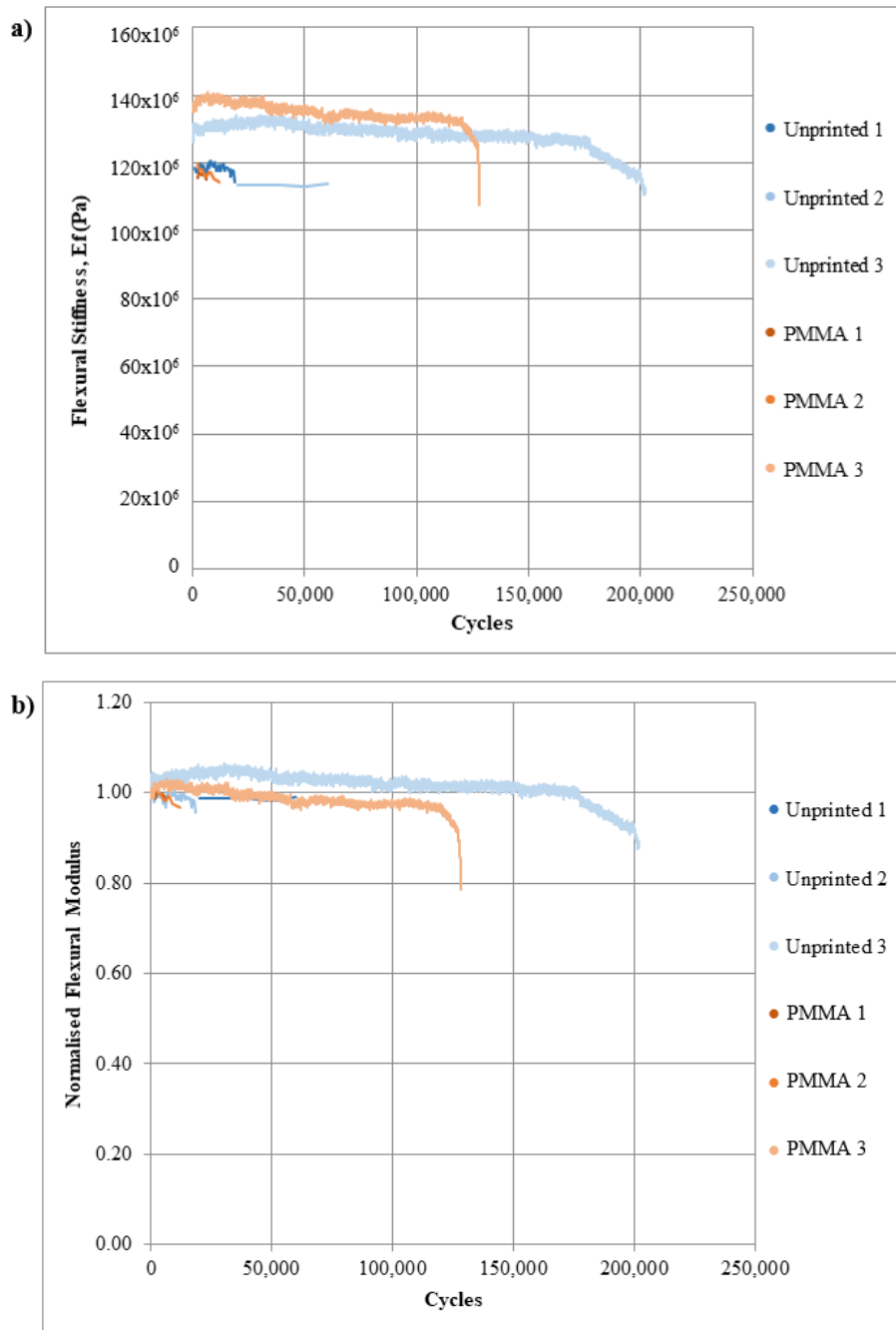


Figure 5.7: a) Flexural modulus of samples in cyclic flexural loading at a stress factor of 0.65. b) Normalised flexural modulus of samples in cyclic flexural loading at a stress factor of 0.65.

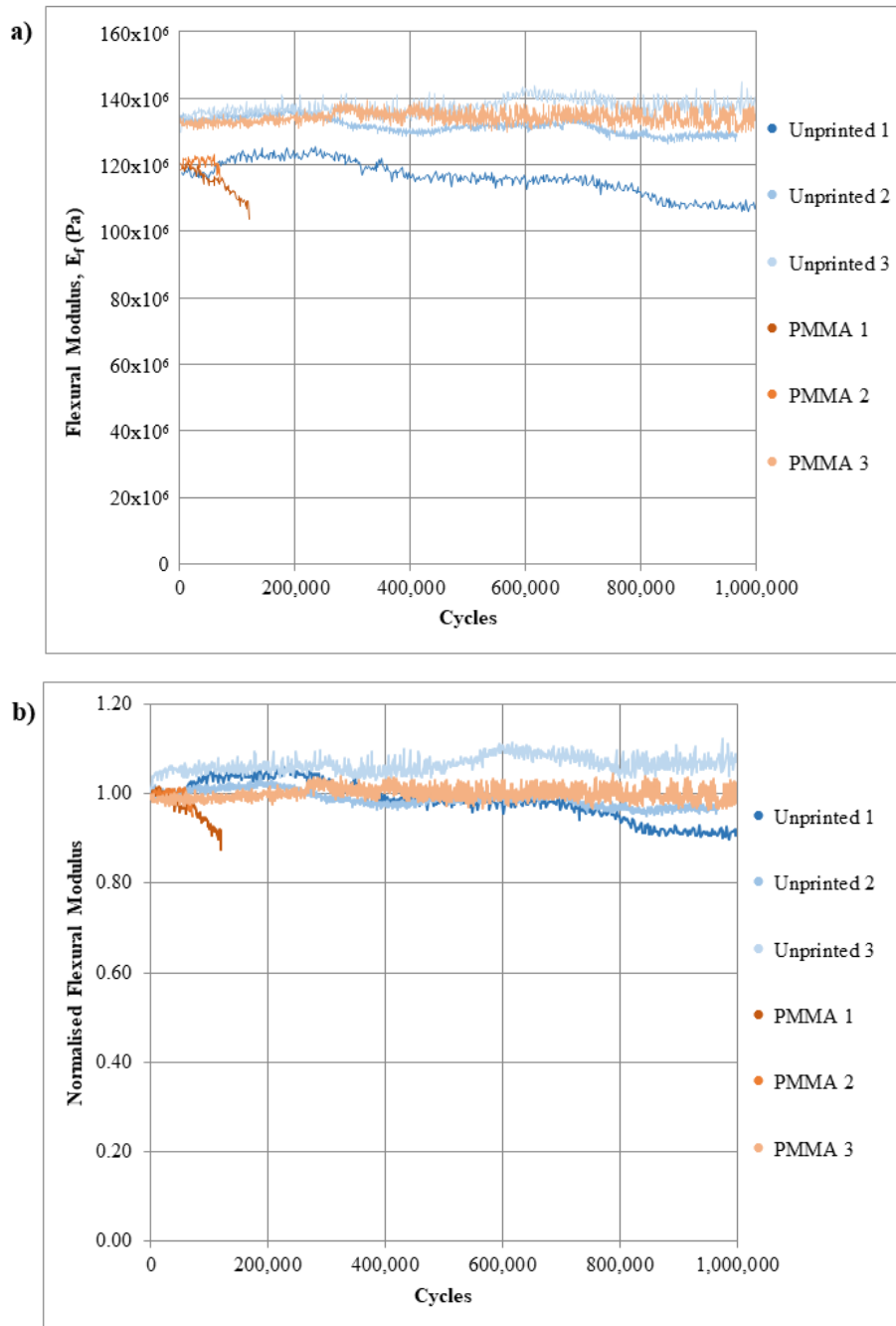


Figure 5.8: a) Flexural modulus of samples in cyclic flexural loading at a stress factor of 0.6.
 b) Normalised flexural modulus of samples in cyclic flexural loading at a stress factor of 0.6.

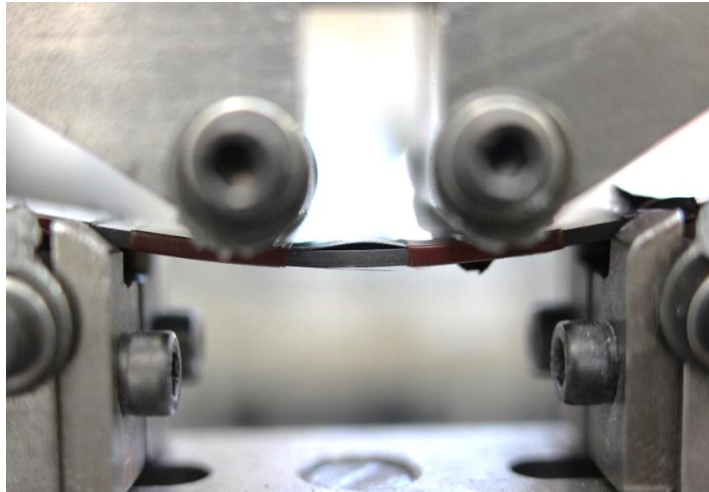


Figure 5.9: Delamination observed in an unprinted flexural sample under cyclic loading at a stress factor of 0.7

5.2.3 Evaluation of the Test Method

From the results presented in the previous section, it became apparent that although four point bending had practical advantages, it was not necessarily sensitive to the subtle changes made by the extremely low amounts of polymers added to composites by inkjet printing. Another factor in deciding this was the analysis of fractured samples.

Figure 5.10 shows fractured fatigue samples over the whole range of stress factors. It was immediately noticeable that all of the samples failed at the loading rollers. As was shown in Figure 4.2 (Section 4.1) shear stress is equal between the rollers, but will be marginally higher at the loading points because the compressive stress there will create a region of higher stress. It was at these points that all samples failed.

Fracture at the loading points would be acceptable (and expected) if it were a result of the global degradation of material properties. However, Figure 5.11 shows an SEM micrograph of an incomplete crack (viewed from the sample edge) originating from the load application point, and propagating through the thickness of the sample (from the left of the image to the right). This crack occurred as a result of compressive stresses on the upper surface of the sample caused by stress concentrations from the loading roller. Furthermore, Figure 5.12 shows the fracture surface of a similar sample which fractured at one of the load application points in cyclic loading. A compressive fatigue crack grew from the load application point, and extended through the thickness of the specimen until the remaining surface area fractured in a tensile manner. The SEM micrograph clearly shows the two different types of fracture

surface, with the smoother fatigue surface on the right side, and the rougher tensile fracture surface on the left.

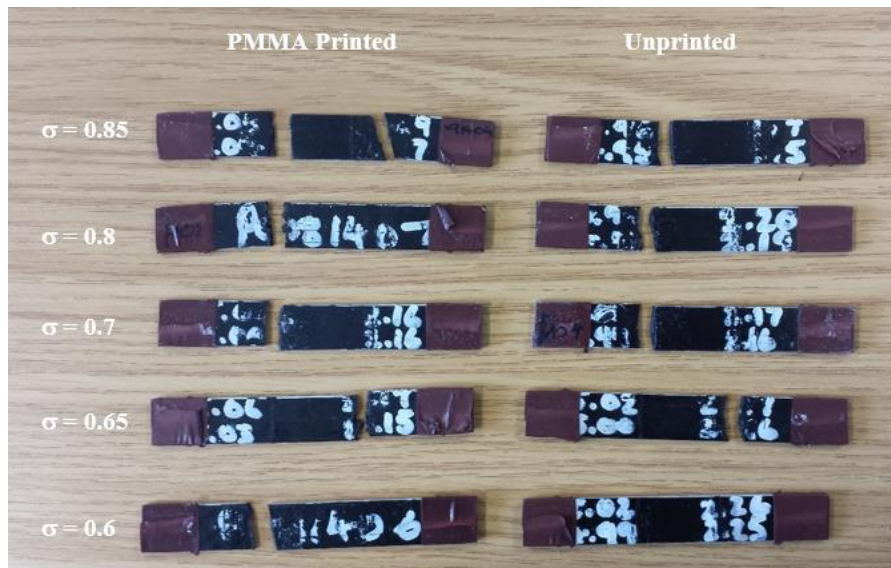


Figure 5.10: Randomly selected samples of ranging stress factors that failed in cyclic loading. In all cases, fracture occurred at the loading points.

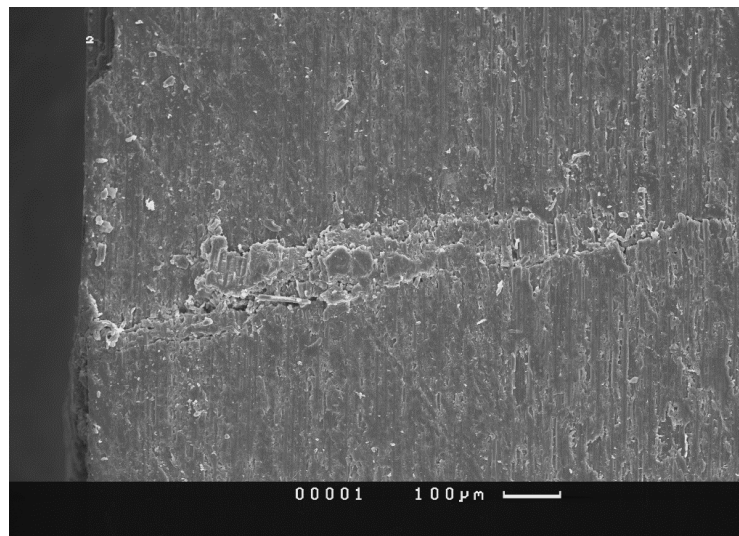


Figure 5.11: SEM micrograph of an incomplete fatigue crack extending through the thickness of a flexural sample. The crack originated on the left of the image, propagating inwards to the right of the image.

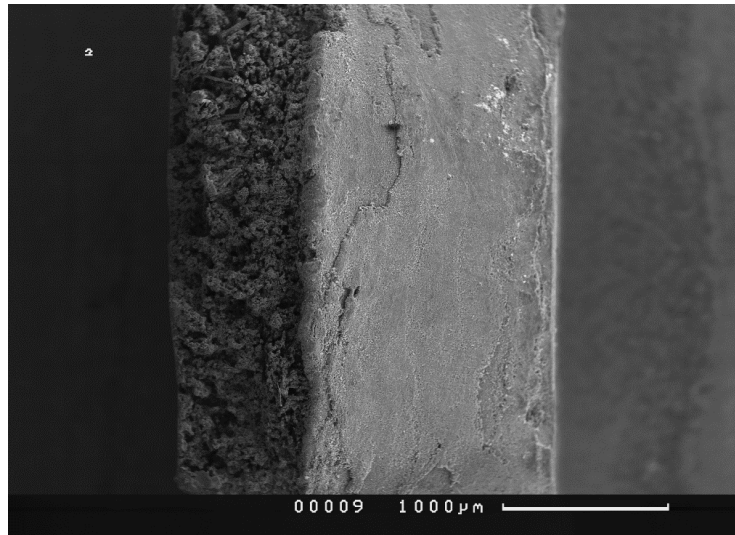


Figure 5.12: SEM micrograph of the fracture surface of a flexural sample. Fracture was through the thickness of the sample, and showed two distinct regions. On the left, tensile fracture. And on the right, a fatigue crack surface.

5.2.3.1 *Concluding Remarks Regarding the Test Method*

On assessment of these images and the results of stiffness degradation measurements, it became clear that despite vastly improving the accuracy of the flexural testing procedure by development of both the testing jig and procedural techniques, stress concentrations were still playing an overwhelming role in the failure of samples. This was judged to be unacceptable. Re-evaluating the test procedure once again may have led to improved results. However, it was decided that changing the test method to a tensile regime was a less risky strategy. It would also provide broader insight into the mechanical behaviour of inkjet printed composites by extending investigations into tensile loading scenarios. These tests were far from fruitless though. They provided invaluable test data, baseline values, and experimental techniques that were carried forward when developing the tensile testing regime, and helped attain much more meaningful and repeatable data.

5.3 STATIC TENSILE TESTS

Tensile testing (more specifically tension-tension testing) was determined to be the best alternative method of testing printed composites. Tensile tests are simple in their setup, requiring only simple sample grips. Sample preparation is also simple since basic tensile tests only require rectangular specimens which may be cut from flat composite panels. They do however, require much greater testing loads than flexural tests due to the high tensile strength

of fibre composites. The deflections produced by testing are also smaller, requiring more sensitive measurement and control.

Static tensile tests were conducted on multidirectional (containing laminae of varying orientations) 977-2 CFRP laminates in order to establish the tensile strength and modulus of the material in both unprinted and printed varieties. These values were used to provide the basis for future fatigue testing of the material. Tests were conducted as described in Section 4.2.4.

Figure 5.13 shows typical stress-strain curves for these tests. These are representative samples taken from each sample type, and were chosen for this representation because their mechanical properties were closest to the average values for their particular sample type.

Tensile stress, σ_t , was calculated by;

$$\sigma_t = \frac{F}{A} \quad 5.6$$

where F is load, and A is the cross-sectional area of the specimen.

Tensile strain, ε_t , was calculated by;

$$\varepsilon_t = \frac{\Delta x}{x} \quad 5.7$$

where x is the gauge length, and Δx is the change in gauge length. As with flexural tests, stress/strain measurements were taken at points between values measured at 5% and 10% of the strain at fracture of the specimens. These points are marked in Figure 5.1 for visual representation. This range was significantly lower than that which was intended by the test standard. However, this mistake was only realised late into the work. Therefore the tensile modulus values carried forward were calculated using this incorrect method. However, the values were recalculated using the dictated method and were found to be in very good agreement with those calculated using the incorrect method. Therefore no further action was taken to correct this mistake.

Tensile modulus, E_t , was calculated by;

$$E_t = \frac{\sigma_t}{\varepsilon_t} = \frac{Fx}{A\Delta x} \quad 5.8$$

It was noticeable that these curves were not perfectly linear. 0° unidirectional laminates produce linear stress-strain curves due to their excellent linear strain response. However, the laminates tested here were multidirectional laminates, and their off-axis plies contributed highly to this curvature. This curvature was advantageous in these circumstances though, as it was indicative that interlaminar shear strains were being induced, and these may promote the development of delaminations.

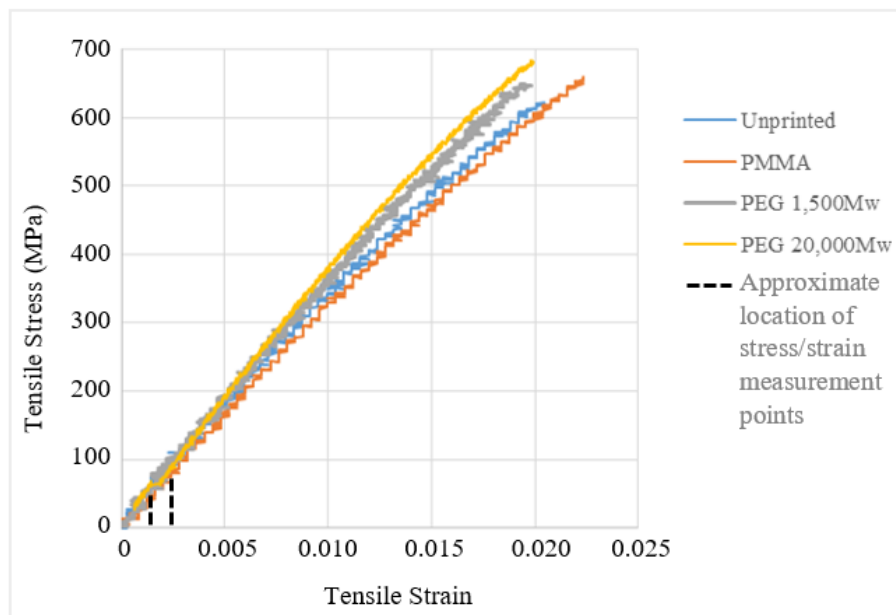


Figure 5.13: Typical stress/strain curves for multidirectional 977-2 tensile test specimens. The points at which the gradient was calculated are marked on the plot. The location of these points varied slightly depending upon the strain at which the individual samples fractured. The limited range of these points stems from a misunderstanding in the requirements of the test standard.

Table 5.3 shows the numerical results of tensile tests conducted on multidirectional laminates. These results are visually represented in Figure 5.14 and Figure 5.15. These results showed that the tensile strengths of these printed laminates were 5.5%, 3.8%, and 4.9% higher than unprinted laminates in the cases of printed PMMA, PEG 1,500M_w, and PEG 20,000M_w inks respectively. There was no overlap of these values within one standard deviation, indicating that printed laminates were in fact stronger than unprinted ones. In the case of PMMA printed laminates, flexural test data presented in Section 5.1 previously suggested that the flexural strength of laminates was increased by 2.9%. Although this was unverifiable due to overlaps in the standard deviation of the results. Those results then, appear to agree with those shown here. It is reasonable that a more significant increase was observed in tensile tests, as the

mechanical properties of laminates containing off-axis plies are less dominated by fibre properties and more dependent upon interlaminar properties. These values represented a significant increase in strength considering the negligible mass of polymer added to the laminates each case.

Similarly, significant increases were observed in the tensile moduli of PEG 1,500M_w, and PEG 20,000M_w printed samples, showing increases of 7.3% and 10.2% respectively. However, this was contrasted by printed PMMA samples which showed a 2.9% decrease in tensile modulus. Again, results from Section 5.1 showed a 0.5% decrease in the flexural modulus of printed PMMA samples. And again, this further reduction may be explained by considering the less fibre-dominated nature of multidirectional tensile laminates. All of the tensile modulus values obtained in these tests lay outside of one standard deviation of unprinted values, indicating a good degree of confidence in these results.

Table 5.3: Results of static tensile testing on multidirectional 977-2 laminates

	Unprinted		PMMA		PEG 1,500M _w		PEG 20,000M _w	
	E _t (GPa)	σ _t (MPa)	E _t (GPa)	σ _t (MPa)	E _t (GPa)	σ _t (MPa)	E _t (GPa)	σ _t (MPa)
Values	31.1	609	30.7	696	33.7	650	32.9	662
	30.2	601	30.3	650	33.9	654	33.0	668
	31.6	674	28.4	665	33.9	668	34.5	683
	30.5	622	30.0	652	34.0	665	38.4	642
	34.2	660	33.6	678	33.6	649	35.0	664
Average	31.5	633	30.6	668	33.8	657	34.7	664
Standard Deviation	0.3	11.0	0.3	3.4	0.3	1.5	0.4	2.6

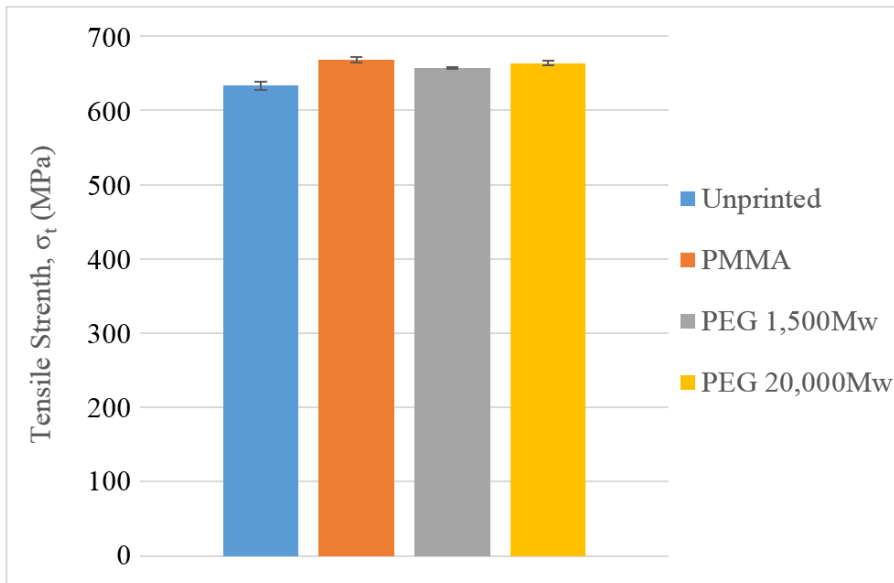


Figure 5.14: Tensile strengths of multidirectional 977-2 laminates. Error bars indicate standard deviation.

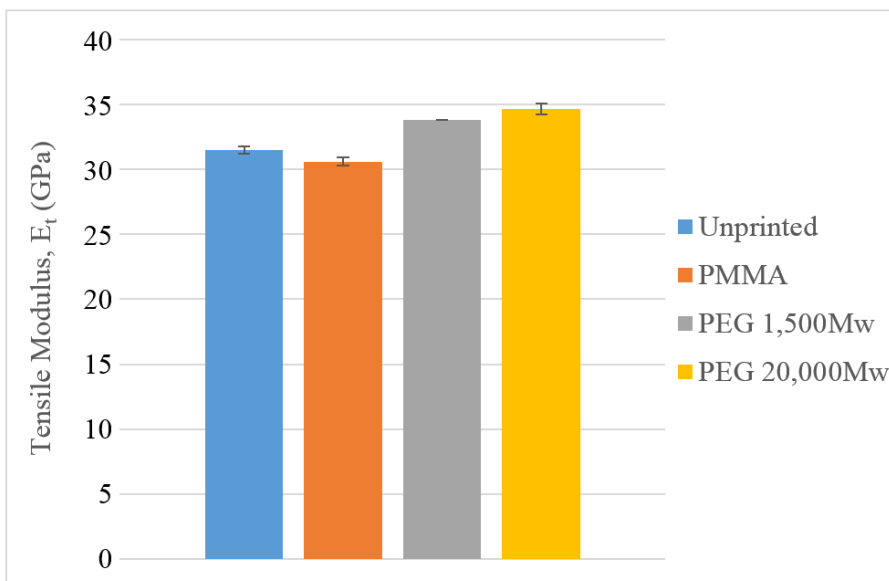


Figure 5.15: Tensile moduli of multidirectional 977-2 laminates. Error bars indicate standard deviation.

5.4 CYCLIC TENSILE TESTS

As was previously the case with flexural testing, the effects of inkjet printing upon the mechanical performance of laminates in fatigue were effectively unknown. Therefore, materials were tested broadly by testing their fatigue lives and stiffness degradation at a wide range of stress factors. If promising results were found then tests were refocussed in these areas. Because of the lengthy time investment of fatigue tests, unprinted and PMMA printed samples were initially used because PMMA samples presented the highest likelihood for successful interlaminar toughening in fatigue based upon results obtained by Zhang [11]. This greatly reduced the necessary sample manufacture and testing time. Once areas of interest were identified, PEG 1,500M_w and PEG 20,000M_w printed samples were used as well.

5.4.1 *Fatigue Life*

Figure 5.16 shows the fatigue life diagram for unprinted and PMMA printed composites. Comparisons may be drawn between this and Figure 5.3 in Section 5.2.1. Where a ■→ is shown, it indicates that at least one sample of each type overlap and occupy the same point. In these results, the fatigue lives of PMMA printed composites were noticeably lower than those of unprinted composites; as was the case with flexural samples in Section 5.2.1. In fact, between the two sample types, the fatigue lives of the two sample types only overlapped as the laminates began to approach their fatigue limits. The fatigue limit of unprinted samples lay at a stress factor of 0.6, whilst for PMMA printed samples this value was 0.5.

The lines used to fit the data were simply logarithmic lines of best fit. It can be seen that these lines fit the data very well, passing through the centre of the data clusters at most stress levels.

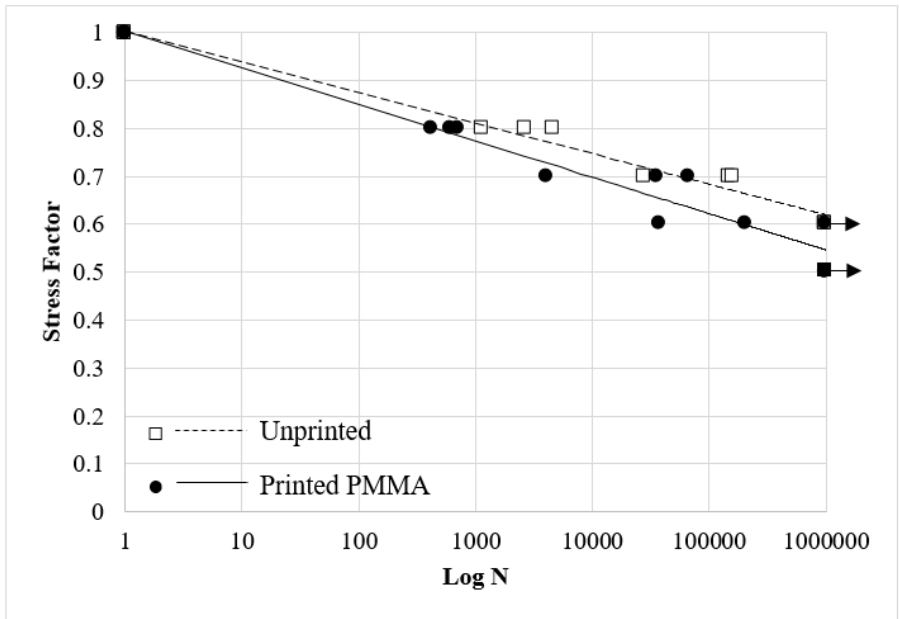


Figure 5.16: Fatigue life diagram of 977-2 laminates under cyclic tensile loading: $R=0.1$, $f=5\text{Hz}$. $\blacksquare \rightarrow$ indicates overlap of printed and unprinted sample types which did not fracture at 1×10^6 cycles.

5.4.2 Stiffness Degradation

As was the case with cyclic flexural tests, the sample stiffness was monitored throughout all tests. It was hoped that tensile tests would create greater interlaminar shear strains, leading to greater and more measurable interlaminar damage.

It is important to note that all figures showing stiffness degradation in this section were manipulated by the use of a moving average function to halve the number of data points shown for each curve. The accuracy of the data remains, but fewer data points are shown. This was done to increase the visibility of each data set for the reader. Similarly to the stiffness degradation plots for flexural testing, plots are presented in both unaltered and normalised forms in order to comply with standard practices and also to indicate the varied starting moduli of samples.

Figure 5.17 shows the stiffness degradation of unprinted and PMMA printed samples at a stress factor of 0.8. It was immediately noticeable that these results were starkly different to those obtained at the same stress factor in flexural tests (Figure 5.5, Section 5.4.2). These results showed significant stiffness degradation, with samples exhibiting a total stiffness drop of more than 30% before failure. It was also observed that the stiffness of PMMA printed samples dropped more rapidly than unprinted ones. All samples appeared to exhibit an

immediate stiffness drop within the first hundred cycles, followed by a phase of decreased gradient. In most unprinted samples this was then followed by a third phase in which the gradient decreased yet again and was shortly followed by ultimate fracture of the samples.

The consistency of the curves between samples of the same type was very good, with only sample Unprinted 1 deviating from the others. Although, the shape of this curve was very similar to the other unprinted samples, and the key difference appeared to be the initial stiffness value of that particular sample. This may have been caused by inaccurate measurement of sample dimensions, meaning that this sample was placed under less stress than others in the same group. Alternatively, human error could have led to the incorrect zeroing of the LVDT used to measure sample deflection. The initial stiffness of the samples showed good consistency with static results obtained in Section 5.3, with unprinted samples being slightly higher in most cases. It should be noted that the modulus recorded is the dynamic tensile modulus, since it was recorded under dynamic conditions.

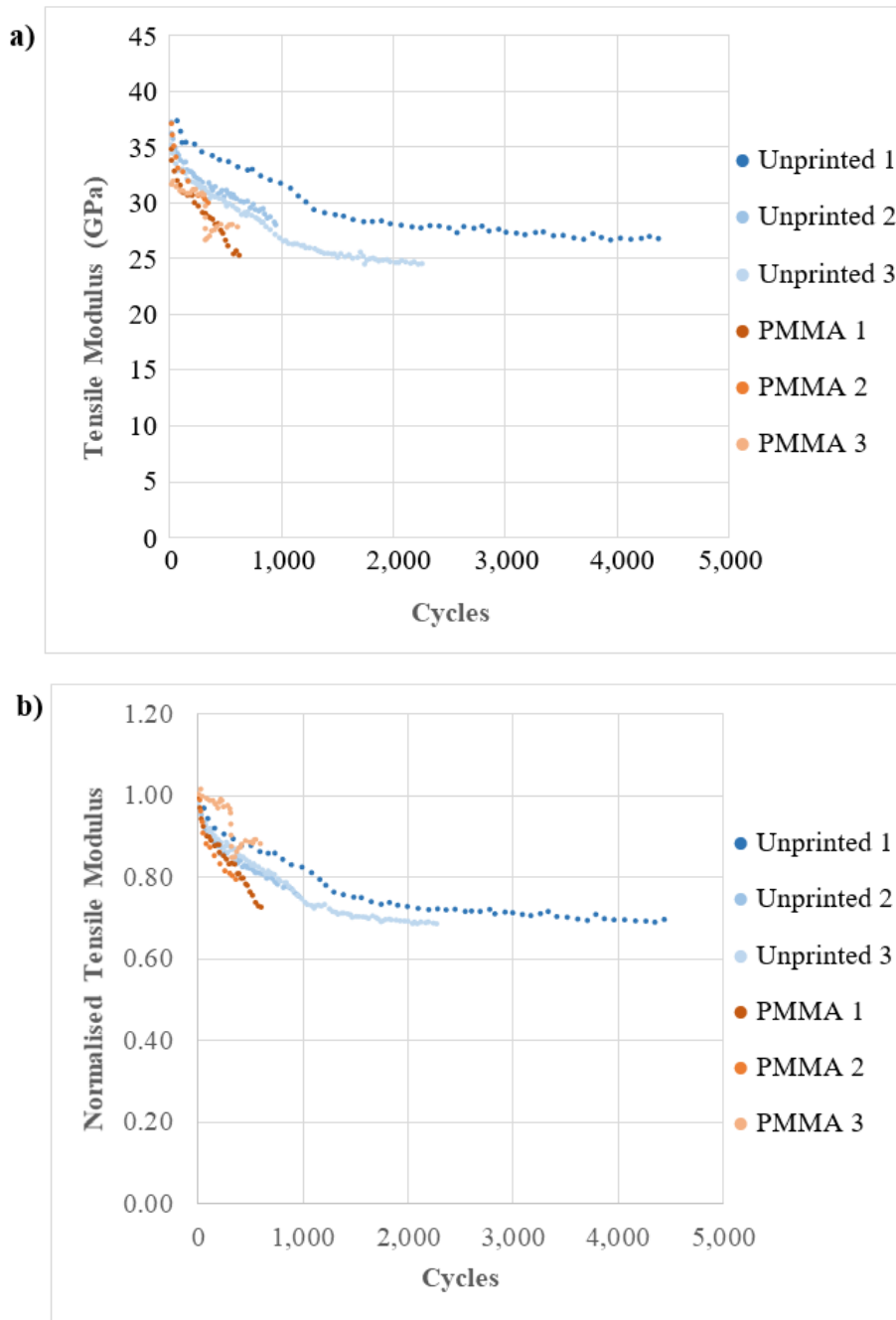


Figure 5.17: a) Tensile modulus of samples in cyclic tensile loading at a stress factor of 0.8. b) Normalised tensile modulus of samples in cyclic tensile loading at a stress factor of 0.8.

Figure 5.18 shows the stiffness degradation of unprinted and PMMA printed samples at a stress factor of 0.7. These curves closely match what was observed in Figure 5.17, showing a large stiffness drop of around 30%. In these tests though, samples did not fracture for some time after this initial drop, levelling off and maintaining a somewhat constant gradient until ultimate failure.

Figure 5.19 shows the same results but with the x axis scaled in order to make the initial stiffness drop more visible. It may now be observed that both sample types exhibited the same behaviour as was previously displayed in Figure 5.17. They exhibited three distinct phases (illustrated in Figure 5.19 by dashed vertical lines and denoted by Ia, Ib, and II): an initial stiffness drop, a slower secondary drop, and a third phase of yet lower gradient that continued until sample failure. The reason for annotating the first phases as Ia and Ib (and not as I and II) is due to the sequence in which damage mechanisms occur in relation to traditional concepts of composite fatigue damage development. This is explained fully in Section 5.5.2.

It is notable that in these tests, Phases Ia and Ib occurred over a period of around 5,000 cycles, whereas in the previous tests these phases occurred over a period of less than 1,500 cycles. These values were determined by using the line intersection method described in Section 3.7.2 which was used to identify the glass transition temperature of samples in DMTA tests. Whilst this method phases was useful in quantifying the transitions points between phases, it should be noted that, like glass transition temperature, the transition point should be thought of more as a region than an exact point.

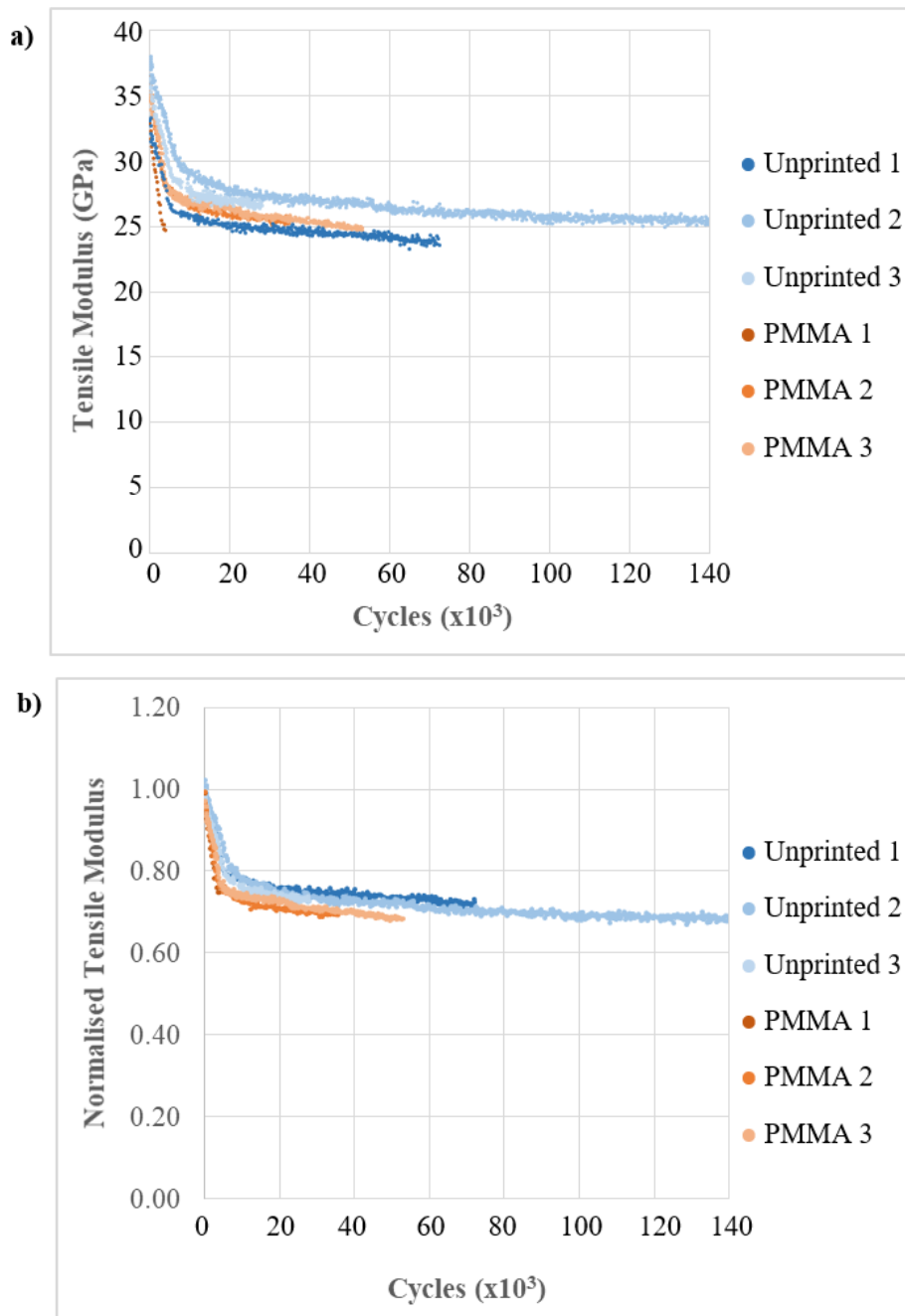


Figure 5.18: a) Tensile modulus of samples in cyclic tensile loading at a stress factor of 0.7.
 b) Normalised tensile modulus of samples in cyclic tensile loading at a stress factor of 0.7.

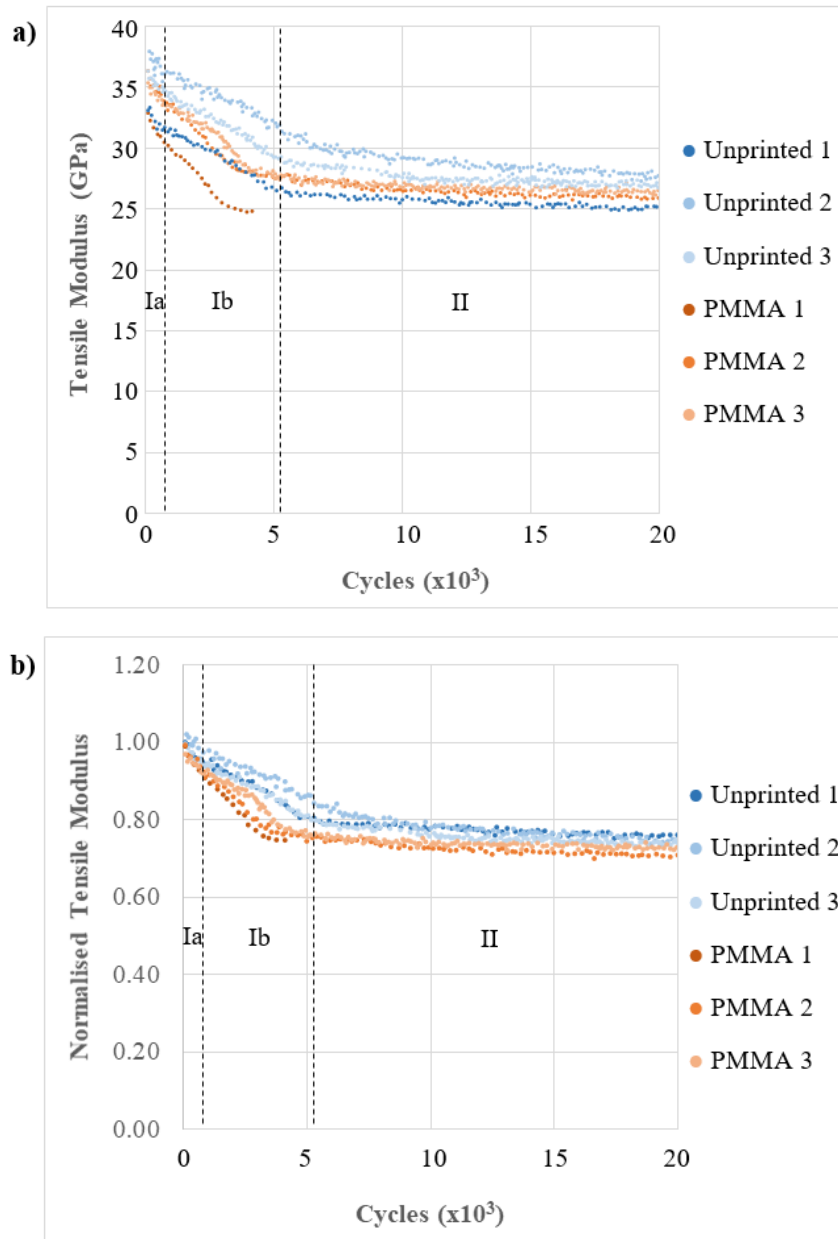


Figure 5.19: a) Tensile modulus of samples in cyclic tensile loading at a stress factor of 0.7. The x axis is scaled to view the initial stiffness degradation of samples. b) Normalised tensile modulus of samples in cyclic tensile loading at a stress factor of 0.7 with scaled x axis.

Figure 5.20 shows the stiffness degradation of unprinted and PMMA printed samples at a stress factor of 0.6. Once again, samples exhibited a similar shape to those in previous tests. It was seen that three distinct phases still existed. At this stress factor the sample types diverged, with PMMA samples decreasing in stiffness through Phase Ib much more rapidly than unprinted samples. This is better illustrated in Figure 5.21 which is scaled to show the progression of samples in their first two phases. The approximate points of transition from Phase Ib to Phase II are indicated by individual dashed lines of colours matching the sample

types. The transition from Phase Ia to Phase Ib occurred at around 2,000 cycles in both sample types. The transition from Phase Ib to Phase II occurred at approximately 13,000 cycles in printed samples, and approximately 25,000 cycles in unprinted samples.

It was also observed that the initial stiffness of PMMA samples was lower than that of unprinted samples. The average initial stiffness value of PMMA printed samples was found to be 6.9% lower than unprinted samples. This is something that was observed to some degree in previous tests (Figure 5.17 and Figure 5.18), but became more prominent in these tests.

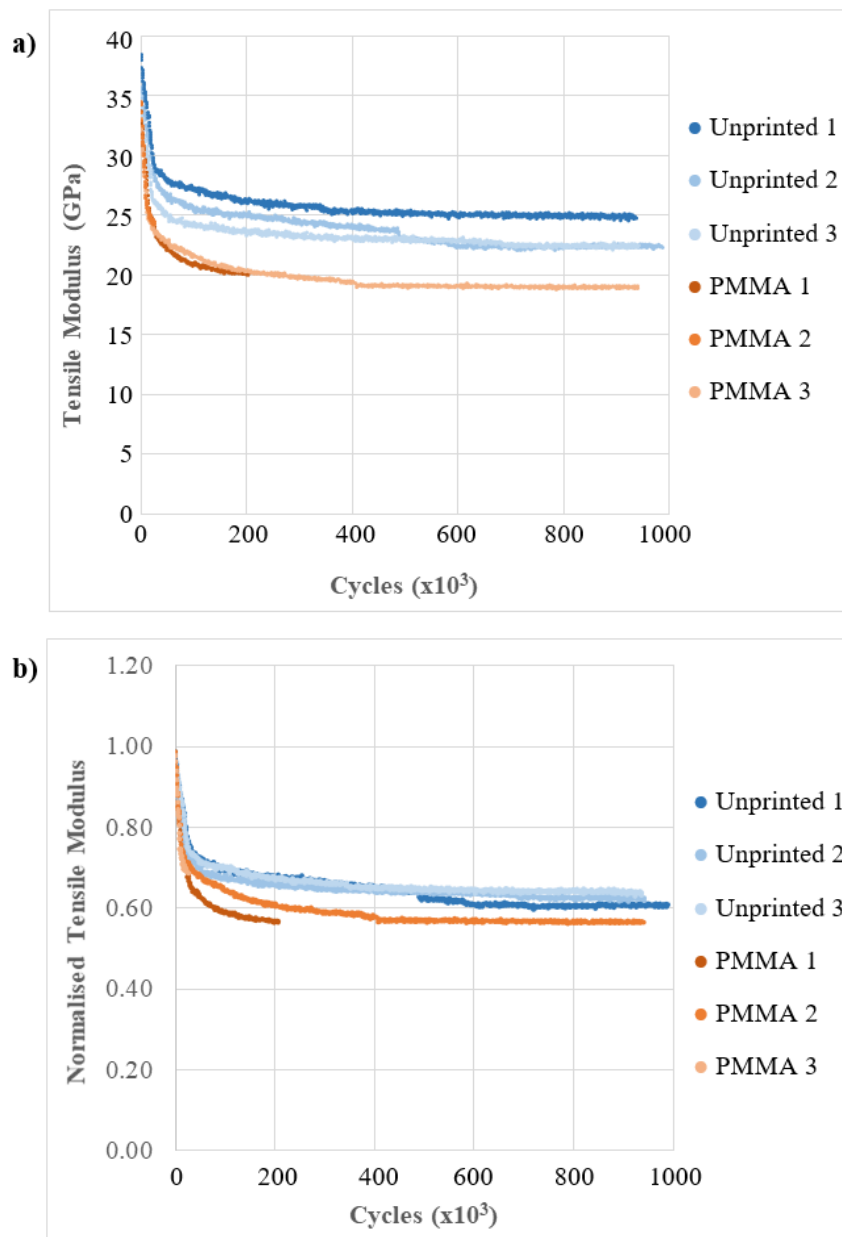


Figure 5.20: a) Tensile modulus of samples in cyclic tensile loading at a stress factor of 0.6. b) Normalised tensile modulus of samples in cyclic tensile loading at a stress factor of 0.6.

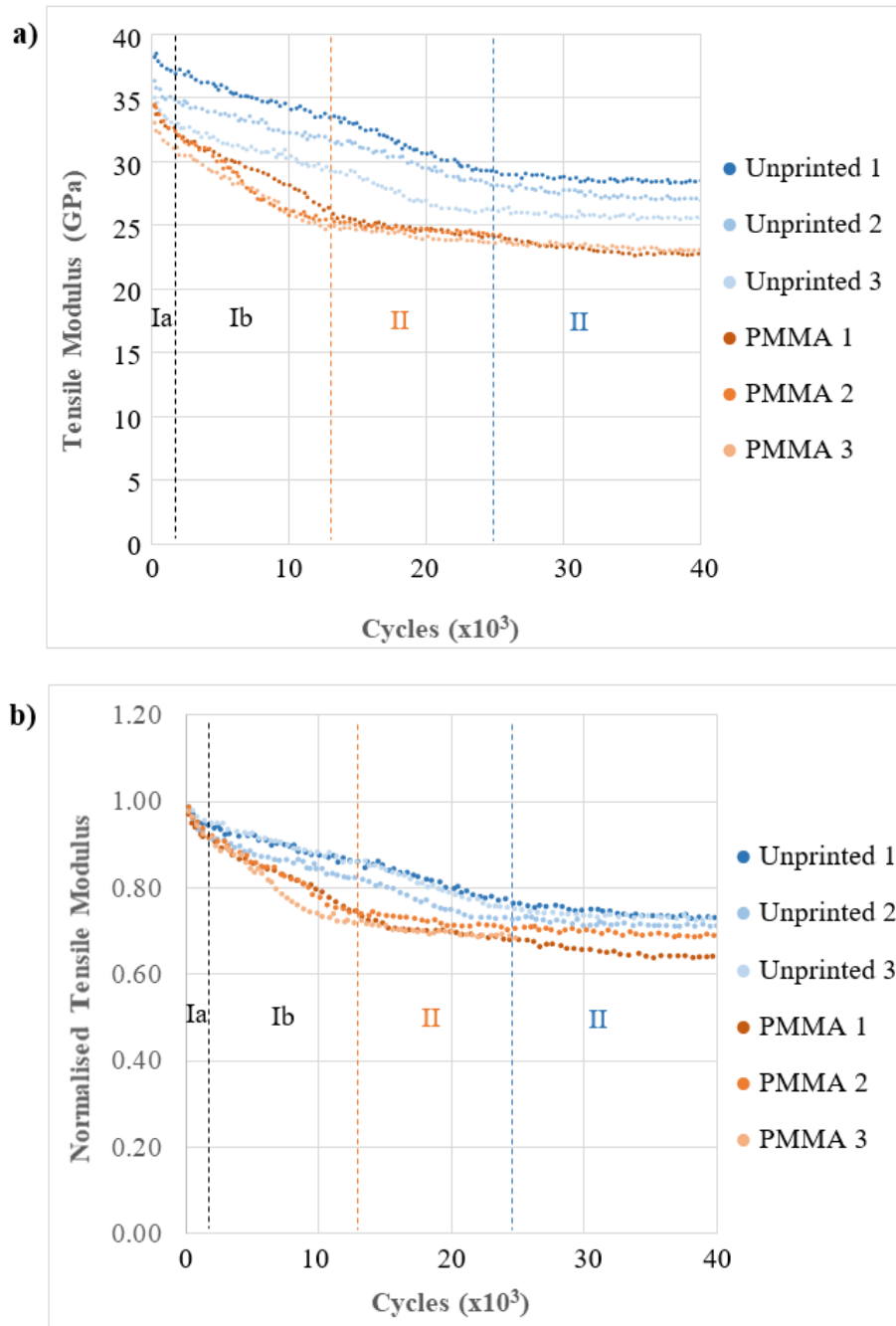


Figure 5.21: a) Tensile modulus of samples in cyclic tensile loading at a stress factor of 0.6. The x axis is scaled to view the initial stiffness degradation of samples. b) Normalised tensile modulus of samples in cyclic tensile loading at a stress factor of 0.6 with scaled x axis.

The lowest stress factor tested was 0.5. The results of tests conducted on unprinted and printed PMMA samples at this level are shown in Figure 5.22. It should be noted that in these tests a measurement artefact was observed in which a sudden stiffness drop occurred past approximately 9×10^5 cycles. Data past this point was left in so that the reader may interpret the continued linearity of the curves past this point. Additionally, some curves are incomplete.

In these tests, data recording was stopped in order to reduce testing time since the main area of interest occurred before 2×10^5 cycles. Due to the very long times associated with fatigue tests, the omission of this data in a minority of samples was deemed acceptable.

At this stress factor, the results for both sample types maintained the same distinct shape and division into three phases. And as in Figure 5.20 and Figure 5.21, PMMA samples exhibited much more rapid progression to Phase II of stiffness degradation. This is better illustrated in Figure 5.23 which is scaled to show the progression of samples in their first two phases. The approximate points of transition from Phase Ib to Phase II are indicated by individual dashed lines of colours matching the sample types. For both sample types, Phase Ia ended after approximately 5,000 cycles. In this phase, stiffness drops of approximately 5-10% occurred in both sample types. The sample types deviated during Phase Ib, with PMMA samples transitioning to Phase II at approximately 50,000 cycles, and unprinted samples at approximately 220,000 cycles. Again, these values were determined by using the line intersection method described in Section 3.7.2 which was used to identify the glass transition temperature of samples in DMTA tests.

At a stress factor of 0.8, unprinted and PMMA samples generally exhibited similar initial stiffness values. This was approximately in line with what was found in static tests (Section 5.3). These values diverged increasingly as the stress factor was lowered, most likely due to the decreasing influence of fibre properties upon the stiffness of samples. In these tests (stress factor 0.5) the initial stiffness of unprinted samples was on average 10.6% higher than PMMA in these tests, being 39.5GPa and 35.7GPa respectively. This also resulted in the average stiffness values at runout (samples reaching 1×10^6 cycles without failure) differing by a similar amount.

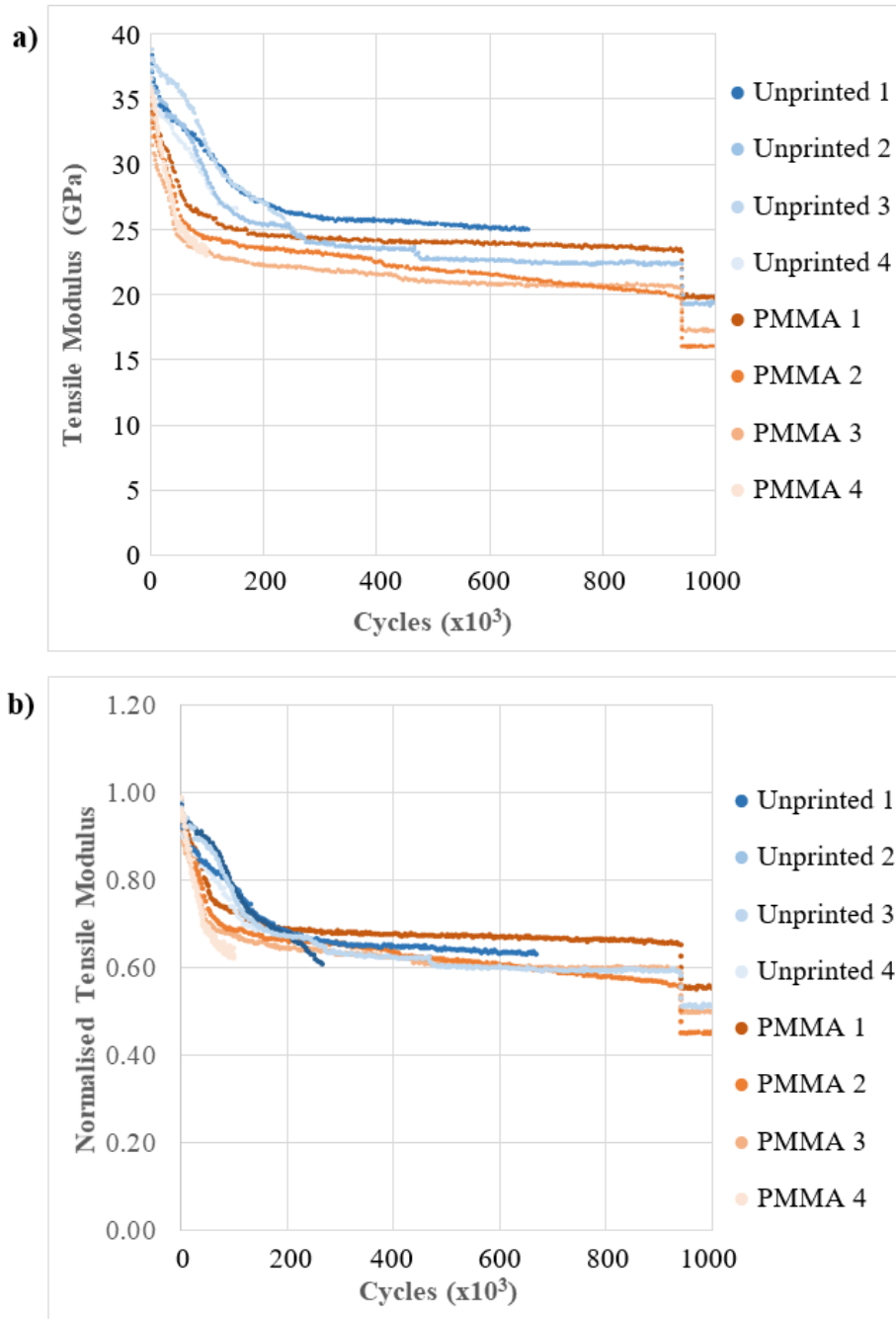


Figure 5.22: a) Tensile modulus of samples in cyclic tensile loading at a stress factor of 0.5. b) Normalised tensile modulus of samples in cyclic tensile loading at a stress factor of 0.5.

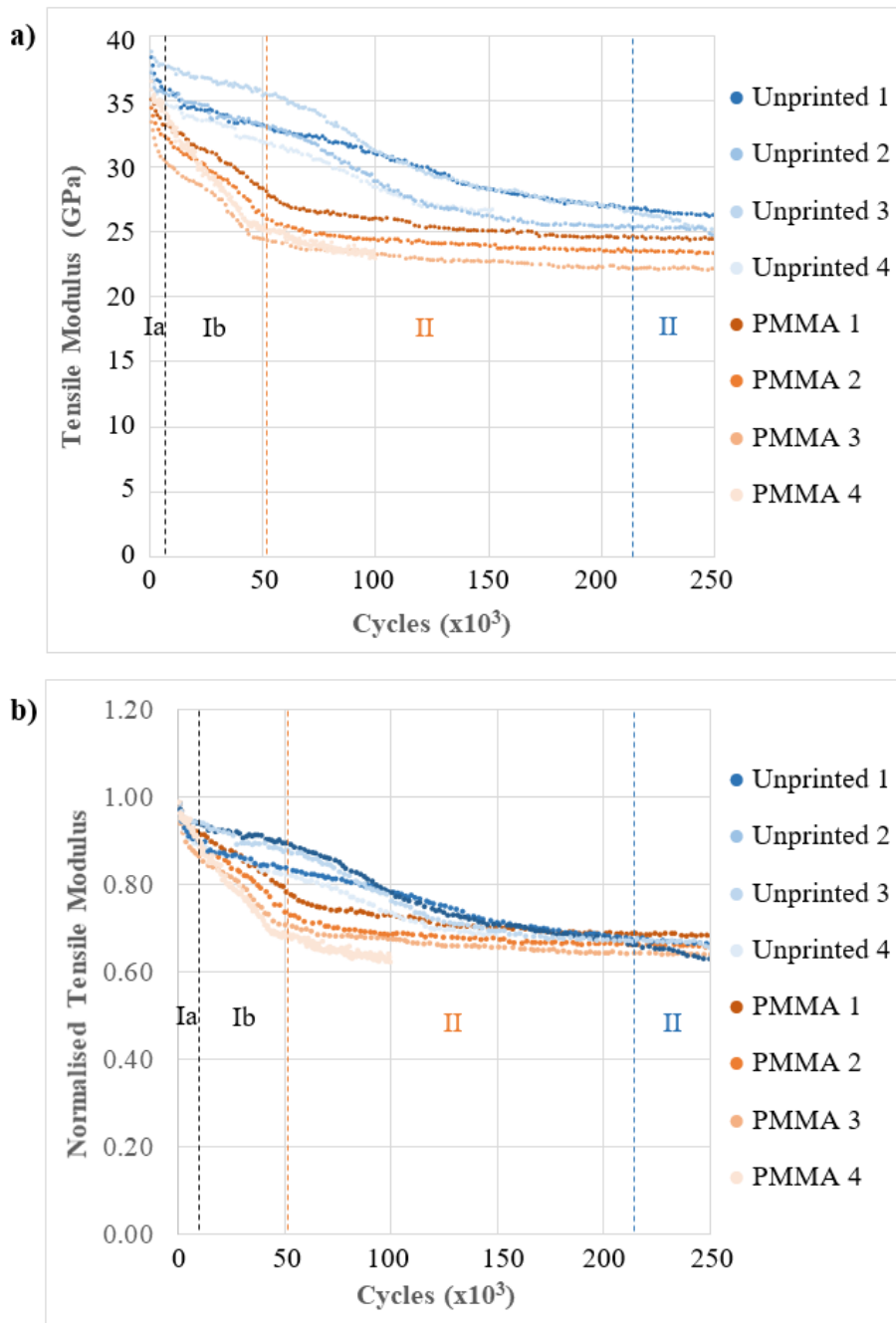


Figure 5.23: a) Tensile modulus of samples in cyclic tensile loading at a stress factor of 0.5.

The x axis is scaled to view the initial stiffness degradation of samples. b) Normalised tensile modulus of samples in cyclic tensile loading at a stress factor of 0.5 with scaled x axis.

The results presented thus far showed excellent consistency. As the stress factor was lowered, the curves showed increasing accuracy and repeatability. The peak of this accuracy was at a stress factor of 0.5, perhaps because at this level fibre fracture was no longer a dominant damage mechanism, allowing transverse cracks and delaminations to dominate.

At this level both sample types had reached their fatigue limit, so it also became possible to observe their behaviours in high cycle fatigue. However, the particular area of interest appeared to be the material behaviour up to Phase II of stiffness degradation. In this region samples exhibited very different behaviours. At a stress factor of 0.5 this divergence of behaviour was of a suitably high degree that damage mechanisms could be inferred from the data.

Until this point, differences between printed and unprinted laminates were difficult to discern. The fatigue lives of the samples implied that printed samples were at detriment because of the introduction of PMMA, but gave no indication of the damage mechanisms at work. Stiffness degradation, particularly at low stress factors, presented a method of inferring damage mechanisms from indirect data. It is therefore at this point that PEG printed laminates were introduced to tests to determine how they might behave under cyclic tensile loads.

PEG 1,500M_w and PEG 20,000M_w samples were tested under cyclic tensile loading. These tests were focused exclusively on the stiffness degradation of samples at a stress factor of 0.5, particularly during Phases Ia and Ib.

Figure 5.24 shows the stiffness degradation of PEG printed samples. In tests upon PEG 1,500M_w samples were only cycled until they transitioned into Phase II of stiffness degradation. This was done in order to save time because it was determined from previous tests that the stiffness in Phase II may be predicted, and was not considered to be particularly relevant in determining the mechanics of interlaminar toughening mechanisms. Justification of these assumptions is described later in Section 5.5.2. In tests upon PEG 20,000M_w samples, three samples were tested. However, data for one of these samples became corrupted, and was not repeated due to time constraints.

From Figure 5.24 it can be seen that the two different molecular weight PEG polymers produced very different results. In PEG 20,000M_w samples, Phase Ia occurred over a period similar to other sample types. Although, the Phase Ia stiffness drop was significantly larger than in other sample types. The Phase Ia stiffness drop for PEG 20,000M_w samples was measured to be around 17% on average, which contrasted sharply with the 5% drop of PEG 1,500M_w samples. Phase Ib extended over a long period similar to unprinted samples. The transition from Phase Ib to Phase II was somewhat ambiguous though, as it occurred very gradually. It may be inferred from this that in PEG 20,000M_w laminates, the later stages of Phase Ib damage were slowed.

Figure 5.25 shows the same data scaled in order to show the progression of PEG 1,500 M_w samples in their first two phases. These results bore resemblance to those of PMMA samples.

Phase Ia in these samples occurred over a similar period to all other samples, but Phase Ib occurred over a period similar to that of PMMA samples.

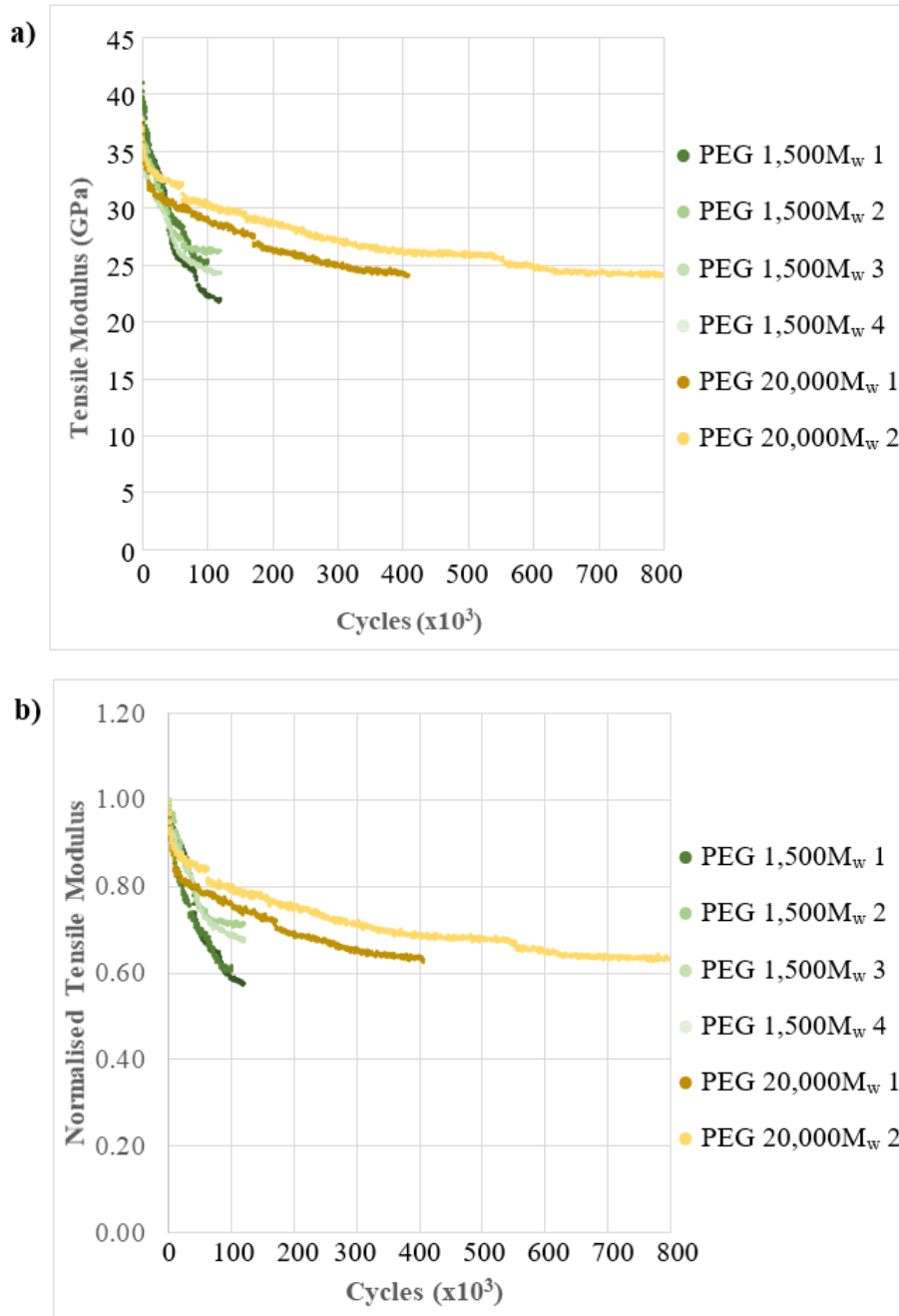


Figure 5.24: a) Tensile modulus of PEG printed samples in cyclic tensile loading at a stress factor of 0.5. b) Normalised tensile modulus of PEG printed samples in cyclic tensile loading at a stress factor of 0.5.

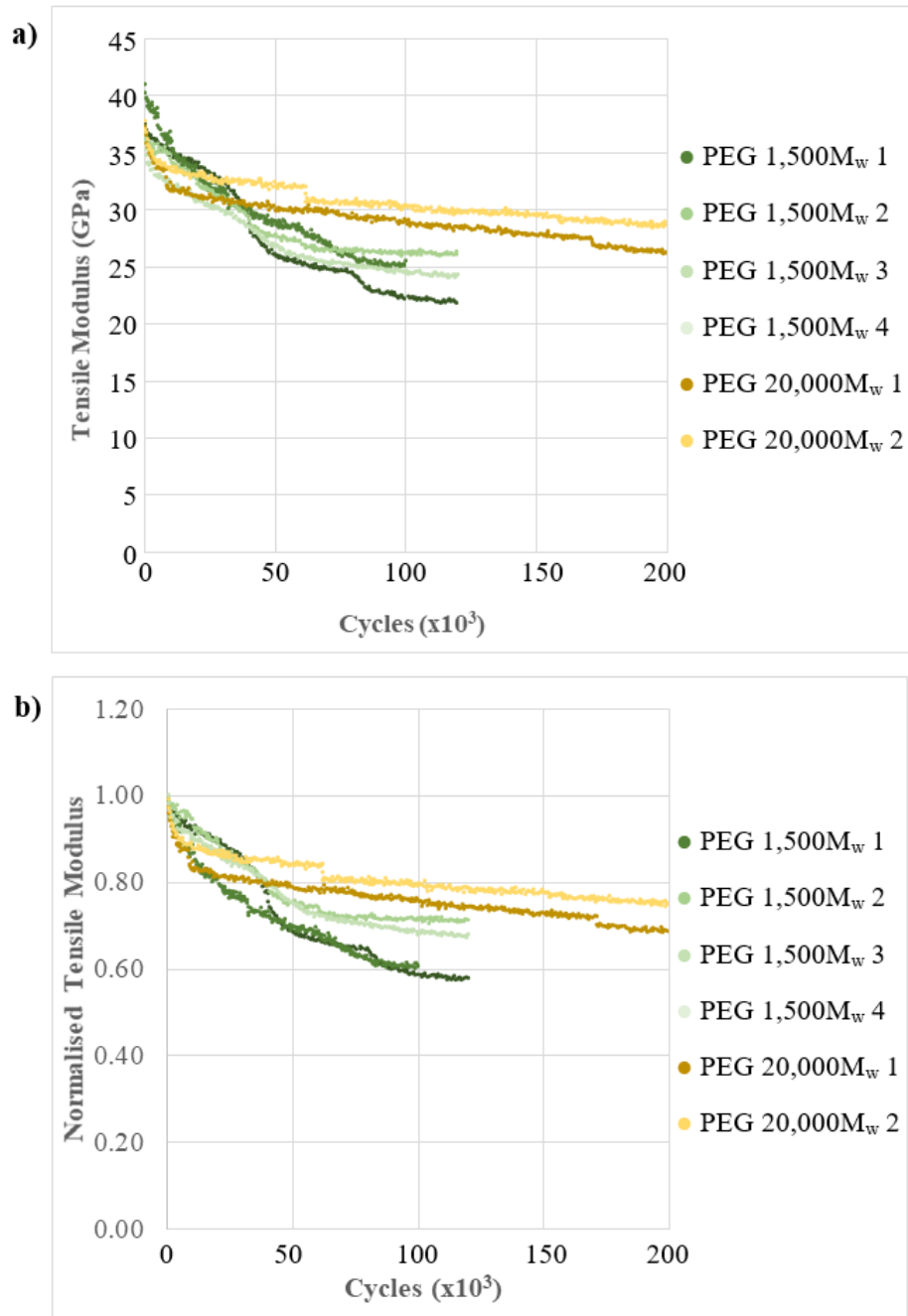


Figure 5.25: a) Tensile modulus of PEG printed samples in cyclic tensile loading at a stress factor of 0.5. The x axis is scaled to view the initial stiffness degradation of samples. b) Normalised tensile modulus of PEG printed samples in cyclic tensile loading at a stress factor of 0.5 with scaled x axis.

Figure 5.26 and Figure 5.27 show the combined results of all sample types. These curves were produced by calculating the mathematical average of all samples within a set. These averaged curves were then processed using a smoothing spline function in Mathworks Matlab to produce the curves shown.

It may be seen that two distinct classes of curves were produced. The key distinction between these types was the period over which Phase Ib occurred. In PMMA and PEG 1,500M_w samples, Phase Ib occurred over a period of around 50k-100k cycles. In unprinted and PEG 20,000M_w samples, it occurred over a period of 220k-300k cycles.

There was very little difference in the curves produced by PMMA and PEG 1,500M_w samples, suggesting that similar rates of damage took place within them. Although, the average initial stiffness of PEG 1,500M_w samples was 6.3% higher than that of PMMA samples. This was consistent with static test results shown in Table 5.3.

Unprinted and PEG 20,000M_w samples also exhibited broadly similar behaviour. However, they differed in key areas. The Phase Ia stiffness drop of PEG 20,000M_w samples was considerably greater than in unprinted samples. Whilst in Phase Ib their rate of decrease of stiffness was around 53% lower than unprinted samples, with PEG 20,000M_w samples decreasing on average at around 20.7kPa per cycle, and unprinted samples decreasing at around 39.1kPa per cycle. These values were measured by taking three points near the start of Phase Ib, and three near the end. The points were then averaged, and the gradient between them calculated. In unprinted samples, Phase Ib transitioned to Phase II quite suddenly. Whereas in PEG 20,000M_w samples, this transition point was gradual and more difficult to quantify.

In summary, samples exhibited very different behaviours to each other. At high stress factors these behaviours were less noticeable, perhaps due to the predominance of fibre fractures. As the stress factor was lowered, fibre fracture proved less dominant and key differences between samples became more easily identifiable. Although these differences only occurred in a portion of the stiffness degradation curves which represented less than 20% of the total number of cycles that samples were subjected to. In this region the presence of both PMMA and PEG 1,500M_w droplets appeared to accelerate stiffness degradation, whilst PEG 20,000M_w droplets appeared to decrease the rate.

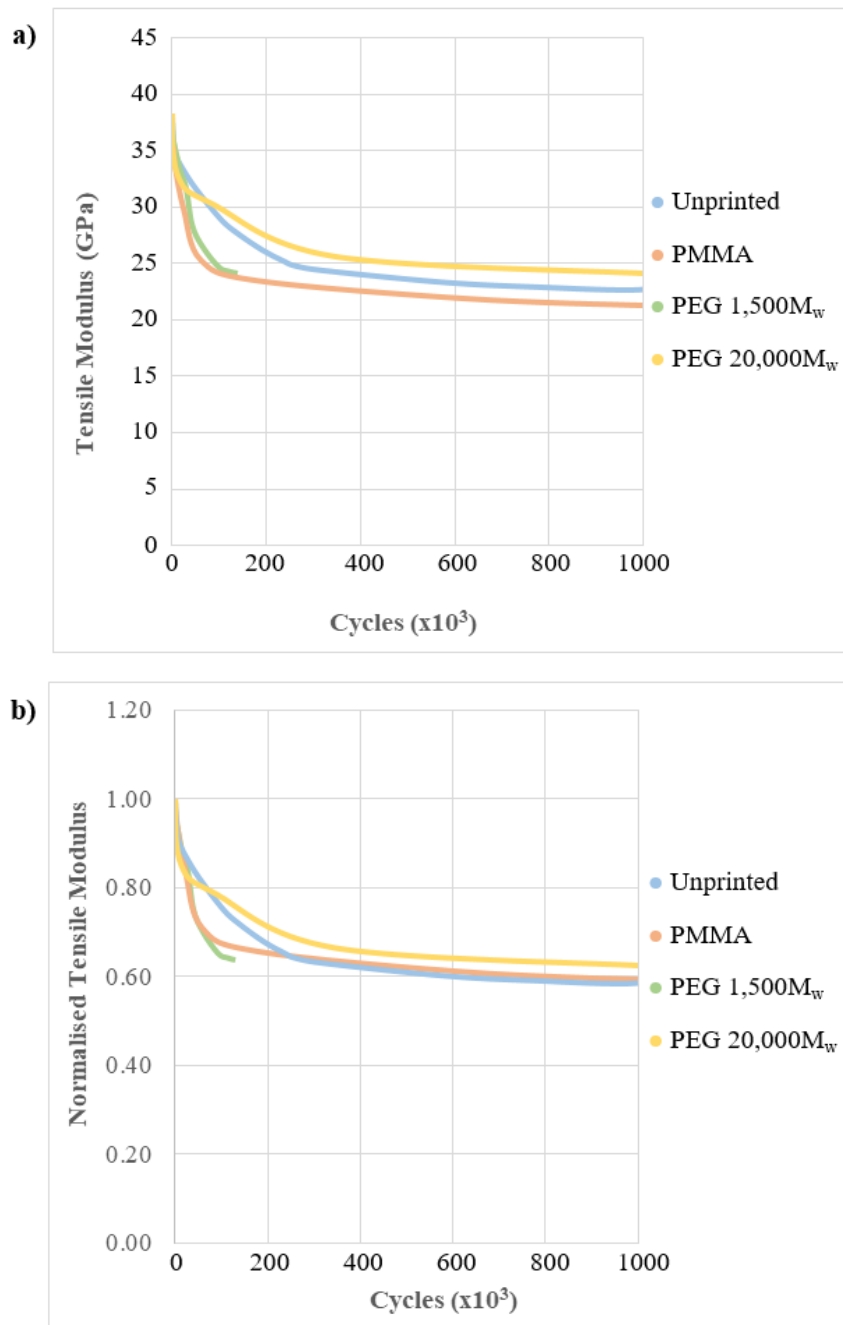


Figure 5.26: a) Average curves of all sample types in cyclic tensile loading at a stress factor of 0.5. b) Normalised average curves of all sample types in cyclic tensile loading at a stress factor of 0.5.

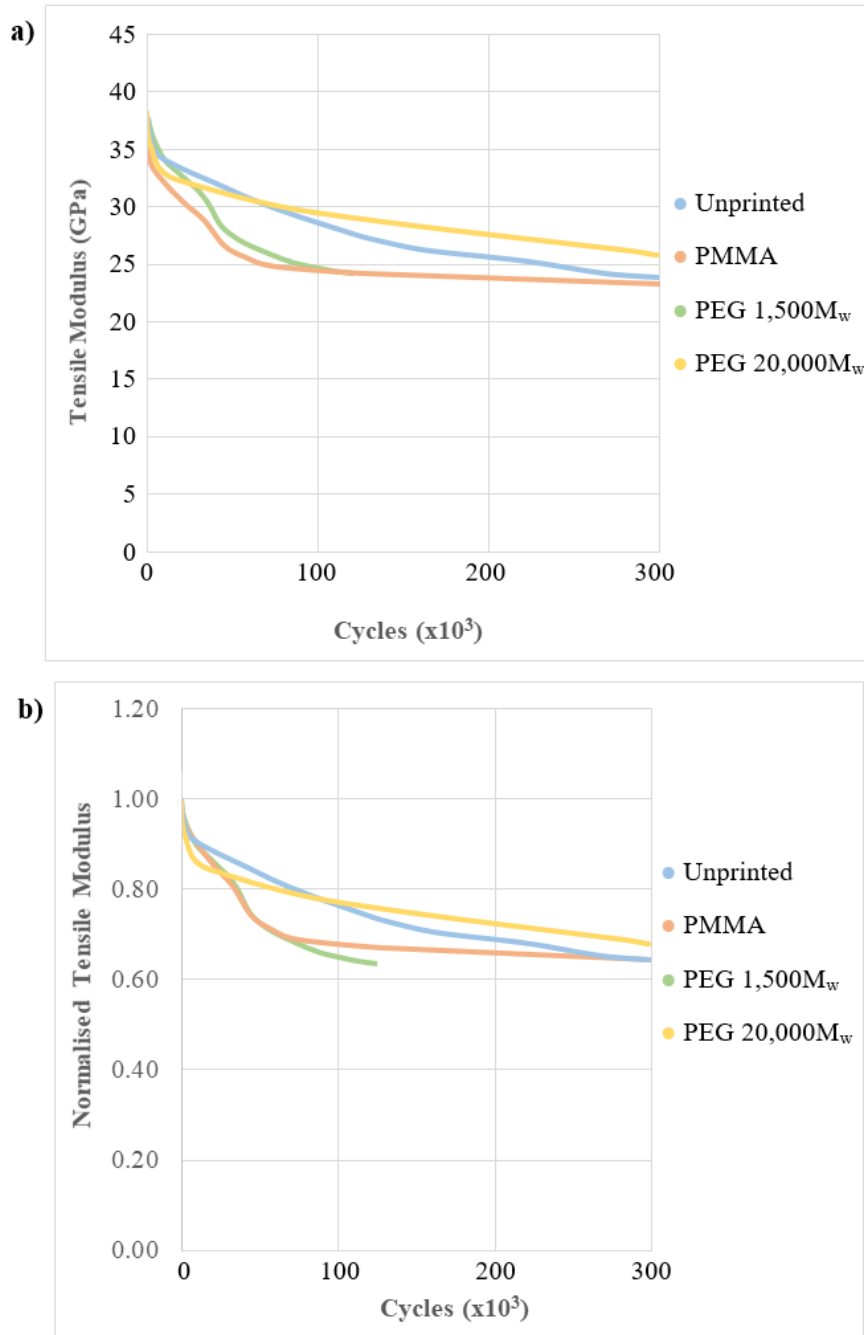


Figure 5.27: a) Average curves of all sample types in cyclic tensile loading at a stress factor of 0.5. The x axis is scaled to view the initial stiffness degradation of samples. a) Normalised average curves of all sample types in cyclic tensile loading at a stress factor of 0.5 with scaled x axis.

5.5 DISCUSSION

In this section the experimental results obtained in this chapter are discussed in order to determine what can be understood from them.

5.5.1 *Flexural Testing*

Initial flexural tests focussed on the optimisation of the flexural testing method. It was shown in Section 5.1 that substantial increases in measured flexural strength could be obtained through a combination of an optimised jig design, and by the use of electrical insulation tape as shims between the rollers and samples. Both of these methods worked on the principle of reducing stress at the roller contact points by increasing contact area.

It was described in Section 2.5 that Cui and Wisnom [120] carried out detailed stress analysis of both three and four point bending unidirectional glass fibre specimens using ABAQUS. They found that the specimens were very sensitive to the length of the contact surface and the distribution of contact stresses. In the results presented in Section 5.1, it was shown that increasing the roller diameter greatly reduced contact stresses by increasing the contact area. Additionally, the adjustability of the four point bending jig allowed the full length of the roller surface to make contact with the specimens, increasing the contact length. Finally, the introduction of insulation tape shims further increased roller contact area.

Following these initial tests, full flexural testing was carried out on unprinted and PMMA printed specimens. Averaged static stress/strain curves (Figure 5.1) showed good resemblance to those predicted by the test standard [205]. Results (Table 5.2) showed that the static tensile moduli of both sample types was almost identical. Because of the interlaminar nature of the printing process, some change in tensile modulus may have been expected. However, it is well established that the tensile moduli of unidirectional composites are highly dictated by fibre properties and fibre/matrix bonds, and therefore changes may be small and difficult to identify [217, 218]. The static flexural strengths of samples differed somewhat, showing that PMMA printed samples were on average 2.9% stronger than unprinted samples. But due to experimental data scatter no definitive conclusions could be drawn because these results lay within one standard deviation of one another. It should be noted, as was described in Section 5.1, that the samples used in these tests were produced in multiple batches. Typically, samples from two to three (and in some cases, more) different batches were mixed and used in tests. Therefore, variation in mechanical properties due to batch to batch variation should have been minimised.

In cyclic testing, the merits of the upgraded four point bending jig were proven again by demonstrating that the experimental data scatter of the fatigue lives of samples was greatly reduced. Up to two orders of magnitude in most cases (Figure 5.2 and Figure 5.3). This falls in line with typical scatter in fatigue tests upon composites [141, 219, 220]. Figure 5.28 shows an example of such results, showing scatter similar to that observed here. As in static tests, it should be noted that the samples used in these tests were produced in multiple batches. Therefore, variation in mechanical properties due to batch to batch variation should have been minimised. Results shown in Figure 5.3 indicated that the fatigue lives of PMMA printed samples were reduced compared to those of unprinted samples. However, the damage mechanisms which caused this reduction could not be inferred from the fatigue life diagram alone, as fatigue life is only a broad indication of material performance, and not of damage development, which was the key interest of this work.

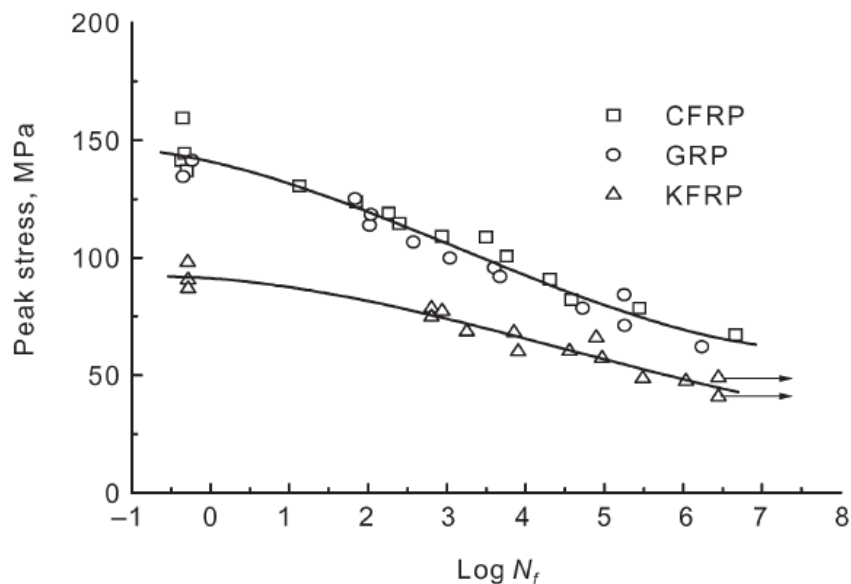


Figure 5.28: Fatigue life diagram published by Jones et al. showing the fatigue lives of $\pm 45^\circ$ tensile laminates consisting of carbon, glass, and Kevlar reinforced epoxy matrix laminates: $R=0.1$, constant load rate of 100kNs^{-1} [220]

Stiffness degradation data was also collected from cyclic flexural tests as a method of inferring the damage mechanisms taking place in samples. It was observed in Section 5.2.2 that the flexural moduli of samples were greater than those of the static moduli. It is well documented that under high strain rates, the elastic moduli of materials increase by the effects of mass inertia forces and by the adiabatic character of the deformation process [221]. This was demonstrated by Sabbagh et al. [222] who investigated the effects of strain rate upon numerous resin-based materials in flexural loading, and finding that the dynamic moduli of the materials

they tested were 31% to 72% higher than in static tests. However, they used the resonant frequency of samples to induce extremely high strain rates, which resulted in a much higher rise in modulus than in results presented in this thesis. In these tests, the initial dynamic flexural moduli were found to be 8-30% higher than in static flexural tests.

It was noted in high stress factor tests (0.85 to 0.8) shown in Figure 5.4 and Figure 5.5 that the stiffness of samples was actually recorded as increasing until failure. It was hypothesised that this increase in stiffness was due to the increased alignment and straightening of fibres under cyclic loading. This effect has been noted by many groups such as Pitarresi et al, Genedy et al, and others [223-225]. These authors also suggested that the act of fibre straightening may also contribute to the stiffness degradation of samples in subsequent loading cycles by causing fibre/matrix debonding.

Sample failure at high stress factors was ultimately caused by fibre fractures. This was evident due to their rapid failure, as well as their lack of stiffness degradation until immediately prior to fracture. Because fibre fractures tend to accumulate exponentially, they do not tend to result in stiffness degradation until very close to ultimate failure. This is due to the fact that fibre stiffnesses and strengths are generally described by stochastic methods. The Weibull distribution [70] is one of the most favoured models. Statistical models suggest that the strength of fibres in a composite may be described by a statistical distribution. This ultimately results in some fibres fracturing at stresses below the average fracture stress of the composite, usually due to high localised stresses or the build-up of smaller damage events, resulting in increased loading on remaining fibres. This generally causes fibre fracture rates to increase exponentially, increasing ever more rapidly as the statistical peak of fibre strengths is neared, at which point failure occurs shortly after.

As the peak stress was lowered (stress factors of 0.7 to 0.6), samples began to exhibit linear decreases in stiffness (Figure 5.6, Figure 5.7, and Figure 5.8). This was consistent with expectations. As stress is lowered, fibre fracture decreasingly becomes a dominant damage mechanism, allowing damage due to other mechanisms to accumulate. Intralaminar matrix cracks accumulate with increasing numbers of loading cycles, which decreases load sharing capabilities between fibres. There are two main mechanisms for crack initiation that are discussed in the literature. These are crack initiation from matrix fracture, and crack initiation from fibre/matrix interface failure [226]. These further lead to fibre/matrix debonding and delaminations. It has been demonstrated by numerous authors that these mechanisms result in stiffness degradation in composites [80, 134, 135, 137, 139, 140, 226]. Section 2.3.1 of this thesis covers these damage mechanisms in more detail. As discussed above, it has been suggested that fibre straightening can cause fibre/matrix debonding. Because of the

unidirectional nature of the samples used, it is possible that fibre/matrix debonding accounted for a significant proportion of the stiffness drop that was observed.

The stiffness degradation observed in these tests was consistent with some of the general theories of stiffness degradation. These were previously discussed in Section 2.6.1. However, the curves that were produced featured minimal stiffness degradation, and were inconsistent. Therefore little could be inferred from them that could not previously be seen from the fatigue life diagrams and static test results. At this stage it seemed likely that the negligible amounts of polymer added to the composite likewise produced negligible effects. But it may have equally been due to the fundamental issues experienced with the four point bending technique, coupled with an insensitivity of the method to interlaminar toughening due to a lack of off-axis plies.

Analysis of sample fracture points in Section 5.2.3 revealed that compressive fatigue cracks formed at the load application points despite efforts to reduce stress concentrations at these points. It is probable that the development of these cracks introduced additional damage to the samples which was not intended. These cracks would also undoubtedly have contributed to the stiffness degradation of the samples, somewhat hiding minute effects caused by interlaminar toughening. Additionally, these cracks resulted in the premature failure of samples, preventing them from reaching high cycle ranges in which matrix and interlaminar damage mechanisms would accumulate to the greatest degrees.

Tensile tests were chosen as an alternative to flexural tests due to their simplicity. Although multidirectional laminates had to be used to introduce differences in Poisson's ratios between plies, which ultimately added complexity to the analysis of results when compared to the 0° unidirectional specimens used in flexural tests.

5.5.2 Tensile Testing

Static tensile results in Section 5.3 showed that the presence of inkjet printed polymers increased the static strength of laminates in all cases. The tensile strengths of unprinted, PMMA, PEG 1,500M_w, and PEG 20,000M_w samples were found to be 633MPa, 668MPa, 657MPa, and 654MPa respectively. These were increases of 5.5%, 3.8%, and 3.3% over unprinted laminates. It should be noted, as was described in Section 5.3, that the samples used in these tests were produced in multiple batches. Typically, samples from two to three (and in some cases, more) different batches were mixed and used in tests. Therefore, variation in mechanical properties due to batch to batch variation should have been minimised. Results heavily indicated that these increases were due to the presence of printed polymers. This may

have arisen as a result of a number of mechanisms. Firstly, and perhaps most likely, is that the introduction of polymers resulted in an increased interlaminar fracture toughness in mode II loading. Mode II loading in these samples was caused by the disparity in Poisson's ratios between plies which was discussed in Section 2.3.3. It was shown by Zhang [11] that the mode I interlaminar fracture toughness of 977-2 laminates was increased by the introduction of PMMA and PEG 20,000M_w polymers. It is therefore reasonable to assume that this toughening would extend into toughening in mode II. A toughened interface would reduce the tendency of laminates to fracture at the ply interfaces. This, in turn, would extend the load sharing capabilities of the laminates at higher stresses. Additionally, it is possible that dissolution of the polymers into the matrix during the curing process resulted in increased fibre/matrix interface bond strength close to the interlaminar region, where fibre/matrix debonding would be most likely to occur. However, this seems unlikely to have been the case in all sample types because it was shown in Section 3.9.2 that only PEG 1,500M_w dissolved into the matrix. Although PEG 20,000M_w also showed some degree of dissolution. Therefore, this effect alone could not produce the results obtained in all samples, but may have played a role in PEG printed samples.

The static tensile modulus of laminates was also affected by inkjet printing. The tensile moduli of unprinted, PMMA, PEG 1,500M_w, and PEG 20,000M_w samples were found to be 31.5GPa, 30.6GPa, 33.8GPa, and 34.7GPa respectively. Therefore, PMMA showed a decrease of 2.9%, whilst PEG 1,500M_w and PEG 20,000M_w showed increases of 7.3% and 10.2% respectively. None of these values overlapped within one standard deviation. From the static test results it was clear that different mechanisms were operating in the different sample types.

In PEG printed samples, results suggested that the toughening method described above also resulted in an increased laminate stiffness. The tensile modulus of PEG was significantly lower than that of cured 977-2 resin. Therefore, it is conceivable that the presence of PEG droplets should have resulted in a decreased tensile modulus. This was evidently not the case. Zavareh and Samandari suggested that mechanisms such as crack pinning, particle bridging, crack path deflection, and energy absorption through microcracking work simultaneously in PEG toughened composites to retard damage events [97]. These theories were also backed up by Huang et al. [227] and Pearson and Yee [228]. Zavareh and Samandari also suggested that strong interactions between PEG and epoxy in the interfacial region may increase interlaminar bond strengths, but did not elaborate on these claims. These mechanisms operating to various degrees may have allowed PEG toughened composites to maintain load sharing capabilities between fibres and plies, and therefore allowed the laminates to maintain their stiffness to a higher degree than in unprinted laminates.

In PMMA printed samples, an opposite effect was observed. The tensile moduli of these samples was reduced slightly compared to the tensile moduli of unprinted samples. This was indicative that different damage mechanisms operate in PMMA and PEG printed samples because PEG samples showed an increase in both static strength and modulus. It was shown in Section 3.9.2.1 that PMMA forms a discrete phase from the surrounding matrix in cured samples. This ruled out the possibility of dissolved PMMA creating a tougher interlaminar region. A model which complied with the observed results was formed. The strength of PMMA printed laminates may be increased if the discrete droplets inhibit the development of interlaminar cracks, and hence maintain load sharing between fibres and plies. This may operate by one of three mechanisms:

1. Cracks are forced to circumvent the droplets, increasing their path length, and hence the fracture energy required to extend the crack.
2. Cracks extend through the PMMA droplets, which are tougher than the surrounding matrix because they are thermoplastics. Again, this would increase the energy necessary to propagate the cracks by yielding of the thermoplastic.
3. Droplets separate easily from the surrounding matrix either during cooling due to differing rates of thermal contraction, or by weak bonds between the phases. This would effectively create voids within the matrix. These voids may then arrest cracks by crack-tip blunting. This is analogous to findings by Brown et al. [229] who studied microcapsule toughened epoxy composites.

These mechanisms are illustrated in Figure 5.29. Of these mechanisms, it was theorised that a combination of ideas one and three fitted the observed data best. If the phases separate easily under strain then this may have provided a method of dissipating energy, potentially increasing the strength of the laminates. It may also result in crack tip blunting. However, it would equally decrease the stiffness because these weak bonds would be poor at transferring loads between plies. If the phases did not separate easily then stiffness would be maintained to a higher degree because retarded cracking coupled with the load sharing of connected phases would result in an overall stiffer laminate. This was not observed, indicating that the theory of weak polymer-matrix bonds seems promising.

It was hypothesised that this behaviour was not observed in PEG 20,000M_w (which was also shown in Section 3.9.2.3 to remain as discrete droplets) because the slight solubility of PEG 20,000M_w in 977-2 resin created a transition region around droplets, increasing the bond strength between the droplets and matrix. These theories provide one way of reasoning why the changes in strength and stiffness properties of PMMA printed laminates differed in nature to those of PEG printed laminates.

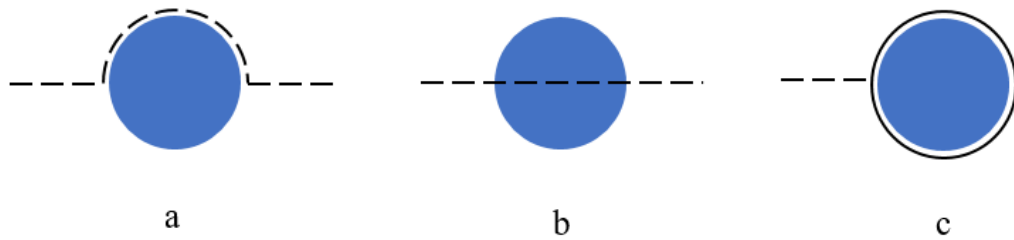


Figure 5.29: Possible crack mechanisms in PMMA printed laminates, where cracks are represented by dashed lines. a) A crack circumventing a droplet by travelling around its boundary, b) A crack propagating through a droplet, c) A crack meeting the separated interface of a droplet, halted by crack tip blunting.

In cyclic tensile testing in Section 5.4.1 it was shown that, just as in cyclic flexural tests, the fatigue lives of PMMA printed samples were less than those of unprinted samples. At lower stress factors this difference was as much as two orders of magnitude. These results matched very well with those of flexural samples obtained in Section 5.2.1. This indicated that fatigue life measurement was consistent. However, as previously stated, the damage mechanisms which caused this reduction could not be inferred from the fatigue life diagram alone because fatigue life is only a broad indication of material performance, and not of damage development, which was the key interest of this work. As in static tests, it should be noted that the samples used in these tests were produced in multiple batches. Therefore, variation in mechanical properties due to batch to batch variation should have been minimised.

Stiffness degradation (Section 5.4.2) was used as a primary method of evaluating the damage mechanisms taking place in samples. At high stress factors (0.8 to 0.7) it was found that PMMA printed samples did not differ from unprinted samples to any significant degree. Both sample types exhibited a sharp drop in stiffness, which in some samples was followed by a secondary period of decreased rate of degradation before ultimate failure.

At lower stress factors (0.7 to 0.5) it was observed that the period to failure was extended, and showed that samples exhibited three distinct phases of stiffness degradation (see Figure 5.34): an initial stiffness drop, a slower secondary drop, and a third phase of yet lower gradient that continued until sample failure or runout. These are hereby denoted as Phase Ia, Phase Ib, and Phase II. Similar behaviour was noted in experiments conducted by Ivanov et al. [230]. They attributed it to ‘a state of well-developed damage’, but did not attribute it to any particular damage mechanisms.

Theories which aim to explain the mechanisms behind these stiffness degradation phases are presented here, and are later supported by data presented in the following chapter. It was hypothesised that Phase Ia was caused by the rapid formation of transverse cracks (Section

2.3.1.1) in off-axis plies. This is often the first damage event to occur in multidirectional laminates [4], and is a result of the low tensile strength and strain to failure of off-axis plies.

Phase Ib was thought to be caused by the onset and propagation of delaminations (delamination was covered in detail in Section 2.3.1.3), particularly between the highly strained $0^\circ/90^\circ$ ply pairs. This theory is well supported by similar experiments conducted by Poursartip et al. [231] (described shortly) who also noticed similar behaviour and concluded that this stage was due to delamination. These delaminations would be seeded by the previously mentioned transverse cracks, a phenomenon also well noted by authors [65, 231, 232]. This idea is also supported by the fact that the most significant differences in unprinted and printed laminates occurred during Phase Ib. Because the inkjet printing method deposits material exclusively in the interlaminar region, changes to the mechanical properties of laminates would most likely be observed in damage mechanisms that operate in this region (particularly delamination).

Phase II was thought to occur when delamination was complete. A minimal stiffness decrease was still observed in this phase. This is most likely explained by work by Steif [233] who showed that fibre fractures in the 0° plies combined with debonding of the fibre/matrix interface leads to stiffness reductions of ‘typically a few percent’. This may explain why Phase II stiffness degradation was effectively identical in different sample types, because Phase II damage mechanisms would not be affected by the presence of printed polymers. However, the gradual delamination of adjacent plies with lower interface angles, such as at the $0^\circ/45^\circ$ and $90^\circ/45^\circ$ interfaces may also have been a contributing factor. Readers are reminded that the stacking sequence of tensile samples was outlined in Section 4.2.1. Figure 5.30 shows a typical example of a tensile specimen that was cycled to 1×10^6 cycles. It can be clearly seen when placed under compression by hand that a complete delamination was visible. This was at the $0^\circ/90^\circ$ interface. An identical delaminated surface also occurred at the second $0^\circ/90^\circ$ interface. In this sample, only minor delaminations of other interfaces were visible.



Figure 5.30 Example of a fatigued tensile specimen cycled to 1×10^6 cycles. Compressive force was applied to the ends of the specimen by hand in order to open and emphasize the delamination.

Work conducted by Poursartip et al. [231] bears excellent resemblance to the results obtained in Section 5.4.2 (particularly at a stress factor of 0.5). Their stiffness degradation results at a stress factor of 0.56 are shown in Figure 5.31. They used a similar $[45/90/-45/0]_s$ layup (compared to the $[45/0/90/-45]_s$ layup used in this work). From their results they also identified that their specimens experienced an initial stage of rapid stiffness degradation, followed by a second linear stage of reduced gradient, and a third stage of yet further slowed degradation. They attributed the first stage to transverse cracks in off-axis plies, and the secondary stage to delaminations that were seeded by transverse cracks, exactly as was theorised above. Delaminations formed at the sample edges due to edge stresses and then propagated inwards. They observed that at higher stress factors, the delaminations in this second stage caused off-axis plies to be freed from loading, and this eventually led to the ultimate failure of samples due to fibre fractures in the now overloaded 0° plies. Where the stress factor was sufficiently low as to not allow fracture of the remaining load bearing plies, a third stage developed which was caused by fibre fractures and fibre/matrix debonding. This stage resulted in stiffness reductions of ‘typically a few percent’. These results match very closely the results obtained in Section 5.4.2, and their conclusions as to the mechanisms which caused the changes are identical to those theorised here. Furthermore, their stacking sequence was very similar to that used here. However, the way in which they used this information differed to the approach taken in this thesis. Whilst they acknowledged the difference between their results and the standard model of stiffness degradation (described in Section 2.6.1), they used their results to develop numerical models of damage level evolution. They did not consider the further applicability of their results to the general model of damage mechanisms in stiffness degradation.

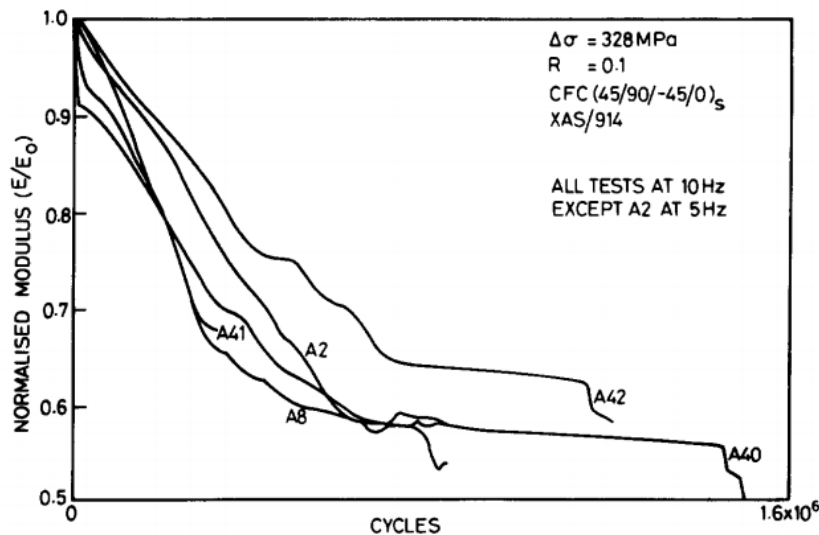


Figure 5.31 Stiffness degradation curves obtained by Poursartip et al. for $[45/90/-45/0]_s$ laminates at a stress factor of 0.56. These curves show excellent resemblance to the stiffness degradation curves obtained in these tests.

Somewhat similar behaviours were observed by other authors [141, 234], including Van Paepegem and Degrieck [131], who noted such experimental stiffness degradation data as that shown in Figure 5.32. Their results show more curvature in the Phase Ib region than results presented in Section 5.4.2, but a slight linearity may still be observed there. This is most likely due to the lack of off-axis plies in their specimens, since they used unidirectional 0° flexural specimens.

They based their interpretation of their results upon the widely used model of stiffness degradation shown in Figure 5.33, which was developed in part by Schulte [235-237] and Reifsneider [134, 140, 238]. This features three phases of stiffness degradation, but at different points to those proposed here. The region denoted as Stage I is often broadly attributed to a collection of damage mechanisms operating simultaneously rather than damage mechanisms which operate at different rates and which causally affect each other. It is likely that little attention is paid to stiffness degradation in the initial cycles because it represents such a small proportion of the stiffness degradation curve. It therefore goes unobserved that the area denoted as Stage I may be further divided. And even in work by Reifsneider et al. [140], who were forerunners of this model, results they obtained bear more resemblance to the results presented in Section 5.4.2 than to the subsequent model that they developed. Gradual transitions between phases due to minimal disparity between the orientations of adjacent plies may also hide these separate phases, making them appear to be one.

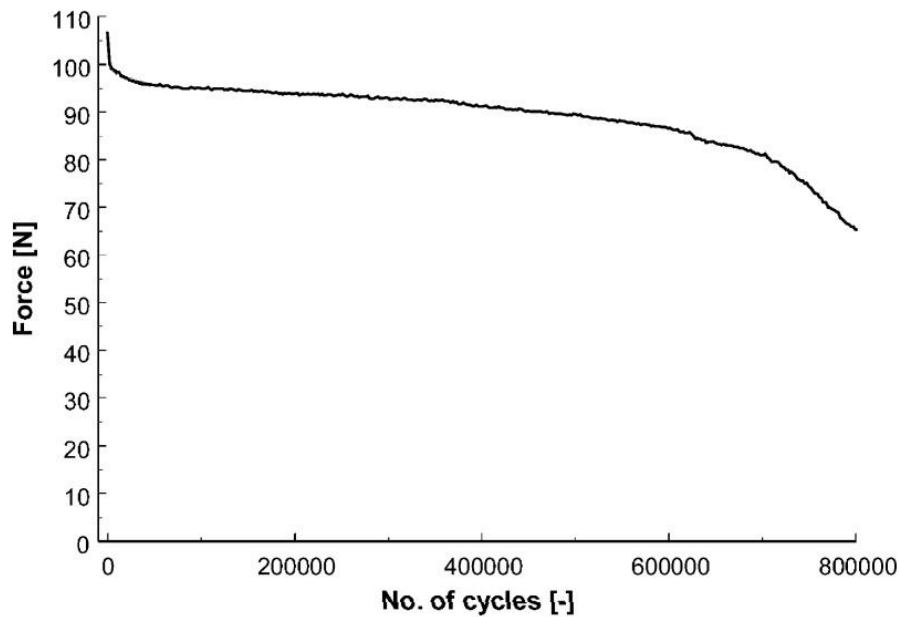


Figure 5.32: Experimental stiffness degradation data obtained by Paepegem and Degrieck [131]. Taken from fully reversed flexural fatigue tests on unidirectional samples.

A new proposed format of this model based on experimental results obtained in these tests divides the phase described in Figure 5.33 as Stage I into two separate stages (or phases) in which matrix cracking and delamination in off-axis plies occur sequentially rather than simultaneously. The initial phase is split into Phase Ia and Ib rather than I and II in order to convey that these phases are not entirely independent. In multidirectional laminates matrix cracking and delamination may occur simultaneously to a degree, although matrix cracking in off-axis plies tends to precede delamination. In unidirectional laminates, a single curved Phase I may be most appropriate as Figure 5.33 shows. However, even in unidirectional laminates, matrix cracking and delamination would still occur sequentially. But subsequent matrix cracking may still occur whilst delaminations are forming. An illustration of this is shown in Figure 5.34. This model features four phases, although in these tests only three were actually observed. The final phase was added in order to make it applicable to a wide range of tests, many of which do feature a final stiffness drop due to accelerated damage and fibre failures; for example, the data collected by Van Paepegem and Degrieck [131] in Figure 5.32.

It is anticipated that this new model will extend the functionality of stiffness degradation beyond a broad indication of residual mechanical properties, allowing further insight into the damage mechanisms which cause such changes. It should be noted that this model in its current form may not necessarily be applicable to unidirectional laminates. This is due to their lack of off-axis plies, causing them to experience a different series of damage mechanisms to those described here.

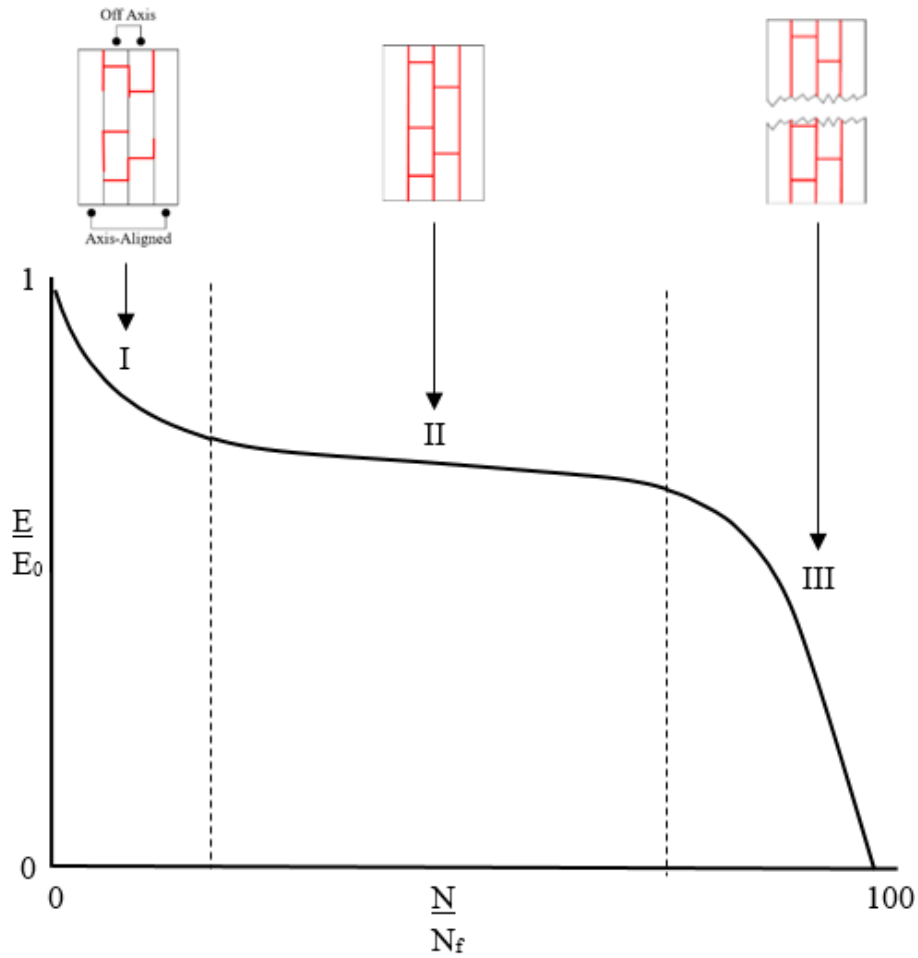


Figure 5.33: Typical stiffness degradation curve for a wide range of fibre-reinforced composite materials. Based on work by Nijssen [141]. This curve is considered to have three phases (I, II, and III) which are not mutually exclusive. The damage mechanisms operating in these phases are: I) Matrix cracking and delamination in off axis plies, II) Delamination growth and interfacial debonding, III) Fibre fracture and crack coupling resulting in ultimate failure. These mechanisms are also shown in the figure, where red lines indicate cracks and delaminations.

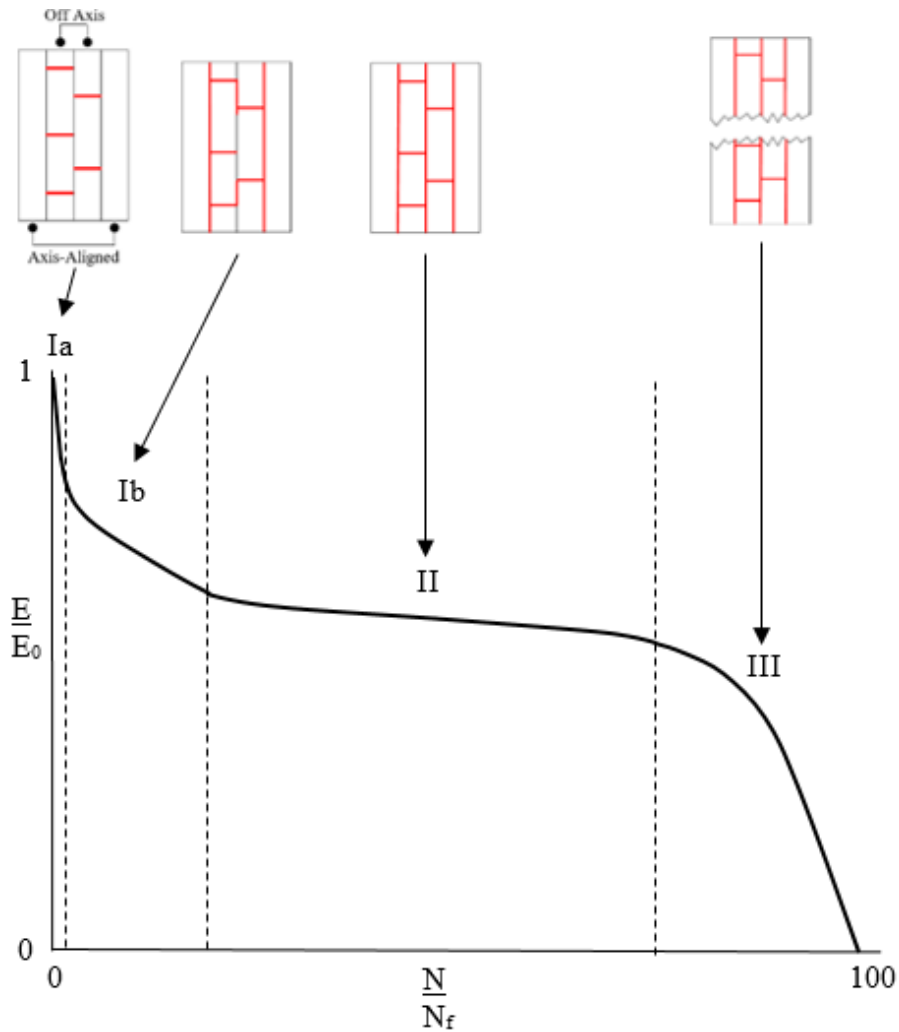


Figure 5.34: Newly proposed model of stiffness degradation in composites. This curve recognises the same phases as the above figure, but further divides phase I into two (Ia and Ib) in which matrix cracking and delamination are sequential. The damage mechanisms operating in these phases are: Ia) Matrix cracking, Ib) Delamination at off-axis ply boundaries, II) Continued delamination growth and interfacial debonding, III) Fibre fracture and crack coupling resulting in ultimate failure. These mechanisms are also shown in the figure, where red lines indicate cracks and delaminations.

Differences in both initial stiffness and stiffness degradation rates of the sample types were increasingly noted at stress factors between 0.7 and 0.5. At a stress factor of 0.6 a significant degree of difference was observed (Figure 5.21), showing that PMMA printed samples degraded more rapidly than unprinted samples. This was further observed at a stress factor of 0.5 (Figure 5.23). And at this point such noticeable and repeatable effects were visible that PEG printed samples were introduced to the testing regime in order to study their properties in cyclic loading.

It was shown that at a stress factor of 0.5, sample types exhibited very different behaviours, particularly in Phase Ib of stiffness degradation. Figure 5.26 and Figure 5.27 illustrated these

results. Applying the theories regarding damage mechanisms under static loading conditions suggested above, the reasons for key differences may be inferred. This must be the case, as no literature currently exists on PMMA or PEG polymers used as toughening agents in composite fatigue.

Firstly, unprinted samples showed a Phase Ia stiffness drop of approximately 9% due to transverse cracking. This was followed by a further 28% reduction in Phase Ib. The transition from Phase Ia to Phase Ib was gradual, indicating that delaminations began propagating to some degree before transverse cracking was completed. This was also true in all other sample types. This may be expected because delaminations would begin to form as soon as transverse cracks reached ply interfaces, but before saturation of transverse cracks was complete. Once transverse cracking was completed, delamination was the dominant damage mechanism. Delamination may occur at all ply interfaces, but would have occurred most rapidly at highly strained interfaces. In this case, at the $0^\circ/90^\circ$ interfaces, as previously shown in Figure 5.30. The progression of these $0^\circ/90^\circ$ delaminations was highly linear, indicating little variation in the rate of the process. Once complete, only minor fibre/matrix debonding and minor delaminations at other ply interfaces remained active damage mechanisms, producing what was seen in Phase II.

PMMA and PEG 1,500M_w samples exhibited very similar behaviours at a stress factor of 0.5 (Figure 5.26 and Figure 5.27). In Phase Ib their stiffnesses dropped on average a rate of around four times faster than was observed in unprinted samples. Yet their Phase Ia and Phase II gradients were almost identical to that of unprinted samples. This heavily indicated that the introduction of these polymers negatively affected delamination in these laminates, whilst other damage mechanisms remained relatively uninfluenced. It was shown in Section 3.9.2 that the different types of printed droplets behaved differently when cured within 977-2 resin, with PMMA remaining as discreet droplets, and PEG 1,500M_w fully dissolving into the matrix. Therefore different mechanisms were obviously responsible for their behaviours. In PMMA printed laminates it was previously proposed that PMMA formed weak bonds with the surrounding matrix providing a method of energy dissipation. In static loading (effectively a single loading cycle) this was beneficial, but under multiple loading cycles, the interface between PMMA droplets and the matrix would gradually fracture, effectively creating voids. These voids would then provide a path of interlaminar stress concentrations that delaminations would follow. If this were true then Phase Ib in PMMA laminates would increase in gradient over time as the energy dissipation effect of the droplets was exhausted, and delamination accelerated due to void formation. This effect is exactly what was observed in PMMA laminates (Figure 5.27).

It was shown in Section 5.3 that both the static strength and modulus of PEG 1,500M_w laminates was increased, most likely due to the toughening effects caused by the addition of the polymer. Assuming a homogeneous distribution of the PEG in the interlaminar region (which may rightly be assumed given observations in Section 3.9.2.2), the toughening effect caused by the addition of PEG should also have resulted in the retardation of fatigue damage mechanisms. This was not the case however. No literature exists on the toughening effects of PEG in fatigue. Therefore, damage mechanisms must be inferred from the results obtained here.

The key difference between static and cyclic tests was the applied strain rate. Viscous heating caused by high strain rates may have lowered the strength of the blend (since the strength of low molecular weight PEG is highly dependent upon temperature [179]). In cyclic tests, temperature rises of up to 3.5°C (peak temperature 29.5°C) were observed in PEG 1,500M_w samples during Phase Ib of stiffness degradation. Whilst low, this temperature may have raised the polymer very close to its melting point of 43-49°C [183], and it is therefore possible that this resulted in a significant decreases of strength and stiffness of the blend. It was also described in Section 2.3.1.3 that in ductile matrices the thickness of the resin-rich region is of particular importance. In ductile matrices the process zone of cracks are larger than in brittle matrices, allowing greater levels of energy dissipation. However, if the resin-rich region is thinner than the size of the process zone, then the process zone becomes elongated, driving it further forward, increasing the rate at which cracks propagate [63]. This may have played a role in PEG 1,500M_w samples, but because similar behaviours were not observed in PEG 20,000M_w samples, it is more likely that temperature effects were the greater cause of increased delamination rates.

PEG 20,000M_w samples differed greatly from PEG 1,500M_w samples, exhibiting behaviour more similar to that of unprinted samples. Firstly, unlike other sample types, their Phase Ia stiffness degradation was very large, being on average around 15% of their initial value. Nearly double that of all other sample types (7% in unprinted samples). Because it was established that Phase Ia was primarily caused by transverse cracking, this meant that PEG 20,000M_w samples would have exhibited more transverse cracking than other sample types. This is a theory which will be discussed in the following chapter. This may have been caused by strong interlaminar bonds which resisted shear strains between plies. This is in line with results obtained by Zavareh and Salmandari [97], who conducted interlaminar fracture toughness tests upon PEG toughened epoxy polymers, and attributed increases in toughness to strong PEG/epoxy interactions which resulted in increased interfacial bonds. This is also evident from the high static stiffness values of these samples which were shown to be on average 10.2% higher than unprinted samples (Section 5.3). As a result, transverse cracks may

have developed quickly as a consequence of the constrained and hence highly strained off-axis plies.

During Phase Ib, PEG 20,000M_w samples exhibited an average rate of stiffness degradation significantly lower than that of unprinted samples, with PEG 20,000M_w samples decreasing at around 20.7kPa per cycle, and unprinted samples decreasing at around 39.1kPa per cycle. Just over half (0.52 times) the rate of unprinted samples. And this was achieved despite the possibly higher degrees of transverse ply cracking. If transverse cracking were reduced, then it is likely that this rate would be reduced further. By comparison, the average rate of stiffness degradation in PMMA and PEG 1,500M_w samples was found to be 149.0kPa per cycle and 148.1kPa per cycle respectively. Therefore, both experienced stiffness degradation approximately 3.8 times more rapid than in unprinted samples. This therefore indicates that the addition of PEG 20,000M_w was beneficial to the retardation of delamination in laminates, but PMMA and PEG 1,500M_w were not.

It was suggested that temperature effects played a role in the increased rate of stiffness degradation due to delamination in PEG 1,500M_w samples. Such detrimental effects were not found in PEG 20,000M_w samples. The melting temperature of PEG 20,000M_w is 58-63°C [178]. In cyclic tests, a peak temperature rise of 2.2°C was recorded (peak temperature 31.1°C), similar to the 3.5°C increase recorded in PEG 1,500M_w tests. Due to the higher melting point of PEG 20,000M_w, temperature evidently played a much less significant role. This appears to suggest that even higher molecular weight PEGs may exhibit even better toughening capabilities, particularly in warmer service environments.

It was also discussed how the increased ductility of PEG 1,500M_w blended with the epoxy matrix may have led to an enlarged process zone, which was then constrained by the fibres either side of it, extending it further forward into the laminate, and increasing the rate of delamination. If the ductility of the matrix in PEG 1,500M_w samples was suitably high as to allow this mechanism to have a significant effect then it is likely that it would be much less pronounced in PEG 20,000M_w samples. The much higher molecular weight of PEG 20,000M_w would introduce much less ductility into samples. Furthermore, it was shown in Section 3.9.2.3 that PEG 20,000M_w droplets exhibited some degree of dissolution, but generally remained as discreet droplets in the matrix, with a transition boundary between themselves and the matrix. This would limit the ductile regions of the matrix to areas in the centre of the resin-rich region, allowing areas of high energy dissipation, but maintaining a small process zone that would not be constrained and driven forward.

It is clear from these results that despite the high Phase Ia stiffness degradation of PEG 20,000M_w, these samples appeared to be successful in retarding the development and/or

propagation of delaminations. Although the mechanisms that caused this are theoretical, the evidence presented thus far very much supports these assumptions.

In these tensile tests, a stacking sequence was used which deliberately introduced interlaminar shear strains by the placement of greatly differing orientations between adjacent plies in order to induce delaminations. This invariably caused transverse cracks to develop, which in turn further encouraged delamination. However, it was also discussed above that rapid transverse crack formation was most probably the cause of large Phase Ia stiffness degradation in PEG 20,000M_w samples, which accounted for a large proportion of the total stiffness drop of those samples. Gamstedt and Andersen [80] discussed that if the off-axis plies contribute to a substantial part of the laminate, the damage that develops in those plies will lead to damage evolution in the longitudinal plies. Therefore, in in-service composite parts, designers typically avoid such high angular disparities and numbers of off-axis plies in order to reduce damage. It is therefore noteworthy that if more typical stacking sequences were used, then it is conceivable that PEG 20,000M_w laminates would not experience such large Phase Ia stiffness losses, and would therefore outperform unprinted laminates to an even greater degree. Further investigation would be necessary to prove this theory, but this was not conducted as part of the work done in this thesis.

5.6 CONCLUSIONS

In this chapter, the results of tests relating to the fatigue of inkjet printed composites were presented and discussed.

Both static and cyclic tests were conducted on printed and unprinted samples. Firstly, four point bending tests were conducted. Results showed that in static flexural tests, neither the flexural strength nor stiffness of laminates was influenced by the printing of 10%/wt PMMA in DMF ink. In cyclic flexural tests it was observed that PMMA printed samples exhibited significantly shorter fatigue lives than unprinted samples, being around one order of magnitude shorter in most cases, and showing that the fatigue lives of printed samples were at detriment because of the introduction of PMMA. Despite the successful formation of delaminations in cyclic flexural tests, it was found that the stiffness degradation curves that were obtained were difficult to interpret and showed low repeatability. Further investigation using scanning electron microscopy found that issues were most likely caused by fatigue cracks in the through thickness direction which originated from the loading rollers. These cracks contributed to the stiffness degradation of samples, creating uneven and unreliable curves. Following these results, tensile testing was introduced as a potentially more reliable

method of promoting delaminations whilst avoiding undesirable artefacts caused by test geometry. Flexural tests provided invaluable test data, baseline values, and experimental techniques that were carried forward when developing the tensile testing regime, and helped attain much more meaningful and repeatable data. The fatigue lives of these samples were also in agreement with those of tensile samples, providing some validation of the tensile testing method.

Static tensile tests results showed that the static tensile strengths of all printed samples were greater than those of unprinted samples. The tensile strengths of unprinted, PMMA, PEG 1,500M_w, and PEG 20,000M_w samples were found to be 633MPa, 668MPa, 657MPa, and 664MPa respectively. Similarly, the tensile moduli of these samples (in the same order) were 34.2GPa, 30.0GPa, 34.0GPa, and 38.4GPa, showing that the tensile stiffness of laminates was reduced by the inkjet addition of PMMA, but increased by the addition of PEG. Different mechanisms for these properties were proposed, and were supported by evidence from literature, experimental data, and optical microscope observations of resin printed slides obtained in Section 3.9.2.

In cyclic tensile tests, stiffness degradation was found to yield very reliable results, particularly at low stress factors. Therefore, further tests focussed on this particular region of stress. Analysis of stiffness degradation curves showed that curves exhibited three distinct phases of stiffness degradation which defined the start and end of the active periods of particular damage mechanisms. This was contrary to the typical model that many authors use. However, other authors had also observed such behaviours, but failed to recognise the significance of the observations with respect to understanding micromechanical damage mechanisms. A new model of stiffness degradation was therefore proposed which recognises these distinct phases.

It was found that both PMMA and PEG 1,500 exhibited very similar stiffness degradation. However, both proved detrimental to delamination, both decreasing at rates approximately 3.8 times faster than unprinted samples in the delamination phase of tests. PEG 20,000M_w samples however, showed improved delamination resistance. Stiffness degradation due to delamination in PEG 20,000M_w samples was shown to be approximately 0.52 times the rate experienced in unprinted samples; a very significant improvement. A consequence of this improvement was increased levels of transverse cracks in off-axis plies, resulting in greater initial stiffness degradation than in all other sample types. Although it was theorised that stacking sequences which reduce the strain differences between plies may improve this issue.

Theories of the mechanisms which give rise to the different behaviours exhibited by samples were proposed. These were supported either by empirical data and observations from

literature. The following chapter aims to substantiate these theories where possible using microscopic analysis.

CHAPTER 6: FRACTOGRAPHY AND CRACK DENSITY ANALYSIS

This chapter presents results obtained by scanning electron microscope (SEM) observations of fatigued specimens and the cellulose acetate replicas taken from them. These results aim to extend the hypotheses developed in the previous chapter relating to damage mechanisms in fatigue, and also to resolve gaps in the understanding of those damage mechanisms.

6.1 INTRODUCTION TO SEM

SEM, which was previously described in Section 2.6.3, is the most widely used method for studying fracture surfaces. The high resolution and good depth of field of the images it produces make it highly suitable for examining polymer composite surfaces. Also, due to the way SEM works, the images it produces are similar in appearance to optical images, making them more intuitive to interpret [5]. Microscopic methods not only provide a quantitative measure of such things as crack length, no matter how small the crack may be, but they can also identify the path that cracks take and their relationship to microstructural parameters [142].

With carbon fibre reinforced composites, which are opaque to many forms of radiation, the only macroscopic evidence of fatigue may be the presence of surface splitting or delamination. Such features however, also occur under static loading, and therefore the only practical method of distinguishing them is by a detailed examination of the fracture surfaces using optical or scanning electron microscopy [5]. SEM is therefore very commonly used in composite fatigue since it allows some insight into fatigue crack initiation and progression.

6.2 EXPERIMENTAL PROCEDURES

It was found in Section 5.4.2 that key differences between samples occurred in tensile specimens at a stress factor of 0.5. It is here then that was the focus of these observations. This chapter focusses on two main investigations: the fractographic analysis of delaminated surfaces from fatigued tensile test specimens, and the crack densities of acetate replicas taken from the edges of those same tensile specimens.

6.2.1 *Fractography*

One of the main uses of SEM in the context of mechanical testing is in fractography; which is the study of fracture surfaces. Fractography can provide important clues about the cause of failure in a component, the location of the source of failure, and the consequent sequence of events that then resulted.

Observations focussed on ply interfaces which delaminated during cyclic testing conducted at a stress factor of 0.5. Due to the stacking sequence of the laminates used in cyclic tensile tests (Section 4.2.1), the 0°/90° interfaces of samples exhibited far more rapid and severe delamination than others, and were likely the primary cause of stiffness degradation due to delamination because their delamination effectively isolated all other plies from the load bearing 0° plies. The perpendicularity of the 0°/90° plies also made features easier to identify and follow. 90°/45° ply interfaces may also have been selected as they also experienced delamination to some degree, but were disregarded because of concerns that the orientations of fibres may have made artefacts and crack paths more difficult to identify. Therefore, 0°/90° interfaces were chosen for observation.

6.2.1.1 *Preparation of Specimens*

Because SEM uses charged particles to observe samples, it was important that samples used in SEM were electrically conductive. Many modern SEMs have the ability to scan non-conductive materials, but at the detriment of resolution. This is because negative charges build up on the material and repel incoming electrons. For metallic samples this is obviously not a problem, but CFRP is only partially conductive. The carbon fibres themselves are conductive, but the matrix usually is not. And since the matrix insulates the fibres, good conductivity is only really possible along the axis in which the fibres travel. In these tests, high resolution was very much required. Therefore, samples were treated to make them electrically conductive. This was achieved by gold vapour deposition, or ‘sputtering’.

CFRP samples were first cut to an appropriate size. This was done using a diamond cutting saw, avoiding carbon fibre dust infiltration as much as possible. The saw used water as a method of reducing carbon fibre dust released into the atmosphere. Samples were cut with a minimal amount of water in order to avoid dust being washed into cracks. Afterwards, samples were lightly rinsed with clean water and immediately placed in an oven at 50°C until dry.

The dimensions of the samples were limited by the SEM chamber size and the range of movement of the mounting stage. The chamber size of the microscope that was used allowed

reasonably large samples of up to 150x150x30mm (length x width x height), but the observable area was limited further by the movement range of the stage. This limited samples to approximately 70x70x20mm. This meant that samples had to be cut, and therefore destroyed in order to fit them into the SEM chamber. The chosen dimensions of delaminated surface specimens were 25x40mm. These dimensions were chosen to decrease the amount of time spent gold coating. The sputterer's chamber could accommodate larger specimens, but this meant that only one could be coated at a time. Using these dimensions, three could be coated at once.

Cut specimens were mounted on brass specimen stubs (Agar Scientific) similar to what is shown in Figure 6.2. Acheson silver DAG (Agar Scientific) colloidal silver suspension was used as an electrically conductive adhesive to bond the specimens to the specimen stubs. It was applied sparingly to both the specimens and stubs using a fine tipped paint brush, and the two were then joined. The solvent evaporated quickly, bonding the two together.

After mounting, specimens were coated in a nanometre thick coating of elemental gold. This was done using a gold sputterer (Figure 6.1). Specimens were placed inside the vacuum chamber of the machine underneath a gold 'target'. The air was then evacuated, and replaced with a low pressure argon atmosphere. A voltage of around 15kV was applied to the gold target, ejecting gold particles in the form of plasma, which collided with the specimens, evenly coating them. Coating was carried out for 3 minutes at 15kV on all specimens. The result of gold sputtering upon delaminated CFRP samples may be seen in Figure 6.27, and a further gold coated edge specimen is shown in Figure 6.2.



Figure 6.1: Emscope SC 500 gold vapour deposition machine

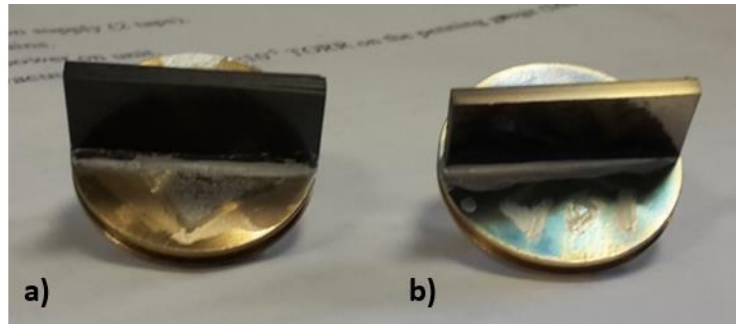


Figure 6.2: Examples of carbon fibre composite samples mounted on brass SEM specimen stubs a) before gold coating, and b) after gold coating. These samples were used for the observation of cracks propagating through the width of specimens.

6.2.1.2 SEM Observation of Fracture Surfaces

SEM observations were carried out using a Hitachi TM3030Plus tabletop microscope, shown in Figure 6.3. This microscope had the ability to observe non-conductive specimens. But it was found that the resolution of the images produced was negatively affected to a significant degree above magnifications of around 500x. Therefore, high magnification observations necessitated the use of gold coating.

SEM settings were adjusted from specimen to specimen as necessary, although it was generally found that specimens of the same type worked well with similar settings. For high magnification (>500x) gold coated specimens, which were primarily used for fracture surface observations, a mixed analysis mode was used. This mode combined topology and material composition information. Although material composition was not required, it was found that the addition of this information increased the image contrast of certain features, allowing for easier interpretation. This analysis mode was used in conjunction with an electron acceleration voltage of 20kV.

The observation angle of SEM specimens can affect the visibility of certain features. However, changing the viewing angle of specimens greatly reduces the observable area. In these tests, a perpendicular viewing angle was used.

The observation of fracture surfaces was straightforward. The surfaces were viewed, and interesting features were scanned at maximum resolution and the images stored for later analysis.

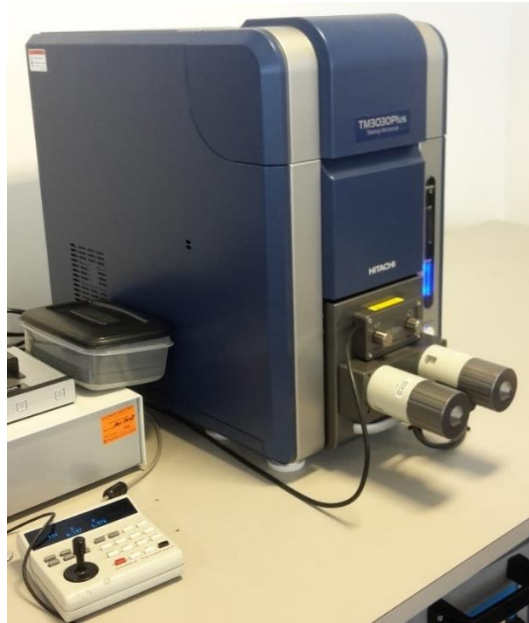


Figure 6.3: Electron microscope used for microscopic analysis. Hitachi TM3030Plus tabletop microscope.

6.2.2 Crack Densities

Cellulose acetate replicas were taken from many of the cyclically loaded tensile specimens tested at a stress factor of 0.5 in Section 5.4. The procedure for the physical replication of samples was previously outlined alongside the procedure for cyclic tensile testing in Section 4.2.3. Records were kept of which edge the replicas were taken from, the number of cycles, and the specimen number. Replicas were taken at 0, 5k, 10k, 20k, 40k, 60k, 80k, and 100k cycles on both edges of the specimen. These intervals were chosen in order to effectively capture the development of damage in different phases of stiffness degradation whilst keeping the number of replicas required to a minimum. Stiffness degradation phases were previously described in Section 5.5.2. In all samples, Phase Ia of stiffness degradation transitioned into Phase Ib between 5k-20k cycles, so 5k cycles was chosen as the first sample point. Taking replicas at 10k and 20k cycles aimed to capture the transition between Phases Ia and Ib. After this point, all other replicas aimed to capture the propagation of delamination. No replicas were taken after 100k cycles because after this point all sample types had either completed Phase Ib of stiffness degradation or were in the later stages of it. It was also observed in early replicas that crack saturation occurred in all samples around this point. Therefore, taking replicas past 100k cycles was deemed unnecessary.

6.2.2.1 *Preparation of Samples*

As described in Section 6.2.1.1, sample dimensions were limited by both the size of the SEM chamber and the range of the movable mounting stage. Because the replicas had to be mounted to a flat rigid base, glass microscope slides were used. These had dimensions of 76x26mm, which was ideal for the limitations of the SEM. Replicas were cut to this size simply using scissors. To keep the replicas flat, they were fixed to the glass microscope slides using double sided adhesive tape. These slides were then mounted on the specimen stubs in the same way as CFRP specimens in Section 6.2.1.1.

Due to the large numbers of replicas that were used in these tests, gold coating was not used in order to greatly reduce sample preparation time. Initial tests showed that below approximately 500x magnification the resolution of the images captured was suitably high for crack density analysis. However, to aid electrical charge dispersion, a track of silver DAG was painted from the specimen stub, around the glass slide, and onto the acetate sheet to ensure good conductivity from the observation site to the specimen stub, ensuring that the regions to be observed were not covered. A specimen prepared in this way may be seen in Figure 4.23 (Section 4.2.3).

6.2.2.2 *SEM Observation of Replicas*

The SEM observation of replicas was almost identical to that outlined in Section 6.2.1.2 for CFRP specimens, and also used the Hitachi TM3030Plus tabletop microscope. For lower magnification images, which were generally used for uncoated acetate replica observations, it was found that a topology analysis mode produced the greatest differentiation of cracks. This was used alongside an electron acceleration voltage of 15kV.

Settings were adjusted as necessary in order to acquire clear images. A magnification of 80x was used for every scan in order to make the measurement of cracks as straightforward as possible. This magnification was chosen as it was the maximum that could be used whilst still providing a full view of all the laminae. Additionally, the height of the mounting platform was kept the same for every replica so as to not change the observable dimensions between specimens.

Accuracy was of great importance in measuring crack densities. Cracks occur stochastically, so it was essential to take measurements from a large representative selection of samples. Two of each sample type from cyclic tensile tests at a stress factor of 0.5 were observed. But of these, replicas from both sample edges were used, and at five evenly spaced locations along

the maximum observable length (limited by the range of the movable SEM stage to 70mm) of each replica. Therefore, for any given data point, a total of twenty crack density measurements were taken. The points at which micrographs were taken were the same for every replica. The maximum observable length of replicas was limited to 70mm, so micrographs were taken at five evenly spaced points along this length. This was achieved by setting the locations in the SEM stage controller's memory. If the view at a chosen location was obscured due to poor replica quality then the view was moved to the nearest available location where the replica quality was good enough to allow unobscured visibility.

Figure 6.4a shows an example of a typical replica micrograph acquired in the following tests. Individual plies were clearly visible due both to their differing fibre orientations, which deflected/absorbed electrons in different ways, and also due to the thin line created by the resin-rich region between plies. In Figure 6.4b each ply is labelled. This stacking sequence was the same in all samples used in tensile tests, and was previously described in Section 4.2.1. It may be seen that the outermost -45° plies are only just visible in this micrograph. This was due to limitations in the set magnifications of the SEM. Lower magnifications were available which would have enabled a complete view of the thickness of replicas, but the next lowest magnification was 40x, and would have reduced the resolution of visible cracks to a degree that would have made crack measurements extremely challenging. On the very infrequent occasions where cracks or delaminations were observed in the outermost plies, they were measured, and the values were recorded for later analysis.

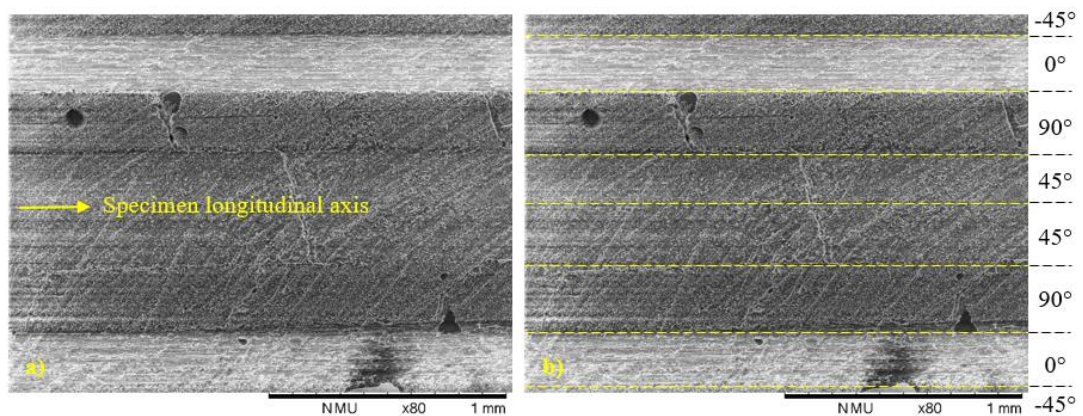


Figure 6.4 Example SEM micrograph of an edge replica. a) Unmodified image, and b) the same image with the individual plies labelled.

6.2.2.3 *Measurement of Cracks*

The measurement of cracks was done using ImageJ Fiji; an open software platform for scientific image analysis. Images were imported into the software, and two types of measurements were recorded.

The software's built in measurement tool was used to measure the length of any cracks or delaminations that were present. A representative replica micrograph is shown in Figure 6.5a, and the same micrograph is shown in Figure 6.5b overlaid with lines representing cracks and delaminations. The measurement of cracks was conducted in a similar way in ImageJ, measuring the lengths of the individual line segments and summing them to get total crack lengths. The length of cracks was recorded, as well as their location (e.g. 0/90° delamination or 45° ply crack). Where cracks were not completely linear, it was necessary to use multiple line segments to achieve a suitably high degree of fit. It was also necessary in many cases to interpret the point at which cracks terminated. This interpretation was manual, and was limited by the resolution of the micrographs. Crack tips were defined as being the furthest point along the length of a crack that could definitively be identified beyond reasonable doubt as being part of the crack. If there was uncertainty past a certain point, then anything past that point was disregarded.

The values obtained from these measurements were subsequently transformed into crack density measurements by dividing the lengths of the desired type of crack by the measurement area. These values had units of mm^{-1} . Because the same magnification (80x) was used for all scans, the length of the observed area was constant (2.126mm). The height used was the thickness of the samples. Sample thicknesses varied slightly, but for consistency across measurements the sample thickness was considered to be the 2mm dictated by the tensile test standard [239]. The crack density values from each micrograph were then averaged to obtain statistically average values at each of the replicated damage states for each sample type.

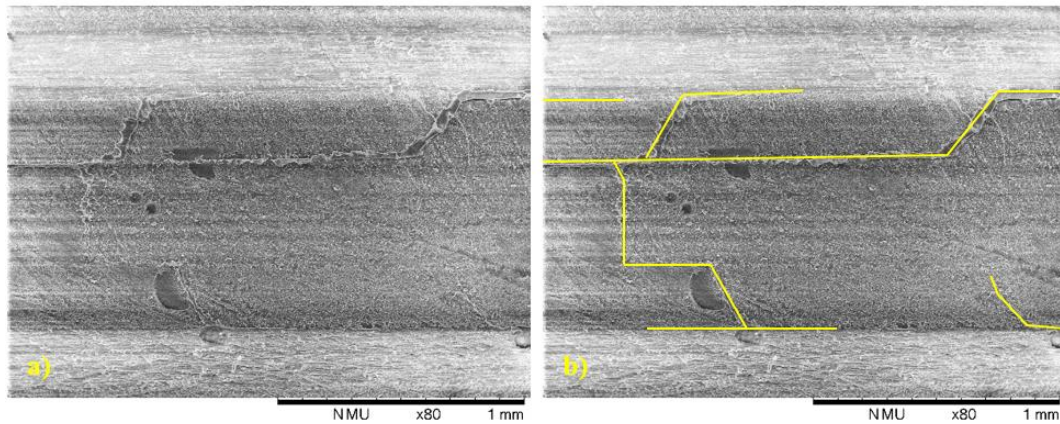


Figure 6.5 a) A typical replica micrograph displaying both transverse cracks and delaminations. b) The same image overlaid with lines indicating the locations of cracks and delaminations

6.3 EXPERIMENTAL RESULTS

6.3.1 *Fractography*

Section 2.6.4 previously described visual artefacts that are common to such samples as these. The information gathered in that section was carefully considered when analysing the fracture surfaces of samples and deciding which artefacts were most noteworthy.

In all images presented in the following sub-sections, arrows in the lower left corners of figures denote the direction of fibres in the given ply. The longitudinal (loading) axis of all samples runs horizontally across the images. Therefore, a horizontal arrow would always denote a 0° ply (with respect to the longitudinal axis), and a vertical arrow a 90° ply.

6.3.1.1 *Unprinted Laminates*

This section presents key observations from the delaminated surfaces of unprinted laminates so that changes due to printed polymers may be identified in later sections. Notable features are described here, but their significance and implications relating to the results obtained in previous chapters are discussed further in Section 6.4.1.

Figure 6.6 shows typical representations of the delaminated surfaces of both 0° and 90° plies at relatively low magnifications. Arrows represent the orientation of the fibre reinforcements. These surfaces feature many of the artefacts described in Section 2.6.4. For example, Figure

6.7 shows typical cusps (Section 2.6.4.2) on the 0° surface. They were seen to be well defined and small, possibly indicating that the matrix failed in a brittle manner.

In these samples, the differing Poisson's ratios of the plies created tension in the 0° ply, and compression in the 90° ply. The matrix dominated surface was primarily the 90° (compressive) surface, with only isolated areas being the reversal of this. As described in Section 2.6.4.1, this is typical behaviour of untoughened composites.

Additionally, little evidence was observed of material toughening. No fibrillation (Section 2.6.4.5) or excessive deformation of the surfaces was seen. And rollers (Section 2.6.4.4) appeared short and unsmearred; even appearing to have been fragmented easily by fretting, further indicating the relatively brittle nature of the unprinted composites as expected.

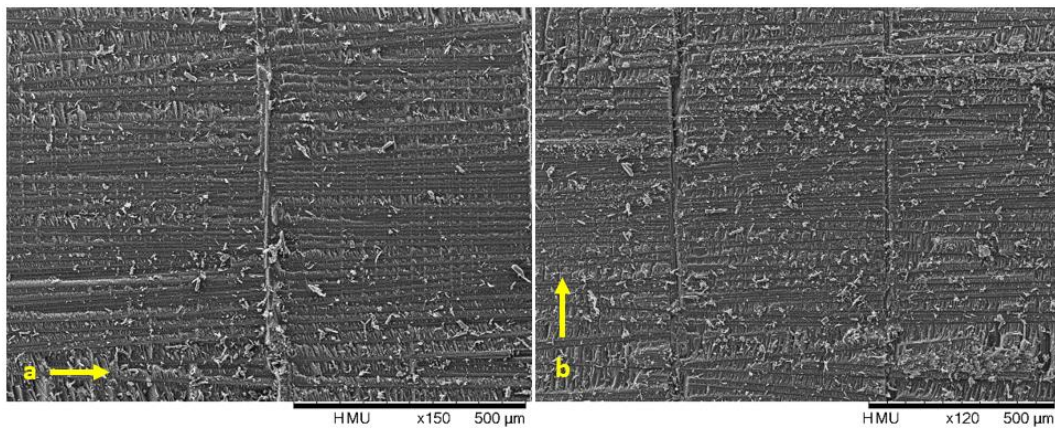


Figure 6.6 Unprinted sample a) 0° delamination surface, b) 90° delamination surface

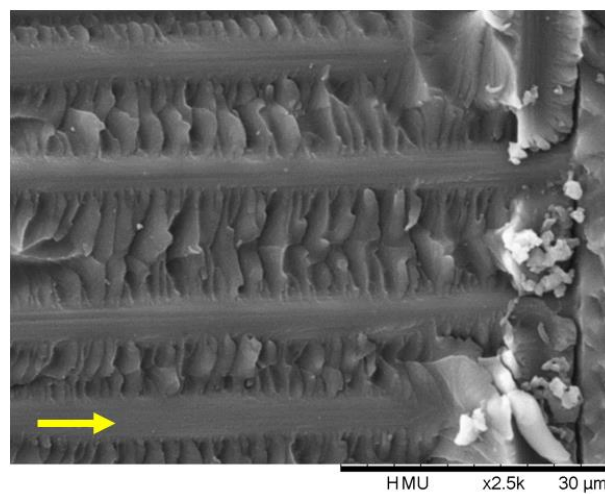


Figure 6.7 Cusps on the 0° surface of an unprinted specimen

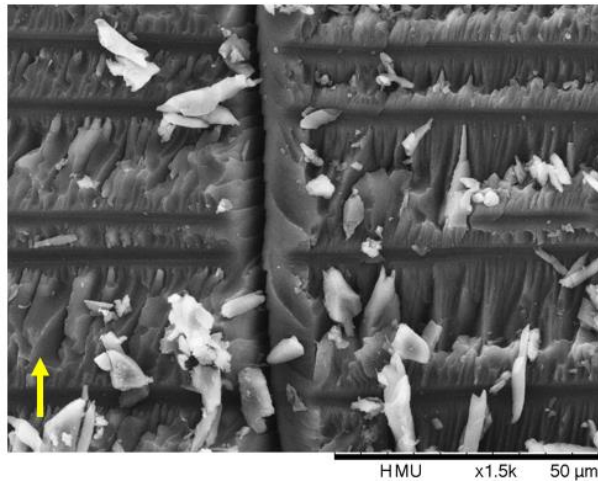


Figure 6.8 Rollers on the 90° surface of an unprinted specimen

6.3.1.2 PMMA Laminates

Typical PMMA printed fracture surfaces are shown in Figure 6.9. These samples bore resemblance to those of unprinted laminates in Figure 6.6. As in unprinted samples, the 90° ply was once again predominantly the matrix dominated surface. Similarly, cusps in PMMA printed samples (Figure 6.10) were effectively indistinguishable from those of unprinted samples. Additionally, roller formation also appeared to be unaffected (Figure 6.11), being similar in in both size and shape. Together, all of these observations indicated that the addition of PMMA had little or no effect on the bulk properties of the matrix in the interlaminar region.

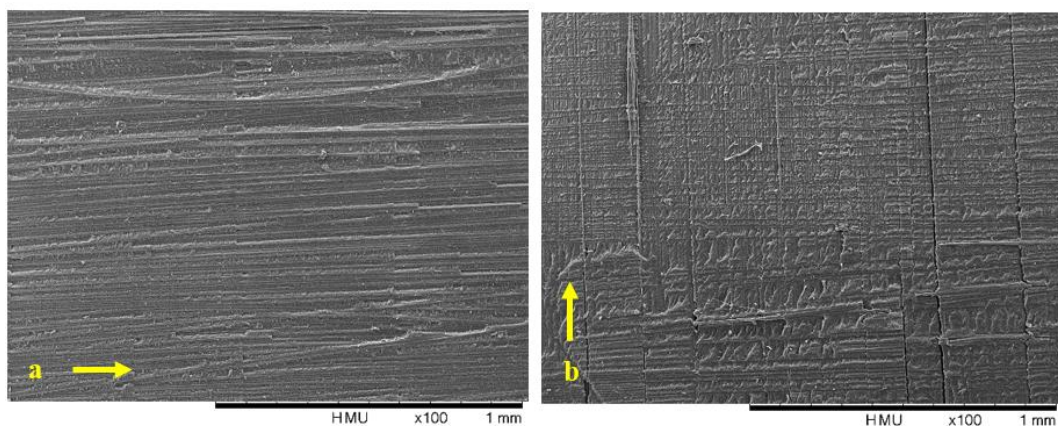


Figure 6.9 PMMA printed sample a) 0° delamination surface, b) 90° delamination surface.

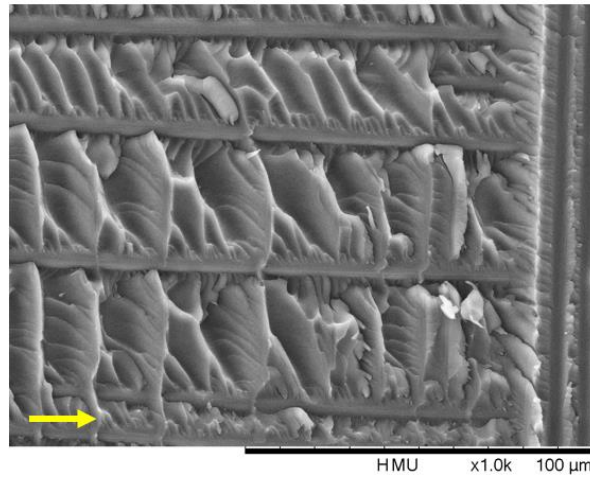


Figure 6.10 Cusps on the 0° surface of a PMMA printed specimen

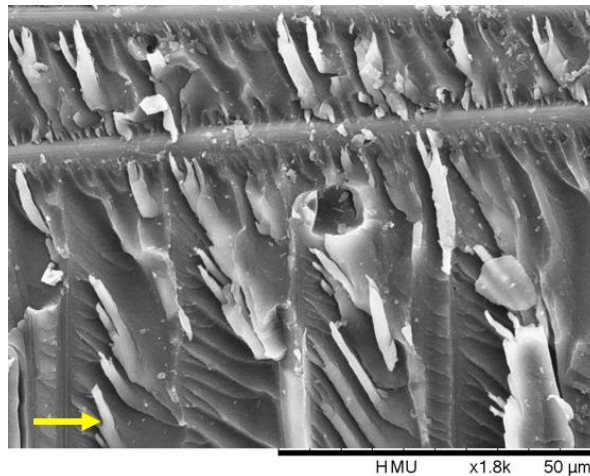


Figure 6.11 Rollers on the 0° surface of a PMMA printed specimen

Although no obvious changes to the bulk matrix properties were observed, multiple regions were observed that contained groups of hemispherical voids. An example of one of these groups is shown in Figure 6.12a. These groups were found to be dispersed throughout both matrix and fibre dominated surfaces in all PMMA printed samples. These voids were typically found in groups of up to twenty, spanning around 100-400 μm . The diameters of these voids ranged from 4-12 μm . They were not observed across the entirety of all surfaces, most probably because delaminations did not intercept all of them. Magnified views of some of these voids may be seen in Figure 6.12b and Figure 6.12c.

The cause of these voids was soon discovered. Spherical particles were found contained within some of the voids, as shown in Figure 6.13. It was shown in Section 3.9.2.1 that printed PMMA droplets formed a discreet phase from the surrounding resin matrix and separated into

groups of smaller droplets of 5-10 μm in diameter. The particles found here were undoubtedly those same droplets. It was clearly observed that they were separated from the surrounding matrix, essentially loose within. This explained why very few were found still contained in the voids seen elsewhere. After having fractured, the particles most likely fell out of the voids, leaving cavities behind. It was also seen that many of the particles fractured in a brittle manner, leaving sharp edges. This may either have occurred due to delaminations propagating through them, or most likely as a result of fretting between surfaces.

The discovery of these particles was highly significant because it validated results obtained in Section 3.9.2.1, as well as many of the other assumptions made in other chapters. The implications of this will be discussed later in Section 6.4.1.

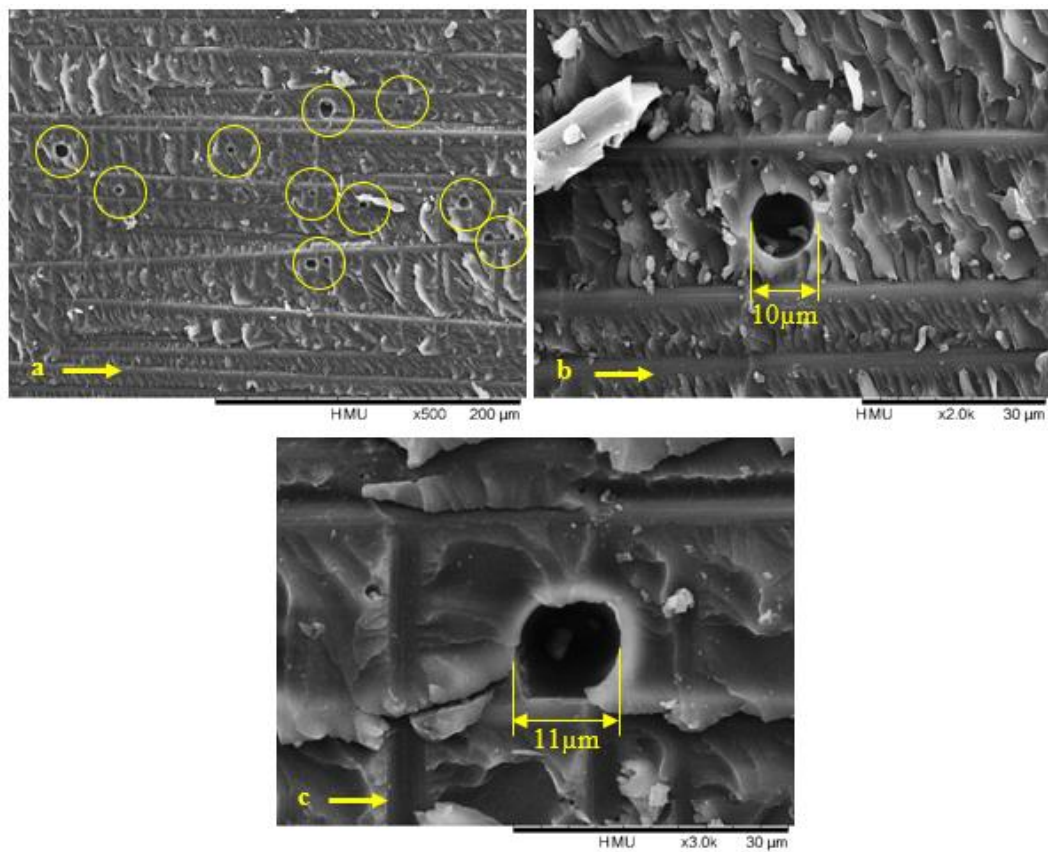


Figure 6.12 a) A group of hemispherical voids of varying diameters within the surface resin of a delaminated specimen. b) & c) Magnified views of individual voids.

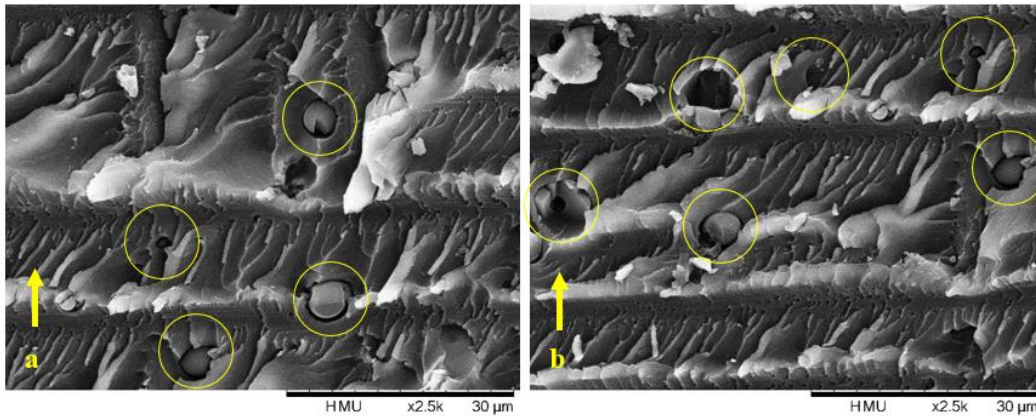


Figure 6.13 Spherical particles contained within voids in the matrix of PMMA printed samples

6.3.1.3 PEG 1,500M_w Laminates

The delaminated surfaces of PEG 1,500M_w samples broadly resembled those of unprinted ones, but a number of differing features became apparent. Firstly, observing Figure 6.14, it was noted that although the 90° surface still remained the matrix dominated surface, many small regions on the 0° surfaces retained the matrix.

It may be observed from Figure 6.15 that very few cusps were produced. And those that were produced were flat, rounded, and possibly smeared. Additionally, no rollers at all were observed. And, as stated in Section 2.6.4.4, this is something that generally only occurs in very ductile matrix materials.

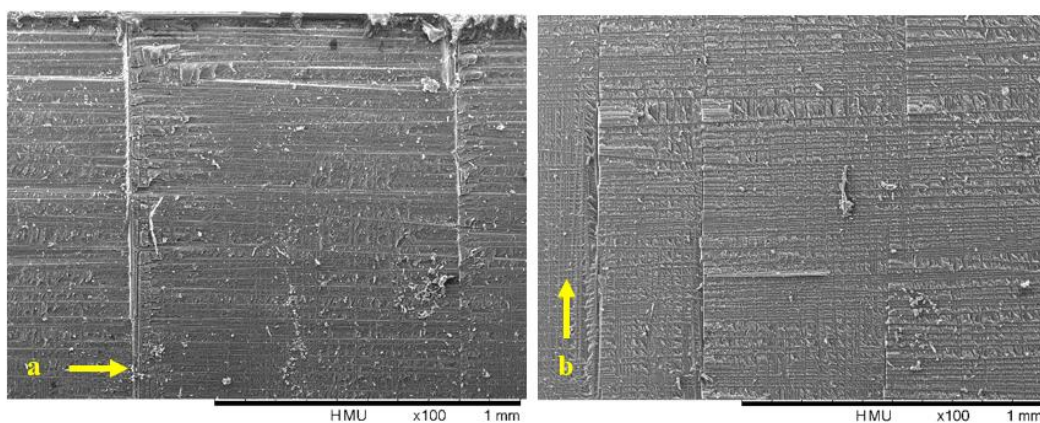


Figure 6.14 PEG 1,500M_w printed sample a) 0° delamination surface, b) 90° delamination surface

Closer inspection of fracture surfaces (Figure 6.15) showed that fibre imprints were visible in many regions across 0° surfaces. But unusually, the thickness of the resin-rich region that the impressions were set on appeared very thin. In some cases, the resin-rich region was so thin that imprints faded into the fibres of the adjacent ply. This behaviour was not typical of all laminates. For example, Figure 6.16 shows an unprinted surface. It was seen that where the surface transitioned from matrix dominated to fibre dominated, significant step changes in level occurred. This indicated that a significant decrease in the thickness of the resin-rich region had occurred because of the addition of PEG.

Following this observation, additional measurements were taken of the thickness of the resin-rich region in the different laminate types. Untested laminates were placed under an optical microscope to view their edges. Optical microscopy was used because it could easily show the shade difference between fibres and matrix, making the resin-rich regions more visible. Two of each sample type were observed, and measurements were taken at around ten points on each. On average it was found that the thickness of the resin-rich regions between plies were $35\mu\text{m}$, $32\mu\text{m}$, $13\mu\text{m}$, and $21\mu\text{m}$ for unprinted, PMMA, PEG 1,500M_w, and PEG 20,000M_w samples respectively. Representative images of these differences are shown in Figure 6.17. This confirmed what was observed in SEM.

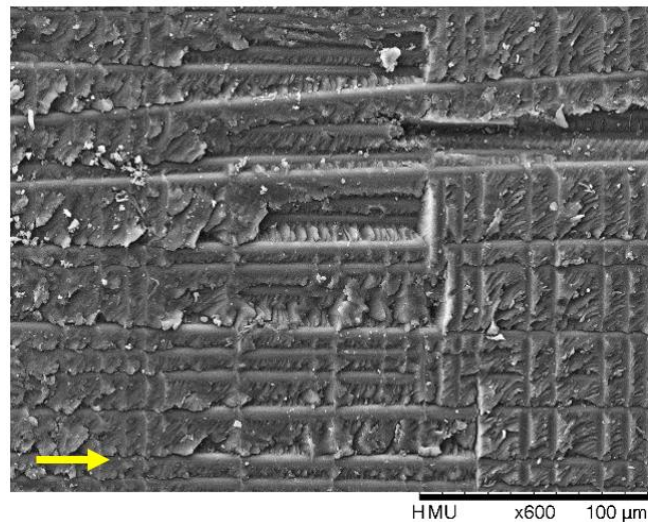


Figure 6.15 0° delamination surface with matrix showing a significant degree of plasticity. Cusps are flat and possibly smeared. Also note that there is no significant step change between fibre and matrix dominated regions, indicating that the resin-rich region was very thin in these samples.

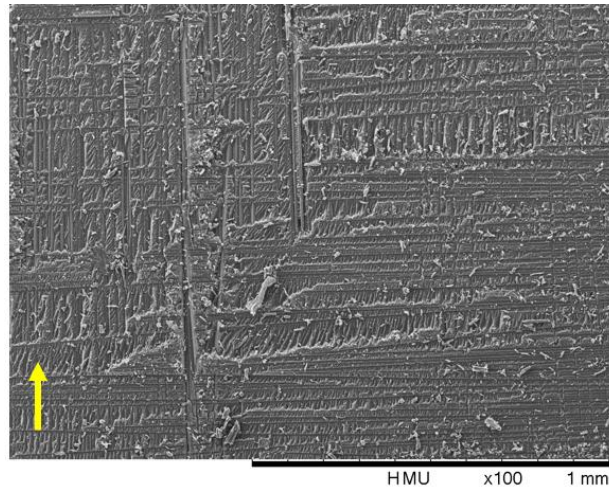


Figure 6.16 Unprinted 90° delaminated surface showing significant ridges where the surface transitions from matrix dominated to fibre dominated

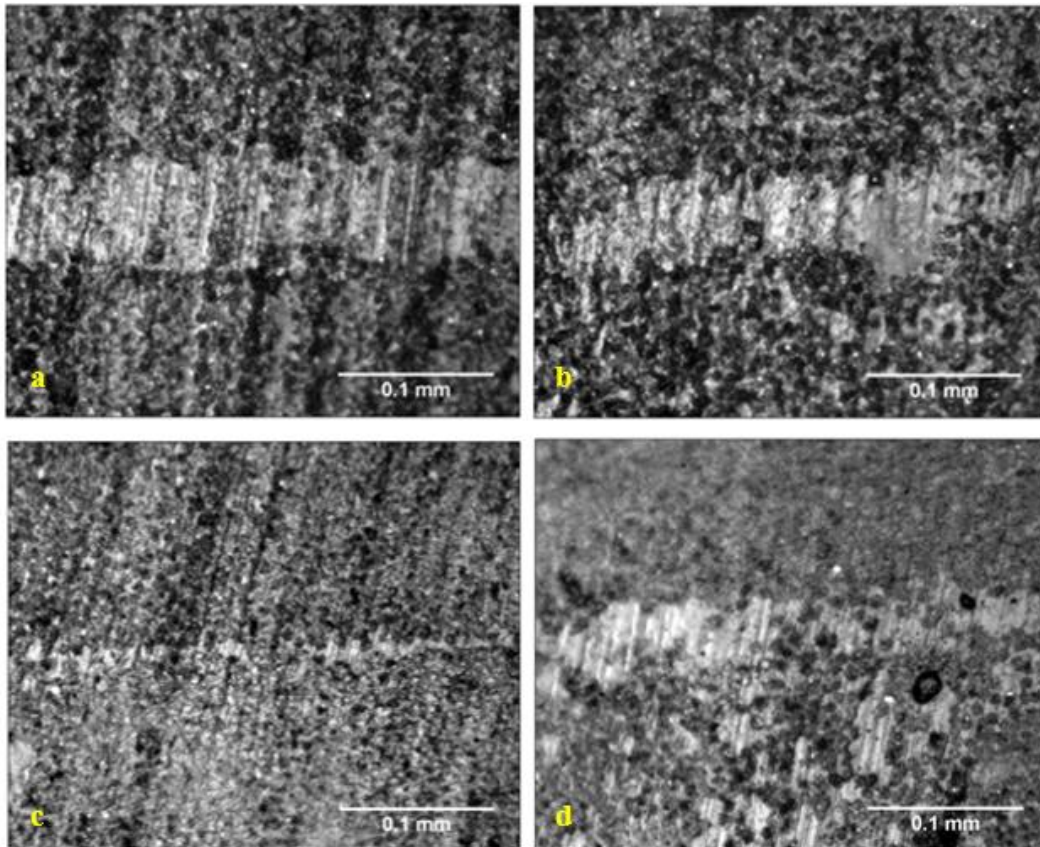


Figure 6.17 Optical micrographs showing the resin-rich regions (lighter shade) of a) unprinted, b) PMMA, c) PEG 1,500M_w, and d) PEG 20,000M_w samples. All micrographs were taken at the same magnification, and hence are the same scale.

6.3.1.4 PEG 20,000M_w Laminates

Figure 6.18 shows typical delaminated surfaces of PEG 20,000M_w specimens. In other sample types, it was generally the 90° ply that was the matrix dominated ply. In PEG 20,000M_w samples, the distribution of matrix was approximately even amongst the 0° and 90° surfaces. This was a strong indicator that significant levels of matrix toughening and/or fibre/matrix interface strength had been achieved. Figure 6.19 shows that unlike in PEG 1,500M_w samples (Figure 6.15), the thickness of the resin-rich region remained thick, with a significant step at the transition point. It was shown in Figure 6.17 that the thickness of the resin-rich region in these samples was not as thick as in unprinted or PMMA printed samples however, being on average 21µm. But this was significantly thicker than was observed in PEG 1,500M_w samples.

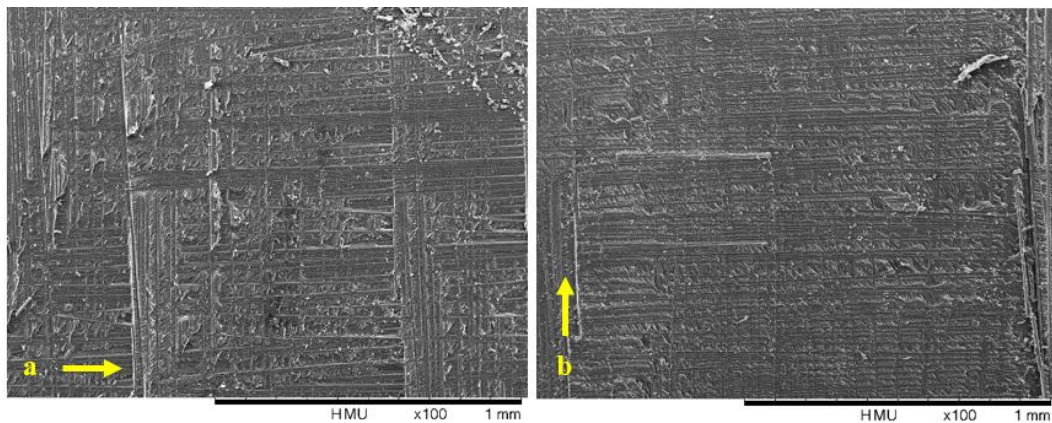


Figure 6.18 PEG 20,000M_w printed sample a) 0° delamination surface, b) 90° delamination surface

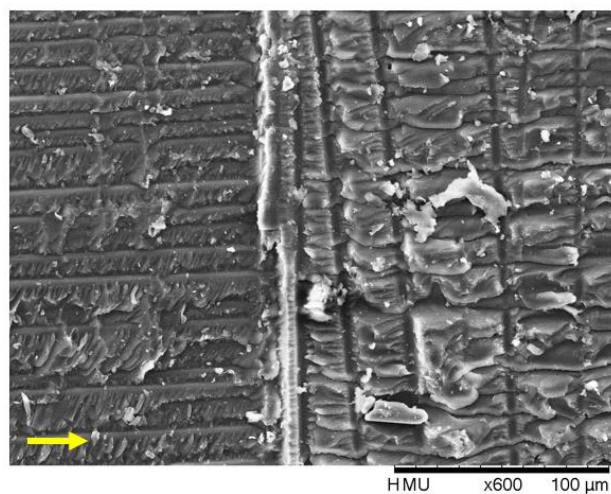


Figure 6.19 Transition between matrix and fibre dominated surfaces on a 0° ply

The matrix of these samples appeared to show a degree of plasticity that was not seen in unprinted samples, but to a lesser degree than was seen in PEG 1,500M_w samples. For example, in Figure 6.20 it was seen that cusps did form on the surfaces, but in most cases were flat and rounded. Also, in unprinted surfaces such as in Figure 6.7, cusps were recessed in the channels between fibres. In PEG 20,000M_w specimens, cusps formed much more level with the tops of fibres, and in many cases the resin and cusps covered fibres. Similar behaviour was noted in PEG 1,500M_w specimens. Again, this pointed towards an increase in fibre/matrix bonding.

Finally, it was observed that the addition of PEG appeared to reduce the amount of rollers that were produced. The addition of PEG 1,500M_w was previously shown to eliminate any indication of rollers. But in PEG 20,000M_w specimens, rollers were still formed, but in many cases were rudimentary and did not separate from the surrounding matrix. This is shown in Figure 6.21.

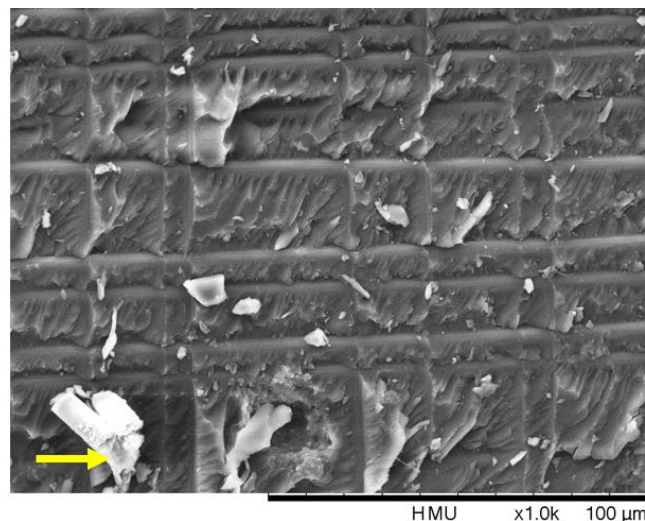


Figure 6.20 Cusps on a 0° PEG 20,000M_w delaminated surface

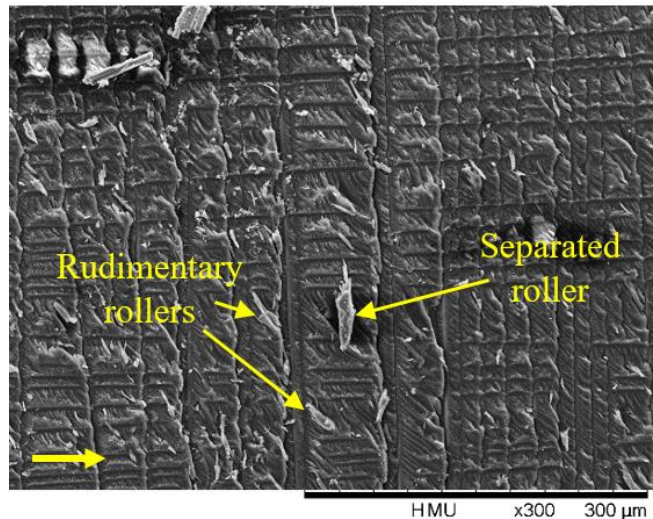


Figure 6.21 Rudimentary rollers on a 0° PEG 20,000Mw delaminated surface. In most cases rollers never separated from the surrounding matrix.

6.3.1.5 Fracture Mechanisms

The evidence provided by fracture surfaces was valuable in determining the fracture mechanisms operating in tensile specimens. A mixture of sample types were used in this analysis, but unprinted samples were of particular use due to their clear fracture surfaces and distinct cracks and cusps. Although the fracture mechanics of different sample types were obviously different at the micro scale, at the macro scale all sample types appeared to fracture by similar mechanisms.

It was hypothesised in Section 5.5.2 that transverse cracks were probably the primary cause of delaminations in tensile samples. Transverse cracks are clearly visible in Figure 6.6b, and evidence of these cracks propagating through to the adjacent 0° ply is visible in Figure 6.6a as a vertically orientated ridge of matrix material. In this image, the delamination was seeded by a transverse crack in the opposing 90° ply, and propagated outwards from it. In Section 2.6.4.2 it was described how the orientation of cusps can be used to infer the direction of delamination propagation. Cusps in fibre dominated surfaces lean towards their point of origin, and those in matrix dominated surfaces lean away. The cusps in Figure 6.22a were clearly observed to lean towards the transverse crack on both sides. The cusps in Figure 6.7 also exhibited this same behaviour, leaning towards the crack on the right side of the image. Figure 6.22b shows the same scenario on a matrix dominated (90°) surface. In this case cusps were observed leaning away from the transverse crack going through the ply. Although, the orientations of cusps on the right side of the image are admittedly more difficult to identify. This evidence

showed that delaminations did indeed originate at transverse cracks; at least they did in the areas surveyed.

It was seen in Figure 6.23 that the orientation and lean of cusps was influenced by their proximity to both a free edge and a transverse crack. Drawn curves indicate the approximate orientations of cusps in bands across the width of the image, and arrows indicate the direction in which delamination propagated according to the lean of cusps. Magnified views of the dashed areas *a* and *b* in this figure are shown in Figure 6.24. These allow a clearer view of the changing orientation of cusps throughout Figure 6.23. This showed that free edges also contributed to the propagation of delaminations. No cusps were visible at the very edges of specimens, most probably due to excessive fretting, which was evident from the highly roughened texture very close to the free edges.

It was seen that the dominance of either the free edge or the transverse crack increased the closer that observations were made to those features; although Figure 6.23 only represents a small fraction of the surface area of the specimen. Away from free edges, the orientation of cusps indicated that delaminations were far more influenced by transverse cracks. This was apparent from their near vertical orientation. This was observed with increasing effect towards the centre of samples. For example, the cusps shown in Figure 6.7, which was captured well away from free edges.

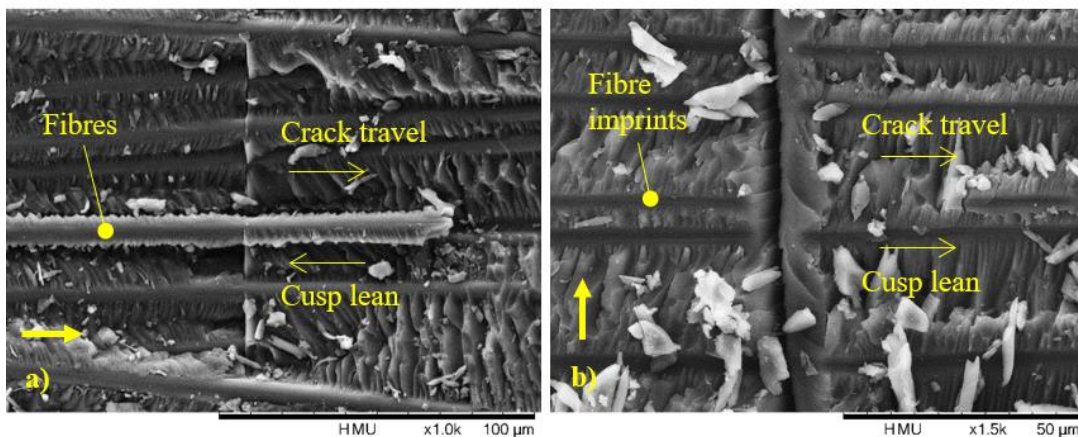


Figure 6.22 a) Cusps leaning towards the origin of a delamination in a fibre dominated ply.
b) Cusps leaning away from the origin of a delamination in a matrix dominated ply. The delaminations were seeded by transverse cracks in 90° plies.

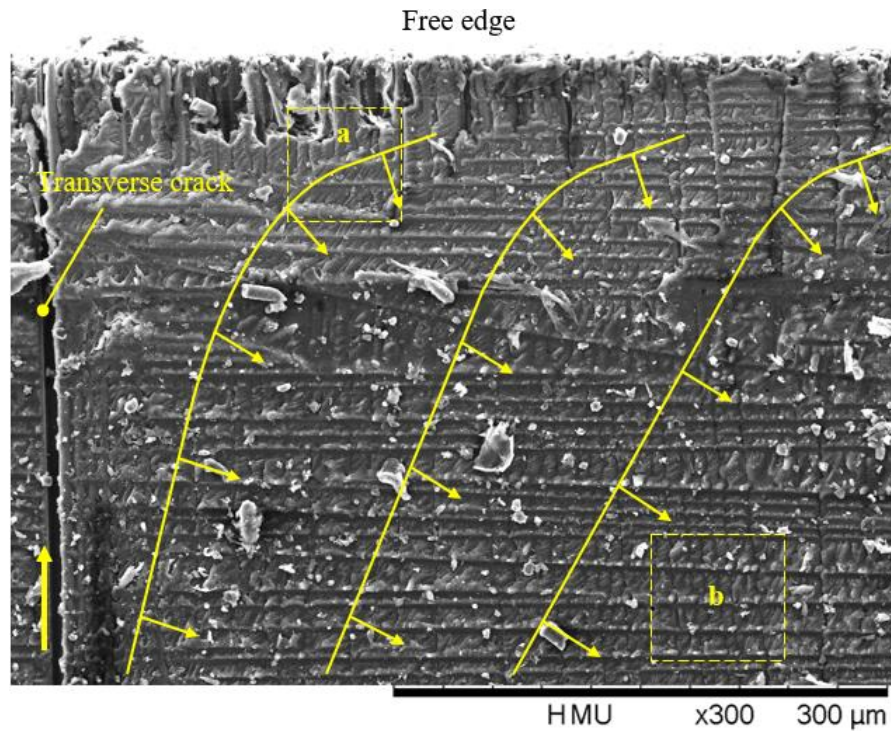


Figure 6.23 Delaminated face of a 90° ply close to both a free edge and a transverse crack. The approximate orientation and lean of the cusps indicate that the delamination front took a path as indicated by lines and arrows. The dashed areas denoted *a* and *b* are shown in the figure below.

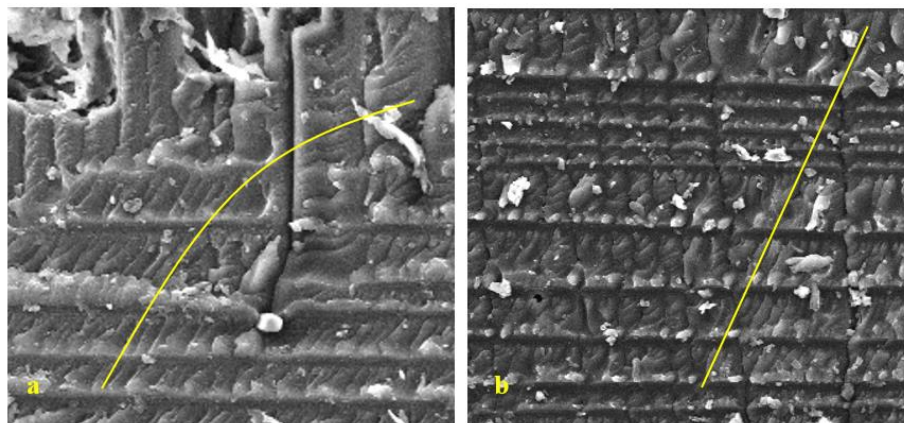


Figure 6.24 Magnified views of regions *a* and *b* from the previous figure. Lines indicate the approximate orientation of cusps in those areas.

Figure 6.25 shows a sample that was halted part way through testing. Delaminations at the $0^\circ/90^\circ$ interfaces were shown terminating some distance from the free edge of the specimen. It was shown above that delaminations emanated from transverse cracks, and also by the

orientation of cusps in Figure 6.7. But Figure 6.25 provides evidence to the contrary, suggesting that delaminations were propagated inwards, perhaps by free edge stresses.

Figure 6.26 shows a transverse crack in a 90° ply. It was observed that the crack terminated somewhere in the centre of the ply. This showed that transverse cracks originated at the free edges of samples, propagating inwards with increasing numbers of cycles. In some cases, the regional strain may have been suitably relieved (by delaminations for example) that incomplete transverse cracks were halted. Alternatively, some cracks may have developed suitably late in the testing of samples that they did not have time to propagate across the width of the 90° plies.

Figure 6.27 shows a photograph of the entire width of an SEM sample (0° horizontal fibre orientation). A distinctive pattern was seen on the surface of the sample. The (vertical) origin lines of delaminations were clearly visible, caused by transverse cracks in the adjacent 90° ply. The horizontal line along the approximate centreline of the sample was indicative that delaminations met in the centre.

The evidence presented thus far appeared to indicate that whilst transverse cracks were the primary driver of delaminations, stress concentrations caused by free edges were in turn the cause of transverse cracks, and perhaps even the primary initiator of delaminations. These theories will be explored later in Section 6.4.1.

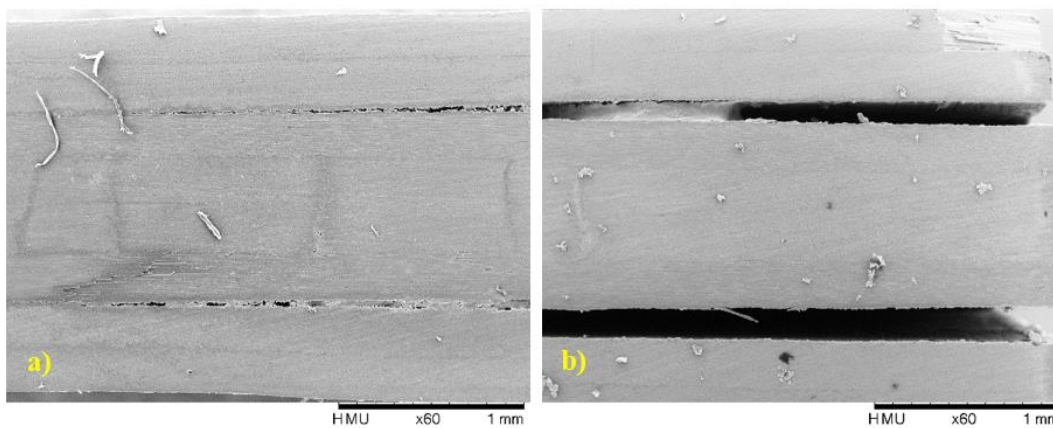


Figure 6.25 Images of incomplete delaminations between $0^\circ/90^\circ$ interfaces in a sample halted before the test was complete. Images are of the same delaminations taken at a) termination, and b) origin. Loading axis of the specimen is towards the reader.

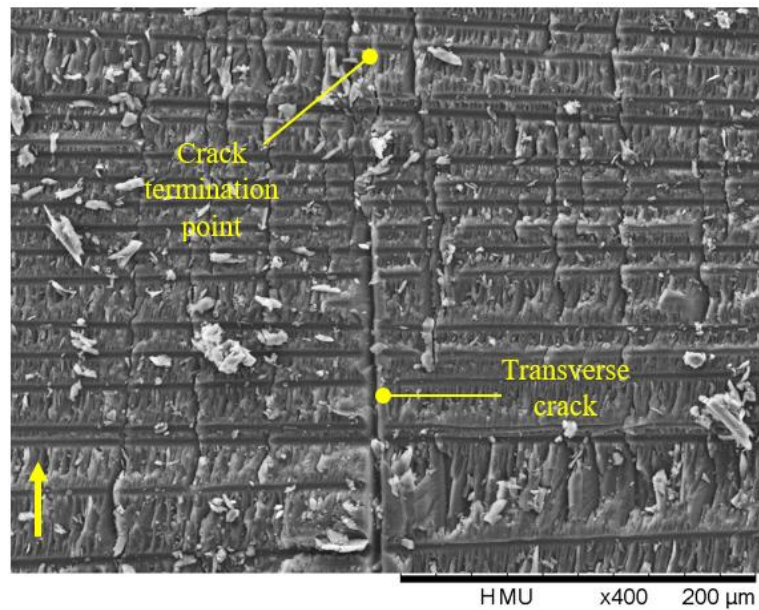


Figure 6.26 A transverse crack in a 90° ply terminating somewhere in the centre of the ply



Figure 6.27 Photograph of a (gold coated) delamination surface (0° horizontal fibre orientation). Transverse crack lines are clearly visible. Delamination fronts propagated outwards from these cracks, driven forward by free edge stresses.

6.3.2 Crack Densities

During cyclic tensile testing, cellulose acetate replicas of many samples were taken at regular intervals. These replicas were of the free edges of samples, and aimed to correlate transverse cracks and delaminations visible at the free edges with what was observed in stiffness degradation and fracture surface measurements in cyclic tensile tests. The primary concern of

these replica observations was to investigate the possibility of differing rates of visible damage in samples printed with different polymers during Phases Ia and Ib of stiffness degradation.

6.3.2.1 *Accuracy of the Acetate Replica Technique*

Before utilising the acetate replica method it was necessary to ensure that replicas could provide a suitably high level of replication so that as much of the fine detail of cracks as possible was captured. Therefore, a simple test was conducted in which a replica was taken from a sample edge with highly distinguishable features. The replica was taken in exactly the same way as in cyclic tests, and scanned using the same SEM settings. The original was then compared to the replica to assess the accuracy of the replication.

Figure 6.28 shows some of the key images from those tests. From Figure 6.28a&b the quality of replication appeared to be very good, even capturing very fine surface details such as sanding marks. It may be noted that replicas produce a mirror version of the original. This is an inherent property of the replica technique, but obviously does not affect their quantitative or qualitative assessment in any way. Replicas also produce a negative impression of the surface topography. This is better illustrated in Figure 6.28d, where it can be seen that the cellulose acetate formed large peaks where it was pressed into wide cracks. It was also observed that the wider the crack, the higher the peak. Although these peaks somewhat obscured the intricacies of the cracks, their general shape and size remained very good matches to the originals.

An important factor in crack density measurements was ensuring that replica crack lengths accurately represented the originals. Figure 6.28e&f show the same collection of cracks in original and replica forms. In these there is a crack which terminated within the frame of the image. This crack was measured in both images, and was found to be 285 μm in the original micrograph, and 275 μm in the replica micrograph. This indicated that the replica technique was able to capture the vast majority of the crack length (96% in this case), but extremely fine sections were beyond its capabilities. This was deemed sufficient for the measurements in this section.

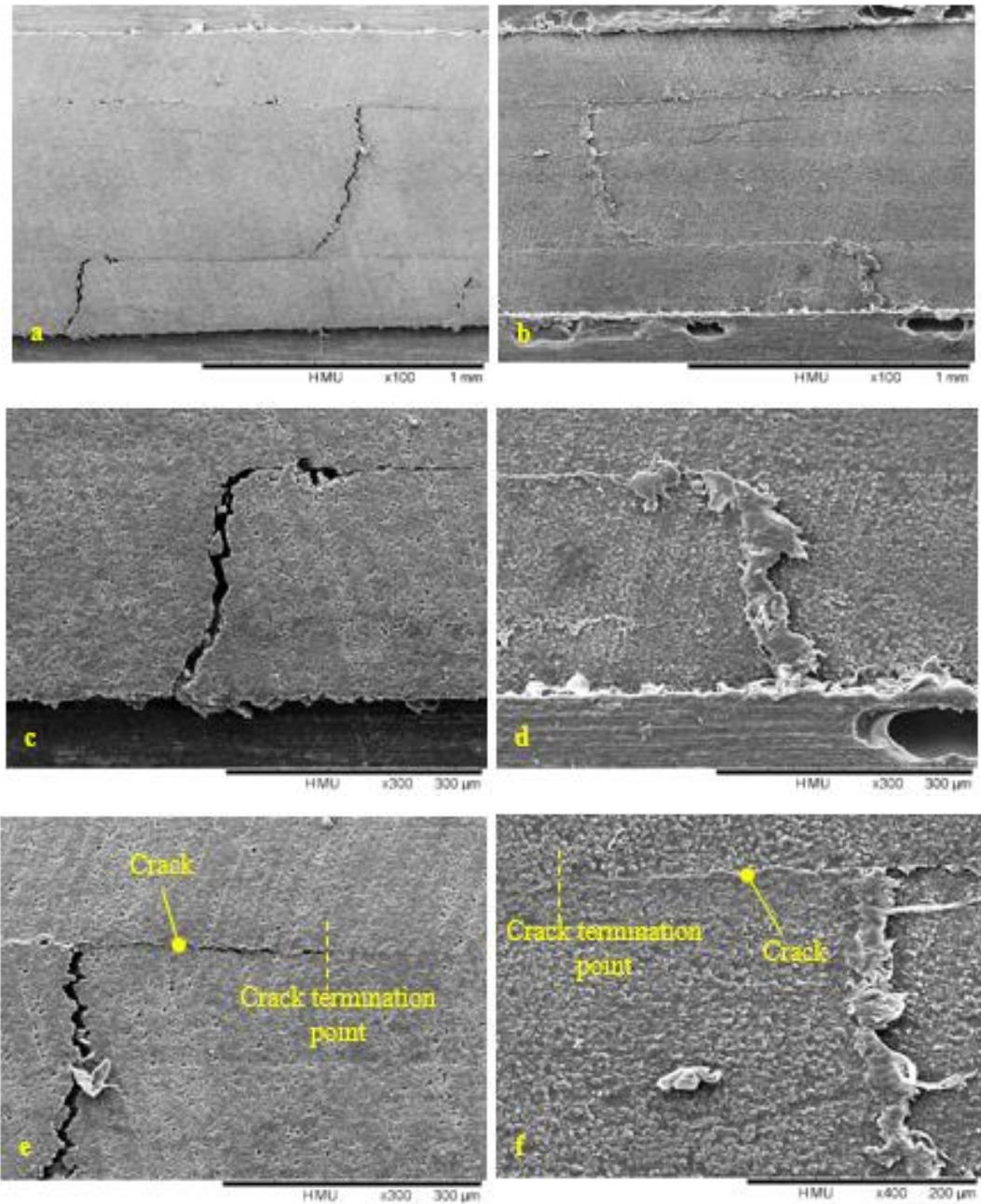


Figure 6.28 SEM micrographs of cracked sample edges and their acetate replicas. a) Full view of a sample edge showing extensive cracking. b) Acetate replica of *a*. Showing highly accurate replication of cracks. c) Higher magnification micrograph of a transverse crack. d) Replica of *c*. e) Micrograph of crack with a delamination stemming from it. The delamination terminates to the right of the image. f) Replica of *e*. Delamination terminates at a point just slightly short of the original.

6.3.2.2 *Crack Density Values*

As mentioned in Section 6.2.2.3, the lengths of cracks were recorded for each individual ply orientation. This allowed certain crack types to be analysed either separately or together as desired. Of all plies and interfaces present in laminates, it was the 90° plies and their interfaces which were predicted and shown to exhibit the majority of cracks. Readers are reminded that the stacking sequence of the samples may be seen in Figure 6.4 or Section 4.2.1.

Firstly, the lengths of 90° transverse cracks were analysed. The results of this are shown in Figure 6.29. A significant degree of scatter was observed in these results. Despite the large degree of scatter, it was observed that crack densities broadly followed a profile of exponential growth. Numbers grew rapidly at first, generally reaching a maximum at 20k cycles, which coincided with the measured Phase Ia to Ib transition region of the various sample types, which occurred between five and twenty thousand cycles in most samples. This may be seen as indicated by the hashed region in Figure 6.29. Crack saturation appeared to directly coincide with the end of this region. This provided evidence that Phase Ia was directly linked to transverse cracking.

In these measurements, PEG 1,500M_w samples appeared to exhibit the highest density of 90° ply cracks at saturation, whilst others exhibited lower but similar values. However, due to the high degree of scatter, this was inconclusive. In some cases, reductions in the total length of cracks were recorded past the saturation point. It was also noted that at 5k cycles the crack density of 90° transverse cracks occurring in PEG 20,000M_w laminates was considerably higher than in all other sample types. Data scatter may have played a role in this measurement, but given the relatively low numbers of cracks observed in other sample types at 5k cycles, it was unlikely that scatter played such a significant role as this. Other sample types subsequently showed greatly increased crack densities, so it was only at 5k cycles that this discrepancy was observed.

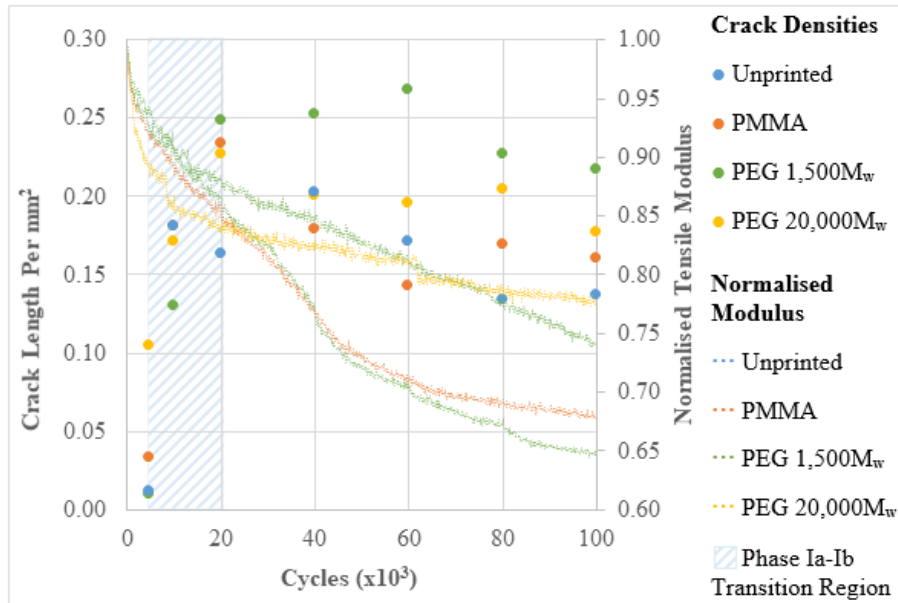


Figure 6.29 Total length of 90° transverse cracks per mm² occurring in samples testing in tensile fatigue with increasing numbers of loading cycles. Also shows the averaged normalised curves of all sample types in cyclic tensile loading at a stress factor of 0.5. The region where stiffness degradation was found to transition from Phase Ia to Ib is marked in the hashed area.

Crack densities were also measured in 45° plies. Figure 6.30 shows the values recorded only in the central 45° plies. These were recorded separately from the outer -45° plies because of their different boundary conditions, which resulted in highly different crack density values. In fact, -45° plies exhibited so few cracks or delaminations that their influence upon the total values was negligible. And in most cases, the outer -45° plies exhibited no apparent delamination whatsoever.

45° cracks were much less frequent than 90° cracks, only making up a small fraction of the total laminate cracks. Their infrequency therefore meant that data points produced from measurements of these cracks were extremely scattered. However, their influence was not negligible. Because they were adjacent to the 90° plies, in regions where 45° ply cracks appeared, they relieved strains in the 90° plies, reducing the number of 90° ply cracks in that region. Likewise, where 90° ply cracks were frequent, the number of 45° ply cracks was simultaneously reduced. Figure 6.31 illustrates this point. By combining the crack density values of all transverse cracks, data scatter was noticeably reduced. It was now much clearer that samples did indeed exhibit an exponential growth, reaching transverse crack saturation between 10k and 20k cycles. Once again, the saturation point of these cracks when combined directly coincided with the Phase Ia to Ib transition region of stiffness degradation.

Although PEG 1,500M_w samples remained the most densely cracked samples once all transverse cracks were summed, final values ultimately showed only minor differences in crack densities between sample types. Due to the degree of scatter that still remained, it was difficult to assess whether the saturation levels of transverse cracks were influenced by the presence of printed polymers. A factor that still remained prominent however, was that PEG 20,000M_w samples exhibited transverse crack densities far beyond other sample types at 5k cycles.

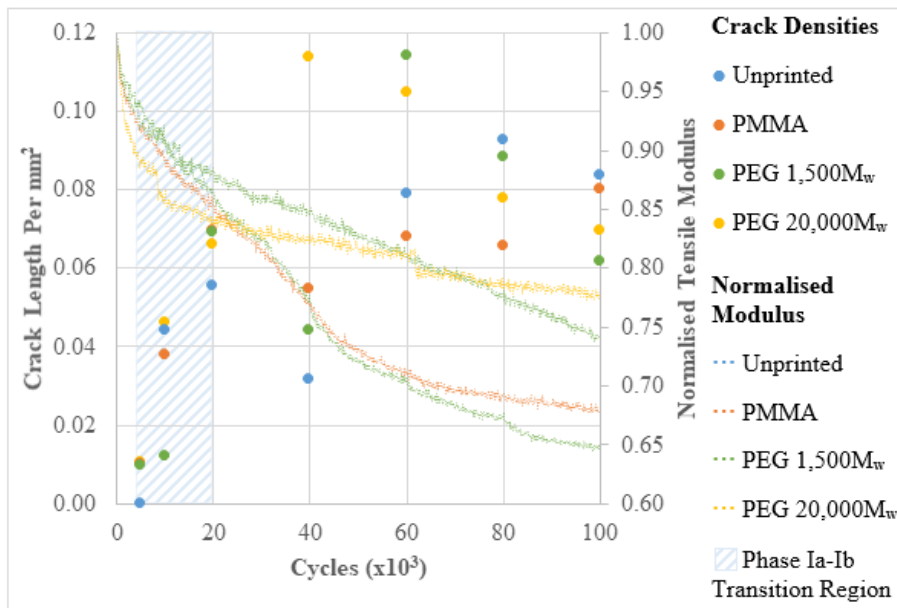


Figure 6.30 Total length of 45° transverse cracks per mm² occurring in samples tested in tensile fatigue with increasing numbers of loading cycles. Also shows the averaged normalised curves of all sample types in cyclic tensile loading at a stress factor of 0.5. The region where stiffness degradation was found to transition from Phase Ia to Ib is marked in the hashed area.

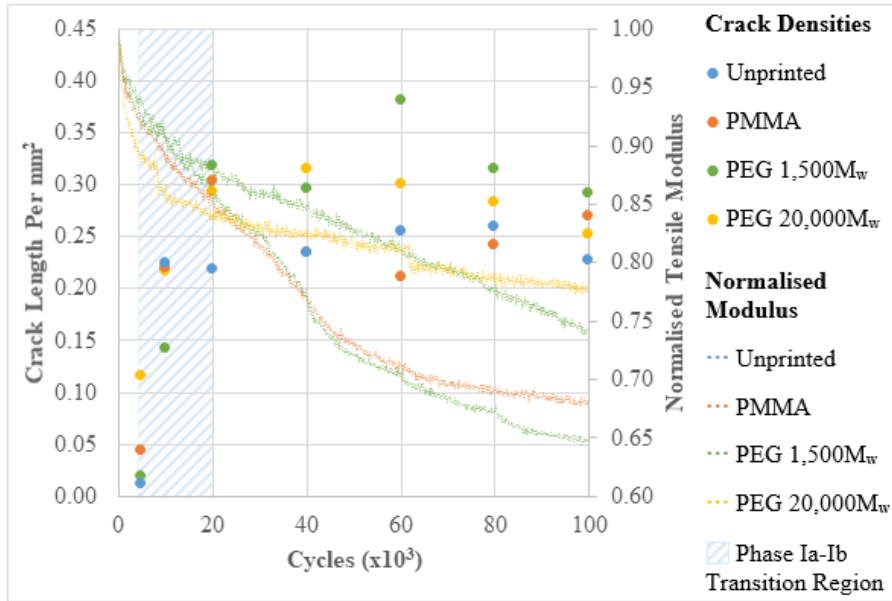


Figure 6.31 Total length of all transverse cracks per mm² occurring in samples tested in tensile fatigue with increasing numbers of loading cycles. Also shows the averaged normalised curves of all sample types in cyclic tensile loading at a stress factor of 0.5. The region where stiffness degradation was found to transition from Phase Ia to Ib is marked in the hashed area.

The total lengths of delaminations per unit area (referred to as delamination density for obvious reasons) were also recorded. Similarly to with transverse cracks, interfaces between 90° plies and adjacent plies exhibited by far the highest degrees of delamination, with other interfaces being ultimately negligible. Figure 6.32 shows the measured values of crack density of 0°/90° interface delaminations at free edges.

Whereas plies could contain very large numbers of transverse cracks, the maximum crack density values for delaminations were constrained by physical limits. Each interface could only be delaminated once, and to a maximum length equalling the width of the observed region. Each laminate contained two 90° plies, and therefore two of each interface type. Therefore, the maximum achievable delamination density (d_a) value for each interface type in a laminate was constrained to;

$$d_a = \frac{2L}{A} = \frac{2L}{Lh} = \frac{2}{h} \quad 6.1$$

where L is the width of the observed region, A is the area of the observed region, and h is the sample thickness. The sample thickness was presumed to be 2mm (discussed in Section 6.2.2.3).

Therefore, the maximum achievable delamination density for a particular interface type in this particular stacking sequence was;

$$d_a = \frac{2}{2mm} = 1mm^{-1} \quad 6.2$$

This maximum value was reached by all samples between 80k and 100k cycles, lagging behind the saturation of transverse cracks. As with transverse cracks, 0°/90° delaminations exhibited an exponential increase but with a much lower degree of scatter. It is important to realise that the measured values are of visible edge delaminations, and do not necessarily translate to complete delaminations through the width of laminates.

Samples showed consistent divergence from each other between 5k to 20k cycles. PMMA samples exhibited the most rapid delamination in this period, with PEG 20,000M_w samples matching them closely. PEG 1,500M_w and unprinted samples appeared to delaminate more slowly, but at similar rates to each other. This point of maximum divergence appeared to coincide with the saturation of transverse cracks, implying that the two processes were linked. After 20k cycles delamination densities began to converge once more. And ultimately reached complete delamination at more or less the same point.

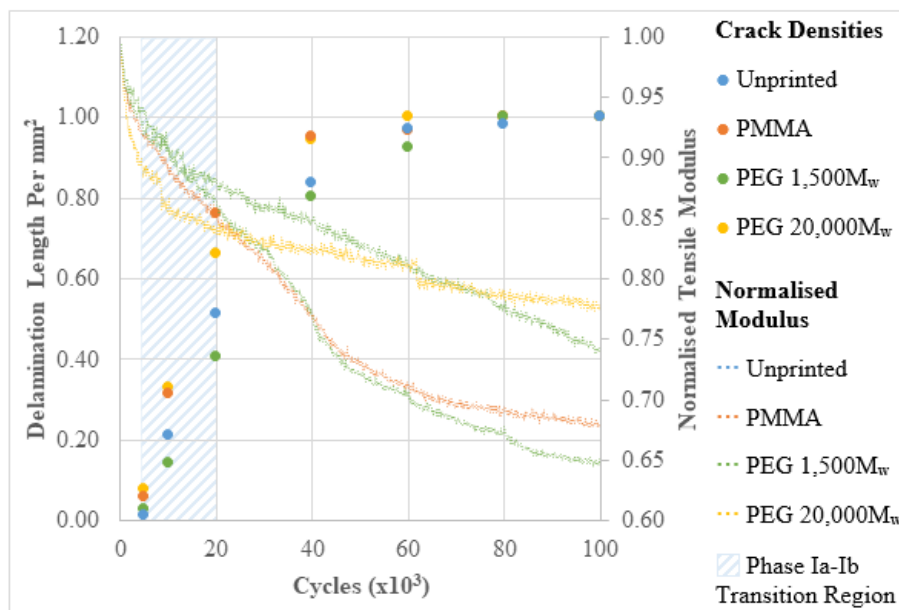


Figure 6.32 Total length of 0°/90° interface delaminations per mm² occurring in samples tested in tensile fatigue with increasing numbers of loading cycles. Also shows the averaged normalised curves of all sample types in cyclic tensile loading at a stress factor of 0.5. The region where stiffness degradation was found to transition from Phase Ia to Ib is marked in the hashed area.

90°/45° delaminations were also tracked. Just as was observed with transverse crack densities, the decreased strain difference between the 90° and 45° plies meant that significantly less delamination growth was observed at 90°/45° interfaces in comparison with the more highly strained 0°/90° interfaces. The delamination densities at 90°/45° interfaces are shown in Figure 6.33. Whilst the scatter of data points was too great to draw many conclusions from these results, one thing was clear. Unlike 0°/90° delaminations, 90°/45° delaminations did not reach saturation by 100k cycles. This was most likely due to the delamination of 0°/90° interfaces. When disconnected from the load bearing 0° plies, 90° and 45° plies would have experienced very little strain, greatly reducing their tendencies to delaminate. But whilst the major strains upon the central plies were removed, they may well have continued to delaminate slowly, and may have contributed to minor stiffness reductions in the later stages of tests. The combined values of all delaminations are shown in Figure 6.34.

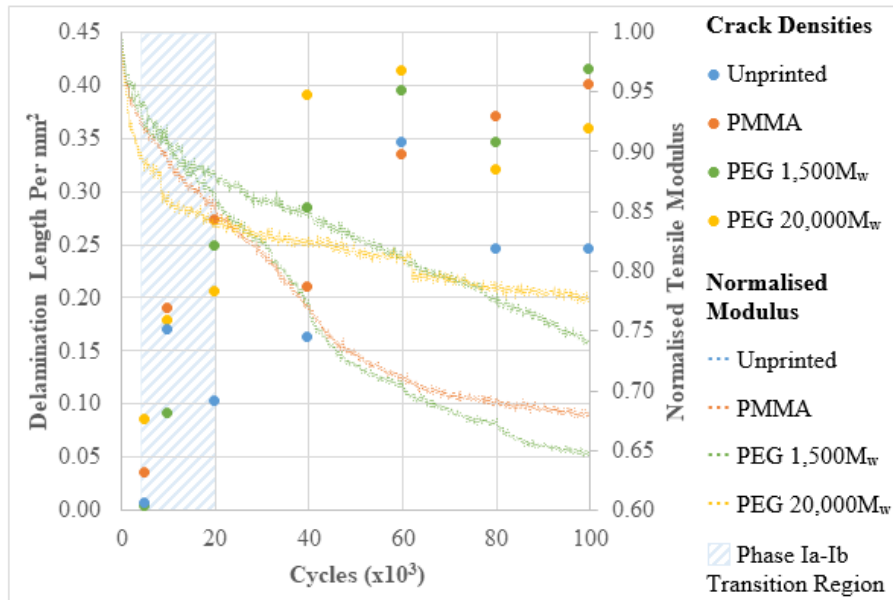


Figure 6.33 Total length of 90°/45° interface delaminations per mm² occurring in samples tested in tensile fatigue with increasing numbers of loading cycles. Also shows the averaged normalised curves of all sample types in cyclic tensile loading at a stress factor of 0.5. The region where stiffness degradation was found to transition from Phase Ia to Ib is marked in the hashed area.

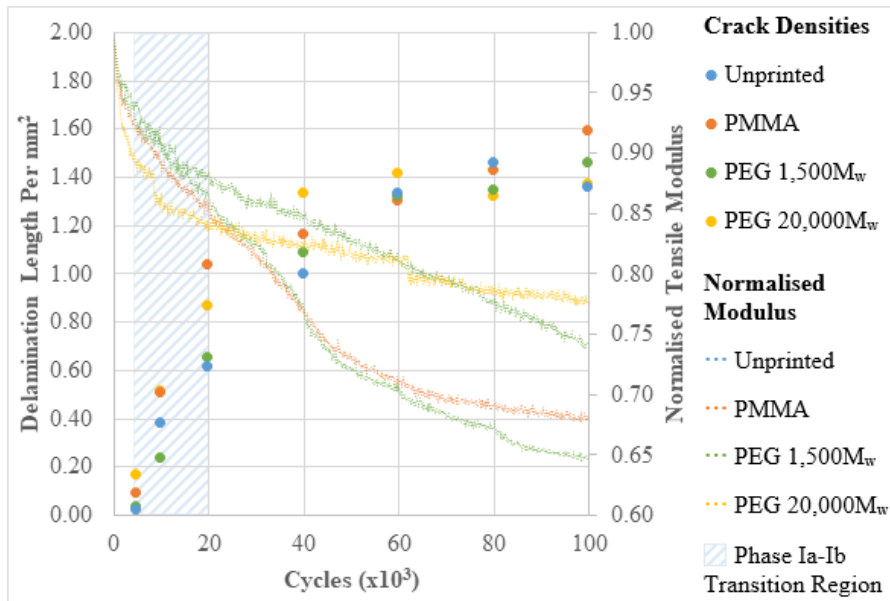


Figure 6.34 Total length of interface delaminations per mm² occurring in samples tested in tensile fatigue with increasing numbers of loading cycles. Also shows the averaged normalised curves of all sample types in cyclic tensile loading at a stress factor of 0.5. The region where stiffness degradation was found to transition from Phase Ia to Ib is marked in the hashed area.

6.4 DISCUSSION

In this section the experimental results presented in this chapter are discussed in order to determine what new information they revealed, and how this further expanded the understanding of inkjet printed composites.

6.4.1 Fractography

It was previously found in Section 5.4.2 that key differences between the stiffness degradation of samples occurred prominently in cyclically loaded tensile specimens at a stress factor of 0.5. Samples from these tests were therefore the key areas of interest in fractographic investigations. The aim of these investigations was to understand the damage mechanisms which caused fatigue progression in inkjet printed composites.

Delaminated regions were of particular interest because it was previously shown in 5.5.2 that the stiffness degradation of samples due to delaminations was significantly affected by the introduction of inkjet printed polymers, particularly at low stress/high cycle loading. Fractography of completely delaminated surfaces offered the most effective insight into

exactly how the inkjet printed polymers influenced delamination propagation without utilising destructive mid-testing techniques or advanced non-destructive techniques such as x-ray computed tomography (Section 2.6.5),

Due to the stacking sequence of the laminates used in cyclic tensile tests (Section 4.2.1), the 0°/90° interfaces of samples exhibited far more rapid and severe delamination than others, and were therefore selected for observation.

Unprinted laminates were observed in order to provide control images of unmodified laminates. Although 977-2 resin is a toughened system, it does not contain any interlaminar toughening, and the interlaminar resin still exhibits many of the characteristics of a brittle resin system. It was observed that unprinted fracture surfaces showed little or no matrix toughening. This was evident from observations of cusps in particular. It was previously described in Section 2.6.4.2 that the physical characteristics of cusps are heavily dictated by the toughness/plasticity of the matrix [5, 168]. Cusps in unprinted laminates were sharp and distinct, which was indicative that the 977-2 matrix failed in a brittle manner.

The presence of cusps was also a definite indication that these fracture surfaces were created as a result of crack fronts propagating through the interlaminar region as a result of mode II strains. As described in Section 2.6.4.2, cusps are artefacts which are produced as a direct result of the shearing action between plies of differing strains [5, 156, 157]. It also confirmed that delamination resulted from differential strains between plies as predicted in Section 4.2.1, and not from tensile or compressive loads which may have resulted from buckling or other undesired loading scenarios.

Where mode II loading is the dominant loading mode, fracture typically occurs along the fibre/matrix interlaminar interface, leaving one surface dominated by matrix, and one by fibres. It is typical for the resin-rich region to delaminate at the ply in tension, and therefore remain adhered to the ply in compression [5, 153]. Of the observed surfaces, it was the 0° ply that experienced tension, and the 90° ply that experienced compression. Which ply interface delaminates may vary according to local variables such as interface strength and toughness. However, in the observed surfaces, the 90° compressive surface remained the matrix dominated surface, further suggesting that the matrix failed in a brittle manner, and that fibre/matrix bond strength was low. As described in Section 2.6.4.1, this is typical behaviour of untoughened composites, and the minority of areas where the 0° ply became matrix dominated may be explained by local variables such as local fibre orientations and contamination.

Additionally, little evidence of material toughening was observed elsewhere. No fibrillation (Section 2.6.4.5) or excessive deformation of the surfaces was seen. And rollers (Section

2.6.4.4) appeared short and unsmearred; even appearing to have been fragmented easily by fretting, further indicating the brittle nature of the unprinted composites as expected.

The brittle nature of the unprinted composites was beneficial to the subsequent fractographic analysis of printed samples, as it made differences between toughened and untoughened systems much more apparent.

PMMA printed fracture surfaces were shown to exhibit no more bulk matrix toughening than unprinted samples. No distinct differences in cusps, rollers, or tendency of matrix/fibre dominated surfaces were observed. And on a macroscopic scale, PMMA printed samples were effectively indistinguishable from those of unprinted samples. This indicated that the addition of PMMA had little or no effect upon bulk matrix properties in the interlaminar region.

However, upon closer inspection, PMMA printed samples were shown to contain large numbers of hemispherical voids across much of the fracture surfaces. These voids were shown to be 4-12 μm in diameter, in groups of up to twenty, spanning regions of around 100-200 μm . This arrangement very closely matched patterns of discrete PMMA droplets observed in the (cured) printed resin slide tests discussed in Section 3.9.2.1 (Figure 3.26d), in which printed PMMA droplets were shown to break up into smaller droplets of around 5-10 μm in diameter, and spanning regions of around 100 μm .

In most regions these voids were seen to be empty. But in some areas they were seen to be occupied by spherical particles. The particles are highly likely to be PMMA droplets. Voids are most commonly caused by trapped gasses or moisture [4, 19], and do not contain solid particles. However, some teams investigating the addition of microparticles and microcapsules into bulk matrices found that they can separate from the surrounding matrix due to poor interfacial bonding, creating voids which contain the microparticles loose within [240-242]. Figure 6.35 (Zhao et al. [242]) illustrates this extremely well. They attributed this separation to strain differences between the matrix and particles caused by the approaching process zone.

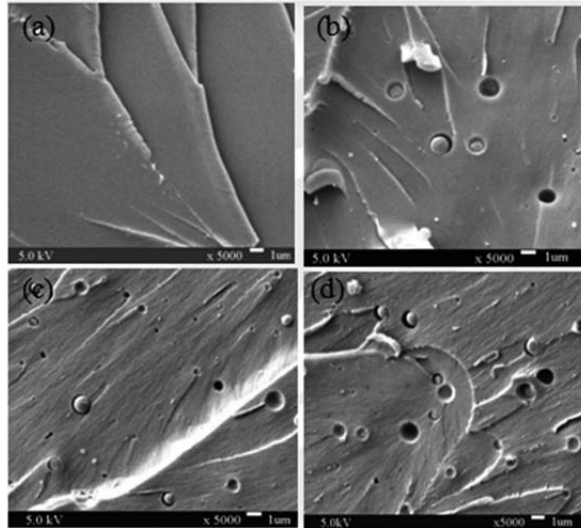


Figure 6.35 Image taken from Zhao et al. [242] showing an epoxy matrix fracturing along the plane of added microcapsule spheres. In some cases the microcapsules remained within the voids they caused, and in others they were absent.

It was clearly observed that the PMMA particles shown in Figure 6.13 were separated from the surrounding matrix, essentially loose within. This explained why very few were found still contained in the voids seen elsewhere. After having fractured, the particles most likely fell out of the voids, leaving cavities behind. Loose particles could have been washed away when specimens were rinsed after cutting, or ground into debris by fretting actions. It was also seen that many of the particles fractured in a brittle manner, leaving sharp edges. This may either have occurred due to delaminations propagating through them, or most likely as a result of fretting between surfaces.

It was previously theorised in Section 5.5.2 (based on results obtained from printed resin slide tests, Section 3.9.2.1) that weak interfacial bonding between PMMA and the matrix (and the subsequent voids formed) may explain the static and cyclic properties of PMMA printed samples. It was discussed how the separation of PMMA from the resin phase could provide a method of energy dissipation, increasing strength whilst simultaneously leading to a reduction in stiffness. Observations of these particles cleanly separating from the surrounding matrix provided evidence which gave weight to these theories. Although it could not be said for certain whether particles became detached from the matrix due to mechanical action in testing, or at the manufacturing stage due to differing rates of thermal expansion between the matrix and PMMA. However, no separation of PMMA particles was observed in the printed resin slide tests presented in Section 3.9.2.1, suggesting that separation due to mechanical action was much more likely.

The voids created by PMMA particles were very likely the cause of the reduced fatigue properties of PMMA printed samples. Voids have long been shown to decrease the interlaminar shear strength of laminates to varying degrees [243, 244]. Wisnom et al. [245] postulated that this is due in part to reductions in cross-sectional area due to distributed voids, and also to the initiation of damage from individual voids. Both of these theories match and reinforce what was hypothesised in Section 5.5.2 regarding the potential damage mechanics of PMMA printed samples.

The observation of PMMA particles had particular significance with regards to the assumptions that were made in previous chapters. Many of the hypotheses developed in Chapter 5 were based upon microscopic observations of polymers printed upon resin coated slides (Section 3.9). In that section it was determined that polymers printed upon 977-20 RTM resin pre-cured for twenty minutes at a temperature of 180°C displayed behaviours which most accurately resembled what was observed when the same polymers were printed upon uncured 977-2 prepreg. From this, it was assumed that the behaviours of polymers cured within resin pre-cured for twenty minutes were analogous to those of polymers cured within 977-2 prepreg. However, due to the opacity of carbon fibres it was impossible to determine if these assumptions were valid at the time.

The discovery of PMMA particles within fractured samples provided evidence which validated those assumptions. Results in Section 6.3.1.2 showed that the sizes of the observed voids and PMMA particles were found to range from 4-12µm. This closely matched what was found in Section 3.9.2.1. PMMA printed, and subsequently cured within, 977-20 resin pre-cured for twenty minutes was shown to break up into many droplets ranging from 5-10µm in diameter, with larger droplets at the centre, and smaller ones at the edges. This was strikingly similar to what was shown in Figure 6.13. In resin slides with lower degrees of pre-cure, the PMMA was partially dissolved, preventing the formation of larger droplets. All of this indicated that 977-20 RTM resin pre-cured for twenty minutes was indeed an accurate facsimile for the resin system used in 977-2 prepreg as previously assumed in Section 3.9.3.

Because of this, it may also be assumed that the observations of PEG 1,500M_w and PEG 20,000M_w printed upon resin cured to the same degree were also correct. And therefore any hypotheses that were developed drawing upon evidence from the printed resin slide tests were built upon accurate information.

It was anticipated that PEG 1,500M_w samples would exhibit characteristics of matrix toughening. Printed resin slide results in Section 3.9.2.2 showed that PEG 1,500M_w droplets completely dissolved into the surrounding matrix. And low molecular weight additives are often used to increase the toughness of bulk matrices [9, 11, 97, 246-248].

Like unprinted samples, the 0° surface of delaminated PEG 1,500M_w samples was predominantly the fibre dominated surface. However, whilst the 0° surface of unprinted samples was fibre dominated in all but a few isolated regions, the 0° surface of PEG 1,500M_w samples exhibited a slightly greater degree of matrix bonded to it. It was described in Section 2.6.4.1 how this may be an indication of increased matrix toughness and/or fibre/matrix interface bond strength. But this minor difference alone was not definitive evidence of matrix toughening, as it may have equally been due to variable such as contamination at the layup stage.

It was observed that very few cusps were produced. And those that were produced were flat, rounded, and possibly smeared. As discussed in Section 2.6.4.5, this is a strong indication that the bulk matrix was heavily plasticised, which may be expected from the introduction of such a low molecular weight polymer. Also, the polymer was contained entirely within the resin-rich region; kept captive by the densely packed fibres either side of it. So despite the extremely low amount of polymer that was added, it would have amounted to a relatively high percentage when just considering the volume of resin in the resin-rich region.

Additionally, no rollers at all were observed. And, as stated in Section 2.6.4.4, this is something that generally only occurs in very ductile matrix materials [157, 167]. All of these factors inferred that the interlaminar matrix material was significantly plasticised by the addition of PEG.

As described in Section 2.6.4.1, the matrix which remains bonded to the matrix dominant surface is known as the resin-rich region: a thin layer between plies containing few or no fibres. The thickness of this region has been shown to affect interlaminar fracture toughness [62-64]. In delaminated PEG 1,500M_w samples, the resin-rich region appeared to be somewhat thinner than in unprinted samples. Subsequent measurements proved this to be true, showing that the thickness of the resin rich-region was on average only 37% as thick as in unprinted samples. In Section 3.9.2.2 it was shown that PEG 1,500M_w fully dissolved into the surrounding matrix, most likely creating a homogeneous blend of PEG and resin which would have had a greater toughness and ductility than the neat resin. This may also have decreased the viscosity of the resin, which then allowed a greater than normal volume of resin to be drawn from the laminates during curing under vacuum and autoclave pressure (total of 104.5psi or 7.2bar). In Section 2.3.1.3 it was shown that in ductile matrices a thin resin-rich region may extend the delamination process zone, increasing the rate at which delamination occurs. This is somewhat complementary to what was hypothesised in Section 5.5.2. Although in that section temperature effects were presumed to be the dominant cause of the increased rate of delamination in PEG 1,500M_w fatigued samples, as it was not anticipated that the

thickness of the resin-rich region would be reduced. The thickness of the resin-rich region, coupled with increased ductility (possibly exacerbated by intrinsic heating effects) may have therefore had a greater influence upon the rate of delamination than previously anticipated.

Combined, these factors led to the conclusion that the addition of PEG 1,500M_w to the composite did indeed lead to a significant increase of material toughness and possibly fibre/matrix bonding in the interlaminar region. However, this was accompanied by an undesirably large increase in matrix ductility and decrease in resin-rich region thickness. The evidence gathered here indicated that the molecular weight of this particular PEG was too low to be beneficial to the system.

PEG 20,000M_w delaminated surfaces presented features which were once again very different to the previously examined samples.

In other sample types, it was generally the 90° ply that was the matrix dominated ply. In PEG 20,000M_w samples, the distribution of matrix was approximately even amongst the 0° and 90° surfaces. As discussed in Section 2.6.4.1, the normal tendency of delaminations to fracture along the fibre/matrix interface of the tensile surface may be interrupted if fibre/matrix interfacial bonding is high. This level of distribution of matrix dominated regions between both 0° and 90° surfaces is something that was not observed in other sample types; not even in PEG 1,500M_w samples. Additionally, in fibre dominated regions of surfaces, matrix material was seen to cover the fibres below to a much greater degree than in unprinted samples, further indicating the increased fibre/matrix bond strength of these samples. This was a significant indication that the addition of PEG 20,000M_w greatly increased the interfacial bond strength of samples, and was evidently highly influenced by the molecular weight of the PEG since equal volumes of both PEG 1,500M_w and PEG 20,000M_w were added.

The matrix of these samples appeared to show a degree of plasticity that was not seen in unprinted samples, but to a lesser degree than was seen in PEG 1,500M_w samples. In PEG 20,000M_w samples it was seen that cusps formed on surfaces, but in most cases were flat and rounded. This was shown in Section 2.6.4.5 to be another indicator of matrix toughness.

The number of rollers present in these samples was also shown to be significantly lower than in unprinted samples. The addition of PEG 1,500M_w was previously shown to eliminate any indication of rollers. But in PEG 20,000M_w specimens, rollers were still formed, but in many cases did not separate from the surrounding matrix. Once again, this is something that was previously discussed in Section 2.6.4.4 as being an indicator of increased matrix toughness.

Importantly, the thickness of the resin-rich region remained much thicker than in PEG 1,500M_w samples. It was shown to be reduced to 60% of the thickness of unprinted samples,

but this was considerably greater than PEG 1,500M_w samples. It was shown in Section 3.9.2.3 that PEG 20,000M_w droplets exhibited a minor degree of dissolution into the surrounding matrix. Evidently, this affected the viscosity of the resin just as it did in PEG 1,500M_w samples. But the minor amount of dissolution and high molecular weight of the PEG did not result in as much extra resin being drawn out. A major consequence of this observation was that if resin was drawn from the interlaminar region, then the droplets would not have remained where they were deposited. However, no evidence was seen that the deposited pattern had any effect upon the mechanical properties of printed composites. And it may be reasonable to assume that resin and PEG were removed together in equal proportions, ultimately leaving the percentage of polymer in the resin-rich region the same.

It was previously discussed how the reduced thickness of the resin-rich region in PEG 1,500M_w samples may have resulted in an extended process zone at crack tips, which was detrimental due to the increased ductility of the matrix in the interlaminar region. The fact that the thickness of the resin-rich region in PEG 20,000M_w samples remained thick was no doubt beneficial to these samples, allowing the enlarged process zone to dissipate more energy, whilst not extending it as much and causing the rate of delamination to increase. This may have been a key mechanism in the successful retardation of delamination growth in PEG 20,000M_w laminates. It is likely then that higher molecular weight PEGs would exhibit thicker resin-rich regions, and may perform even better. Although further work would need to be done to investigate this.

All of the observations made here appeared to indicate that the addition of PEG 20,000M_w resulted in an increase in both matrix toughness and fibre/matrix interface strength. Whilst similar observations were also made in PEG 1,500M_w specimens, in PEG 20,000M_w specimens it was seen that interfacial bonding was increased significantly, but ductility/plasticity was intermediate. This implied that this molecular weight of PEG provided a good balance of toughening properties whilst not being detrimental in such ways as reducing the strength of the matrix.

As well as being instrumental in the identification of micromechanical mechanisms, fracture surfaces were also important in determining the key mechanisms in the formation of delaminations. This was of particular importance in the following paragraphs when analysing crack densities in samples.

It has previously been discussed that transverse ply cracks are well known to be a major initiator of delaminations in multidirectional laminates [65, 231, 232]. It was also discussed in Section 2.3.2 that free edge stresses are also known to initiate and propagate delaminations

[77, 78]. Ultimately, both of these mechanisms proved significant in the propagation of delaminations.

It was seen in all samples that significant levels of transverse cracking occurred. And evidence of these transverse cracks (in the 90° plies) was present in the 0° plies as raised ridges of matrix material. In Section 2.6.4.2 it was described how the orientation of cusps can be used to infer the direction of delamination propagation. Cusps in fibre dominated surfaces lean towards their point of origin, and those in matrix dominated surfaces lean away [5]. SEM micrographs were presented which clearly showed by the analysis of cusp lean, that delaminations propagated outwards from transverse cracks in those samples.

However, it was also found that the orientation of cusps indicated that delaminations also originated from free edges. It was shown in Figure 6.23 that the orientations of cusps in close proximity to both a transverse crack and a free edge were influenced by the presence of both features. This showed that free edges also contributed to the propagation of delaminations, and probably acted as initiation points alongside transverse cracks. No cusps were visible at the very edges of specimens, most probably due to excessive fretting, which was evident from the highly roughened texture very close to free edges. This indicated that free edges were some of the earliest regions to delaminate [5, 153, 167]. It was also seen in Figure 6.23 that the dominance of either the free edge or the transverse crack increased the closer that observations were made to those features; although this image only represented a small fraction of the surface area of the specimen. Away from free edges, the orientation of cusps indicated that delaminations were far more influenced by transverse cracks. This was apparent from their near vertical orientation. This was observed with increasing effect towards the centre of samples.

It was shown in Figure 6.25 that despite the previous findings which suggested that delaminations were primarily propagated outwards from transverse cracks, delaminations were in fact primarily propagated inwards towards the centre of samples. However, subsequent evidence presented in Figure 6.26 provided an explanation for this. It remained true that delaminations were propagated primarily outwards from transverse cracks. But instead it was the transverse cracks themselves which were propagated inwards from the free edges, giving the effect that delaminations as a whole propagated inwards.

This information may be tied together by Figure 6.27. In this image, delaminations created a distinctive pattern on the fracture surfaces.

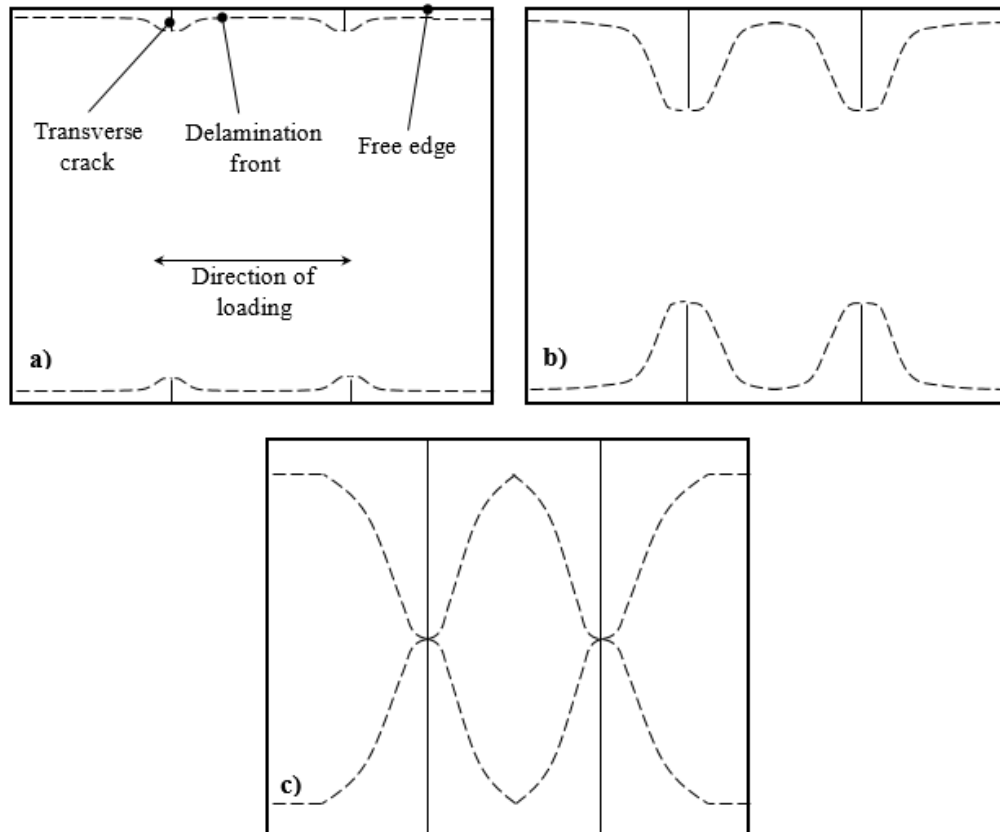


Figure 6.36 An illustration of the theorised way in which delamination propagated through samples. Delamination fronts are driven both forwards and outwards as transverse cracks lengthen, meeting in the centre. a) Transverse cracks and delaminations form at the free edges, seeded by free edge stresses. b) Transverse cracks extend inwards, forcing delaminations inwards with them. c) Transverse cracks and delaminations meet in the centre. The remaining non delaminated area extends inwards due to free edge stresses.

The (vertical) origin lines of delaminations were clearly visible, caused by transverse cracks in the adjacent 90° ply. The horizontal line along the approximate centreline of the sample was indicative that delaminations met in the centre.

Based on the available evidence, a theoretical mechanism of delamination propagation was developed, and is illustrated in Figure 6.36. It shows delaminations emanating from two transverse cracks on either edge of the specimen as they lengthen, and then driven forward under the influence of free edge stresses. This satisfies the evidence that was observed in delaminated samples. It shows how delaminations could appear to emanate from transverse cracks whilst the transverse cracks themselves propagate towards the centre. It also explains why delaminations met in the middle. If they were propagated purely by transverse cracks then no centreline would be visible in Figure 6.27. Likewise, if they were propagated by free edge stresses alone then no transverse crack lines would be visible. The true mechanism was therefore a combination of both. Of course transverse cracks would not necessarily meet in

the middle as shown in the illustration. It was drawn that way for ease of interpretation. It is likely that transverse cracks would develop between different fibres. But when the delamination fronts of opposite sides met, it is likely that the transverse cracks that propagated them would be arrested because they would be subsequently separated from the 0° plies placing strain upon them. This would effectively halt them along the line at which opposing cracks overlapped i.e. the middle of the samples (assuming that all transverse cracks propagated inwards at approximately the same rate).

6.4.2 Crack Density Measurements

Crack density measurements aimed to correlate transverse cracks and delaminations visible at the free edges with what was observed in stiffness degradation and fracture surface measurements in cyclic tensile tests. The primary concern of these replica observations was to investigate the possibility of differing rates of visible damage in samples printed with different polymers during Phases Ia and Ib of stiffness degradation.

Analysis of stiffness degradation results in Section 5.5.2 showed that samples experienced three distinct phases of stiffness degradation. The first of these phases was thought to be caused by the development of transverse cracks in off axis plies. In all samples, Phase Ia of stiffness degradation transitioned to Phase Ib at around 5k-20k cycles, which was indicated in the figures by a hashed region. By combining transverse crack measurements from all non-zero plies, it was shown in Figure 6.31 that transverse crack measurements reached a point of saturation between 10k and 20k cycles, matching the results of stiffness degradation very well, and therefore providing evidence that Phase Ia was indeed mainly a result of transverse cracks in that stage of testing.

Transverse crack measurements also showed that PEG 20,000M_w samples experienced far more transverse ply cracking than all other samples in Phase Ia of stiffness degradation. This supported what was observed in Section 5.5.2 in which it was noted that the Phase Ia stiffness degradation of PEG 20,000M_w samples exceeded that of other sample types. Based on theories developed at the time about the causes of the different stiffness degradation phases, it was hypothesised that PEG 20,000M_w samples should experience a greater degree of transverse ply cracking than other samples, and the data presented here clearly supports that. This further proves that Phase Ia was dominated by the influence of transverse cracks.

This large degree of transverse cracking would also allow delaminations to develop early in PEG 20,000M_w samples. This may explain why the transition between Phases Ia and Ib was much more gradual in PEG 20,000M_w samples than in others (Figure 5.26). This is also

supported by data in Figure 6.34 which showed that PEG 20,000M_w samples exhibited more surface delaminations in the very early stages of testing than other sample types. Additionally, this early onset of delamination may have relieved strain in these samples, reducing the number of transverse cracks which ultimately formed. This may explain why the total amount transverse cracks observed in 20,000M_w samples at saturation was in line with other samples despite the large amount which formed in the early stages of testing.

It was shown in Figure 6.32 that the delaminations at 0°/90° interfaces diverged during the period in which new transverse cracks were still forming. PMMA and PEG 20,000M_w samples exhibited the greatest rate of delamination development during this period. These were also the sample types that exhibited the greatest numbers of transverse cracks prior to the saturation of 0°/90° delamination at around 100k cycles. This implied that the level of transverse crack formation was directly related to the rate of delamination formation. However, these observations may also have been due to data scatter, and so were not conclusive.

In some cases, reductions in the total length of cracks were recorded past the saturation point. This may have been caused when propagating delaminations relieved local strains, allowing cracks to close. It was noted in Section 6.3.2.1 that the replica technique was not good at detecting extremely fine cracks. Therefore, many cracks may have become undetectable past a certain point. Again though, data scatter may have also accounted for these anomalies.

Unlike 0°/90° delaminations, 90°/45° delaminations did not reach saturation by 100k cycles. This was most likely due to the delamination of 0°/90° interfaces. When disconnected from the load bearing 0° plies, 90° and 45° plies would have experienced very little strain, greatly reducing their tendencies to delaminate. But whilst the major strains upon the central plies were removed, they may well have continued to delaminate slowly, and may have contributed to the minor stiffness reductions that were observed in Phase II of stiffness degradation.

Unfortunately, drawing conclusions between delamination rates and Phase Ib stiffness degradation proved impossible. This was due to the fact that delaminations, particularly those at the 0°/90° interfaces, reached saturation rapidly, and at similar rates. It was thought that this was because the stress concentrations in the immediate vicinity of free edges was so great that they caused edge delaminations to occur at a much greater rate than the delaminations propagating inside the samples. And the very similar rates of edge delamination development suggested that this may have been independent of the addition of toughening polymers. Alternatively, microcracks too small to be detected by replicas may have been formed when the samples were being cut during the manufacturing process. These may well have facilitated the rapid development of edge delaminations. Also, stress concentrations caused by the fine

grooves left by polishing could have created additional stress concentrations which accelerated the development of edge delaminations.

Additionally, evidence presented in Section 6.4.1 showed that delamination fronts were propagated inwards from free edges as well as outwards from transverse cracks, so it was likely that delamination density measurements were somewhat redundant because they were incapable of quantifying the true state of delamination occurring inside the laminates. Therefore, it could not be directly confirmed that Phase Ib stiffness degradation was caused by delamination. Although, it is important to remember that all other indirect evidence indicated that it was. Therefore, further work would be required to definitively prove that delaminations were influenced by the addition of inkjet printed polymers. One way in which this might be achievable is through the use of x-ray computed tomography (CT), previously discussed in Section 2.6.5, which could be used to observe the internal progression of delaminations.

6.5 CONCLUSIONS

In this chapter scanning electron microscopy was used to analyse fatigue fracture surfaces and cellulose acetate replicas which showed the development of surface fatigue cracks in samples.

The delaminated surfaces of $0^\circ/90^\circ$ interfaces were analysed using SEM because those interfaces experienced the greatest degree of delamination. The perpendicularity of the $0^\circ/90^\circ$ plies also made features easier to identify and follow.

It was found that unprinted laminates showed evidence of brittle matrix fracture in the interlaminar region which is typical of standard epoxy matrices.

PMMA laminates also displayed brittle matrix fracture which was indistinguishable from unprinted laminates. However, discreet PMMA droplets were discovered embedded in the fracture surfaces along with the voids that they left behind. This discovery was instrumental in validating test results obtained in Section 3.9, and therefore the theories developed in Section 5.5.2 relating to the fracture mechanics of printed composites were also validated.

It was found that the molecular weights of the PEGs that were used greatly affected the toughening properties that they produced in the composites. The complete dissolution of PEG 1,500M_w into the surrounding matrix plasticised the interlaminar matrix greatly. Evidence was also presented showing that the addition of PEG 1,500M_w also reduced the thickness of the resin-rich region, causing increased stress concentrations, which most likely accelerated damage progression in those laminates. Conversely, PEG 20,000M_w printed laminates also

showed evidence of material toughening as well as increased fibre/matrix bonding. Additionally, a decrease in the resin-rich region was observed, but to a far less severe degree than in PEG 1,500M_w samples, so the toughening effect was not detrimental in PEG 20,000M_w samples as it was in PEG 1,500M_w samples.

SEM fractography was also utilised in determining the mechanisms of delamination initiation and progression in tensile specimens. It was found that transverse cracks originated at the edges of the non-zero plies of the laminates, propagating inwards, initiating delaminations which were propagated further by a combination of the growth of transverse ply cracks and free edge stresses.

Crack density measurements were also conducted upon acetate replicas taken from the free edges of tensile fatigue specimens at various points during cyclic tensile testing at a stress factor of 0.5.

Results showed that PEG 20,000M_w samples exhibited a greater degree of transverse ply cracking than other samples in the early stages of testing. This helped to validate theories developed in Section 5.5.2 regarding the mechanisms which cause different phases of stiffness degradation. Unfortunately, possibly due to the effect of free edge stresses, many of the delamination density measurements taken at high numbers of cycles were not representative of the true progression of delamination within samples. This meant that direct observation of retarded or accelerated delamination growth in printed composites could not be measured. And therefore further work is required to remedy this.

CHAPTER 7: CONCLUSIONS AND FURTHER WORK

The main objective of this work was to investigate for the first time the effects of the addition of thermoplastic polymers by inkjet printing methods exclusively into the interlaminar region of carbon fibre reinforced polymer composites in fatigue loading. The work presented in this thesis has generated new understanding of the damage mechanisms operating at the interlaminar interface of cyclically loaded inkjet printed composites. It also demonstrated that such printed composites could potentially outperform unprinted laminates. The effect of the polymer addition upon delamination resistance were of primary interest because delamination is a key damage mechanism in composite failure. The precise deposition of polymers using inkjet printing provided a high degree of controllability over the toughening effects, and presented a novel approach to the interlaminar toughening of composite laminates in fatigue loading.

7.1 CONCLUSIONS

PMMA and PEG thermoplastics were selected for their varying mechanical properties, giving a range of toughening capabilities. These thermoplastics were dissolved in suitable solvents. Three different 'inks' were used. These were:

- 10%/wt PMMA in DMF
- 10%/wt PEG 1,500M_w in deionised water
- 10%/wt PEG 20,000M_w in deionised water

It was demonstrated how the shape and spacing of the printed pattern influences surface coverage and the volumes and masses of polymers added to the completed laminates. In all cases it was calculated that less than 0.01% additional mass was added to laminates. With the aid of inkjet printing, the amount of toughening materials used was considerably smaller than other toughening methods such as bulk matrix toughening and interleaving. The durability of the printed pattern was also investigated, and under controlled conditions it was found that normal manufacturing processes would not affect the integrity of the printed droplets. Additionally, DSC was used to confirm that material properties were consistent between cures. Variations in the degree of cure may affect tensile modulus and matrix toughness. However, the samples tested were found to be very consistent, exhibiting an average degree of cure of 98.2%.

Partially cured 977-20 RTM resin on glass microscope slides were prepared and printed with the polymer inks in order to determine the behaviour of printed polymers when cured within

laminates. It was found that 977-20 RTM resin that was partially cured at 180°C for twenty minutes best represented the properties of the uncured resin of 977-2 prepreg. This was later validated by SEM observation of sample fracture surfaces. Once cured, the different polymers exhibited varying behaviours:

- PMMA droplets remained as a discrete phase within the cured resin, breaking up into multiple smaller droplets ranging from 5-10µm in diameter.
- PEG 1,500M_w droplets dissolved completely into the surrounding resin, potentially creating a homogeneous toughened blend.
- PEG 20,000M_w droplets exhibited partial dissolution, remaining where they were deposited, but transitioning gradually into the surrounding resin.
- Neither water nor DMF were shown to have any adverse effects upon the printed polymers or surrounding resin.

The different behaviours of the polymers provided a range of mechanisms by which the polymers may interact with the surrounding material, ranging from discrete droplets to complete dissolution, allowing a range of effects to be investigated in mechanical tests.

The main mechanical testing regime was conducted in two formats, each consisting of static and cyclic components. The first of these was four point bending tests. Results showed that in static flexural tests, neither the flexural strength nor stiffness of laminates was influenced by the printing of 10%/wt PMMA in DMF ink. In cyclic flexural tests it was observed that PMMA printed samples exhibited significantly shorter fatigue lives than unprinted samples, being around one order of magnitude shorter in most cases, and showing that the fatigue lives of printed samples were at detriment because of the introduction of PMMA. Despite the successful formation of delaminations in cyclic flexural tests, it was found that the stiffness degradation curves that were obtained showed low repeatability. Further investigation using scanning electron microscopy found that this was most likely caused by fatigue cracks in the through thickness direction which originated from the loading rollers. Following these results, tensile testing was introduced as a potentially more reliable method of promoting delaminations whilst avoiding undesirable artefacts caused by test geometry.

Static tensile test results showed that the static tensile strengths of all printed samples were greater than those of unprinted samples. The tensile strengths of unprinted, PMMA, PEG 1,500M_w, and PEG 20,000M_w samples were found to be 633MPa, 668MPa, 657MPa, and 664MPa respectively. Similarly, the tensile moduli of these samples (in the same order) were 34.2GPa, 30.0GPa, 34.0GPa, and 38.4GPa, showing that the tensile stiffness of laminates was increased by the addition of PEG, but reduced by the addition of PMMA. Different mechanisms for these properties were proposed based upon combinations of literature,

experimental data, and microscope observations of resin printed slides. Broadly, these mechanisms were determined to be:

- In PMMA printed samples, weak bonding between the matrix and separate PMMA droplets provided a method of dissipating energy, but also reduced the ability of the laminate to share loads between plies, increasing static strength, but reducing stiffness.
- In PEG 1,500M_w samples, increased fibre/matrix bonding coupled with crack pinning, particle bridging, crack path deflection, and energy absorption through microcracking may have worked simultaneously to retard damage events.
- Damage mechanisms in PEG 20,000M_w samples acted in similar ways to those in PEG 1,500M_w samples due to their similar interactions with the surrounding matrix.

In cyclic tensile tests, stiffness degradation was found to yield very reliable results, particularly at low stress factors. Therefore, further tests focussed on this particular region of testing. Analysis of stiffness degradation curves showed that curves exhibited three distinct phases of stiffness degradation which defined the start and end of the active periods of particular damage mechanisms. These phases (in sequential order) were found to be transverse cracking, delamination, and fibre/matrix debonding. This was contrary to the typical model that many authors use. However, other authors had also observed such behaviours, but failed to recognise the significance of the observations with respect to understanding micromechanical damage mechanisms, instead choosing to group together and generalise the mechanisms. A new model of stiffness degradation was therefore proposed which recognises these distinct points of stiffness change.

It was found that under cyclic loading both PMMA and PEG 1,500M_w samples exhibited very similar stiffness degradation. However, both proved detrimental to delamination, both decreasing at rates approximately 3.8 times faster than unprinted samples in the delamination phase of tests. PEG 20,000M_w samples however, showed improved delamination resistance. Stiffness degradation due to delamination in PEG 20,000M_w samples was shown to be approximately 0.52 times the rate experienced in unprinted samples, which was a very significant improvement. A consequence of this improvement was increased levels of transverse cracks in off-axis plies, resulting in greater initial stiffness degradation than in all other sample types. Although it was theorised that stacking sequences which reduce the strain differences plies may minimise this issue.

Damage mechanisms which elaborated upon those developed as a result of static tests were developed, and aimed to explain why the introduction of polymers produced very different results between static and cyclic tests. Broadly, these mechanisms were:

- In PMMA printed samples, the weak bonding between the matrix and separate PMMA droplets caused the droplets to separate with successive loading cycles, effectively creating large numbers of voids in the interlaminar region which acted as stress concentrations.
- In PEG 1,500M_w samples, viscous heating caused by cyclic loading increased the ductility of the PEG, increasing the size of the crack process zone. The process zone was constrained by the surrounding fibres, extending its length into the interlaminar region, and causing more rapid delamination.
- PEG 20,000M_w was shown to have a higher melting temperature than PEG 1,500M_w. Therefore, the ductility of the matrix was less affected by viscous heating. The semi-discrete nature of the PEG 20,000M_w droplets also confined them, preventing the bulk interlaminar matrix from becoming excessively ductile.

Scanning electron microscopy was used to observe the delaminated surfaces of tensile specimens. The 0°/90° interfaces of specimens were analysed because they experienced the greatest degree of delamination. The perpendicularity of the 0°/90° plies also made features easier to identify and follow. The key observations for each laminate type were:

- Unprinted laminates showed evidence of brittle matrix fracture in the interlaminar region which is typical of standard epoxy matrices.
- PMMA laminates also displayed brittle matrix fracture which was indistinguishable from unprinted laminates. However, discrete spherical PMMA particles were discovered embedded in the fracture surfaces along with the voids that they left behind. This discovery was instrumental in validating printed resin slide test results, and therefore theories relating to the fracture mechanics of printed composites were also validated.
- The complete dissolution of PEG 1,500M_w into the surrounding matrix plasticised the interlaminar matrix greatly. PEG 1,500M_w also reduced the thickness of the resin-rich region, causing increased stress concentrations, which most likely accelerated damage progression in those laminates.
- PEG 20,000M_w printed laminates also showed evidence of material toughening as well as increased fibre/matrix bonding. Additionally, a less significant decrease in the resin-rich region was observed, so the toughening effect was not detrimental in PEG 20,000M_w samples as it was in PEG 1,500M_w samples.

SEM fractography was also utilised in determining the mechanisms of delamination initiation and progression in tensile specimens. It was found that transverse cracks originated at the edges of the non-zero plies of the laminates, propagating inwards, initiating delaminations which were propagated further by a combination of the growth of transverse ply cracks and free edge stresses.

Crack density measurements were also conducted upon acetate replicas taken from the free edges of tensile fatigue specimens at various points during cyclic testing. Results showed that PEG 20,000M_w samples exhibited a greater degree of transverse ply cracking than other samples in the early stages of testing. This helped to validate theories in earlier chapters which were developed to explain the mechanisms which caused different phases of stiffness degradation. Unfortunately, due to high degrees of data scatter, interpretation of the remaining delamination density data proved difficult, and the inwards progression of delamination meant that data could not be used to accurately determine the state of delamination within samples.

Ultimately, the results presented in this thesis indicated that PEG 20,000M_w exhibited significant increases in delamination resistance when compared to unprinted laminates, as well as increased tensile strength and stiffness. The mechanisms by which composite laminates printed with PEG 20,000M_w produced these results were investigated using various experimental and analytical techniques, as well as drawing on the pool of knowledge from literature.

7.2 FURTHER WORK

The work conducted in this thesis has identified that inkjet printed polymers can improve the delamination resistance of prepreg composite laminates. The key mechanisms for the success of printed composites were shown to be improved fibre/matrix bond strength, and the ability of the polymer to blend with the epoxy matrix to improve matrix toughening. However, the relative performance of other toughening polymers requires further work.

The polymers used in this thesis were selected for their varying mechanical properties, and based on investigations conducted by others. However, many other polymers exist which are often used in matrix toughening, and the polymers used here only represent a fraction of the possibilities. Additionally, the molecular weight of PEG was shown here to have a significant effect upon the mechanical properties of laminates. Therefore, careful consideration should be given to the molecular weight of polymer candidates, and higher molecular weight PEGs may be a promising option. It would be advised that higher molecular weight PEGs should be investigated. If a change of toughening polymer is desired, then polymers which are miscible

in resin may show good results. Particularly those typically used as plasticisers, such as glycidyl ethers of aliphatic arylphatic glycols or polyols etc [249]. Of course, it should be ensured that these polymers (or monomers) should be soluble in order for them to be compatible with the inkjet printing process.

Additionally, investigations into delamination resistance should not be solely limited to unidirectional prepregs. Woven prepregs are commonly used composite structures, and they are also susceptible to delamination. To improve the applicability of printed composites to industrial applications, woven prepreg investigations should also be conducted. These tests should be directly comparable to the tensile tests conducted in this thesis, and would give insight into how the toughening methods developed here may be affected by the much higher degree of ductility that woven prepregs would present.

The conclusion that the addition of PEG 20,000M_w to laminates greatly improved delamination resistance was a key point in this work. However, it was found that PEG 20,000M_w samples exhibited greater levels of transverse ply cracking than other sample types. The stacking sequence that was used in tensile samples was specifically designed to induce high levels of delamination by the inclusion of large proportions of off-axis plies. This is obviously not done in well-designed composite parts. Therefore, investigations into different, more realistic stacking sequences should be performed to investigate if transverse ply cracking remains a detrimental factor in PEG 20,000M_w printed laminates. Such stacking sequences may include 15° or 30° lamina orientations, which are commonly used.

It was possible through extensive testing and analysis to determine the damage mechanisms operating in the different printed samples with a good degree of confidence. It was determined that all sample types utilised mechanisms which dissipated fracture energy. In PMMA printed samples, this was through the separation of PMMA droplets from the surrounding matrix. In PEG printed samples, it was through the plastic deformation of the ductile matrix. These mechanisms may therefore prove beneficial in impact scenarios, where high energy dissipation abilities are of particular benefit to prevent the propagation of damage throughout the laminate. Delamination and fibre/matrix debonding are key damage mechanisms in impact [250-252]. These are capabilities that printed composites (particularly PEG printed composites) were shown to possess. An impact test regime is therefore recommended for the complete understanding of printed composite capabilities. It would be advised that both common and strain-inducing stacking sequences be used in these tests in order to further determine the level of transverse ply cracking that occurs in PEG 20,000M_w samples. X-ray tomography or ultrasound C-scanning may be useful techniques in determining the level of damage sustained by impacted specimens. Acoustic emission may also be used in low energy

impact tests. Finally, post-impact strength/modulus tests may be conducted on samples to determine their residual mechanical properties.

It was successfully identified that the delamination rates of specimens were affected by the introduction of inkjet printed polymers. However, this was based upon indirect measurements of laminate stiffness. It was identified that delamination progression acts in an inwards direction, and due to the opacity of carbon fibres, most measurement methods are incapable of directly measuring this progression. X-ray computed tomography (Section 2.6.5) however, is a direct method that could be used to measure delaminations, and therefore confirm what was observed by the measurement of stiffness degradation. Tensile specimens could therefore be partially delaminated to various degrees, and their delamination state quantified by tomography.

Finally, finite element analysis (FEA) is an invaluable tool that is often used to predict and validate experimental behaviours. It may be possible using multiscale FEA techniques to develop models of damage behaviour in printed composites using optical observations of droplet behaviour such as the printed resin slide tests used in this thesis. If these models could be successfully validated against experimental data, then predictive models could be developed which could greatly benefit the selection of appropriate polymers by removing the need to conduct lengthy fatigue investigations.

REFERENCES

1. Jones, R.M., *Mechanics of composite materials*. 1998: CRC Press.
2. Soboyejo, W., *Mechanical properties of engineered materials*. Vol. 152. 2002: CrC Press.
3. Marsh, G., *Airbus takes on Boeing with reinforced plastic A350 XWB*. Reinforced plastics, 2007. **51**(11): p. 26-29.
4. Harris, B., *Fatigue in Composites: Science and Technology of the Fatigue Response of Fibre-Reinforced Plastics*. 2003, Cambridge, England: Woodhead Publishing Limited. 729.
5. Greenhalgh, E., *Failure analysis and fractography of polymer composites*. 2009: Elsevier.
6. Argüelles, A., et al., *Fatigue delamination, initiation, and growth, under mode I and II of fracture in a carbon-fiber epoxy composite*. Polymer Composites, 2010. **31**(4): p. 700-706.
7. Garg, A.C., *Delamination—a damage mode in composite structures*. Engineering Fracture Mechanics, 1988. **29**(5): p. 557-584.
8. de Gans, B.J., P.C. Duineveld, and U.S. Schubert, *Inkjet printing of polymers: state of the art and future developments*. Advanced materials, 2004. **16**(3): p. 203-213.
9. Zhang, Y., et al., *Improvements in Carbon Fibre Reinforced Composites by Inkjet Printing of Thermoplastic Polymer Droplets*. physica status solidi (RRL)-Rapid Research Letters, 2014. **8**(1): p. 56-60.
10. Zhang, Y., et al., *Fabrication of patterned thermoplastic microphases between composite plies by inkjet printing*. Journal of composite materials, 2014.
11. Zhang, Y., *The effect of inkjet printed polymer on the mechanical properties of carbon fibre reinforced plastic*, in *Mechanical Engineering*. 2015, The University of Sheffield. p. 182.
12. Zhang, Y., et al., *Fabrication of patterned thermoplastic microphases between composite plies by inkjet printing*. Journal of Composite Materials, 2014: p. 0021998314533715.
13. Yasaee, M., et al., *Damage control using discrete thermoplastic film inserts*. Composites Part A: Applied Science and Manufacturing, 2012. **43**(6): p. 978-989.
14. Schneider, J., et al. *A meso-fe voxel model of an interlock woven composite*. in *Proceeding of the international conference in composite materials 17th (ICCM17), Edinburgh, Scotland*. 2009.
15. engineering, e. *Digmat-FE*. 2017 [cited 2017 23/06/2017]; Available from: <http://www.e-xstream.com/products/tools/digmat-fe>.
16. Ashby, M.F. and D. Cebon, *Materials selection in mechanical design*. Le Journal de Physique IV, 1993. **3**(C7): p. C7-1-C7-9.
17. redOrbit. *Fibreglass*. [cited 2017 26/06/2017]; Available from: <http://www.redorbit.com/reference/fiberglass/>.
18. Kajzar, F., et al., *Key Engineering Materials: Interdisciplinary Concepts and Research*. Vol. 2. 2014: CRC Press.
19. Barbero, E.J., *Introduction to composite materials design*. 2010: CRC press.
20. DeMerchant, C. *Comparison of Carbon Fiber, Kevlar® (Aramid) and E Glass used in Composites for Boatbuilding*. 2017 [cited 2017 26/06/2017]; Available from: <http://www.christinedemerchant.com/carbon-kevlar-glass-comparison.html>.
21. Nicolais, L., A. Borzacchiello, and S.M. Lee, *Encyclopedia of Composites*, in *Encyclopedia of Composites*, L. Nicolais, A. Borzacchiello, and S.M. Lee, Editors. 2012, Wiley: New York. p. 3444.
22. Bennett, S. and D. Johnson. *Structural heterogeneity in carbon fibers*. in *Proceedings of the Fifth London International Carbon and Graphite Conference*. 1978.

23. Yu, S., *Numerical and experimental investigation of impact behaviour of composite materials used in aerospace*, in *Mechanical Engineerin*. 2014, The University of Sheffield. p. 252.
24. Amsc, N. and A.A. CMPS, *Composite materials handbook*, in *POLYMER MATRIX COMPOSITES MATERIALS USAGE, DESIGN, AND ANALYSIS*. 2002, USA Department of Defence.
25. Chawla, K.K., *Composite materials: science and engineering*. 2012: Springer Science & Business Media.
26. Hundt, G., J.D. Karcher, and P.J. Jones, *Heavy-atom resin formulation for use in subterranean wells*, U.P. office, Editor. 2013, Google Patents: USA.
27. Suzuki, A.H., et al., *BIOLOGICAL MATERIALS AS PRECURSORS FOR THE PRODUCTION OF RESINS*.
28. Ellis, B., *Chemistry and technology of epoxy resins*. 1993: Springer.
29. Gibson, R.F., *Principles of composite material mechanics*. 2016: CRC press.
30. Ghent_University. *Composite Technology*. [cited 2017 27/06/2017]; Available from: https://vtk.ugent.be/w/images/1/10/Composieten_-_CompositesSummary.pdf.
31. Gurit. *Guide to Composites*. 2013 [cited 2017 27/06/2017]; Available from: <http://www.gurit.com/-/media/Gurit/Datasheets/guide-to-compositesv5webpdf.ashx>.
32. Mazumdar, S., *Composites manufacturing: materials, product, and process engineering*. 2001: CrC press.
33. Reinhart, T.J., *Engineering Materials Handbook Vol. 1. Composites*, ASM International, Ed. CA Dostal, 1987.
34. Tang, J.-M., W.I. Lee, and G.S. Springer, *Effects of cure pressure on resin flow, voids, and mechanical properties*. *Journal of composite materials*, 1987. **21**(5): p. 421-440.
35. Strutt, J., *On the instability of jets*. *Proceedings of the London Mathematical Society*, 1878. **10**: p. 4-13.
36. Smith, P.J. and D.H. Shin, *Inkjet-based micromanufacturing*. Vol. 9. 2012: John Wiley & Sons.
37. Saunders, R.E., J.E. Gough, and B. Derby, *Delivery of human fibroblast cells by piezoelectric drop-on-demand inkjet printing*. *Biomaterials*, 2008. **29**(2): p. 193-203.
38. Delaney, J.T., P.J. Smith, and U.S. Schubert, *Inkjet printing of proteins*. *Soft Matter*, 2009. **5**(24): p. 4866-4877.
39. Madec, M.-B., et al., *Enhanced reproducibility of inkjet printed organic thin film transistors based on solution processable polymer-small molecule blends*. *Journal of Materials Chemistry*, 2010. **20**(41): p. 9155-9160.
40. Derby, B., *Bioprinting: inkjet printing proteins and hybrid cell-containing materials and structures*. *Journal of Materials Chemistry*, 2008. **18**(47): p. 5717-5721.
41. RIOT. *Inkjet - Digital printing technologies*. [cited 2017 27/07/2017]; Available from: <http://www.dp3project.org/technologies/digital-printing/inkjet>.
42. Livera, E., *Investigating the Self-Healing Behaviour of Inkjet Printed Carbon Fibre Composites*, in *Mechanical Engineering*. 2016, The University of Sheffield. p. 85.
43. Fertig, R.S. and D.J. Kenik, *Physics-Based Fatigue Life Prediction of Composite Structures*, in *NAFEMS World Congress 2011*. 2011: Boston, USA.
44. Harris, B., *Fatigue and Accumulation of Damage in Reinforced Plastics*. *Composites, Part A: Applied Science and Manufacturing*, 1977. **8**: p. 214-220.
45. Beaumont, P.W.R., *Physical Modelling of Damage Development in Structural Composite Materials Under Stress*, in *Fatigue in Composites*, B. Harris, Editor. 2003, Woodhead Publishing Limited: Cambridge, England. p. 365-410.
46. Boller, K.H., *Some Fatigue Characteristics of Glass-Reinforced Composite Laminates*, in *ASME Paper*. 1970, ASME: New York, NY.
47. Owen, M.J. and R.J. Howe, *The Accumulation of Damage in a Glass-Reinforced Plastic Under Tensile and Fatigue Loading*. *Journal of Physics D: Applied Physics*, 1972. **5**: p. 1637-1649.
48. Baker, A.A., *The Fatigue of Fibre-Reinforced Aluminium*. *Journal of Materials Science*, 1968. **3**: p. 412-423.

49. Reifsnider, K.L. and Z. Gao, *A Micromechanics Model for Composites Under Fatigue Loading*. International Journal of Fatigue, 1991. **13**(2): p. 149-156.
50. Talreja, R., *Fatigue of Composite Materials: Damage Mechanisms and Fatigue Life Diagrams*. Royal Society of London. Proceedings A. Mathematical, Physical and Engineering Sciences, 1981. **378**(1775): p. 461-475.
51. Abrate, S., *Matrix cracking in laminated composites: a review*. Composites Engineering, 1991. **1**(6): p. 337-353.
52. Paris, F., E. Correa, and V. Mantič, *Kinking of transversal interface cracks between fiber and matrix*. Journal of Applied Mechanics, 2007. **74**(4): p. 703-716.
53. Guedes, R.M. and M.F. de Moura, *Matrix-Controlled Failure Modes of Polymeric Composites*. Wiley Encyclopedia of Composites, 2012.
54. Ogin, S., P. Smith, and P. Beaumont, *Matrix cracking and stiffness reduction during the fatigue of a (0/90) s GFRP laminate*. Composites Science and Technology, 1985. **22**(1): p. 23-31.
55. Luthada, P., *Tension-tension fatigue testing of pultruded carbon fibre composite profiles*. 2016.
56. Schaffer, J.P., et al., *The science and design of engineering materials*. 1995: Irwin Chicago.
57. Wells, J. and P. Beaumont, *Debonding and pull-out processes in fibrous composites*. Journal of Materials Science, 1985. **20**(4): p. 1275-1284.
58. Kollár, L.P. and G.S. Springer, *Mechanics of composite structures*. 2003: Cambridge university press.
59. Kawai, M., et al., *Effects of matrix ductility and progressive damage on fatigue strengths of unnotched and notched carbon fibre plain woven roving fabric laminates*. Composites Part A: Applied Science and Manufacturing, 1996. **27**(6): p. 493-502.
60. Deng, S. and L. Ye, *Influence of fibre-matrix adhesion on mechanical properties of graphite/epoxy composites: III. Impact and dynamic mechanical properties*. Journal of reinforced plastics and composites, 2000. **19**(9): p. 689-703.
61. Prakash, R., *A fractographic study of fatigue in cfrp*. Composites, 1979. **10**(3): p. 174-178.
62. Gao, S.-L. and J.-K. Kim, *Cooling rate influences in carbon fibre/PEEK composites. Part II: interlaminar fracture toughness*. Composites Part A: Applied science and manufacturing, 2001. **32**(6): p. 763-774.
63. Bradley, W.L. and R.N. Cohen, *Matrix deformation and fracture in graphite-reinforced epoxies*, in *Delamination and debonding of materials*. 1985, ASTM International.
64. Sue, H.-J., R. Jones, and E. Garcia-Meitin, *Fracture behaviour of model toughened composites under mode I and mode II delaminations*. Journal of materials science, 1993. **28**(23): p. 6381-6391.
65. Takeda, N. and S. Ogihara, *Initiation and growth of delamination from the tips of transverse cracks in CFRP cross-ply laminates*. Composites science and technology, 1994. **52**(3): p. 309-318.
66. Pagano, N. and R.B. Pipes, *The influence of stacking sequence on laminate strength*. Journal of Composite Materials, 1971. **5**(1): p. 50-57.
67. Foye, R. and D. Baker. *Design of orthotropic laminates, presented at the 1 lth annual AIAA structures*. in *Structural dynamics and materials conference, Denver, Colorado*. 1970.
68. Pipes, R.B. and N. Pagano, *Interlaminar stresses in composite laminates under uniform axial extension*. Journal of Composite Materials, 1970. **4**(4): p. 538-548.
69. Matthews, F.L. and R.D. Rawlings, *Composite materials: engineering and science*. 1999: Elsevier.
70. Weibull, W., *A Statistical Distribution Function of Wide Applicability*. Journal of applied mechanics, 1951. **18**: p. 292-297.
71. Crossman, F.W. and A.S.D. Wang, *The Dependence of Transverse Cracking and Delamination on Ply Thickness in Graphite/Epoxy Laminates*, in *ASTM STP 775*, K.L.

- Reifsnider, Editor. 1982, American Society for Testing and Materials: Philadelphia, PA. p. 118-139.
72. Foye, R.L. and D.J. Baker, *Design of Orthotropic Laminates*, in *11th Annual AIAA Structures, Structural Dynamics, and Materials and Conference*. 1970: Denver, CO.
 73. Pipes, R.B., B.E. Kaminski, and N.J. Pagano. *Influence of the Free-Edge Upon the Strength of Angle-Ply Laminates*. in *Committee D-30 on High Modulus Fibers and Their Composites*. 1973. San Antonio, Tex, USA: American Society for Testing and Materials.
 74. Whitney, J.M. and C.E. Browning, *Free-Edge Delamination of Tensile Coupons*. *Journal of Materials*, 1972. **6**(2): p. 300-303.
 75. Whitney, J.M. *Free-Edge Effects in the Characterization of Composite Materials*. in *Committee D-30 on High Modulus Fibers and Their Composites*. 1973. San Antonio, Tex, USA: American Society for Testing and Materials.
 76. Pipes, R.B., *Moire analysis of the interlaminar shear edge effect in laminated composites*. *Journal of Composite Materials*, 1971. **5**(2): p. 255-259.
 77. Rybicki, E., D. Schmueser, and J. Fox, *An Energy Release Rate Approach for Stable Crack Growth in the Free-Edge Delamination Problem*. *Journal of Composite Materials*, 1977. **11**(4): p. 470-487.
 78. O'Brien, T.K., *Characterization of Delamination Onset and Growth in a Composite Laminate*, in *ASTM STP 775*, K.L. Reifsnider, Editor. 1982, American Society for Testing and Materials: Philadelphia, PA. p. 140-167.
 79. Whitney, J.M. *Analysis of the test methods for high modulus fibers and composites*. 1973. American Society for Testing & Materials.
 80. Gamstedt, K. and S.I. Andersen, *Fatigue Degradation and Failure of Rotating Composite Structures – Materials Characterisation and Underlying Mechanisms*. 2001, Risø National Laboratory: Roskilde, Denmark. p. 55.
 81. Veedu, V.P., et al., *Multifunctional composites using reinforced laminae with carbon-nanotube forests*. *Nature materials*, 2006. **5**(6): p. 457-462.
 82. Arai, M., et al., *Mode I and mode II interlaminar fracture toughness of CFRP laminates toughened by carbon nanofiber interlayer*. *Composites Science and Technology*, 2008. **68**(2): p. 516-525.
 83. Lee, S.-H., et al., *Interlaminar fracture toughness of composite laminates with CNT-enhanced nonwoven carbon tissue interleave*. *Composites Science and Technology*, 2012. **73**: p. 1-8.
 84. White, K.L. and H.-J. Sue, *Delamination toughness of fiber-reinforced composites containing a carbon nanotube/polyamide-12 epoxy thin film interlayer*. *Polymer*, 2012. **53**(1): p. 37-42.
 85. Hamer, S., et al., *Mode I interlaminar fracture toughness of Nylon 66 nanofibrilmat interleaved carbon/epoxy laminates*. *Polymer Composites*, 2011. **32**(11): p. 1781-1789.
 86. Aksoy, A. and L. Carlsson, *Interlaminar shear fracture of interleaved graphite/epoxy composites*. *Composites science and technology*, 1992. **43**(1): p. 55-69.
 87. Lu, W., et al., *Effect of interleaving on the impact response of a unidirectional carbon/epoxy composite*. *Composites*, 1995. **26**(3): p. 215-222.
 88. Hojo, M., et al., *Modes I and II interlaminar fracture toughness and fatigue delamination of CF/epoxy laminates with self-same epoxy interleaf*. *International Journal of Fatigue*, 2006. **28**(10): p. 1154-1165.
 89. Takeda, N., et al., *Effects of toughened interlaminar layers on fatigue damage progress in quasi-isotropic CFRP laminates*. *International journal of fatigue*, 1999. **21**(3): p. 235-242.
 90. Ogihara, S., et al., *Damage mechanics characterization of transverse cracking behavior in quasi-isotropic CFRP laminates with interlaminar-toughened layers*. *International journal of fatigue*, 2002. **24**(2): p. 93-98.

91. Donhowe, I.G. and O. Fennema, *The effects of plasticizers on crystallinity, permeability, and mechanical properties of methylcellulose films*. Journal of Food Processing and Preservation, 1993. **17**(4): p. 247-257.
92. Entwistle, C. and R. Rowe, *Plasticization of cellulose ethers used in the film coating of tablets*. Journal of Pharmacy and Pharmacology, 1979. **31**(1): p. 269-272.
93. Guo, J.-H., *Effects of plasticizers on water permeation and mechanical properties of cellulose acetate: Antiplasticization in slightly plasticized polymer film*. Drug Development and Industrial Pharmacy, 1993. **19**(13): p. 1541-1555.
94. Kulinski, Z. and E. Piorkowska, *Crystallization, structure and properties of plasticized poly (L-lactide)*. Polymer, 2005. **46**(23): p. 10290-10300.
95. Martin, O. and L. Averous, *Poly (lactic acid): plasticization and properties of biodegradable multiphase systems*. Polymer, 2001. **42**(14): p. 6209-6219.
96. Murariu, M., et al., *Poly(lactide (PLA)–CaSO₄ composites toughened with low molecular weight and polymeric ester-like plasticizers and related performances*. European Polymer Journal, 2008. **44**(11): p. 3842-3852.
97. Zavareh, S. and G. Samandari, *Polyethylene glycol as an epoxy modifier with extremely high toughening effect: Formation of nanoblend morphology*. Polymer Engineering & Science, 2014. **54**(8): p. 1833-1838.
98. Sala, G., *Impact behaviour of heat-resistant toughened composites*. Composites Part B: Engineering, 2000. **31**(3): p. 161-173.
99. Garoushi, S., et al., *Static and fatigue compression test for particulate filler composite resin with fiber-reinforced composite substructure*. dental materials, 2007. **23**(1): p. 17-23.
100. Söderholm, K.-J., *Relationship between compressive yield strength and filler fractions of PMMA composites*. Acta Odontologica Scandinavica, 1982. **40**(3): p. 145-150.
101. Gilbert, J.L., D.S. Ney, and E.P. Lautenschlager, *Self-reinforced composite poly (methyl methacrylate): static and fatigue properties*. Biomaterials, 1995. **16**(14): p. 1043-1055.
102. Kishi, H., et al., *Damping properties of thermoplastic-elastomer interleaved carbon fiber-reinforced epoxy composites*. Composites Science and Technology, 2004. **64**(16): p. 2517-2523.
103. Yasae, M., et al., *Mode I interfacial toughening through discontinuous interleaves for damage suppression and control*. Composites Part A: Applied Science and Manufacturing, 2012. **43**(1): p. 198-207.
104. Aksoy, A. and L. Carlsson, *Crack tip yield zone estimates in mode II interlaminar fracture of interleaved composites*. Engineering fracture mechanics, 1991. **39**(3): p. 525-534.
105. Scott, J. and D. Phillips, *Carbon fibre composites with rubber toughened matrices*. Journal of Materials Science, 1975. **10**(4): p. 551-562.
106. Pearson, R.A. and A.F. Yee, *Toughening mechanisms in thermoplastic-modified epoxies: I. Modification using poly (phenylene oxide)*. Polymer, 1993. **34**(17): p. 3658-3670.
107. Cardwell, B. and A.F. Yee, *Toughening of epoxies through thermoplastic crack bridging*. Journal of materials science, 1998. **33**(22): p. 5473-5484.
108. Shih, G. and L. Ebert, *The effect of the fiber/matrix interface on the flexural fatigue performance of unidirectional fiberglass composites*. Composites science and technology, 1987. **28**(2): p. 137-161.
109. Newaz, G.M., *Influence of matrix material on flexural fatigue performance of unidirectional composites*. Composites Science and Technology, 1985. **24**(3): p. 199-214.
110. Caprino, G. and G. Giorleo, *Fatigue lifetime of glass fabric/epoxy composites*. Composites Part A: Applied Science and Manufacturing, 1999. **30**(3): p. 299-304.
111. Agarwal, B. and S. Joneja, *Strain-Controlled Flexural Fatigue of Unidirectional Composites* 1982, DTIC Document.

112. Cox, K.B., N.-P. Vedvik, and A.T. Echtermeyer, *Flexural Fatigue of Unbalanced Glass-Carbon Hybrid Composites*. Journal of Solar Energy Engineering.
113. Weber, I. and P. Schwartz, *Monitoring bending fatigue in carbon-fibre/epoxy composite strands: a comparison between mechanical and resistance techniques*. Composites Science and Technology, 2001. **61**(6): p. 849-853.
114. Couillard, R.A.A. and P. Schwartz, *Bending fatigue of carbon-fiber-reinforced epoxy composite strands*. Composites science and technology, 1997. **57**(2): p. 229-235.
115. Caprino, G. and A. D'Amore, *Flexural fatigue behaviour of random continuous-fibre-reinforced thermoplastic composites*. Composites science and technology, 1998. **58**(6): p. 957-965.
116. Belingardi, G., M. Cavatorta, and C. Frasca, *Bending fatigue behavior of glass-carbon/epoxy hybrid composites*. Composites Science and Technology, 2006. **66**(2): p. 222-232.
117. Drissi-Habti, M., et al., *BENDING FATIGUE BEHAVIOR OF SMART GLASS-FIBER REINFORCED VINYLESTER COMPOSITE MATERIALS*.
118. Reis, P., et al., *Flexural behaviour of hybrid laminated composites*. Composites Part A: Applied Science and Manufacturing, 2007. **38**(6): p. 1612-1620.
119. Van Paepegem, W. and J. Degrieck, *Experimental set-up for and numerical modelling of bending fatigue experiments on plain woven glass/epoxy composites*. Composite structures, 2001. **51**(1): p. 1-8.
120. Cui, W.C. and M.R. Wisnom, *Contact finite element analysis of three-and four-point short-beam bending of unidirectional composites*. Composites science and technology, 1992. **45**(4): p. 323-334.
121. Jamison, R.D., et al., *Characterization and Analysis of Damage Mechanisms in Tension-Tension Fatigue of Graphite/Epoxy Laminates*, in *ASTM STP-836*. 1984, American Society for Testing and Materials: Philadelphia, PA. p. 21-55.
122. Zhang, J., et al., *Interlaminar Fracture Toughness and Fatigue Delamination Growth of CF/EP Composites with Matrices Modified by Nano-silica and CTBN rubber*, in *13th International Conference on Fracture (ICF13)*. 2013: Beijing, China.
123. Manjunatha, C., et al., *The tensile fatigue behavior of a glass-fiber reinforced plastic composite using a hybrid-toughened epoxy matrix*. Journal of composite materials, 2010. **44**(17): p. 2095-2109.
124. Hojo, M., et al., *Mode I delamination fatigue properties of interlayer-toughened CF/epoxy laminates*. Composites Science and Technology, 2006. **66**(5): p. 665-675.
125. Chan, W.S., *Delamination arrester—an adhesive inner layer in laminated composites*, in *Composite Materials: Fatigue and Fracture*. 1986, ASTM International.
126. Chan, W.S., C. Rogers, and S. Aker. *Improvement of edge delamination strength of composite laminates using adhesive layers*. in *Composite materials: testing and design (seventh conference)*. 1986. ASTM International.
127. Sela, N. and O. Ishai, *Interlaminar fracture toughness and toughening of laminated composite materials: a review*. Composites, 1989. **20**(5): p. 423-435.
128. Philippidis, T. and V. Passipoularidis, *Residual strength after fatigue in composites: Theory vs. experiment*. International Journal of Fatigue, 2007. **29**(12): p. 2104-2116.
129. Whitworth, H., *Evaluation of the residual strength degradation in composite laminates under fatigue loading*. Composite Structures, 2000. **48**(4): p. 261-264.
130. Yang, J.N., *Fatigue and residual strength degradation for graphite/epoxy composites under tension-compression cyclic loadings*. Journal of Composite Materials, 1978. **12**(1): p. 19-39.
131. Van Paepegem, W. and J. Degrieck, *A new coupled approach of residual stiffness and strength for fatigue of fibre-reinforced composites*. International Journal of Fatigue, 2002. **24**(7): p. 747-762.
132. Shirazi, A. and A. Varvani-Farahani, *A stiffness degradation based fatigue damage model for FRP composites of (0/θ) laminate systems*. Applied Composite Materials, 2010. **17**(2): p. 137-150.

133. Haojie, S., Y. Weixing, and W. Yitao, *Synergistic Damage Mechanic Model for Stiffness Properties of Early Fatigue Damage in Composite Laminates*. Procedia Engineering, 2014. **74**: p. 199-209.
134. Highsmith, A.L. and K.L. Reifsnider, *Stiffness-reduction mechanisms in composite laminates*. Damage in composite materials, ASTM STP, 1982. **775**: p. 103-117.
135. Gudmundson, P. and S. Östlund, *First order analysis of stiffness reduction due to matrix cracking*. Journal of composite materials, 1992. **26**(7): p. 1009-1030.
136. Yao, W. and N. Himmel, *A new cumulative fatigue damage model for fibre-reinforced plastics*. Composites Science and Technology, 2000. **60**(1): p. 59-64.
137. Whitworth, H., *Modeling stiffness reduction of graphite/epoxy composite laminates*. Journal of composite materials, 1987. **21**(4): p. 362-372.
138. Yang, J., et al., *A stiffness degradation model for graphite/epoxy laminates*. Journal of Composite Materials, 1990. **24**(7): p. 753-769.
139. Talreja, R., *Stiffness properties of composite laminates with matrix cracking and interior delamination*. Engineering Fracture Mechanics, 1986. **25**(5): p. 751-762.
140. O'Brien, T.K. and K.L. Reifsnider, *Fatigue damage evaluation through stiffness measurements in boron-epoxy laminates*. Journal of composite materials, 1981. **15**(1): p. 55-70.
141. Nijssen, R.P.L., *Fatigue life prediction and strength degradation of wind turbine rotor blade composites*. 2006.
142. Marsh, K.J., R.A. Smith, and R.O. Ritchie, *Fatigue Crack Measurement: Techniques and Applications*. 1991, London, UK: Chameleon Press Ltd.
143. Larsen, J.M., *Small-crack test methods*. Vol. 1149. 1992: ASTM International.
144. Laz, P. and B. Hillberry, *Fatigue life prediction from inclusion initiated cracks*. International Journal of Fatigue, 1998. **20**(4): p. 263-270.
145. Pameijer, C. and R. Stallard, *Application of replica techniques for use with scanning electron microscopes in dental research*. Journal of dental research, 1972. **51**(2): p. 672-672.
146. Newman, J.A., et al., *Replica-based crack inspection*. Engineering Fracture Mechanics, 2009. **76**(7): p. 898-910.
147. Vallittu, P., *Fracture surface characteristics of damaged acrylic-resinbased dentures as analysed by SEM-replica technique*. Journal of oral rehabilitation, 1996. **23**(8): p. 524-529.
148. Pang, H. and P. Reed, *Microstructure effects on high temperature fatigue crack initiation and short crack growth in turbine disc nickel-base superalloy Udimet 720Li*. Materials Science and Engineering: A, 2007. **448**(1): p. 67-79.
149. Lindley, T., *Fretting fatigue in engineering alloys*. International journal of fatigue, 1997. **19**(93): p. 39-49.
150. Chaloner, W.G. and M.E. Collinson, *Application of SEM to a sigillarian impression fossil*. Review of Palaeobotany and palynology, 1975. **20**(1-2): p. 85-101.
151. Skilbred, A. and H. Fjeld. *Scanning electron microscopy (SEM)*. 2013 [cited 2017 27/07/2017]; Available from: <https://www.slideshare.net/waqasjavaid547/scanning-electron-microscopy-28066279>.
152. Humphreys, F.J., *Scanning Electron Microscopy(of High Temperature Materials)*. The Institute of Metals, Microstructural Characterisation, 1988: p. 94-159.
153. Greenhalgh, E.S., *Characterisation of mixed-mode delamination growth in carbon-fibre composites*. 1998, Imperial College London (University of London).
154. Johannesson, T., P. Sjöblom, and R. Seldén, *The detailed structure of delamination fracture surfaces in graphite/epoxy laminates*. Journal of Materials Science, 1984. **19**(4): p. 1171-1177.
155. Singh, S. and E. Greenhalgh. *Micromechanisms of interlaminar fracture in carbon-epoxy composites at multidirectional ply interfaces*. in *4th International Conference on Deformation and Fracture of Composites*. 1997.

156. Sjögren, A., et al., *Interlaminar crack propagation in CFRP: Effects of temperature and loading conditions on fracture morphology and toughness*, in *Composite Materials: Testing, Design, and Acceptance Criteria*. 2002, ASTM International.
157. Hiley, M., *Fractographic study of static and fatigue failures in polymer composites*. *Plastics, rubber and composites*, 1999. **28**(5): p. 210-227.
158. O'Brien, T.K., *Composite Interlaminar Shear Fracture Toughness, G IIc: Shear Measurement or Sheer Myth?*, in *Composite Materials: Fatigue and Fracture: 7th Volume*. 1998, ASTM International.
159. WALKER, G., *COMPOSITE FAILURE ANALYSIS HANDBOOK*. 1997.
160. Datta, S., *Investigation of the micromechanics of delamination in fibre reinforced composites*. 2005, Imperial College London (University of London).
161. Smith, B.W. and R.A. Grove, *Determination of crack propagation directions in graphite/epoxy structures*, in *Fractography of Modern Engineering Materials: Composites and Metals*. 1987, ASTM International.
162. Shikhmanter, L., B. Cina, and I. Eldror, *Fractography of multidirectional CFRP composites tested statically*. *Composites*, 1991. **22**(6): p. 437-444.
163. Franz, H., *Microfractography of fibre reinforced composite materials*. *Microstructural and Microanalytical Characterization in Material Development and Quality Control*, 1990: p. 221-232.
164. Asp, L.E., A. Sjögren, and E.S. Greenhalgh, *Delamination growth and thresholds in a carbon/epoxy composite under fatigue loading*. *Journal of Composites, Technology and Research*, 2001. **23**(2): p. 55-68.
165. Hiley, M., *GARTEUR AG27 Fractographic Aspects of Fatigue Failure in Complex Laminates and Structures*. GARTEUR Final Report TP, 2007. **151**.
166. Heutling, F., H.E. Franz, and K. Friedrich, *Mikrofraktographische Analyse des Delaminationswachstums in zyklisch belasteten Kohlenstoffaser/Duroplastharz-Verbundwerkstoffen*. *Materialwissenschaft und Werkstofftechnik*, 1998. **29**(5): p. 239-253.
167. Baas, S., *GARTEUR AG14: Fractography of Composites*. GARTEUR TP, 1994(083).
168. Friedrich, K., *Application of fracture mechanics to composite materials*. Vol. 6. 2012: Elsevier.
169. *General introduction to X-ray tomography imaging*. 2011 [cited 2017 21/09/2017]; Available from: <http://www.mxif.manchester.ac.uk/resources/introduction/x-ray-tomography-imaging>.
170. Tsao, C. and H. Hocheng, *Computerized tomography and C-Scan for measuring delamination in the drilling of composite materials using various drills*. *International Journal of Machine Tools and Manufacture*, 2005. **45**(11): p. 1282-1287.
171. Griffiths, B. *A350 & A400M wing spars: A study in contrasts*. 2013 [cited 2017 28/07/2017]; Available from: <http://www.compositesworld.com/articles/a350-a400m-wing-spars-a-study-in-contrasts>.
172. Jones, S., *Email: 977-2 prepreg*, S. Jones, Editor. 2013, Cytec
173. ASM_Aerospace. *Aluminum 6061-T6; 6061-T651*. [cited 2017 28/07/2017]; Available from: <http://asm.matweb.com/search/SpecificMaterial.asp?bassnum=ma6061t6>.
174. Cytec, *Cycom 977-2 Epoxy Resin System - Technical Data Sheet*. 2013.
175. Performance_Composites. *Mechanical Properties of Carbon Fibre Composite Materials, Fibre / Epoxy resin (120°C Cure)*. 2009 [cited 2017 28/07/2017]; Available from: http://www.performance-composites.com/carbonfibre/mechanicalproperties_2.asp.
176. ASM_Aerospace. *AISI Type 302 Stainless Steel, tested at 21°C (70°F)*. [cited 2017 28/07/2017]; Available from: <http://asm.matweb.com/search/SpecificMaterial.asp?bassnum=MQ302AN>.
177. Baker, A., J. Mead, and C. Harper, *Modern Plastics Handbook*. 1999, Harper, CA ed.

178. Sigma_Aldrich. *Polyethylene glycol 20000*. 2017 [cited 2017 28/07/2017]; Available from: <http://www.sigmaaldrich.com/catalog/product/mm/818897?lang=en®ion=GB>.
179. Soule, S. and K. Cashman, *The mechanical properties of solidified polyethylene glycol 600, an analog for lava crust*. Journal of volcanology and geothermal research, 2004. **129**(1): p. 139-153.
180. Al-Nasassrah, M.A., F. Podczek, and J.M. Newton, *The effect of an increase in chain length on the mechanical properties of polyethylene glycols*. European journal of pharmaceuticals and biopharmaceuticals, 1998. **46**(1): p. 31-38.
181. Microfab_Inc. *Pneumatics & Temperature Controllers*. [cited 2017 29/07/2017]; Available from: <http://www.microfab.com/pressuretemp-control>.
182. Microfab_Inc. *Low Temperature Devices*. [cited 2017 29/07/2017]; Available from: <http://www.microfab.com/dispensing-devices/low-temp-devices>.
183. Sigma_Aldrich. *Polyethylene glycol 1500*. [cited 2017 29/07/2017]; Available from: <http://www.sigmaaldrich.com/catalog/product/usp/1546503?lang=en®ion=GB>.
184. Sigma_Aldrich. *N,N-Dimethylformamide dimethyl acetal*. [cited 2017 29/07/2017]; Available from: <http://www.sigmaaldrich.com/catalog/product/aldrich/140732?lang=en®ion=GB>.
185. Sigma_Aldrich. *Poly(methyl methacrylate)*. [cited 2017 29/07/2017]; Available from: <http://www.sigmaaldrich.com/catalog/product/aldrich/200336?lang=en®ion=GB>.
186. NetComposites. *Vacuum Bagging*. [cited 2017 30/07/2017]; Available from: <http://netcomposites.com/guide-tools/guide/manufacturing/vacuum-bagging/>.
187. ISO, E., *527-4: 1997 Plastics*. Determination of tensile properties. Test conditions for isotropic and orthotropic fibre-reinforced plastic composites.
188. PerkinElmer, *Characterization of Electronic Materials Using Thermal Analysis*, PerkinElmer, Editor. 2011, PerkinElmer: Waltham, MA. p. 5.
189. Labronici, M. and H. Ishida, *Effect of degree of cure and fiber content on the mechanical and dynamic mechanical properties of carbon fiber reinforced PMR-15 polyimide composites*. Polymer composites, 1999. **20**(4): p. 515-523.
190. Lee, W.I., A.C. Loos, and G.S. Springer, *Heat of reaction, degree of cure, and viscosity of Hercules 3501-6 resin*. Journal of Composite Materials, 1982. **16**(6): p. 510-520.
191. Mutlur, S., *Thermal Analysis of Composites Using DSC*. Advanced Topics in Characterization of Composites, 2004: p. 11-33.
192. Menard, K.P., *Dynamic mechanical analysis: a practical introduction*. 2008: CRC press.
193. Akay, M., *Effects of prepreg ageing and post-cure hygrothermal conditioning on the mechanical behaviour of carbon-fibre/epoxy laminates*. Composites science and technology, 1990. **38**(4): p. 359-370.
194. Sabzevari, S.M., S. Alavi-Soltani, and B. Minaie, *Effect of thermoplastic toughening agent on glass transition temperature and cure kinetics of an epoxy prepreg*. Journal of thermal analysis and calorimetry, 2011. **106**(3): p. 905-911.
195. Arnold, F. and s. Thoman. *B-Staging of toughened epoxy composites*. 1996 [cited 2017 31/07/2017]; Available from: http://www.thinkcompositesllc.com/files/barcelona/What%20is%20B-stage_.pdf.
196. Polyankiy, M. *Optical constants of (C5H8O2)n (Poly(methyl methacrylate), PMMA)*. 2016 [cited 2017 31/07/2017]; Available from: [https://refractiveindex.info/?shelf=organic&book=poly\(methyl_methacrylate\)&page=Szczurowski](https://refractiveindex.info/?shelf=organic&book=poly(methyl_methacrylate)&page=Szczurowski).
197. NTT_AT. *High Refractive Index / Low Refractive Index Resins*. [cited 2017 31/07/2017]; Available from: http://www.ntt-at.com/product/hl_resins/.
198. Division, M.I.A.a.T. *Surface energy and wetting*. 2015 [cited 2018 06/01/2018]; Available from: <https://multimedia.3m.com/mws/media/7555260/innovations-in-bonding-to-low-surface-energy-white-paper.pdf>.

199. Liu, D. and T. Wang, *Instability of hydrophobic and viscoelastic polymer thin films in water at room temperature*. Journal of Physics: Condensed Matter, 2013. **25**(41): p. 415101.
200. Reiter, G., *Dewetting of thin polymer films*. Physical Review Letters, 1992. **68**(1): p. 75.
201. Sasaki, T., T. Uchida, and K. Sakurai, *Effect of crosslink on the characteristic length of glass transition of network polymers*. Journal of Polymer Science Part B: Polymer Physics, 2006. **44**(14): p. 1958-1966.
202. Truscott, T.T. and A.H. Techet, *A spin on cavity formation during water entry of hydrophobic and hydrophilic spheres*. Physics of Fluids, 2009. **21**(12): p. 121703.
203. AZO_Materials. *Wafer Testing – A Guide to Testing Wafer Fracture Strength*. 2017 [cited 2017 06/08/2017]; Available from: <https://www.azom.com/article.aspx?ArticleID=13812>.
204. Amiri, A. and M. Cavalli, *Experimental investigation of fatigue behavior of carbon fiber composites using fully reversed four point bending test*, in *Composite Materials and Joining Technologies for Composites, Volume 7*. 2013, Springer. p. 131-137.
205. BSI, *Fibre-Reinforced Plastic Composites - Determination of Flexural Properties*. 2011: Brussels, Belgium. p. 26.
206. Kalpakjian, S. and S.R. Schmid, *Manufacturing processes for engineering materials*. Vol. 5. 2010: Pearson education.
207. Gowayed, Y. and H. Fan, *Fatigue behavior of textile composite materials subjected to tension-tension loads*. Polymer composites, 2001. **22**(6): p. 762-769.
208. Lee, B. and D. Liu, *Cumulative damage of fiber-reinforced elastomer composites under fatigue loading*. Journal of Composite Materials, 1994. **28**(13): p. 1261-1286.
209. Wang, H. and A. Belarbi, *Static and fatigue bond characteristics of FRP rebars embedded in fiber-reinforced concrete*. Journal of Composite Materials, 2010. **44**(13): p. 1605-1622.
210. Cvitkovich, M.K., T.K. O'Brien, and P.J. Minguet, *Fatigue debonding characterization in composite skin/stringer configurations*, in *Composite Materials: Fatigue and Fracture: 7th Volume*. 1998, ASTM International.
211. Peck, A.W., *An experimental investigation of transverse tension fatigue characterization of IM6/3501-6 composite materials using a three-point bend test*, in *Composite Materials: Fatigue and Fracture: 7th Volume*. 1998, ASTM International.
212. John, R., J.R. Jira, and J.M. Larsen, *Effect of stress and geometry on fatigue crack growth perpendicular to fibers in Ti-6Al-4V reinforced with unidirectional SiC fibers*, in *Composite Materials: Fatigue and Fracture: 7th Volume*. 1998, ASTM International.
213. Buchanan, D.J., R. John, and K.E. Goecke, *Influence of Temperature and Stress Ratio on the Low-Cycle Fatigue Behavior of Trimarc-1/Ti-6Al-2Sn-4Zr-2Mo*, in *Composite Materials: Fatigue and Fracture: 7th Volume*. 1998, ASTM International.
214. Hutchinson, J.W. and T.Y. Wu, *Advances in applied mechanics*. Vol. 27. 1990: Academic Press.
215. Fereshteh-Saniee, F., G. Majzoobi, and M. Bahrami, *An experimental study on the behavior of glass-epoxy composite at low strain rates*. Journal of Materials Processing Technology, 2005. **162**: p. 39-45.
216. Dalai, R. and B. Ray, *Loading Rate Sensitivity of Fibrous Composite Materials*. 2010.
217. Banakar, P., H. Shivananda, and H. Niranjana, *Influence of fiber orientation and thickness on tensile properties of laminated polymer composites*. Int. J. Pure Appl. Sci. Technol, 2012. **9**(1): p. 61-68.
218. Ku, H., et al., *A review on the tensile properties of natural fiber reinforced polymer composites*. Composites Part B: Engineering, 2011. **42**(4): p. 856-873.
219. Gamstedt, K. and R. Talreja, *Fatigue Damage Mechanisms in Unidirectional Carbon-Fibre-Reinforced Plastics*. Journal of Materials Science, 1999(34).

220. Jones, C., et al. *The environmental fatigue behaviour of reinforced plastics*. in *Proceedings of the Royal Society of London A: Mathematical, Physical and Engineering Sciences*. 1984. The Royal Society.
221. El-Magd, E., *Mechanical properties at high strain rates*. *Le Journal de Physique IV*, 1994. **4**(C8): p. C8-149-C8-170.
222. Sabbagh, J., J. Vreven, and G. Leloup, *Dynamic and static moduli of elasticity of resin-based materials*. *Dental Materials*, 2002. **18**(1): p. 64-71.
223. Genedy, M., et al., *Improving Fatigue Performance of GFRP Composite Using Carbon Nanotubes*. *Fibers*, 2015. **3**(1): p. 13-29.
224. Pitarresi, G., D. Tumino, and A. Mancuso, *Thermo-mechanical behaviour of flax-fibre reinforced epoxy laminates for industrial applications*. *Materials*, 2015. **8**(11): p. 7371-7388.
225. Chou, T.-W., *Microstructural design of fiber composites*. 2005: Cambridge University Press.
226. Joffe, R., *Damage accumulation and stiffness degradation in composite laminates*. 1999, Luleå tekniska universitet.
227. Huang, Y., et al., *Mechanisms of toughening thermoset resins*. 1993, ACS Publications.
228. Pearson, R. and A. Yee, *Influence of particle size and particle size distribution on toughening mechanisms in rubber-modified epoxies*. *Journal of Materials Science*, 1991. **26**(14): p. 3828-3844.
229. Brown, E.N., S.R. White, and N.R. Sottos, *Retardation and repair of fatigue cracks in a microcapsule toughened epoxy composite—Part II: In situ self-healing*. *Composites Science and Technology*, 2005. **65**(15): p. 2474-2480.
230. Ivanov, D.S., et al., *Failure analysis of triaxial braided composite*. *Composites Science and Technology*, 2009. **69**(9): p. 1372-1380.
231. Poursartip, A. and P.W.R. Beaumont, *The Fatigue Damage Mechanics of a Carbon Fibre Composite Laminate: I--Development of the Model*. *Composites Science and Technology*, 1986. **25**(3): p. 193-218.
232. Gamstedt, E. and B. Sjögren, *Micromechanisms in tension-compression fatigue of composite laminates containing transverse plies*. *Composites Science and Technology*, 1999. **59**(2): p. 167-178.
233. Steif, P.S., *Stiffness reduction due to fiber breakage*. *Journal of composite materials*, 1984. **18**(2): p. 153-172.
234. Jespersen, K.M., et al. *Micromechanical time-lapse X-ray CT study of fatigue damage in uni-directional fibre composites*. in *20th International Conference on Composite Materials (ICCM20)*. 2015. ICCM20 Secretariat.
235. Schulte, K., *Stiffness reduction and development of longitudinal cracks during fatigue loading of composite laminates*. *Mechanical characterisation of load bearing fibre composite laminates*, 1985: p. 36-54.
236. Schulte, K., C. Baron, and N. Neubert, *Damage development in carbon fibre epoxy laminates: cyclic loading*. *Advanced Materials Research and Developments for Transport*. 1985. *Composites*, 1985: p. 281-288.
237. Schulte, K., E. Reese, and T. Chou. *Fatigue behaviour and damage development in woven fabric and hybrid fabric composites*. in *Sixth International Conference on Composite Materials (ICCM-VI) & Second European Conference on Composite Materials (ECCM-II)*. 1987.
238. Reifsnider, K.L. *Life prediction analysis: directions and divagations*. in *Sixth International Conference on Composite Materials and Second European Conference on Composite Materials (ICCM & ECCM)*. 1987.
239. BSI, *Plastics - Determination of Tensile Properties*, in *Part 5: Test Conditions for Unidirectional Fibre-Reinforced Plastic Composites*. 2009: Brussels, Belgium. p. 20.
240. Lv, L., et al., *Micromechanical Properties of a New Polymeric Microcapsule for Self-Healing Cementitious Materials*. *Materials*, 2016. **9**(12): p. 1025.

241. Ji, G., et al., *Mechanism of interactions of eggshell microparticles with epoxy resins*. Polymer Engineering & Science, 2009. **49**(7): p. 1383-1388.
242. Zhao, C., et al., *Flame retardant and toughening mechanisms of core-shell microspheres*. RSC Advances, 2015. **5**(104): p. 85329-85337.
243. Bishop, S.M., *The significance of defects on the failure of fibre composites*. 1981, ADVISORY GROUP FOR AEROSPACE RESEARCH AND DEVELOPMENT NEUILLY-SUR-SEINE (FRANCE).
244. Cantwell, W. and J. Morton, *The significance of damage and defects and their detection in composite materials: a review*. The journal of strain analysis for engineering design, 1992. **27**(1): p. 29-42.
245. Wisnom, M.R., T. Reynolds, and N. Gwilliam, *Reduction in interlaminar shear strength by discrete and distributed voids*. Composites Science and Technology, 1996. **56**(1): p. 93-101.
246. Thio, Y.S., J. Wu, and F.S. Bates, *Epoxy toughening using low molecular weight poly (hexylene oxide)– poly (ethylene oxide) diblock copolymers*. Macromolecules, 2006. **39**(21): p. 7187-7189.
247. Hodgkin, J., G. Simon, and R. Varley, *Thermoplastic toughening of epoxy resins: a critical review*. Polymers for Advanced Technologies, 1998. **9**(1): p. 3-10.
248. Varley, R.J., *Toughening of epoxy resin systems using low-viscosity additives*. polymer International, 2004. **53**(1): p. 78-84.
249. Borodulin, A., *Plasticizers for epoxy adhesives and binders*. Polymer Science Series D, 2013. **6**(1): p. 59-62.
250. Liu, D., *Impact-induced delamination—a view of bending stiffness mismatching*. Journal of composite materials, 1988. **22**(7): p. 674-692.
251. Kim, J.-K. and M.-L. Sham, *Impact and delamination failure of woven-fabric composites*. Composites Science and Technology, 2000. **60**(5): p. 745-761.
252. Chamis, C.C., M.P. Hanson, and T.T. Serafini. *Impact resistance of unidirectional fiber composites*. in *Composite Materials: Testing and Design (Second Conference)*. 1972. ASTM International.